Experimental quantification of seismic signals induced by wind turbines

Zur Erlangung des akademischen Grades eines
DOKTORS DER NATURWISSENSCHAFTEN (Dr. rer. nat.)
von der KIT-Fakultät für Physik des
Karlsruher Instituts für Technologie (KIT)
genehmigte

DISSERTATION

von

M.Sc. Toni Zieger
aus Schkeuditz

Tag der mündlichen Prüfung:	05. Juli 2019
Referent:	apl. Prof. Dr. Joachim Ritter
Korreferent:	Prof. Dr. Andreas Rietbrock

Für Opa ...

Abstract

The effect of climate change has a global impact and affects our environment more and more. As a consequence climate-friendly technologies to produce green electricity are developing rapidly. One way to produce such electricity is the transformation of kinetic energy of the natural wind field into electrical energy by wind turbines (WTs). These WTs are controversial in a number of ways due to emissions which could for instance disturb sensitive measurements like seismic recordings. For this reason, a detailed knowledge of the radiation pattern and the propagation of WT-induced seismic signals with distance for different wind conditions is needed. This is the goal of the present study. In order to investigate the influence of the local subsurface on the attenuation behavior of the induced seismic signals this thesis analyzes recordings of more than twenty measurement campaigns at several single WTs and wind farms, focussing on different geological settings. It has been found that the different geological conditions have a clear impact on the signal propagation along linear profiles for frequencies higher than 4 Hz, illustrated by calculating an attenuation factor b. For low frequencies, geometrical spreading mostly dominates the seismic amplitude decay with distance. The resulting attenuation models form an essential basis for future prediction models with regard to the increase of the seismic noise level in a certain distance to the WTs. Furthermore, the results show an impact of WT-induced signals on recordings of seismic stations in the frequency range from 0.1 Hz to 20 Hz up to 9 km distance away relative from the location of the WTs. This specific frequency range is highly important for the detection of local earthquakes or the monitoring of the Comprehensive Nuclear-Test-Ban Treaty (CTBT).

This thesis demonstrates that the major power spectral density (PSD) peaks at seismic stations near WTs correspond to the blade-passing frequency (BPF) of the WT and its multiples. Therefore, we combined seismic recordings with high-resolution Supervisory Control and Data Acquisition (SCADA) data and numerical simulations. It was found that current numerical models are highly capable of mapping the complex process of seismic and acoustic emissions. Moreover, this interdisciplinary approach within the scope of the research project *TremAc* shows that the most prominent peak around 1.6 Hz in the PSD spectrum constitutes a result of an interaction of the first harmonic of the BPF (also known as the 6-P excitation) with the second bending mode of the tower in combination with eigenfrequencies of the WT's blades. The excited oscillations, whether they are eigenfrequencies or correspond to the BPF, are coupled through the WT's tower and the foundation to the subsurface and propagate to nearby seismic stations. Several shutdown experiments of the WTs were implemented to clearly identify the effect of a rotational motion in seismic recordings. In addition, the impact of vibrations induced by WTs on residents is analyzed with regard to the noticeability limit given in the DIN standard 4150/2+3. Observations in the free-field indicate no significant amplitudes of the ground velocity above the noticeability limit of 0.1 mm/s. These new observations provide information to improve the knowledge of WTs as a seismic source and are important for the understanding of how WT-induced signals interact with the human health as well as for finding strategies to reduce the aforementioned signals, which is important for owners of seismic stations.

Contents

Publications

Publications related to this thesis

Several chapters of this thesis have already been published in peer-reviewed scientific journals:

- *Zieger, T. and Ritter, J.R.R.* (2018), **Influence of wind turbines on seismic stations in the upper rhine graben, SW Germany**, J. Seismol., 22: 105 - 122, DOI: https://doi.org/10.1007/s10950-017-9694-9
- *Friedrich, T., Zieger, T., Forbriger, T. and Ritter, J.R.R.* (2018), **Locating wind farms by seismic interferometry and migration**, J. Seismol., 22: 1469 - 1483, DOI: https://doi.org/10.1007/s10950-018-9779-0
- *Zieger, T., Nagel, S., Lutzmann., P., Kaufmann, I., Ritter, J.R.R., Ummenhofer, T., Knödel, P. and Fischer, P.*, **Simultaneous identification of wind turbine vibrations by using seismic data, elastic modeling and laser Doppler vibrometry**, Wind Energy, *submitted*
- *Nagel, S., Zieger, T., Luhmann, B., Knödel, P., Ummenhofer, T. and Ritter, J.R.R.* (2019), **Erschütterungsemissionen von Windenergieanlagen**, Stahlbau, 88(6): 559 - 573,
  DOI: https://doi.org/10.1002/stab.201900039
- *Zieger, T., Lerbs, N., Ritter, J.R.R. and Korn, M.* (2019), **Seismic recordings for SMARTIE1: Seismic Monitoring And Research of Wind Turbine Induced Emissions 1, DEC 2018 – JAN 2019, Pfinztal, SW Germany**, GIPP Experiment and Data Archive, Potsdam, GFZ German Research Centre for Geosciences, *in press*

Presentations

Results of this thesis have already been presented at scientific national and international conferences:

- *Zieger, T. and Ritter, J.R.R.*, **Vibrations due to Wind Turbines and their Influence on Seismic Records near Landau (Germany) as part of the ongoing "TremAc" Project**, BGA 2016 Postgraduate Research in Progress Meeting, UCL London (UK), 2016
- *Zieger, T. and Ritter, J.R.R.*, **Seismische Signale an Windenergieanlagen – Lang- und Kurzzeitmessungen in SW Deutschland**, 77. Jahrestagung der Deutschen Geophysikalischen Gesellschaft (DGG), Potsdam (Germany), 2017
- *Zieger, T. and Ritter, J.R.R.*, **The Interaction between Wind Turbines and Seismic Stations - New Results at Locations with Different Ground Conditions**, 78. Jahrestagung der Deutschen Geophysikalischen Gesellschaft (DGG), Leoben (Austria), 2018
- *Zieger, T. and Ritter, J.R.R.*, **Wind Turbines and their Emitted Seismic Wavefields: Results from Different Locations**, European Geosciences Union General Assembly (EGU), Vienna (Austria), 2018
- *Zieger, T. and Ritter, J.R.R.*, **Wind turbines and their emissions – an interdisciplinary approach to validate the induced seismic and acoustic wavefields**, European Geosciences Union General Assembly (EGU), Vienna (Austria), 2019

Publications not related to this thesis

Scientific publications by the author that are not related to this thesis:

- *Zieger, T., Sens-Schönfelder, C., Ritter, J.R.R., Lühr, B.G., Dahm, T.* (2016), **P-wave scattering and the distribution of heterogeneity around Etna volcano**, Ann. of Geophys., 59(4), DOI: https://doi.org/10.4401/ag-7085

1 Introduction

1.1 Motivation

Using seismic recordings of very sensitive instruments, seismologists are able to resolve inner structures of the Earth, including small heterogeneities inside the lower and upper mantle and the crust. Significant technical progress in the development of seismic sensors allows scientists to detect extremely weak ground motion amplitudes generated by small local earthquakes or microseismic noise. These recordings help to understand regional, small-scale structures in much more detail as before. Additionally, they are important for monitoring induced seismicity, for example close to geothermal power plants (e.g. Spies et al., 2017).
To detect earthquakes with magnitudes $M_L < 2$, which are common for induced seismic events (Baisch and Vörös, 2010), it is necessary for seismological stations to record at very low seismic noise level smaller than $\pm$ 1 $\frac{\mu m}{s}$ for 95 % of the ground velocity amplitudes (Baisch et al., 2012). To achieve this objective, those sensitive sensors must be deployed at protected sites far away from cities or industrial areas where the natural and the anthropogenic impact on seismic recordings is very low. An alternative is the use of borehole stations in order to reduce the seismic noise level and to fulfill the tasks assigned to each specific station (Withers et al., 1996).
Following the Fukushima nuclear disaster in 2011 and the change of the energy policy in Germany, the number of operating wind turbines (WTs) has increased rapidly. Such WTs, which constitute an opportunity for environmental-friendly electrical power in contrast to nuclear or coal-fired power plants, are often located in sparsely populated regions in order to reduce the impact of vibrations and sound emissions on residents. These regions, however, are also likely areas for existing and future seismometer deployments for the reasons mentioned above. Moreover, this spatial coincidence already generates a significant impact on seismic recordings of existing deployments within a frequency range from 0.1 Hz to 20 Hz, which is highly important for the detection of local earthquakes (Hensch et al., 2019) or the monitoring of the Comprehensive Nuclear-Test-Ban Treaty (CTBT, Stammler and Ceranna, 2016). Besides the influence on seismic recordings, also other highly sensitive technologies which rely on a motionless subsurface (e.g. gravitational wave observatories or high-resolution microscopy) could be influenced by WT-induced signals (e.g. Saccorotti et al., 2011). It is therefore of fundamental importance for all those facilities to understand the seismic radiation pattern of nearby WTs and the attenuation of emitted seismic signals with distance, dependent on the dominant local geology. However, systematic observations of WT-induced signals are rather sparse and the excitation of such signals are not fully understood, especially in comparison with meteorological and plant-specific data, respectively, like the rotation rate of a WT.
There are only a few investigations with regard to the influence of WT-induced signals on seismological recordings, especially in comparison with different geological subsurfaces. The most comprehensive study has been published by Styles et al. (2005). They studied effects of wind farms on seismic recordings at the Eskdalemuir Array in Scotland, United Kingdom. In the framework of this study they were able to identify the characteristic frequencies of WTs inside the wind farm such as the blade-passing frequency (BPF, three times their rotation rate) and its multiples. They assumed seismic wave propagation for induced seismic signals happens as vertically polarized P-SV (Rayleigh) wave excited by nearby WTs and observed an increasing amplitude with increasing wind speed. Schofield (2001) determined a $1/r$ attenuation model (r is defined as distance between the WT and the observation point) for seismic measurements at the Stateline Wind Project. A spectral peak at around 4.3 Hz was detected at a site about 18 km away from the wind farm. Furthermore, Schofield (2001) assumed a prediction model for the

seismic amplitude at the Laser Interferometer Gravitational-Wave Observatory (LIGO) after the start-up of future wind farms, depending on the number of WTs and the distance to the recording stations. Widmer-Schnidrig et al. (2004) analyzed seismic recordings in the vicinity of a single WT at Lossburg, Germany. They detected a tilt up to $\pm$ 50 µrad of the baseplate and determined an attenuation model with $1/r$ (for frequencies between 9.5 Hz and 12 Hz) and $1/r^2$ (for 2.5 Hz). Saccorotti et al. (2011) observed the influence of WT-induced seismic signals in the vicinity of the Virgo Gravitational Wave Observatory in Italy. By calculating several power spectral density (PSD) spectra they detected the most significant PSD peak at a frequency of about 1.7 Hz up to 11 km distance away relative from the wind farm. A recent study on the influence of wind farms on seismic recordings was presented by Stammler and Ceranna (2016). The authors observed significant signals in the background noise of seismic stations at the Gräfenberg array (GRF) in southern Germany which correlates with the deployment of new WTs in the vicinity of the array. To prove the correlation between an increasing background noise with the installation of WTs they analyzed data before and after the installation and compared the corresponding PSD spectra. The wind-dependent seismic noise level of the GRF seismic stations increased significantly after the start-up of new WTs. This led to a higher threshold for signal detections during time periods with high wind speeds, especially for seismic stations in the immediate vicinity of the WTs. Another recent study on seismic analysis at two wind farms in Germany was published by Flores Estrella et al. (2017). They proposed an amplitude attenuation model for both wind farms, depending strongly on the different local geology. Therefore, the factor b differs significantly from 0.73 to 1.87 when fitting a model proportional to $1/r^b$. Westwood and Styles (2017) analyzed the seismic wavefield around a WT using polarization analysis. They identified polarized surface waves as the predominant wave type for blade rotation harmonics. The impact of WTs on a seismic monitoring network for natural gas fields in northern Germany was shown by Neuffer and Kremers (2018). They found evidence for emitted Rayleigh waves with a back-azimuth pointing to WTs located near the network in a frequency range from 3 Hz to 4 Hz. Marcillo and Carmichael (2017) developed an algorithm to automatically detect WT-induced signals in seismic data and tested the approach within the United States National Seismic Network (USNSN) in Texas, USA.

As part of the research project *TremAc* which has the goal of developing objective criteria for vibration and sound emissions of onshore WTs, this thesis provides a valuable contribution to understand WTs as a seismic noise source. The project includes several partners of different German universities, namely Karlsruhe Insitute of Technology (KIT), University of Stuttgart, Technical University of Munich (TUM), Bielefeld University and Martin Luther University Halle–Wittenberg as well as MesH Engineering GmbH and Enercon as industrial partners. *TremAc* is funded by the Federal Ministry for Economic Affairs and Energy (project number: 0325839). Main goals of this project are the development of prognosis and simulation models for sound and vibration emissions related to WTs and their interaction with structures as well as their propagation with distance. An example of a generic WT model is given in Klein et al. (2018). Here the authors developed a process chain in order to regard airborne noise and structure-borne noise using multi-body simulations (MBS). These models are validated using seismic (Fig. 1.1, red) and acoustic (Fig. 1.1, black) measurements. Furthermore, a sound data base is created in terms of environmental health and environmental psychology to promote an objective discussion of potential health risks of WTs (Fig. 1.1, red cross).

The main goal of this thesis is to identify WT-induced seismic signals in terms of their spectral content and to evaluate their impact on seismic recordings. Therefore, it is necessary to determine the attenuation behavior of such signals with respect to the local geological setting. These results can be used to develop prediction models for future WTs, particularly with regard to the potential increase of the seismic noise level of permanent seismic stations in their vicinity. Furthermore, several seismic measurements are used to validate numerical simulations of generic WT models developed in the framework of the research project *TremAc* and compared to acoustic sound measurements made by Stuttgart Wind Energy (SWE) of the University of Stuttgart. This highly interdisciplinary approach gives the opportunity to identify the main parameters for an objective assessment of vibration and sound

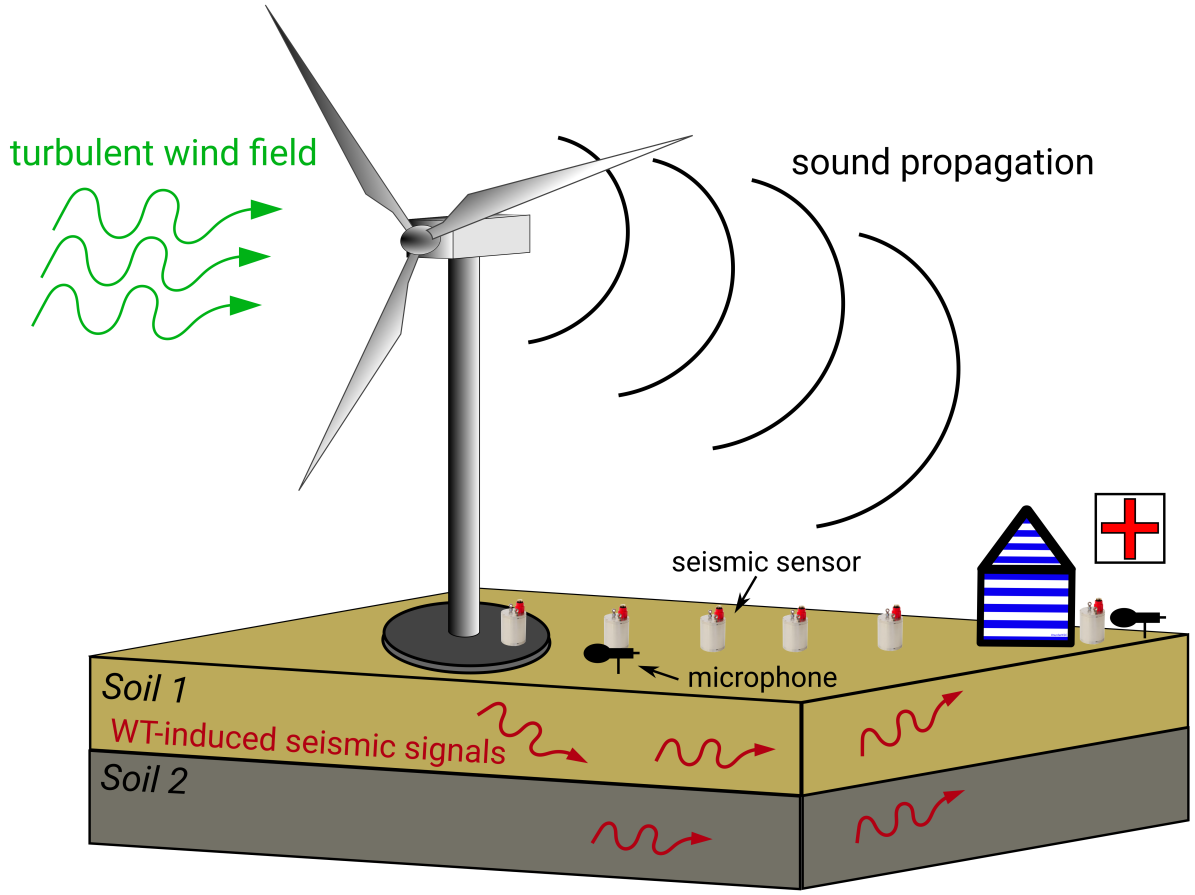

Figure 1.1: Schematic overview of the research project *TremAc*, which validates numerical simulations with seismic (red) and acoustic (black) measurements. Moreover, environmental psychological investigations of residents (red cross) should evaluate the impact on the human health.

emissions generated by WTs. In the following I formulate three key question which will be answered in the scope of this thesis:

1. Is it possible to identify WT-induced seismic signals based on their spectral content and allocate them to the BPF or different parts of the WT using seismic recordings in combination with numerical simulations?
2. What is the influence of the local subsurface on the attenuation behavior of the induced seismic signals with respect to distance?
3. Is there a significant impact of emitted vibrations on residents living in the immediate vicinity of WTs?

The answering of these key questions will form the focus of the final chapter (chapter 10) by means of results presented within this thesis.

1.2 Outline of the thesis

The structure of this thesis is briefly outlined in the following section. Several chapters have already been published in peer-reviewed journals. A short summary and the reference to the corresponding publication is given in the beginning of each chapter.
Chapter 2 is devoted to the seismological basics used in the scope of this thesis. Section 2.1 deals with the origin of the seismic noise field and its propagation with distance. In a next step the most important processing methods to analyze stochastic signals with regard to the spectral content are introduced (section 2.2.1) and evaluated (section

2.2.2). Section 2.3 describes the fundamental design and operating principles of WTs.
Chapter 3 deals with the influence of WTs on seismic stations in the Upper Rhine Graben near the town of Landau, SW Germany. The content of this chapter has already been published in Zieger and Ritter (2018).
In chapter 4 the results of a Master's thesis by Tobias Friedrich are presented about the location of wind farms using a seismic interferometry approach. The results are based on the findings of the previous chapter and, thus, directly related to this thesis. This content was published by Friedrich et al. (2018).
Chapter 5 focuses on the comparison of seismic data with numerical simulations of a single WT in Pfinztal, SW Germany, as well as the validation by optical measurements which leads to the identification of the main eigenfrequencies of the tower-nacelle-system and the influence of a rotational motion on nearby seismic recordings. This chapter has been submitted for publication (Zieger et al., 2019).
The large-scale SMARTIE1 (seismic monitoring and research of wind turbine induced emissions) experiment at the same single WT in Pfinztal is described in chapter 6. The aim of this experiment is to investigate and predict the induced seismic signal of a single WT with regard to the radiation pattern and the propagation along linear profiles.
Chapter 7 determines the differences between WT-induced seismic signals of a single WT and a wind farm. The first part of the chapter deals with the allocation of related frequency peaks in the PSD spectrum to different parts of a single WT by comparing seismic records for different operational conditions with numerical simulations. These results are submitted for publication (Nagel et al., 2019). As a next step, the seismic emissions of a wind farm are analyzed and compared to results of measurements at the single WT, using a dedicated start-up experiment where we start the wind farm turbine by turbine to determine possible interference effects.
Chapter 8 gives an overview of all detected attenuation models of WT-induced seismic signals for different geological settings, including further seismic measurement campaigns near the Black Forest Observatory (BFO) and at the "Energieberg" in Karlsruhe, Germany. These observations form the basis of future prediction models with regard to a protection radius around sites for sensitive measurements or local residents.
The results as well as recommendations for monitoring concepts found in this thesis will be discussed in chapter 9. Moreover, this chapter deals with the possible impact of WT-induced seismic signals on residents living in the vicinity of WTs.
An overall summary as well as a brief outlook is finally given in chapter 10.

2 Wind turbines as a seismic source

In this chapter I give an introduction to the seismic noise field and its sources, the main methods of seismic noise processing which I used for the present study and the fundamental functionality of wind turbines (WTs). This chapter should be treated as a brief introductory guide to the main parts of the physical theory rather than a complete review. However, it is important to understand the functional principles of WTs to put them into context along other seismic sources, such as tides or anthropogenic effects. Seismic recordings, especially in terms of arbitrary noise signals, can just give a cumulative sum of different immissions and site effects. To split these recordings into their individual sources is a main part of this study.

2.1 The seismic noise field and its sources

Any displacement or velocity of the ground is the result of forces interacting with the medium. The link between these parameters for a linearly elastic medium is represented by the Hooke's law as a first order approximation:

$$\sigma_{ij} = C_{ijkl}\varepsilon_{kl}, \tag{2.1}$$

with σ_{ij} as the stress tensor, ε_{kl} as the strain tensor and C_{ijkl} is termed the elastic tensor, representing the elastic properties of the medium. The *Einstein summation convention* will be used for the index notation. A medium is defined as *elastic* when particles return to their natural state with zero energy loss or attenuation immediately after the applied forces are removed (Aki and Richards, 1980).
For reasons of symmetry and under the assumption of an adiabatic process (which is valid for small particle velocities vs. the wave velocity), the fourth-order tensor C_{ijkl} with 81 components reduces to a tensor with 21 independent parameters for the anisotropic case (properties varying with direction) and to a tensor with only two independent parameters for an isotropic medium:

$$C_{ijkl} = \lambda\,\delta_{ij}\delta_{kl} + \mu(\delta_{il}\delta_{jk} + \delta_{ik}\delta_{jl}), \tag{2.2}$$

where λ and μ are the Lamé parameters of the material and therefore dependent on the specific medium. The parameter μ is the so-called *shear modulus* and it is defined as the ratio of shear stress to shear strain, whereas the parameter λ has no clear physical explanation. The symbol δ_{ij} is the Kronecker Delta ($\delta_{ij} = 1$ for $i = j$, $\delta_{ij} = 0$ for $i \neq j$). As mentioned before, this is the isotropic definition of the elastic tensor C_{ijkl} where the elastic properties are the same in all directions of the medium.
Inserting (2.2) into (2.1) and using the definition of the strain tensor $\varepsilon_{ij} = \frac{1}{2}(\partial_i u_j + \partial_j u_i)$, we can write the stress-strain relationship for a linearly elastic solid as

$$\sigma_{ij} = \lambda\,\delta_{ij}\partial_k u_k + \mu(\partial_i u_j + \partial_j u_i). \tag{2.3}$$

The Lamé parameters λ and μ fully describe the relation between stress and strain for an assumed isotropic medium.
If we would now like to describe the time-dependent propagation of a seismic wave (in contrast to stress and strain

which we consider as time-independent), we start with the three-dimensional *homogeneous equation of motion* (Shearer, 2009):

$$\rho \frac{\partial^2 u_i}{\partial t^2} = \partial_j \sigma_{ij}, \tag{2.4}$$

where ρ is the density.
Here we neglect body forces (gravity and source term, respectively), which is suitable for typically observed wavelengths regarding the gravity term.
Substituting (2.3) in (2.4), we get the following equation:

$$\rho \frac{\partial^2 u_i}{\partial t^2} = \partial_j [\lambda \delta_{ij} \partial_k u_k + \mu(\partial_i u_j + \partial_j u_i)]. \tag{2.5}$$

With the assumption of a homogeneous medium and by neglecting the velocity gradient terms ($\partial_j \lambda = 0$ and $\partial_j \mu = 0$) and the gravity, we can now write the seismic wave equation for a linear, isotropic Earth model. A detailed derivation can be found in Shearer (2009):

$$\rho \frac{\partial^2 \mathbf{u}}{\partial t^2} = (\lambda + 2\mu)\nabla\nabla \cdot \mathbf{u} - \mu \nabla \times \nabla \times \mathbf{u} \tag{2.6}$$

Here we used the vector notation for a clearer illustration of the equation.

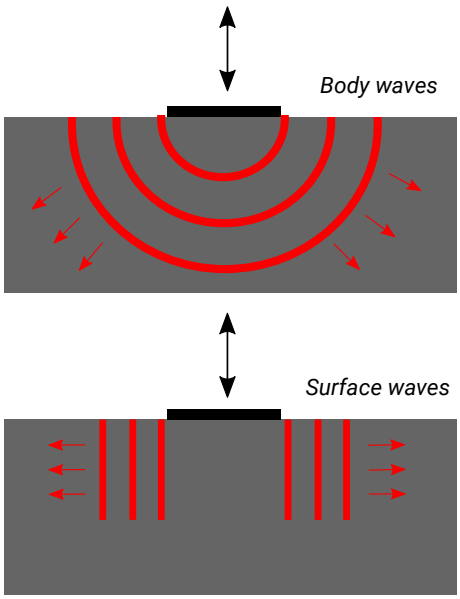

Figure 2.1: Sketch of the propagation of body waves (top) and surface waves (bottom). A distinction can be made between the spherical spreading loss of body waves on the one hand, and the cylindrical spreading loss of surface waves on the other hand, which leads to a different amplitude decay (after Ziegler, 2017).

We would now like to solve equation (2.6) for the displacement $\mathbf{u}(\mathbf{x},t)$ by assuming a point source. First, we express the displacement $\mathbf{u} = \mathbf{u}(\mathbf{x},t)$ in terms of Helmholtz potentials to work out further simplifications for the elastic wave equation (Aki and Richards, 1980):

$$\mathbf{u} = \nabla\phi + \nabla \times \mathbf{\Psi}, \qquad \nabla \cdot \mathbf{\Psi} = 0 \tag{2.7}$$

Thereby we rewrite the displacement field $\mathbf{u}$ as a sum of the gradient of a scalar potential ϕ and the curl of a vector potential $\mathbf{\Psi}$ by using the *Helmholtz theorem*. We can seperate this equation (2.7) into a P-wave component $\nabla\phi$ (zero curl) and an S-wave component $\nabla \times \mathbf{\Psi}$ (zero divergence) of $\mathbf{u}$:

$$\nabla^2\phi = \frac{\rho}{\lambda + 2\mu}\frac{\partial^2\phi}{\partial t^2} = \frac{1}{\alpha^2}\frac{\partial^2\phi}{\partial t^2}, \qquad \text{with} \quad \nabla^2\phi = \nabla \cdot \mathbf{u} \tag{2.8}$$

and

$$\nabla^2\mathbf{\Psi} = \frac{\rho}{\mu}\frac{\partial^2\mathbf{\Psi}}{\partial t^2} = \frac{1}{\beta^2}\frac{\partial^2\mathbf{\Psi}}{\partial t^2}, \qquad \text{with} \quad -\nabla^2\mathbf{\Psi} = \nabla \times \mathbf{u}. \tag{2.9}$$

These equations show that $\alpha = \sqrt{\frac{\lambda+2\mu}{\rho}}$ and $\beta = \sqrt{\frac{\mu}{\rho}}$ are equivalent to the P-wave and the S-wave velocity, respectively. The seismic velocities of a specific material can therefore be determined by the Lamé parameters and the density of the material.
By using spherical coordinates, which is necessary for spherical wave propagation, we can write (2.8) as

$$\frac{1}{r^2}\frac{\partial}{\partial r}\left[r^2\frac{\partial\phi}{\partial r}\right] - \frac{1}{\alpha^2}\frac{\partial^2\phi}{\partial t^2} = 0. \tag{2.10}$$

The propagation of a spherical seismic wave can then be expressed as

$$\phi(r,t) = \frac{1}{r} f\left(t \pm \frac{r}{\alpha}\right) \tag{2.11}$$

for a solution of the P-wave potential.
The amplitudes of the propagating body waves decay proportional to the distance due to the factor $\frac{1}{r}$. This can also be shown by the distribution of energy along the surface area of a sphere, which can be expressed as $A = 4\pi r^2$. So the amplitudes scales as $1/r$ (spherical spreading loss) for body waves, whereas e.g. surface waves decay with $1/\sqrt{r}$ due to cylindrical spreading loss (see Fig. 2.1).

The aforementioned linear approximations of wave propagation are accurate only at large distances to the source. The situation is different if the source-receiver distance is small (r $\ll \lambda$). Here we need to consider a *near-field* term: $\frac{1}{r^3}\int_{r/\alpha}^{r/\beta} \tau f(t-\tau) d\tau$. This near-field term behaves like $1/r^2$ if the source-time function $f(t)$ is short compared to the time difference $r/\beta - r/\alpha$ ($f(t)$ corresponds to a delta function with amplitude proportional to time) and has nonzero values only between r/α and r/β. For $r \to \infty$, the *far-field* terms $(1/r)$ for *P*- and *S*-waves, respectively, become dominant and the near-field term is negligible.
For $r \to 0$, the near-field term dominates the decay over $1/r$ and the waveform is nearly identical to the source-time function $f(t)$ (Lokmer and Bean, 2010). I refer to Aki and Richards (1980) for a detailed description.

2.2 Seismic noise processing

In this section I would like to give an overview of seismic processing methods to analyze ambient seismic noise, including WT-induced signals, whereby *spectral analysis* has a high importance and priority. The identification of the spectral content of the seismic time series and thus an allocation to different seismic sources with different frequency content is possible after the transformation into the frequency domain. In the following I describe the physical principles of the used spectral methods and give an evaluation of different methods.

2.2.1 Spectral analysis

As mentioned before, working in the frequency domain is an established method in scientific research to evaluate time series in terms of their frequency or energy content. Here, energy is defined as the integral of the squared magnitude of the signal, also referred to as *signal energy*.
First of all, I would like to characterize a model of a seismic time series in the frequency domain. To find an equivalent function $F(\omega)$ in the frequency domain for an arbitrary transient function $f(t)$, we need to calculate the *Fourier transform* of $f(t)$ (Bormann and Wielandt, 2002):

$$f(t) = \frac{1}{2\pi}\int_{-\infty}^{\infty} F(\omega) e^{i\omega t} d\omega, \tag{2.12}$$

$$F(\omega) = \int_{-\infty}^{\infty} f(t) e^{-i\omega t} dt = |F(\omega)| e^{i\phi(\omega)}, \tag{2.13}$$

where $|F(\omega)|$ represents the amplitude spectral density, $\omega = 2\pi f$ the angular frequency and $\phi(\omega)$ the phase spectrum.
An arbitrary signal X_t can be modeled by a sum of a constant term μ with linear combinations of sines and cosines with different frequencies (f) and random amplitudes A and B (Percival and Walden, 1998):

$$X_t = \mu + \sum_f [A(f)\cos(2\pi f t) + B(f)\sin(2\pi f t)]. \tag{2.14}$$

In contrast to earthquake waves, which represent transient signals and thus fulfill the integrability conditions of the Fourier transform due to a defined start and end time of the seismic source, seismic noise can be described as a stationary stochastic process of multiple, often continuous sources without a defined phase spectrum. After Bormann and Wielandt (2002), an amplitude spectral density or a phase spectrum cannot be calculated for such signals. To evaluate the spectral content of ambient seismic noise, the calculation of the *power spectral density* (PSD) is necessary and will be explained below.

In the following I would like to derive a spectral representation for a stationary process after Cramér (1942) and I adopt the notations used by Percival and Walden (1998).

A real-valued discrete time series $\{X_t\}$ with zero mean can be described by a summation of L harmonic functions

$$X_t = \sum_{l=1}^{L} D_l \cos(2\pi f_l t + \phi_l), \tag{2.15}$$

where $L \geq 1$, f_l corresponds to frequencies, D_l represents the amplitudes and ϕ_l are the phase shifts with $\phi_l \in [-\pi, \pi]$. The variable ϕ_l is independent and random in a stationary process.

Using Euler's formula $D_l \cos(2\pi f_l t + \phi_l) = \frac{D_l}{2}(e^{i\phi_l} e^{i2\pi f_l t} + e^{-i\phi_l} e^{-i2\pi f_l t})$, we can rewrite (2.15) as

$$X_t = \sum_{l=-L}^{L} C_l e^{i2\pi f_l t}, \tag{2.16}$$

with $C_{\pm l} = \frac{D_l e^{\pm i\varphi_l}}{2}$. The phase shift ϕ_l is assumed to be independent, which means that C_l is also independent.

By using the Riemann-Stieltjes integral

$$\int_{-1/2}^{1/2} g(f)dH(f) = \sum_{k=1}^{N} g(a_k)b_k$$

with a continuous function $g(\cdot)$ over the interval [-1/2, 1/2] and a step function $H(\cdot)$ with jumps of finite sizes $(b_1, b_2, ..., b_N)$ at -1/2 $< a_1 < a_2 < \cdots < a_N <$ 1/2, it is possible to define the spectral representation theorem for discrete parameter stationary processes (Percival and Walden, 1998):

$$X_t = \sum_{l=-L}^{L} C_l e^{i2\pi f_l t} = \int_{-1/2}^{1/2} e^{i2\pi f t} dZ(f) \tag{2.17}$$

Equation (2.17) is called a stochastic version of the Riemann-Stieltjes integral and represents the spectral representation theorem for a discrete parameter stationary process. The complex-valued stochastic process $Z(f)$ is defined as

$$Z(f) \equiv \sum_{j=0}^{l} C_j, \qquad f_l < f < f_{l+1} \equiv 1/2 \quad \text{with} \quad l = 0, ..., L.$$

For a more detailed derivation I refer to Percival and Walden (1998), section 4.1.

$\{Z(f)\}$ has the following properties (with $E\{\cdot\}$ as the expectation operator):

a) $E\{dZ(f)\} = 0$ for all $| f | \leq 1/2$.

b) $E\{| dZ(f) |^2\} \equiv dS^{(I)}(f)$, where $S^{(I)}(\cdot)$ is a bounded nondecreasing function called *integrated spectrum* of $\{X_t\}$.

c) $\text{cov}\{dZ(f'), dZ(f)\} = E\{Z^*(f')dZ(f)\} = 0$, for f and f' contained in the interval $[-1/2, 1/2]$ (Percival and Walden, 1998).

Due to the properties of $\{Z(f)\}$, there is a fundamental relationship between the autocovariance $\{s_\tau\}$ and the integrated spectrum $S^{(I)}(\cdot)$ for any stationary process $\{X_t\}$:

$$s_\tau = E\{X_t X_{t+\tau}\} = \int_{-1/2}^{1/2} e^{i2\pi f\tau} dS^{(I)}(f) = \int_{-1/2}^{1/2} S(f) e^{i2\pi f\tau} df \tag{2.18}$$

with $E\{|\, dZ(f)\,|^2\} = dS^{(I)}(f) = S(f)df$.
This assumption is true if $S^{(I)}(\cdot)$ is differentiable everywhere with a derivative indicated by $S(\cdot)$. The function $S(\cdot)$ is called the *spectral density function* (SDF, Percival and Walden, 1998; Sudhaus and Ritter, 2009). Since (2.18) indicates that the autocovariance $\{s_\tau\}$ is the inverse Fourier transform of $S(\cdot)$ and we assume that $S(\cdot)$ is square integrable, we can show:

$$S(f) = \sum_{\tau=-\infty}^{\infty} s_\tau e^{-i2\pi f\tau} \tag{2.19}$$

The spectrum $S(f)$ is the Fourier transform of the autocovariance $\{s_\tau\}$ of the stationary process $\{X_t\}$. Here we used the fact that s_τ and $S(f)$ have a Fourier relationship for the discrete and continuous case if s_τ is a square summable deterministic sequence (because $S(\cdot)$ is square integrable), which can be assumed for seismic signals. The variance of a stationary process $\{X_t\}$ can be now written as

$$\mathrm{var}\{X_t\} = E\{X_t^2\} = s_0 = \int_{-1/2}^{1/2} dS^{(I)}(f) = \int_{-1/2}^{1/2} S(f) df. \tag{2.20}$$

The way of calculation I just described is suitable for my purposes only to a limited extent, as an infinitely long stochastic signal also contains infinite energy. If just a time section is considered, which will be the case in this study, this signal energy becomes finite and depends on the properties of the signal and the length of the time section.
If $\{x_t\}$ is any realization of a stationary process $\{X_t\}$ with zero mean, than the infinite signal energy is:

$$\lim_{N\to\infty} \sum_{t=1}^{N} x_t^2 = \infty, \tag{2.21}$$

but the power should be finite:

$$\lim_{N\to\infty} \frac{1}{N} \sum_{t=1}^{N} x_t^2 = \sigma^2. \tag{2.22}$$

So the variance σ^2 can be defined as the power of a stationary process $\{x_t\}$. As a consequence of equation (2.20), we find that the power (or variance) of the overall stochastic process $\{X_t\}$ (average over all realizations) is

$$\int_{-1/2}^{1/2} S(f) df$$

with $S(\cdot)$ now defined as the *power spectral density function*. In the following I will describe the approach of calculating the PSD of a seismic noise signal $\{X_t\}$, considering these relationships mentioned before.
We first calculate the mean signal power:

$$P = \frac{1}{T_2 - T_1} \int_{T_1}^{T_2} |\, X(t)\,|^2 \, dt, \tag{2.23}$$

where we obtain the PSD with

$$P(\omega) = \frac{1}{T_2 - T_1} |\, \tilde{X}(\omega)\,|^2 \tag{2.24}$$

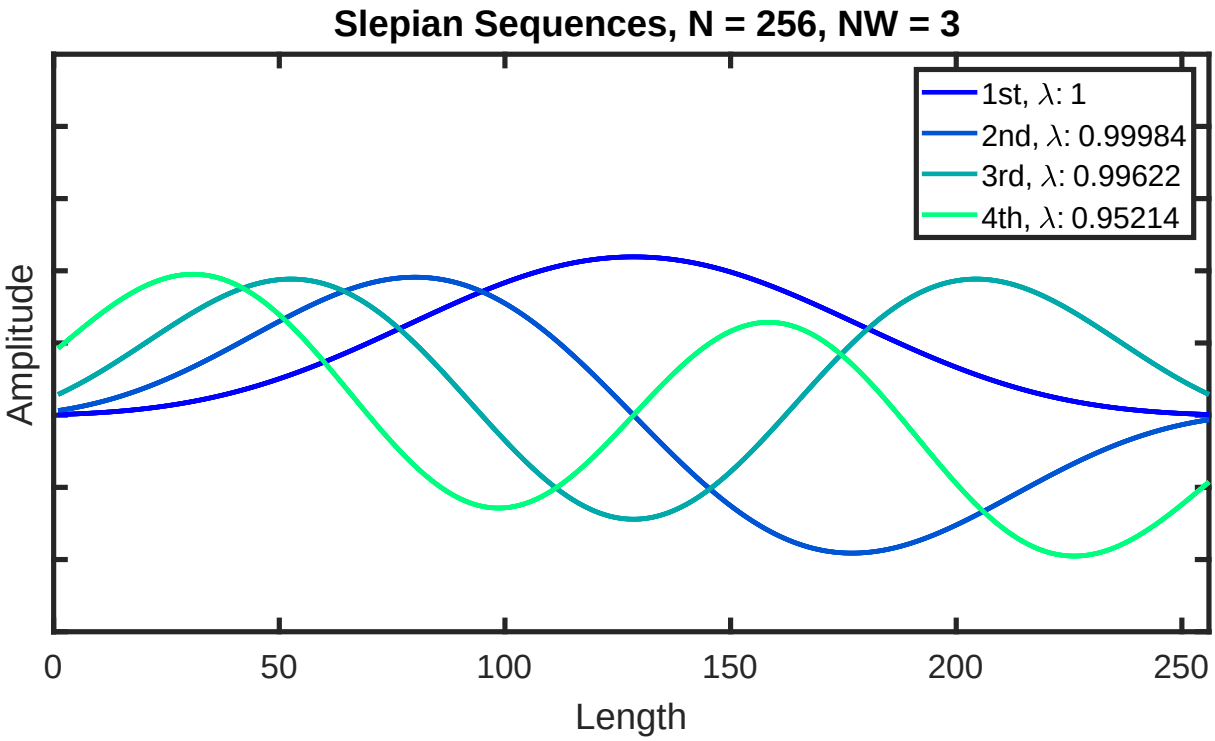

Figure 2.2: The first four discrete prolate spheroidal sequences (or Slepian sequences) for a total length of N = 256. The first sequence will lead to a strong weighting of the middle section of the time series. With increasing order of the sequence also the weighting of the margins of the time series increases. The summation of all sequences will lead to a smooth weighting of the overall time series. The value λ in the legend represents the eigenvalue of each sequence.

by using the Fourier transform

$$\tilde{X}(\omega) = \int_{T_1}^{T_2} X(t) e^{-i\omega t} dt. \tag{2.25}$$

The unit of $P(\omega)$ clearly depends on the unit of $X(t)$. The measured output of our seismic instruments is the ground velocity with the unit $[X(t)] = 1\text{m/s}$. Hence the PSD unit is

$$[P(\omega)] = \frac{[X(t)]^2}{\text{Hz}} = 1\frac{\text{m}^2/\text{s}^2}{\text{Hz}} \tag{2.26}$$

As mentioned before, this specific approach of calculating the PSD is necessary for describing a stochastic process (like seismic noise including WT-induced signals) in terms of evaluating the frequency content. This is important to keep in mind when comparing spectra of seismic noise with spectra of transient signals like earthquakes, where a defined start and end time exists.

2.2.2 Influence of a tapering function

In the previous section I introduced the mathematical concept for a spectral representation of a stochastic process. As mentioned before, the PSD calculation of a stochastic signal clearly depends on the used randomly chosen finite time window. By extending this time window, the number of Fourier coefficients increases but the uncertainty for every single coefficient remains the same. Furthermore, often only a limited suitable time interval is available in this study containing stable wind conditions. To reduce the variability of the PSD calculation of a finite time window and to minimize the spectral leakage effect (creating new frequency components due to the calculation of a finite time period of the signal) or the Gibbs phenomenon (oscillation near a discontinuity), respectively, I shortly introduce different methods which, when combined, will give an optimal spectral representation of the seismic recordings in a period of time.

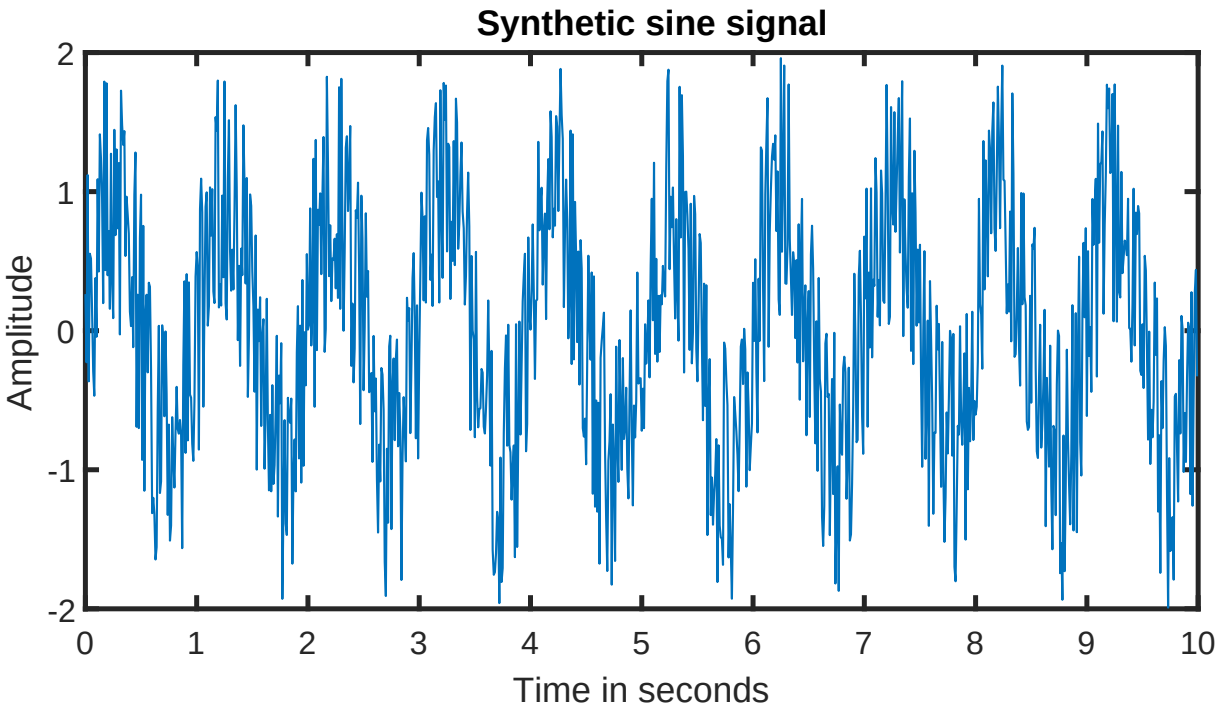

Figure 2.3: Synthetic sine signal section with a main frequency of 1 Hz and a superposition of random noise.

The method of Welch (Welch, 1967) splits the time series into various overlapping time segments. The calculation of the periodograms is executed using the approach of section 2.2.1 in each individual segment and averaged across all time segments to form an overall periodogram. To reduce a potential bias due to leakage in the spectra, Welch (1967) suggested the use of a *single data taper*.

This single taper can still suffer from spectral leakage for a spectrum with very high dynamic ranges (Percival and Walden, 1998) and also reduces the used sample size, which leads again to an increase in variance. To avoid such phenomena, Thomson (1982) introduced the *multi-taper* spectral estimation, which involves a number of multiple orthogonal tapers (Slepian or discrete prolate spheroidal sequences, also known as dpss, see Fig. 2.2). The following description is just a short overview of the so-called *adaptive multi-taper method*. For further explanations I refer to the book of Percival and Walden (1998).

A number of k uncorrelated data tapers is multiplied by the seismic signal and an eigenspectrum is computed for $k = 0, ..., K-1$ with $K = 2NW\Delta t$ (Shannon Number). Since each taper is orthogonal to another one and contains a good protection against spectral leakage, also each eigenspectrum of the signal provides a statistically independent estimate of the power.

The resolution bandwidth $2W$ is calculated as a multiple of the fundamental Fourier frequency $j/(N\Delta t)$ with $j > 1$. In my case, I fix the value of W using the product $NW = 3$, which corresponds to the number of samples (N) multiplied by half the bandwidth (W). The value of W corresponds to the used number of uncorrelated tapers, which is shown in Fig. 2.2. In this particular example, the time window length N is equivalent to 256 data points which corresponds to W = 3/256. With increasing W, the variance decreases but the resolution of the calculated periodogram also decreases. After choosing W, we are able to calculate K eigenspectra.

The related eigenvalue λ gives the ratio of the signal energy for the interval [-W, W] to the signal energy contained in the overall frequency band [-f_N, f_N] for each taper, with $f_N \equiv \frac{1}{2\Delta t}$ as the *Nyquist frequency*. This value should be close to 1, which is the case for the first four sequences (see Fig. 2.2). The dpss data tapers and the corresponding values λ were calculated with the function *dpss* implemented in MATLAB.

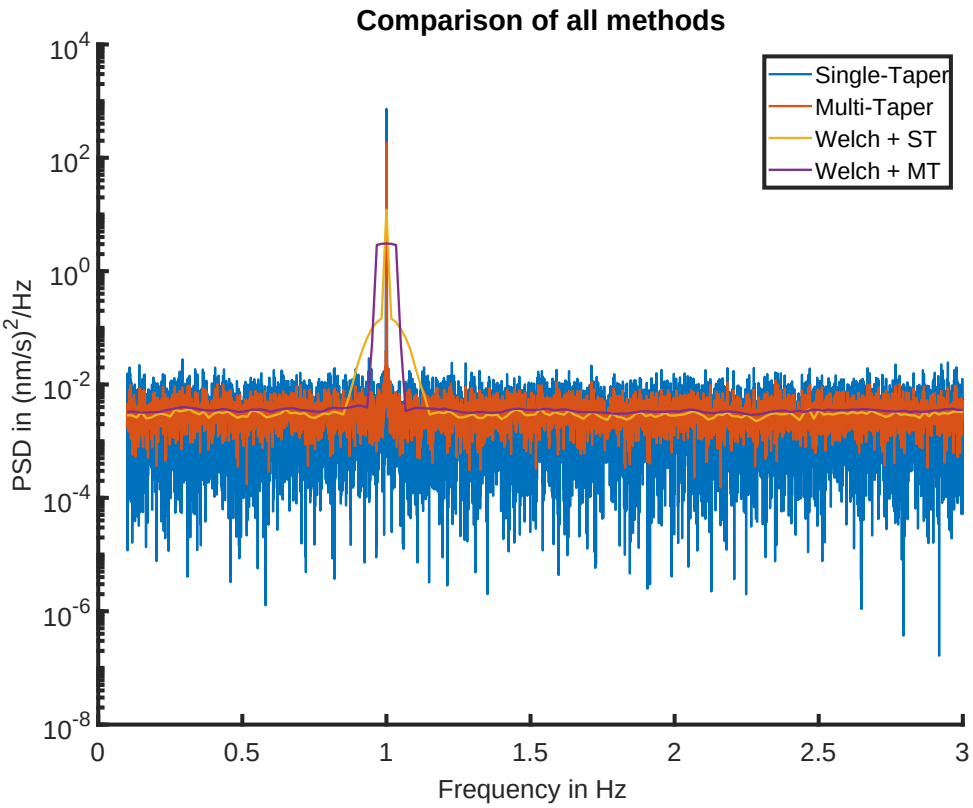

Figure 2.4: The PSD of the synthetic sine signal with noise (Fig. 2.3) using different approaches: The blue line represents the PSD spectrum using the single-taper method. The red line is the PSD spectrum using the adaptive multi-taper method after Thomson (1982). The yellow and purple line represent the PSD spectrum after splitting the time series into overlapping time segments (Welch, 1967) and the use of a single- (yellow) or multi-taper (purple) method, respectively.

By averaging over all K eigenspectra, a final spectrum of the total time window is obtained. In this study I use an adaptive approach after Percival and Walden (1998) with a frequency-dependent weighting factor for a weighted average of the different tapered PSD estimates to compensate the unequal energy concentration of the Slepian sequences. The calculation of the weighting factors $b_k(f)$ is carried out iteratively. The weighting factors with a first spectral estimation $\hat{S}^{(mt)}(f)$, based on the first two eigenspectra, are given by:

$$b_k(f) = \frac{\hat{S}^{(mt)}(f)}{\lambda_k \hat{S}^{(mt)}(f) + (1-\lambda_k)\sigma^2} \qquad \text{with} \quad \sigma^2 = \text{var}\{X_t\}, \tag{2.27}$$

for orders $k = 0, ..., K-1$ with $K = 2NW - 1$.
The adaptive multi-taper spectral estimator is then given by:

$$\hat{S}^{(amt)}(f) \equiv \frac{\sum_{k=0}^{K-1} b_k^2(f)\lambda_k \hat{S}_k^{(mt)}(f)}{\sum_{k=0}^{K-1} b_k^2(f)\lambda_k} \tag{2.28}$$

This weighted spectral estimation $\hat{S}^{(amt)}(f)$ is now the basis of a new calculation of weighting factors $b_k(f)$. I use 10 iteration steps to obtain the final weighted spectrum.
In this way, several combinations of different methods are now available to reduce the variability of the PSD calculation for a random finite time window of noise signals and to receive the „real“ spectral representation with a minimization of disturbing influences. To evaluate the different combinations, I create a randomly disturbed sine signal with a frequency of 1 Hz (Fig. 2.3).

By using the synthetic sine signal, I compute the PSD using the following combinations:

1: Multiply a **single taper** (Tukey window) with the overall time window and calculate the periodogram by using (2.24).

2: Compute the PSD by using the **adaptive multi-taper method** introduced by Thomson (1982).

3: **Split** the time series into several overlapping blocks after Welch (1967) and calculate the PSD by using a **single taper** (Tukey window).

4: Again, **split** the time series but now using the **adaptive multi-taper method** for each block instead of the single-taper approach.

Fig. 2.4 shows the different PSD spectra using the four different approaches. As can be seen, all methods are appropriate to find the dominant frequency of 1 Hz. However, the calculated periodograms show clear variations. The blue curve in Fig. 2.4 shows a very dynamic behavior, which is due to the corresponding number of calculated Fourier coefficients.

The number would decrease for a smaller time window, but the uncertainty of each coefficient remains the same. Using the multi-taper approach (red curve), a clear smoothing effect can be observed due to the averaging effect of different orthogonal tapers. This also leads to a small decrease of the peak at about 1 Hz. By using the method of Welch, where I split the time interval into various segments, a further smoothing of the overall periodogram could be achieved, along with artifacts around the peak at 1 Hz. The smoothest curve is obtained by combining the method of Welch and the multi-taper method (purple curve). A broadening of the peak at 1 Hz can be observed, which depends on the length of the splitting interval. However, in terms of reducing the variability of the periodogram, a combination of Welch and tapering should be the method of choice to calculate a representative PSD spectrum of the seismic signal. To test the difference of both approaches (Welch + single- or multi-taper approach, respectively) using real data, I select a randomly chosen time window of 10 minutes for an exemplary seismic broadband station located in an area with many anthropogenic activities. The calculated PSD spectrum should be able to visualize the different excited frequencies of the single WT in 1500 m distance. Both methods show hardly any differences for the location of the main peaks (Fig. 2.5). The multi-taper approach leads to a smoothing of the curve and a slight reduction of the PSD values for the main peaks, which was to be expected (Fig. 2.4). It can be concluded that the selection of a particular method has no clear effect on the identification of the main peaks. I therefore decide an appropriate method on a case by case basis. However, for a clearer illustration of the WT-induced seismic signals in large distances or noisy environments (like shown in Fig. 2.5) I prefer the use of the multi-taper approach in combination with the method of Welch.

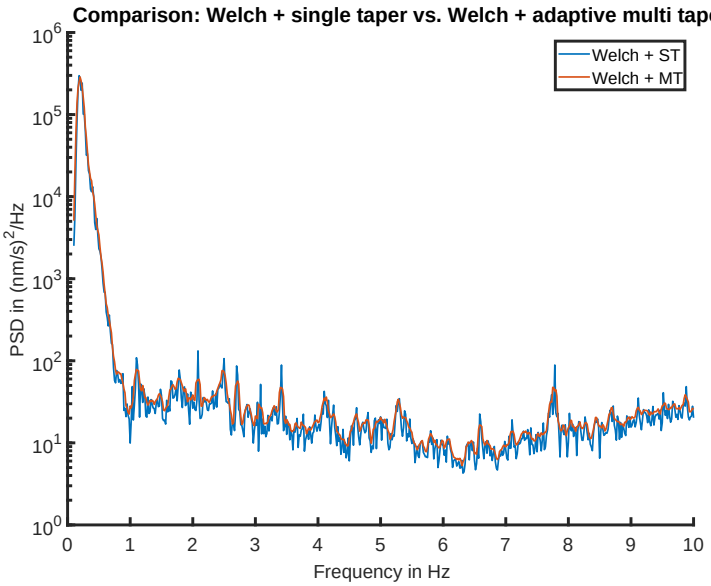

Figure 2.5: The calculated PSD spectrum of a 10-minute-long time window for a seismic station located on the foundation of a WT, using the method of Welch in combination with a single- or multi-taper approach.

2.3 Fundamental functionality of wind turbines

Wind turbines (WTs) are designed to transform wind power into mechanical power and finally into electrical power (electricity). Thereby WTs constitute an opportunity for eco-friendly electrical power instead of using fossil resources or nuclear power. The number of WTs has been steady increasing worldwide in the last few years, especially in Germany after the Fukushima nuclear disaster in 2011 and a change of the energy policy. New developments in this field lead to redesign concepts in terms of increased WT dimensions (repowering) along with a higher electrical output. In this section, I describe the fundamental functionality of WTs and consider different components with regard to their possible emission of seismic signals into the subsurface.

2.3.1 Physical principles

In general, wind is a result of moving air due to pressure gradients in our atmosphere. The wind speed depends on the pressure gradient, the Coriolis effect and, especially on local scale and low heights, on the topography (including trees, buildings etc.) of the surface. The so called "roughness" of the Earth leads to frictional forces and induces wind shear (Lott et al., 2017). The energy of wind (or moving air) can be described by its kinetic energy:

$$E = \frac{1}{2} m \bar{v}^2, \tag{2.29}$$

where m represents the mass of the moving air and $\bar{v}$ the mean velocity of wind over an observed time window. The power (energy per unit time) contained in this time window can be written as (Tong, 2010)

$$P = \frac{1}{2} \dot{m} \bar{v}^2 = \frac{1}{2} \rho A \bar{v}^3, \tag{2.30}$$

with the flow rate of the wind mass

$$\dot{m} = \rho A \bar{v}, \tag{2.31}$$

where ρ corresponds to the density of the air and A to the plane area swept by the rotating blades of the WT (similar to A1 in Fig. 2.6).

Equation (2.30) shows the dependence of power to the swept area A of a WT (spanned by the blades), the density of air and, in particular, the wind speed. As the wind power is proportional to the cubic power of the wind speed, even small changes in v lead to a significant change in wind power. Choosing a location of a WT with good and stable wind conditions is therefore necessary. Also the linear relationship between the power and the swept area leads to a quadratic increase of the power with the diameter spanned by the blades. This can be achieved by an enlargement of the blades and with that an increase of the total size of the WT.

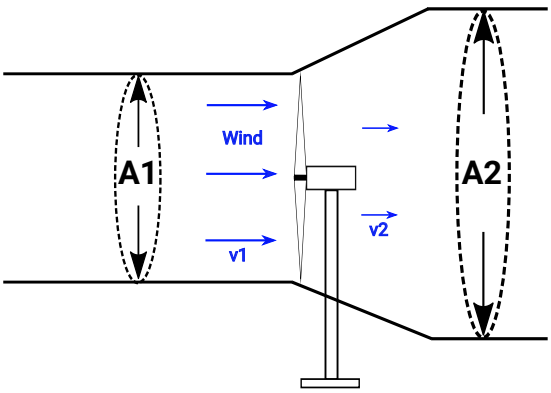

Figure 2.6: Illustration of the wind flow before and after the WT with the related cross-sectional areas A1 and A2.

It is not possible to extract 100 % of the kinetic energy since the wind speed behind the blades cannot be equal to

zero. Only a part of the overall kinetic energy is extracted by the WT, which leads to lower wind speeds behind the swept area of the turbine and thereby an increase of the cross section with constant mass flow. This is illustrated in Fig. 2.6. This means the extraction of mechanical power from the wind field results in a decrease of the wind speed behind the rotor area (Hau, 2008).
This brings us to the following question: what is the maximal power that can theoretically be extracted from the wind field? To answer this question I introduce the power coefficient C_p, which is the ratio of the captured mechanical power P_m, mainly by the blades of the turbine, to the overall available power in the wind field P_w:

$$C_p = \frac{P_m}{P_w} = \frac{P_m}{(1/2\rho A\bar{v}^3)}. \tag{2.32}$$

Betz (1920) found a theoretical maximum efficiency $C_{p,max}$ of 16/27 or 59 %, which is also known as the "Betz's law" and indicates the maximum power that can be extracted from the wind field. This value can be achieved by a wind speed ratio of $v_2/v_1 = 1/3$, where v_1 is the wind speed in front of the rotor plane and v_2 behind. This relationship influences the design of the rotor blades. In real-world conditions C_p is lower due to various aerodynamic losses at the WT. However, modern WTs can reach a maximum efficiency of $C_p \approx 0.5$, which is close to the theoretical maximum of Betz. At long distances from the WT, the wind speed returns to its initial value (as well as the area A1 in Fig. 2.6), which is important for the design of a wind farm.

2.3.2 The relation of power and wind speed

The relation of the rotation rate and the produced power of an exemplary WT to the wind speed is shown in Fig. 2.7 (blue and red, respectively). The rotation rate shows a linear behavior with wind speeds from 4 m/s to 10 m/s. No clear relation between the rotation rate and the wind speed can be seen in the range of 0 m/s to 5 m/s. This range is below the *cut-in* wind speed, where the blades "tumble" in the wind. Above a wind speed of 10 m/s, the internal system of the WT starts to *pitch* the blades to achieve a constant rotation rate, even for an increase of the wind speed. At this point, the WT reaches the nominal power ($\sim$ 1.5 MW), which can be observed for the red curve. The output power shows a approximately similar linear relation in the wind speed range between 4 m/s and 10 m/s as the rotation rate. A *cut-off* wind speed (typically above 20 m/s), where the WT stops to rotate by feathering the blades to protect the turbine from damage, will not be reached in this example.
It is important to mention that each WT behaves in a different way depending on its specification, so that the relation of rotation rate and power to the wind speed can often vary widely. A consideration of WT-induced seismic signals should therefore always be made in a combination with SCADA (supervisory control and data acquisition) data of the WT.

2.3.3 Onshore vs. offshore

The aim of this study is to determine the WT-induced seismic signals of onshore turbines. Nevertheless, it is important to point out the main differences between onshore and offshore WTs in order to clarify that results of this study cannot easily be adopted for offshore purposes. Although WTs in an offshore region tend to be more efficient than onshore due to a more stable and consistent wind field, several disadvantages can be mentioned. Besides the difficult connection to the national grid or the challenges during the installation of these WTs, the different design of the foundation and the size of the turbine are of special interest regarding the induced seismic signals. Especially *monopiles* or *jackets* are deployed as foundation of WTs in deep water (Burton et al., 2011), whereas onshore WT designs prefer a flat foundation in circular form. Also, other concepts like floating WTs find their way into offshore applications. Moreover, the capacity of offshore WTs is much higher compared to onshore. In 2018, General Electric (GE) introduced the most powerful offshore WT ("Haliade-X 12 MW") to date with a capacity of 12 MW and a rotor diameter of 220 m (Url: https://www.ge.com/renewableenergy/wind-

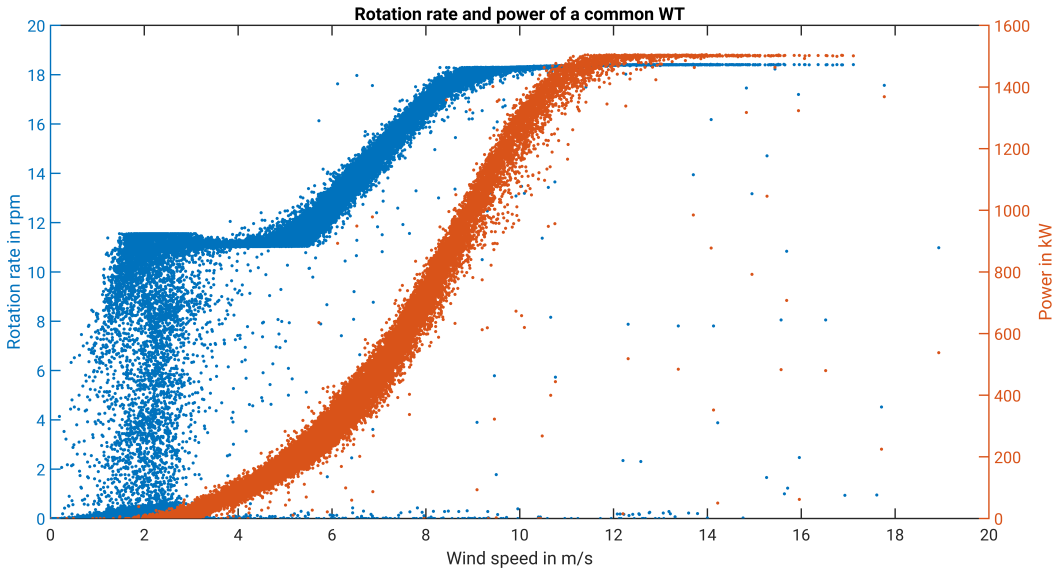

Figure 2.7: The rotation rate (left axis, blue) and the produced power (right axis, red) as a function of the wind speed for an exemplary WT.

energy/turbines/haliade-x-offshore-turbine, as consulted online in May 2019). By comparison, large onshore WT have a capacity of around 3 MW to 4 MW and much smaller rotor diameter. All these facts lead to a totally different character of WT-induced seismic signals and should be investigated in future work.

2.3.4 The drive train – different generator concepts

Current WTs differ significantly in their design, e.g. the tower height or the design of the foundation, depending on the manufacturer. Another significant difference is the design of the *drive train* (which includes all rotating components of a WT) and the use of a gear box. In this study, different types of WTs with and without gear boxes have been studied, which is why this section briefly summarizes the main differences. The drive train is subjected to extreme mechanical loads due to high variations in the rotational speed. However, all modern WTs are utilized with variable rotor speed due to new developments in this field. This is important for a maximum yield of the kinetic energy.

Most of the WTs use a gear box in combination with a Doubly-Fed Induction Generator (DFIG). The gear box is necessary to transmit the rotational rate (up to 20 rpm) to the rotational speed of the generator (several thousands rpm). The relative movement of the rotor and the stator within the generator converts the rotating magnetic field into electric power. The rotor windings are directly connected to the grid by using a pair of back-to-back voltage source converters, which allow operations above and below the synchronous speed (also known as *asynchronous generator*) of the stator field (Burton et al., 2011). By converting the produced current to DC (direct current) and then back to AC (alternating current), the varying frequency due to the flexible rotor rate can be fixed to the values of the grid.

The market leader for onshore WTs in Germany is the manufacturer *Enercon*. They eliminate the gear box by using a *synchronous generator* together with a frequency converter, where the rotor is directly connected to the multi-pole generator. This generator is completely decoupled from the grid. Thereby the generator spins with the same speed as the rotor, which leads to a high efficiency (especially at light wind conditions) and a higher variability of the rotor speed. In order to obtain the required frequency of the grid, a higher number of poles is necessary. The synchronous generator of an Enercon E-82 WT, for example, contains 72 poles. Other advantages of this design are the lower maintenance due to fewer parts after the elimination of the gear box and a longer lifetime

due to lower machine loads. On the downside, direct drive wind turbines have higher masses of the rotor-nacelle assembly (RNA). This is caused by the high power density demand of the generator, leading to very large generator diameters.

2.3.5 Possible sources for WT-induced seismic signals

WTs are highly susceptible to vibrations due to their complex interaction of different components and the elastic design. A so-called *Campbell diagram* represents the eigenfrequencies of the system as a function of the rotation speed of the rotor. The aim of this diagram is the identification of speed ranges leading either to instability or resonance for a specific WT, in particular the interaction of crucial interaction of eigenmodes, like bending modes of the tower or torsional vibrations of the drive train, with the rotation speed and its multiples. The major excitation frequency (assuming a WT with three blades) is the blade-passing frequency (BPF) with three times the rotation speed. In some literature this is also called *3P*. This excitation leads to aerodynamic imbalances, for instance due to the interaction of the blades with the tower. An exemplary Campbell diagram is shown in Fig. 2.8. The blue lines represent the 1P and 3P excitation, respectively. A possible resonance can be detected by the intersection between the speed-dependent excitation lines and the eigenfrequencies of the WT (marked as a circle) and should be avoided inside the range of operation.

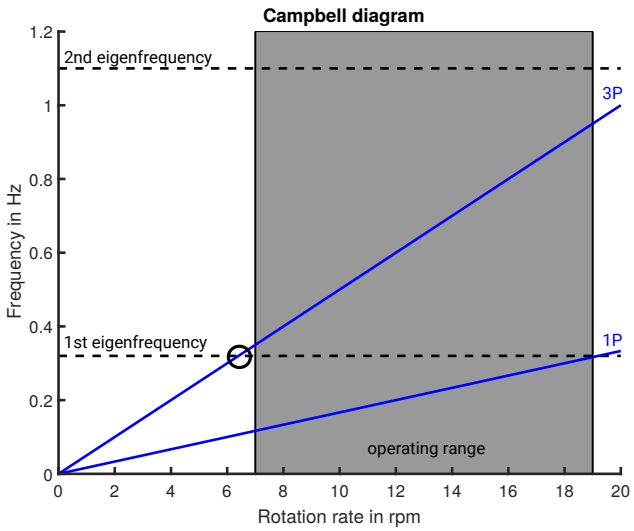

Figure 2.8: Exemplary Campbell diagram for the dynamic design of a WT.

The main parts of a common WT are shown in Fig. 2.9 and they are now evaluated with regard to their potential excitation of vibrations:

- The blades: Current WTs are equipped with three blades which rotate clockwise with a certain speed (sometimes up to 20 rpm, depending on the type of turbine). These blades are subjected to high aerodynamic loads and centrifugal forces. This may cause, e.g., chordwise bending, flapwise bending or torsional vibrations which could be transmitted through the tower and the foundation into the ground. Also the interaction with the tower, as mentioned before, due to a tower shadow effect (tower induced flow perturbation) may lead to significant excitation of the entire system. This excitation is also known as the blade-passing frequency (BPF) or 3P excitation. This frequency can be calculated by BPF = $\frac{3 \cdot \text{rotation rate}}{60\text{s}}$. Using a typical rotation rate of 18 rpm (Fig. 2.7), the BPF corresponds to 0.9 Hz.

- The nacelle: The nacelle is located on top of the WT and contains the drive train, including the generator and the gear box (depending on the type of the WT). As mentioned before, the drive train is subjected to variable external rotational loads, which may lead to torsional oscillations. Within the generator the pole pair passage leads to an internal excitation of the drive train. As the field coils pass each other, the magnetic field between them changes periodically. The excitation frequency is correlated with the product of the rotational

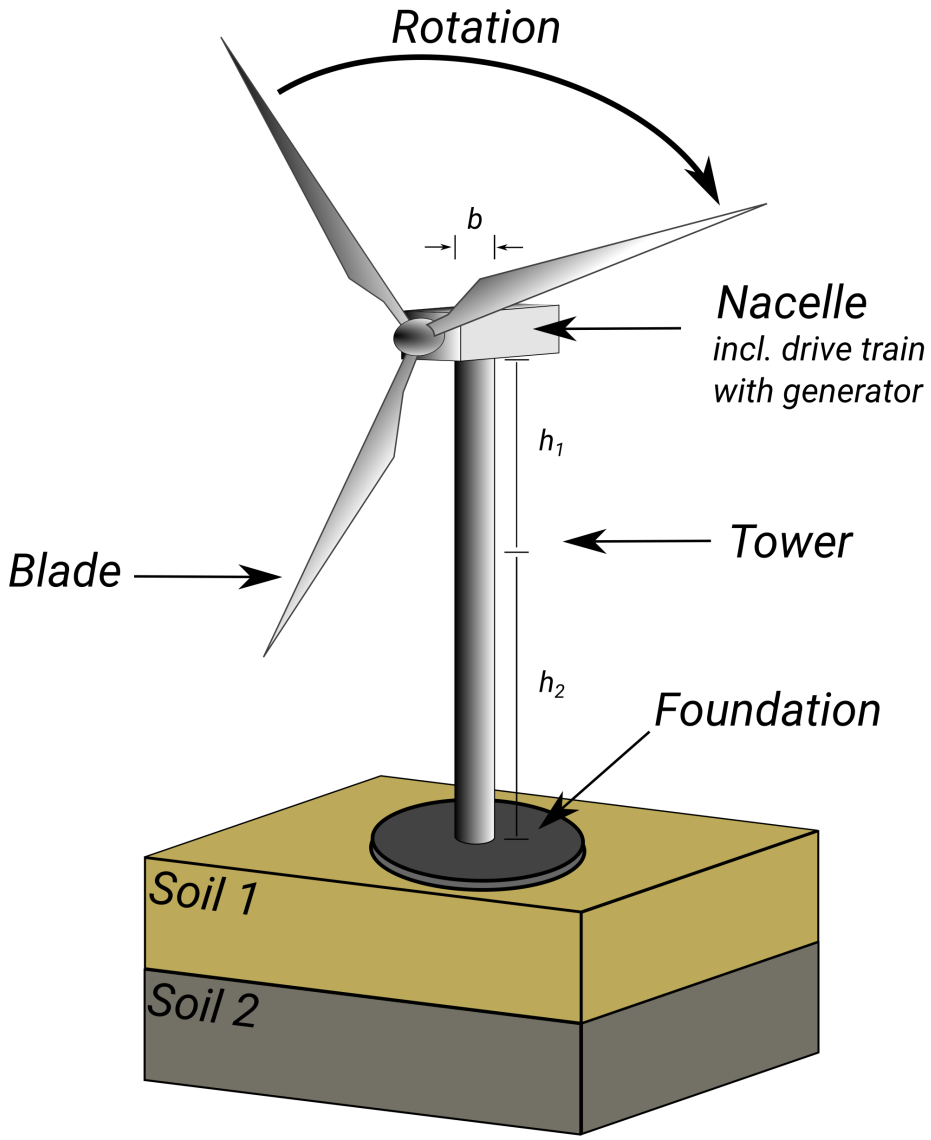

Figure 2.9: Sketch of a common WT showing the essential components. An interaction of the blade rotation with the eigenfrequencies of the components leads to a seismic emission into the subsoil.

speed and the pole pair number. If a gear box is employed, a similar excitation frequency can be observed linked to the tooth engagements. The tooth number within the individual stages determines the possible excitation frequencies, which is proportional to the rotor speed. For both a geared and a direct drive, the signal of internal excitation usually contains several superharmonics, called orders. Several base frequencies and their corresponding superharmonics are transferred into the foundation and can be detected.

- The tower: The tower constitutes the biggest part of the vibrational WT. Therefore, several bending modes or torsional oscillations can be identified, excited by the passing blades or the wind load on the tower. The first bending mode is the most important one in relation to the BPF. To estimate the first bending mode of a WT, I use a simple approximation according to *DIN EN 1991-1-4 (Appendix F)*:

$$f = \frac{\varepsilon_1 b}{h_{\text{eff}}^2}\sqrt{\frac{W_s}{W_t}} \qquad \text{with} \quad h_{\text{eff}} = h_1 + \frac{h_2}{3} \tag{2.33}$$

Here $b = 3$ m corresponds to the upper diameter of the tower, $h_1 = 30$ m and $h_2 = 70$ m represent heights according to Fig. 2.9, $W_s = 3000$ t is the weight of parts which contribute to the bending stiffness and $W_t = 7000$ t corresponds to the total weight of the tower. ε_1 is assumed to be 700 for reinforced concrete. Inserting all these assumed values into (2.33), the eigenfrequency of the first bending mode corresponds to $f = 0.48$ Hz.

A coincidence of both frequencies must be avoided to prevent the system from resonance effects, which is usually achieved by an appropriate operational speed range. The second and third bending modes of the tower, however, are in certain operating conditions subject to an excitation by one of the BPF multiples.

- The foundation: The foundation is the connection between the tower and the subsurface below the WT. Vibrations will be induced through the foundation, which is why the design and the coupling to the subsoil play an important role for the calculation of induced seismic signals. The design of the foundation is also important in relation to directional radiation at high frequencies (large foundation compared to the wavelength).

3 Influence of wind turbines on seismic stations in the Upper Rhine Graben, SW Germany

This chapter will evaluate the WT-induced signals of a wind farm near the town Landau, SW Germay. Landau is located in the Upper Rhine Graben consisting of a thick layer of unconsolidated sediments. I will determine frequencies of emitted signals, a frequency-dependent attenuation factor for the far- and near-field as well as the attenuation of the induced signals with depth using seismic surface and borehole measurements.
This chapter has been published in:

Zieger, T., Ritter, J.R.R. (2018),
Influence of wind turbines on seismic stations in the upper rhine graben, SW Germany,
J. Seismol., 22: 105 - 122
DOI: https://doi.org/10.1007/s10950-017-9694-9

3.1 Abstract

By analysing long- and short-term seismological measurements at wind farms close to the town of Landau, SW Germany, we present new insights into ground motion signals from wind turbines (WTs) at local seismic stations. Because of their need to be located in similar regions with sparsely anthropogenic activities, wind turbines impact seismic stations and their recordings in a way that is not yet fully understood by researchers. To ensure the undisturbed recording tasks of a regional seismic array or a single station by a protected area around those endangered stations, it is very important to investigate the behavior of WTs as a seismic source. For that reason we calculate averaged one hour long spectra of the power spectral density (PSD) before and after the installation of a new wind farm within the investigated area. These PSD are ordered according to the rotation speed. We observe a clear increase of the PSD level after the WT installation in a frequency range of 0.5 Hz to 10 Hz up to a distance of 5.5 km away from the WT. By analysing seismic borehole data, we also observe a decrease of the PSD of wind dependent signals with depth. The impact of wind dependent signals is found to be much more pronounced for the shallower station (150 m depth) than for the deeper one (305 m depth). Using short-term profile measurements, we fit a power-law decay proportional to $1/r^b$ to the main WT-induced PSD peaks and differentiate between near field and far field effects of ground motions. For low frequencies in the range from 1 Hz to 4 Hz we determine a b value of 0.78 to 0.85 for the far field, which is consistent with surface waves. The b value increases (up to 1.59) with increasing frequencies (up to 5.5 Hz), which is obviously due to attenuating effects like scattering or anelasticity. These results give a better understanding of the seismic wavefield interactions between wind turbines (or wind farms) with nearby seismic stations, including borehole installations, in a sedimentary setting.

3.2 Introduction

Local seismic stations play an important role for detecting small earthquakes in close vicinity to their locations and also to resolve in the geological structures of the regional subsurface. Additionally, they are important for monitoring induced seismicity, for example due to geothermal power plants. For detecting small events with magnitudes $M_L < 2$, which are common for induced seismicity (Baisch and Vörös, 2010), it is necessary for seismological

stations to record with a very low ambient noise level. To achieve such a low ambient noise level, which should be smaller than $\pm$ 1 $\frac{\mu m}{s}$ for 95 % of the ground velocity amplitudes (Baisch et al., 2012), seismic stations are often placed at locations far away from cities or industrial areas, where the natural and the anthropogenic noise is minimized. Another option is the use of borehole stations to reduce seismic noise (Withers et al., 1996).
Since the change of the energy policy within Germany in 2011, the number of new wind turbines (WTs) has been increasing. In order to reduce anthropogenic impact, often WTs are built in the same regions as seismic stations. This spatial coincidence generates a significant impact on seismic recordings of wind dependent signals due to WTs in the low frequency range (0.5 Hz to 10 Hz). However, systematic observations of influences due to WT-induced signals on seismic stations are very sparse and the dynamics of signal propagation are not fully understood, especially in comparison with meteorological resp. plant-specific measurements, like the rotation speed of a WT. Accordingly, the topic is of increasing importance inside the seismological community.
The most comprehensive study on the influence of WT-induced signals on seismic recordings comes from Styles et al. (2005). They studied effects of wind farms on the Eskdalemuir Array in Scotland, Great Britain. The study was able to identify the characteristic frequencies of the WTs such as the blade-passing frequency (3 times of their rotation frequency) and their multiples. They assume a seismic wave propagation as vertically polarised P-SV (Rayleigh) waves excited by the WTs and observed an increasing amplitude with increasing wind speed. Schofield (2001) found a $1/R$ (with R defined as distance between WT and observation point) attenuation model for seismic measurements at the Stateline Wind Project. A spectral peak around 4.3 Hz was detected at a site about 18 km away from the wind farm. Widmer-Schnidrig et al. (2004) measured near a single WT at Lossburg (Germany). They detected a tilt up to $\pm$ 50 μrad of the baseplate and found an attenuation model with $1/R$ (at 9.5 Hz to 12 Hz) and $1/R^2$ (at 2.5 Hz). Saccorotti et al. (2011) analyzed influences of WT induced signals in the vicinity of the Virgo Gravitational Wave Observatory in Italy. They calculated Power-Spectral-Density (PSD) spectra and detected the most significant peak at a frequency of about 1.7 Hz, which could be observed at distances up to 11 km away from the wind farm.
A recent study on the influence of wind farms on seismic recordings was presented by Stammler and Ceranna (2016). They observed significant signals in the background noise of seismic stations at the Gräfenberg array in southern Germany, which correlates with the installation of new WTs. To prove the correlation between an increasing background noise with the installation of WTs, they used data before and after the installation of WTs in the vicinity of the seismic stations and compared the corresponding PSD spectra to each other. After the installation of WTs, the wind-dependent noise level of the seismic stations increased significantly. This led to a higher threshold for signal detection at seismic stations at time periods with high wind speed, especially at seismic stations within close vicinity of the WTs. Another recent study on seismic analysis at two wind farms in Germany comes from Flores Estrella et al. (2017). They propose an amplitude attenuation model for both wind farms, depending strongly on the different local geology. Therefore the attenuation factor differs significantly from 0.73 to 1.87, depending on the frequency and geology, by fitting a $1/r^b$ model. Westwood and Styles (2017) analysed the seismic wavefield around a WT by using polarization analysis. They identified polarised surface waves as the predominant wave type at blade rotation harmonics.

3.3 Setting

The town of Landau and its surroundings are located in the central part of the Upper Rhine Graben, SW Germany. The area is relatively flat and there are several small villages (population around 2,000 to 10,000 inhabitants each). The main near-surface geological setting is a thick layer of poorly unconsolidated sediments (Cenozoic sediments). The region is of special interest, because there are two geothermal power plants with dense seismic networks including borehole stations and four wind farms (Offenbach, Bellheim, Herxheimweyher and Rülzheim, see Fig. 3.1). The seismological monitoring of the two geothermal power plants (Vasterling et al., 2017) and a

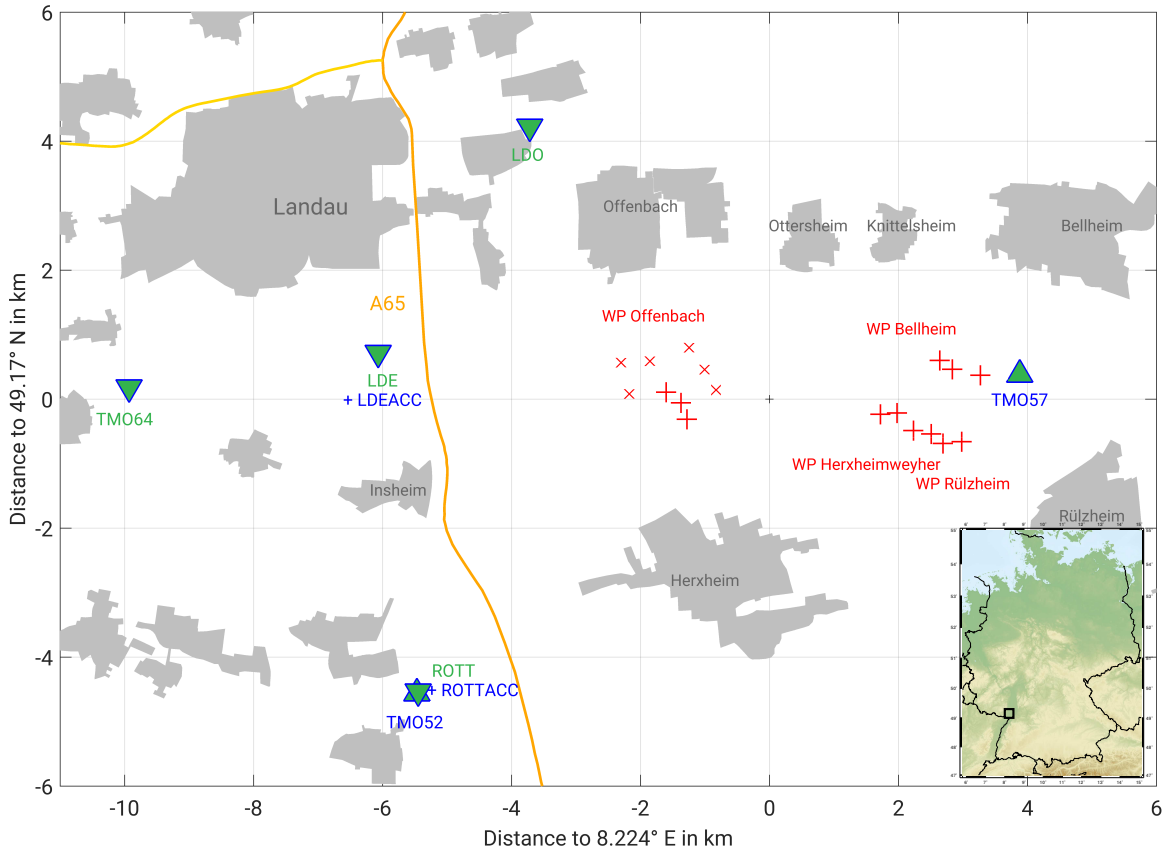

Figure 3.1: Map of the study area. Seismic stations are indicate as triangles (surface stations) and reversed triangles (borehole stations), wind turbines are indicated as crosses. Six turbines marked with an "x"-symbol were installed in September 2014 and will be discussed in section 3.5.3.

previous temporary broadband experiment TIMO - Deep Structure of the Central Upper Rhine Graben (Ritter et al., 2008), allow us to use long term waveform recordings from dense seismic networks over a time period of several years. The seismic stations for this study are shown in Figure 3.1 as triangles. The focus of this study will be on the investigation of borehole stations and their interference with WTs, as well as attenuation effects up to 3 km distance. Borehole stations are marked in green (LDO, LDE, ROTT and TMO64 in Fig. 3.1). In addition to these stations we will analyse data from accelerometer sensors at the surface of the borehole (LDEACC and ROTTACC). The area around Landau is characterised by strong anthropogenic activities, which lead to a relatively high noise level at our seismic stations (Groos and Ritter, 2010). Therefore, results from this study may be representative for seismic monitoring in populated regions. Seismic recordings in a more remote environment with a generally lower noise level should be more affected by WTs than this study suggests compared to data in populated regions.

Since 2004, so even before the TIMO - Project (2005 - 2009), there have been several WTs in the area around Landau. Until today, there are four wind farms with 18 WTs overallof different types inside of a relatively small area (see red crosses, Fig. 3.1). An extension of a new wind farm including six new WTs is still in progress in this area.

As shown in Table 3.1, the last WTs of type GE 2.5-120 were deployed in 2014. These WTs differ from the existing ones in an increased power generation (2.5 MW) and tower height (139 m). This will be studied and discussed in detail in section 3.5.3.

Table 3.1: Wind farm description with their location (Fig. 3.1), the start time of the turbines and their type. Important for this study are the turbines with a start time in 2014 at Offenbach. These wind turbines are significantly larger in their geometry than the existing ones (URL: www.energieatlas.rlp.de).

Wind farm location	Start	WT type
Bellheim	27-09-2004	GE Wind Energy 1.5sl
Bellheim	27-09-2004	GE Wind Energy 1.5sl
Bellheim	27-09-2004	GE Wind Energy 1.5sl
Rülzheim	18-05-2005	Fuhrländer FL MD77
Rülzheim	18-05-2005	Fuhrländer FL MD77
Rülzheim	23-03-2006	Fuhrländer FL MD77
Heryheimweyher	28-09-2005	Fuhrländer FL MD77
Heryheimweyher	30-09-2005	Fuhrländer FL MD77
Heryheimweyher	10-10-2005	Fuhrländer FL MD77
Offenbach	22-02-2008	Vestas V90
Offenbach	22-02-2008	Vestas V90
Offenbach	22-02-2008	Vestas V90
Offenbach	16-09-2014	General Electric (GE) 2.5-120
Offenbach	16-09-2014	General Electric (GE) 2.5-120
Offenbach	16-09-2014	General Electric (GE) 2.5-120
Offenbach	16-09-2014	General Electric (GE) 2.5-120
Offenbach	16-09-2014	General Electric (GE) 2.5-120
Offenbach	16-09-2014	General Electric (GE) 2.5-120

3.4 Method and data processing

As a first step, we preprocessed the acquired continuous vertical-component ground motion data by restitution of the instrument response in order to achieve the true ground motion velocity. Then, we divided each month in one hour long time segments and calculated the power spectral density spectra (PSD) for each segment after applying a simple taper. The spectra are smoothed with a width of 0.05 Hz and compared to the averaged rotation speed. Finally, we averaged the PSD-spectra within each rotation speed interval, respectively, rotation speed bin (0-5 rpm, 5-7 rpm, 7-9 rpm, 9-11 rpm, 11-13 rpm, 13-15 rpm, 15-17 rpm and 17-19 rpm) with the 75 % percentile, to minimize anomalies and to eliminate distortions (see Fig. 3.2 for process chart). Because of the spectra calculation over a relatively long duration of one hour and the following averaging over one month, effects of local seismic events would be averaged out and can be neglected for the PSD calculation. Also transient signals, e.g. due to anthropogenic activities, are only minor present in the frequency range from 0.5 to 10 Hz. The plant-specific measurements have a temporal resolution of 10 minutes. For comparison with the seismological data we calculated the hourly mean value of the rotation speed.

The PSD spectra are shown in a frequency range from 0.5 Hz to 10 Hz. Below this range, the ocean generated microseismicity dominates our spectra and does not enable us to detect any indications for WT-induced signals. For higher frequencies, a WT-induced signal would be too much attenuated at longer distances ($>$ 1 km). Moreover, the frequency window 0.5 - 10 Hz is of high relevance for detecting local seismicity. We defined eight different rotation speed bins, most of them in a 2 rpm interval except the first (0-5 rpm) bin. The colors in Fig. 3.3 range

from blue (low rotation speed < 11 rpm) to green (high rotation speed > 11 rpm), and the related PSD curves indicate a clear rotation dependence of the ground motion related to rotation speed.

3.5 Results

3.5.1 Surface-Stations

Figure 3.3 shows one-sided logarithmic PSD spectra for the time period of one month (October 2011) for the seismic stations TMO57 and TMO52 (see Fig. 3.1 for locations). The number of hourly windows used for the calculation to determine the averaged PSD spectrum is shown in the legend right behind the rotation speed interval, indicated with "n ". The rotation speed interval of 11-13 rpm dominates the distribution.

Station TMO57 is located 600 m away from the next WT. Figure 3.3 shows a clear increase of the PSD values with increasing rotation speed over the whole frequency range. The dependency of ground motion velocity to wind, which is more or less equivalent with the rotation speed, was analyzed by Lott et al. (2017) and is defined as the susceptibility *S*, which is the gradient of the linear increase of the detection threshold with wind speed. They observed a clear increase of the overall noise level with increasing wind speed, dependent on several factors like topography or wind direction.

Thanks to the company "pfalzwind GmbH (Ludwigshafen/Germany)", which operates the wind farm in Bellheim, we are able to compare our seismic data with plant-specific measurements of the WT, like wind speed or rotation speed. The coherence of wind speed and rotation speed is illustrated in Figure 3.4. The distribution shows a clear upward trend of the rotation speed from 4 m/s to approximately 9 m/s. At this wind speed, the WTs reach their maximum rotation speed and start to pitch the blades to keep the rotor speed stable and to avoid damage to the whole system due to high centrifugal forces. The maximum rotation speed for this WT type is 18.4 rpm. This Figure shows a clear dependency of the rotation speed with the wind speed, especially at wind speeds of more than 4 m/s.

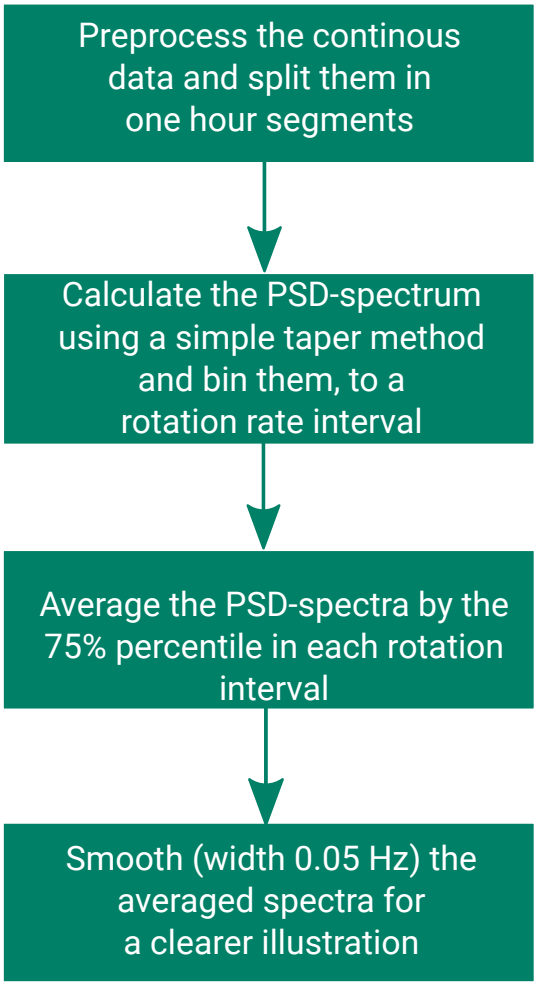

Figure 3.2: Processing steps used for the PSD-calculation in this study. The approach is based on Stammler and Ceranna (2016).

In Figure 3.3 there are noticeable major peaks at 0.9 Hz, 1.8 Hz, 2.7 Hz, 3.7 Hz, 4.6 Hz and 5.5 Hz which were not observed in the study by Lott et al. (2017). These discrete peaks arise with rotation speeds of more than 11 rpm and increase significantly in their intensity level with increasing rotation speed. There are other peaks visible which are not rotation dependent, e.g. the peak at 3.1 Hz (Fig. 3.3, top panel). This peak is noticable in all PSD-calculations for different months at this specific station. It is mostly observed at low rotation speeds, where the noise level of the station is minimized. This is probably a specific site effect of the station due to anthropogenic activities (a farm is located close-by to the station) and the 3.1 Hz peak disappears at high rotation speeds (resp. wind speeds) with

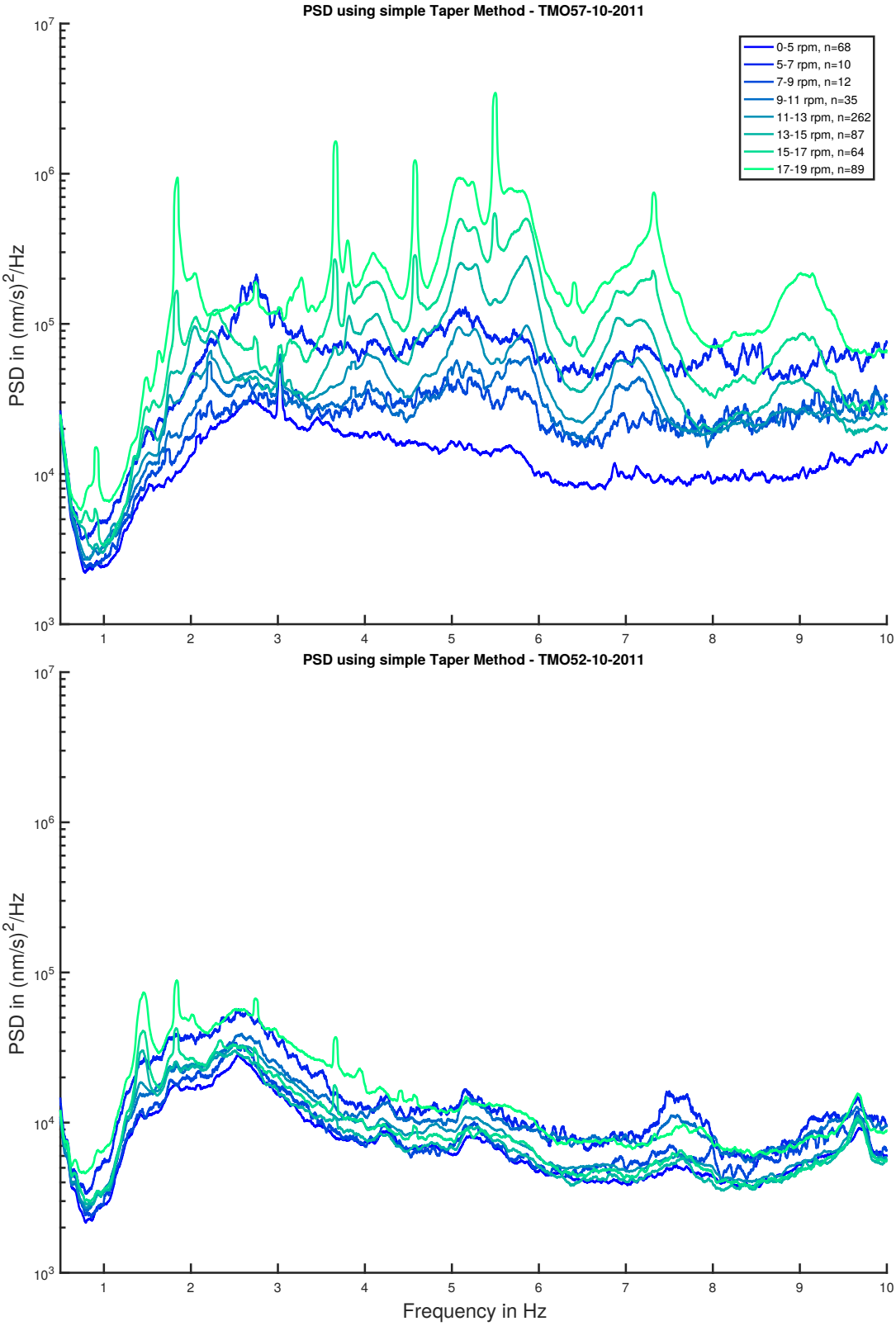

Figure 3.3: The Power-Spectral-Density (PSD) over the frequency range of 0.5 Hz to 10 Hz. Shown are station TMO57 (top panel) and station TMO52 (bottom panel) for October 2011. The legend indicates the defined rotation speed bins with corresponding colors and the number of PSD-spectra of one-hour long segments used for the mean calculation (75% quantile). Note the rotation dependent discrete frequency peaks at 0.9 Hz, 1.8 Hz, 2.7 Hz, 3.7 Hz, 4.6 Hz and 5.5 Hz for the station TMO57 with a distance of 600 m to the next WT. Station TMO52 has a distance of more than 5.5 km to the next WT; however we can also recognize rotation dependent signals in the lower frequency range.

the increase of the PSD level.

However, we also find an increase of the overall noise level at these aforementioned discrete frequencies by a factor of nearly 100 between low ($<$ 11 rpm) and high rotation speeds of more than 17 rpm (e.g. for 1.8 Hz: $3 \cdot 10^4$ $(\text{nm/s})^2$/Hz at low rotation speeds to $1 \cdot 10^6$ $(\text{nm/s})^2$/Hz at high rotation speeds). Over the whole frequency range, the PSD increase varies depending on the rotation speed.

The bottom panel of Fig. 3.3 shows results from the surface seismic station TMO52 at more than 5.5 km distance to the next WT. The seismic station and the WT are separated by a highway (see orange line at Fig. 3.1). There is a clear rotation dependence of discrete frequencies (0.9 Hz, 1.5 Hz, 1.8 Hz, 2.7 Hz and 3.7 Hz), but predominantly for the lower part of the frequency range (0.5 Hz - 2 Hz). Due to scattering and anelastic attenuation effects in the subsurface, high frequencies will probably attenuate strongly with increasing distance (e.g. Sato et al., 2012). The peak at 0.9 Hz is significantly smaller than at station TMO57. The peak around 1.5 Hz dominates the PSD spectrum and differs from TMO57, especially in shape (more broadly than the sharp peaks at seismic data near to the WT) of the peak. This peak can be also observed in the data of the station TMO57 (Fig. 3.3, top panel), but less strong. This is probably due to the local geological conditions or interference effects by multiple WTs and must be analysed in further studies.

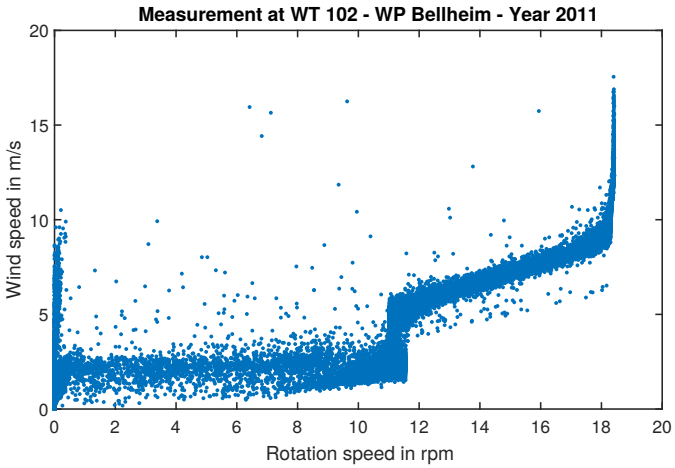

Figure 3.4: Relation of wind speed and the rotation speed of one WT at the wind farm Bellheim over one year (2011).

The frequency range of the signals recorded above 2 Hz is also affected by a rotation dependence, but it is unclear whether these effects are due to WTs or due to other noise sources which are also influenced by wind, like vegetation or buildings.

We infer that the origin of the discrete frequency peaks are multiples of the blade-passing frequency of the WTs. This frequency is three times the rotation speed. If we suppose a maximum rotation speed of 18.4 rpm at the related WT, we expect a blade-passing frequency of 0.92 Hz. Figure 3.3 confirms this assumption for station TMO57, top panel. Here we can find the first clear WT-related peak at around 0.9 Hz. The multiples of this first peak are also noticable at lower rotation speeds. These frequency peaks are more or less stable. This stands in contrast with our observations in Fig. 3.4, where we can see a clear increase of the rotation speed with the wind speed. We would therefore expect a decrease of the multiples frequencies with a decrease of the rotation speed of the blades. For that reason we can not infer the blade-passing frequency as the only source of our observed WT-related signals in the PSD-spectra. There are several other effects which interact with the blade-passing, like eigenfrequencies of the tower-nacelle-system. Therefore we infer that the generation of the emitted seismic signals can not just be explained by the blade-passing frequency of the WT alone, but by an interaction of several plant-specific interference effects. To exclude interferences of e.g. other WTs nearby the seismic station, it is necessary to measure in the vicinity of one single WT and to compare this data with plant-specific data.

To test a relationship between ground motion signals and the blade-passing frequency of one WT, we installed a seismic station at a distance of 10 m to the turbine and another seismic station further away as a marker. Every time a blade passed the tower of the WT in downward direction we tapped the marker station and compare the data with the seismic data in close vicinity to the WT (Fig. 3.5). The vertical component of the ground velocity of both stations was normalized to its maximum. We filtered the trace of the close station from 0.7 Hz to 1 Hz,

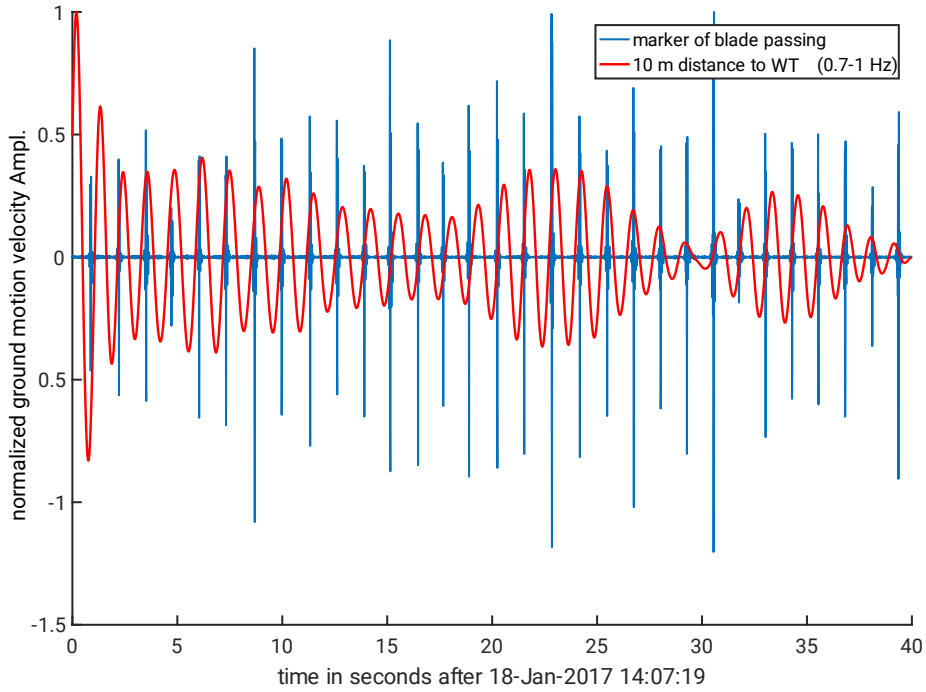

Figure 3.5: Vertical component of the ground motion velocity of a seismic station in the vicinity of a WT (red) and a marker station at a longer distance (blue). Traces are normalized to their maxima. Every time a blade passed the tower in downward direction we tapped the marker station, which is indicated by the peaks (blue). The red curve is bandpass filtered from 0.7 Hz to 1 Hz and shows the WT-induced ground motion at a seismic station in 10 m distance. The amplitude variation of the marker (blue) are due to a tapping on the marker station with different strength.

to highlight the influence of the blade-passing frequency. The small difference in phase is probably caused by an unclean tapping of the blade-passing of this specific WT, which was visually observed. Another visible effect is the interference pattern of the seismic signal (various amplitude magnitudes, see Fig. 3.5 red curve), which we associate with the blade-passing frequency of this type of WT (GE Wind Energy 1.5sl). This variation in amplitude is probably due to acoustic effects. The blade-passing generates a second impact on the seismic station through an air pressure signal at this small distance, besides the impact through the foundation of the WT. At a distance of 10 m it might be possible that the seismic station is still located on top of the foundation. This should be considered for the interpretation. A challenge for further studies would be a distinction between seismic and acoustic effects as well as acoustic effects, e.g. infrasound, which couple into the ground and transform to seismic waves.

3.5.2 Borehole-Stations

The seismic network contains four borehole stations at different depths (70 m - 307 m under surface) and different distances to the next WT (Fig. 3.1). An investigation was undertaken concerning which factor causes the strongest impact on the WT-induced signals: the distance to the next turbine or the depth under the surface. Based on the assumption that a turbine emits primarily surface waves (Styles et al., 2005; Westwood and Styles, 2017), we expect a reduction of the wind-induced signals with increasing depth. For this reason, we compare the stations LDE (150 m depth) and ROTT (305 m depth) (Fig. 3.6, top panel).

As expected, the deeper borehole station ROTT (yellow-red colors) has a lower noise level over the whole frequency range. Station ROTT is about 150 m deeper than LDE and is located at a longer distance to the next turbine. However, there are clear rotation dependent frequency peaks around 1 Hz, which correlate with the signals at the shallower borehole-station LDE (blue-green colors). These peaks are a clear evidence of wind dependent signals, probably due to WTs, at a depth of about 300 m under the surface. The station LDE with 150 m depth

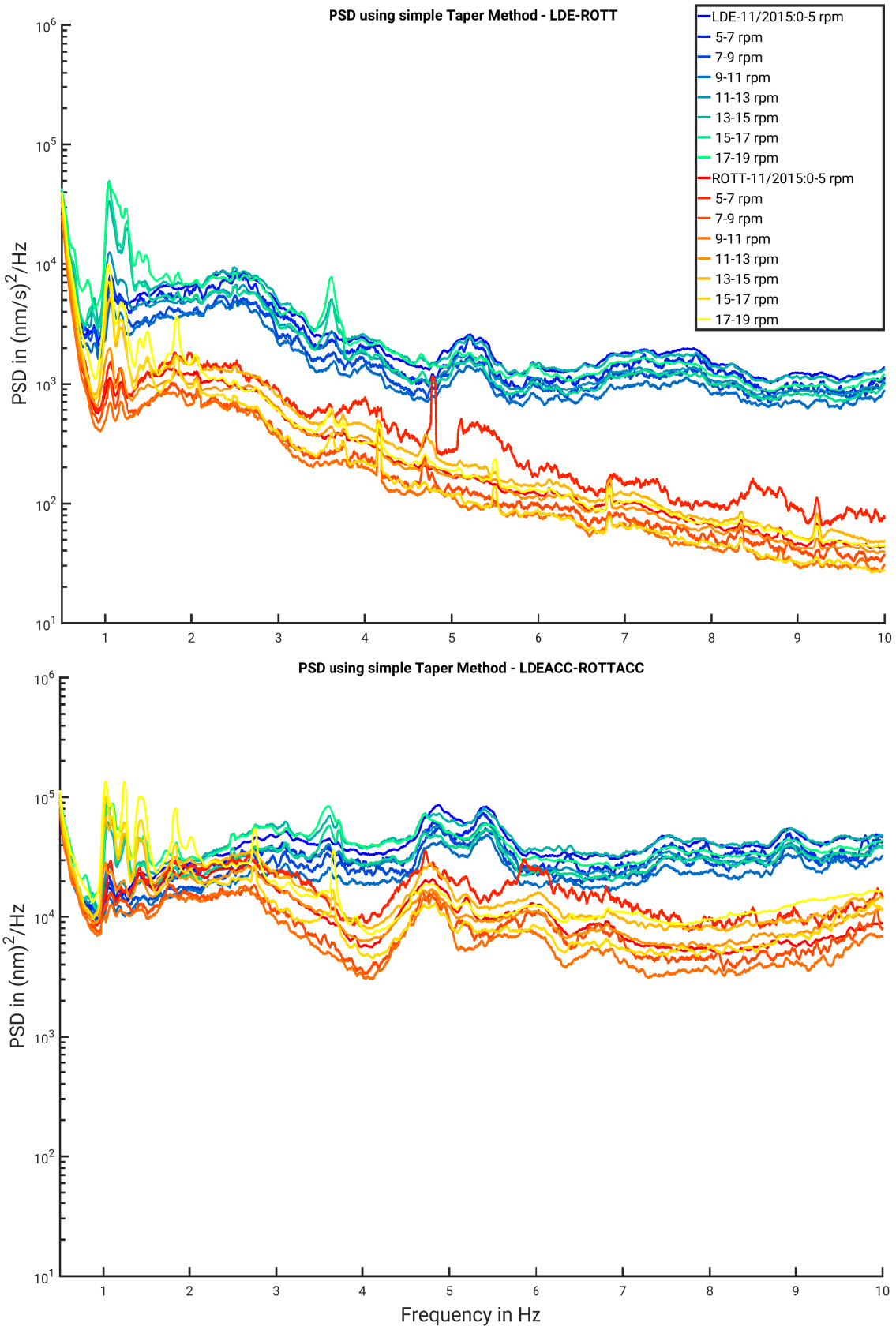

Figure 3.6: The Power-Spectral-Density (PSD) over the frequency range of 0.5 Hz to 10 Hz. Shown are spectra of the borehole-stations LDE and ROTT (top panel) as well as their associated spectra of the surface stations of their locations (bottom panel) for November 2015. The legend indicates the defined rotation speed bins with corresponding colors and the number of PSD-spectra of one-hour long segments used for the mean calculation (75% quantile). Station ROTT (305 m depth), which is deeper than LDE (150 m depth), has a lower noise level over the whole frequency range. However, the surface measurements indicate no difference between both locations, and the frequency peaks coincide with each other.

shows a higher noise level but with similar discrete frequencies like ROTT. A low rotation dependent frequency peak around 0.8 Hz is also visible at station LDE. To separate the distance and depth effects, we compare surface measurements from both locations.
The bottom panel of Figure 3.6 shows the comparison of the signals between the two surface stations. Note that ROTTACC (5.5 km) is further away from the next WT than LDEACC (3.8 km). However, both stations observe nearly the same maximum value (1 - 2 $\cdot$ 10^5 $(nm/s)^2/Hz$) at the rotation dependent frequency peaks in the lower part of the spectrum (around 1 Hz). For this reason, we infer that the distance attenuation is much smaller than the attenuation with depth. This phenomenon is also observed for the borehole station LDO, which has nearly the same distance to the WTs than LDE but with a depth of about 105 m and thus higher PSD-values for WT-induced signals than station LDE. Here we can not differentiate between surface and borehole data in absence of a surface station at LDO, however, it confirms our results by assuming a radial wave propagation away from the WTs.
If this conclusion can be apply to other wind farms or if this is just a local effect of the specific geological conditions of the Upper Rhine Graben must be analyzed in further studies.

3.5.3 Identification of Turbine Types

After the first installation of WTs in 2004 - 2008, six additional WTs were built in September 2014. They differ significantly in geometry, more precisely, through a taller tower height (139 m) and a higher power rating (2.5 MW). To investigate the impact due to taller WTs at the wind farm in Offenbach, we compare data from January 2014 (before the installation of the new WTs) and October 2014 (after the installation). Note that smaller WTs already existed at Offenbach before the installation in 2014.
As demonstrated in Figure 3.7, we can identify the signals of the new WTs in our PSD spectra. After the installation, the PSD displays a clear increase at discrete frequencies of 0.8 Hz, 1.05 Hz, 1.23 Hz and 3.6 Hz. These peaks are rotation dependent and they are obviously due to the new type of wind turbines in Offenbach. The first peak at 0.8 Hz has a much smaller amplitude (up to 7 $\cdot$ 10^3 $(nm/s)^2/Hz$) than the following peaks at 1.07 Hz (up to 3 $\cdot$ 10^4 $(nm/s)^2/Hz$) and 1.26 Hz (up to 4 $\cdot$ 10^4 $(nm/s)^2/Hz$). The appearance of the frequency peaks can be detected at all analysed stations used for this study after the installation in September 2014. The peak around 1.07 Hz can probably not be associated with a multiple of one specific blade-passing frequency, like e.g. the peak around 1.8 Hz at Fig. 3.3. Stammler and Ceranna (2016) also observed a wind dependent peak around 1.15 Hz. They provide two explanations for the origin of this peak:

1. Various types of WTs lead to a type-driven distribution of the 1.15 Hz peak heights by emitting different spectra.

2. Focusing and defocusing of seismic signals by resonance effects within the limestone layer, which can be identified in the area of the Gräfenberg array.

Stammler and Ceranna (2016) found it difficult to distinguish between these two explanations. However, they attributed a large jump in PSD values of the 1.15 Hz signal to the installation of ten new WTs within 6 km distance of a seismic station.
To conclude, the 1.07 Hz and the 1.26 Hz peaks can be directly associated with the installation of the new turbines, but are probably a type-driven distribution of different emitted signals by various types of WTs and containing focusing and defocusing effects of the present geological layering. However, observations before and after the installation of new WTs can be used to investigate interference effects of different types of turbines inside a wind farm. We also can give a first impression how future (taller) turbines impact sensitive facilities like seismological instruments. The noise level will increase especially in the lower part of the frequency range (0.5 - 2 Hz). The intensity of the impact is most probably dependent on the geology, the distance to the WT and of course the type of the WT with their particular heights and blade-passing frequencies. In this example, the installation of six new

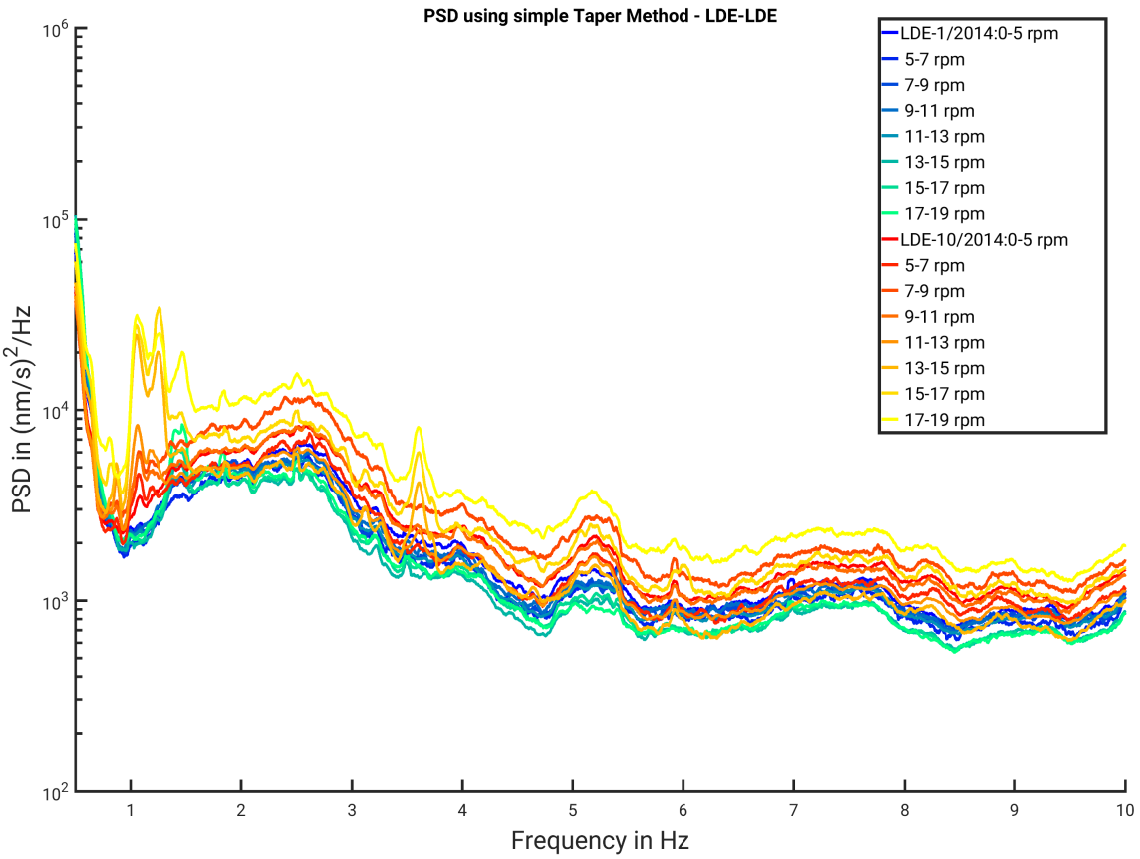

Figure 3.7: The Power-Spectral-Density over the frequency range of 0.5 Hz to 7 Hz. Shown is the borehole station LDE in January 2014 (blue-green, before the new installation of WTs in Offenbach) and in October 2014 (red-yellow, after the installation of WTs). The legend indicates the defined rotation speed bins with corresponding colors. After the installation of 6 new high turbines, clear rotation dependent frequency peaks appear at 0.8 Hz, 1.05 Hz, 1.23 Hz and 3.6 Hz, leading to a significant increase of the seismic noise level.

WTs leads to an increase by a factor of about 100 of the noise level at high wind speeds at a borehole station with 150 m depth and a distance of 3.8 km to the next WT.

3.6 Attenuation of WT-related signals

One fundamental property of the propagation of WT-induced seismic waves is the attenuation along the wave path. The attenuation depends on the wave frequency and ground properties, e.g. intrinsic (anelastic) attenuation or scattering attenuation based on structural heterogeneities in the subsurface. We assume the wind turbine as a point source with radial wave propagation. We will discuss this assumption in section 3.8.

For detecting the attenuation of the signals, we performed profile measurements in the vicinity of the Bellheim wind farm near Landau (see Fig. 3.8). We measured along two profiles with different azimuth to the wind turbine to detect possible changes in the radiation of seismic waves, depending on the wind direction. After combining both profiles into one plot for fitting the maximum values of the PSD in different frequency bands, we determine that the difference in radiation between these two profiles at distances up to 3 km can be neglected because of no significant differences in the PSD values relative to the azimuth for WT-related peaks (Fig. 3.9). The PSD spectrum was calculated of each station for 3 hours in the daytime and moderately smoothed (width 0.05 Hz). Ten seismic stations (A - J, including TMO57) were used for this measurement (7x Nanometrics Trillium Compact Posthole 20s, 3x Nanometrics Trillium Compact Posthole 120s). Additionally, we were able to use the data of station TMO57, provided by the Federal Institute for Geosciences and Natural Resources (BGR). Unfortunately,

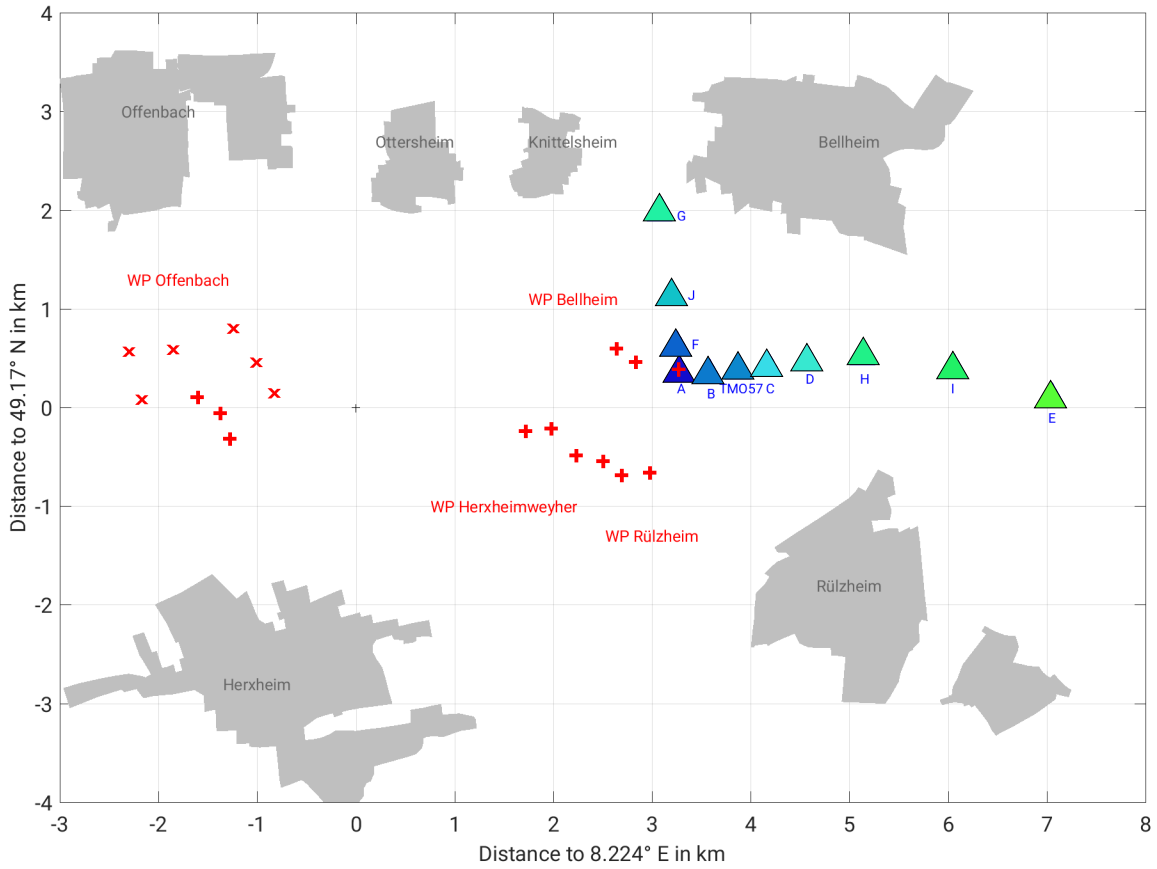

Figure 3.8: Map of the short-term profile measurement on 17.11.2016. Stations are indicated as triangles, wind turbines are indicated as cross-symbols. The recording time was up to 3 hours.

station C failed after the installation, so altogether, we collected data from ten stations. The wind speed on this day was about 8 m/s to 10 m/s (resp. 16 rpm to 18 rpm).

Figure 3.9 is comparable with the plots described before. The different colors indicate the distance from the recording station to the nearest WT (blue = short distance, green = long distance). Station A is located just about 10 m away from the WT, which explains the high noise level of the recordings over the whole frequency range. At this distance, several effects will impact the signal like tower vibration or acoustic effects. For this reason we will exclude this station from the continuing analysis. Clearly visible are significant peaks around the multiples of the blade-passing frequency (0.9 Hz). The peaks in the lower frequency range (such as 1.8 Hz) can be tracked to all stations up to distances of more than 3 kilometers. Obviously higher frequencies are stronger affected by attenuation and cannot be detected at larger distances. We selected four different PSD-peaks at different frequencies to calculate the attenuation depending on the frequency. These peaks are plotted as a function of the distance from station site to the nearest WT (Fig. 3.10). We assume a power-law decay proportional to $1/r^b$ (Stammler and Ceranna, 2016) by using a nonlinear least square method, which consistently fits the decay very well. The samples at the shortest distance (first point) in Fig. 3.10 differ widely to other measurement points with a longer distance to the WT. This could be explained, as mentioned before, with near field effects of the wave propagation, thus we exclude these points from the regression. In the lower frequency range (1 Hz to 4 Hz), we obtain b values of around 0.77 - 0.85. However, it should mention that the fit for 4.6 Hz shows a large uncertainty for the 95% confidence bounds (see Tab. 3.2).

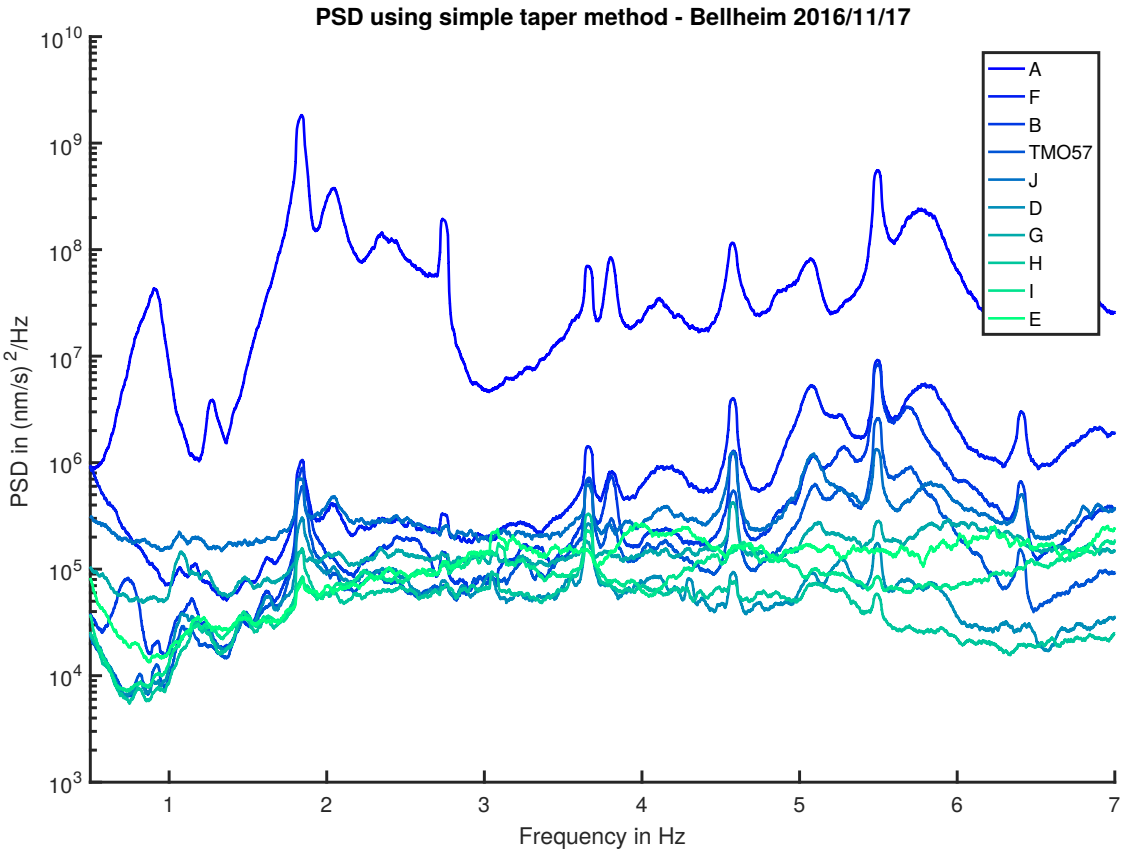

Figure 3.9: The Power-Spectral-Density over the frequency range of 0.5 Hz to 7 Hz. Shown are all stations during the measured time interval of 3 h. The color indicates the station (Fig. 3.8) and is ordered by distance to the WT (blue to green). Clear peaks can be observed at 1.8 Hz, 3.6 Hz, 4.5 Hz, 5.4 Hz and 6.3 Hz.

Table 3.2: Table with the results of the attenuation measurement for the far field, as well as the 95% confidence bounds for the *b* value and the root means square error (RMSE) of the fit.

Frequency in Hz	b	95% confidence bounds	RMSE in $\frac{(\frac{nm}{s})^2}{Hz}$
1.8	0.78	(0.52, 1.04)	1.14e+05
3.7	0.77	(0.4, 1.14)	1.83e+05
4.6	0.85	(0.14, 1.56)	3.29e+05
5.5	1.59	(1.2, 2)	5.86e+05

With increasing frequency ($>$ 5 Hz) the *b* value rises to 1.59. The increase of the *b* value with higher frequencies can be explained by scattering and anelastic attenuation effects along the ray path (e.g. Sato et al., 2012).

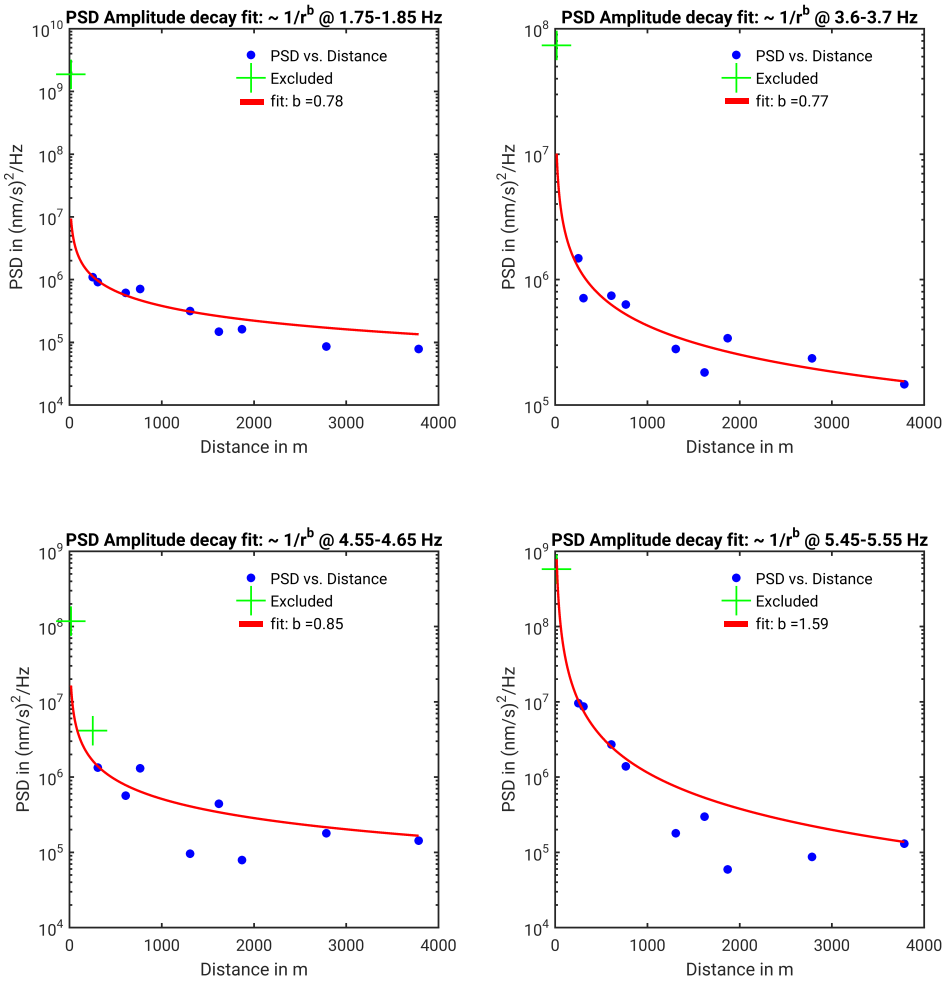

Figure 3.10: Attenuation relation at four different frequencies. We fit a power-law decay proportional to $1/r^b$ to the seismic data (dots). Note that the nearest samples (for 4.6 Hz also the second sample, indicated as crosses) are excluded because of near field effects.

3.7 Attenuation of wind turbine-related signals in the near field

3.7.1 Attenuation with distances less than 600 m

To analyse near field effects of the seismic wave propagation and to observe the attenuation of WT related signals within the order of hundreds of meters, we accomplished a second profile measurement with a closer distance between each seismic station and a total profile length of 600 meters to the next turbine.

The setting is shown in Figure 3.11. Note that station TMO57 has the same location as in Figure 3.8 for orientation. The distance between the stations starts at 15 m and becomes longer with increasing distance to the WT.

The different PSD curves in Figure 3.12 show nearly the same shape at all stations. This observation means that the WT-related signals, observed at the first station A, propagate above 1.5 Hz with the same behaviour and just attenuate in strength. Below 1.5 Hz, the PSD curves of the first 30 m differ from the other curves. This will be discussed in section 3.8. It is not possible to fit all data points with a $1/r^b$ model, thus we have to exclude the first value for fitting an attenuation curve (see Fig. 3.13, red line). The nearest station to the turbine for the far field (Fig. 3.8) as well as the near field measurement (Fig. 3.11) has the same location and is probably located on the foundation of the WT.

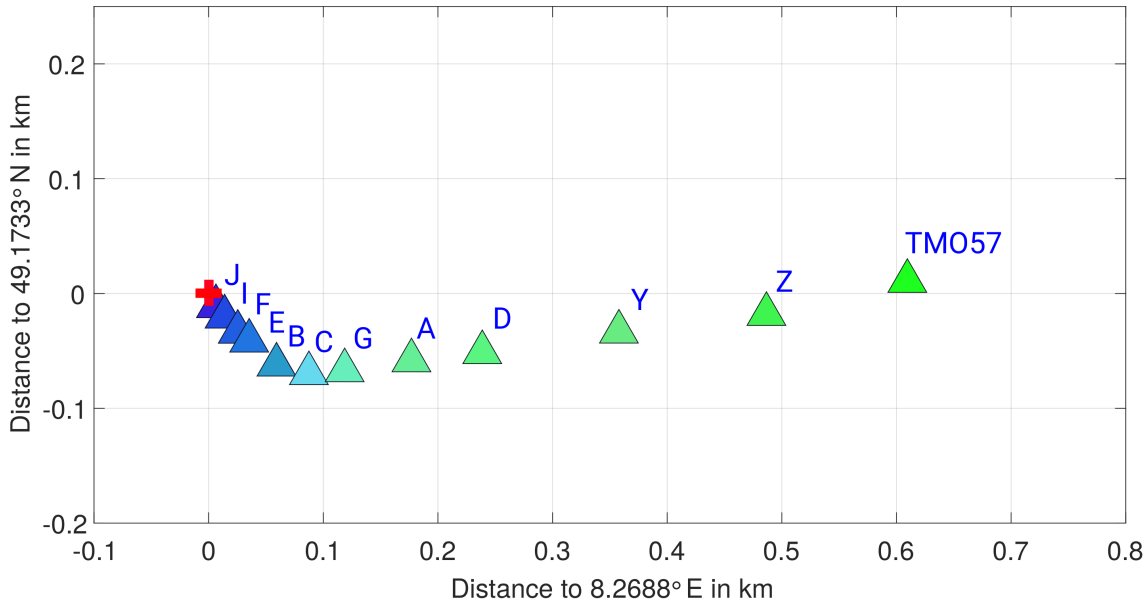

Figure 3.11: Map of the near field profile measurement on 18.01.2017. Stations are indicated as triangles, the wind turbine is indicated as cross-symbol. The measurement time was up to 3 h. Station TMO57 has the same location as in Figure 3.8.

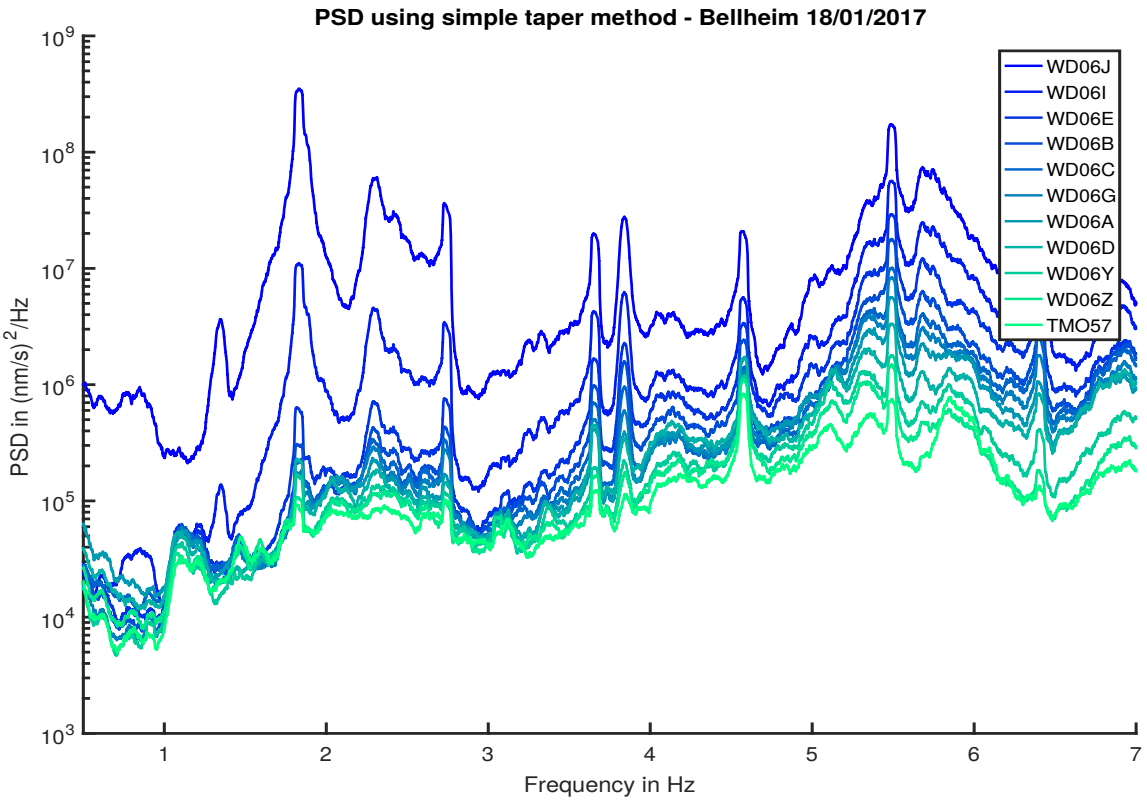

Figure 3.12: The Power-Spectral-Density over the frequency range of 0.5 Hz to 7 Hz. Shown are all seismic stations during a time interval of 3 h. The color indicates the station (Fig. 3.11) and is ordered by distance to the WT (blue to green). Clear peaks can be observed at 1.8 Hz, 2.7 Hz, 3.6 Hz, 3.7 Hz, 4.5 Hz and 5.4 Hz.

Table 3.3: Table with the results of the attenuation measurement for the first 600 m, as well as the 95% confidence bounds for the b value and the root means square error (RMSE) of the fit.

Frequency in Hz	b	95 % confidence bounds	RMSE in $\frac{(\frac{\mathrm{nm}}{\mathrm{s}})^2}{\mathrm{Hz}}$
1.8	1	(0.55, 1.45)	7.27e+04
2.7	1.17	(0.99, 1.35)	3.21e+04
3.7	1.31	(1.22, 1.39)	7.96e+04
4.6	0.71	(0.54, 0.87)	4.18e+05
5.5	1.17	(1.03, 1.31)	2.11e+06
6.4	1.22	(1.14, 1.31)	2.67e+05

For frequencies higher than 5 Hz, the power-law decay can explain also the first values in the immediate vicinity of the WT (Fig. 3.12). However, in contrast to the far field measurement (Fig. 3.10), we can not observe any systematic dependency of the *b* value (0.71 - 1.31) with frequency in the near field at distances less than 600 m (Fig. 3.13, red line). This is probably due to the minor effect of scattering and anelastic attenuation along the ray path at such small distances. Also the uncertainties of the fits are relatively stable (except the fit at 1.8 Hz, which are characterised by larger 95% confidence bounds, see Tab. 3.3).

3.7.2 Attenuation with distances less than 100 m

To investigate also the wave field in the first 100 m distance in the near field of a WT, we fit the same power-law decay to the amplitudes of the first four seismic stations without excluding data points (see Fig. 3.13, black line). The attenuation along the first part of the profile is very strong, particularly in the lower frequency range ($<$ 3 Hz). In contrast to section 3.6, the *b* values decrease from 5.82 to 1.46 with increasing frequency. In the upper frequency range ($>$ 5 Hz), the black and the red curves are nearly similar to each other and the attenuation model can explain all data samples, which was already mentioned in section 3.7.1. On the other hand, the different fit curves in the lower frequency range differ significantly, depending on whether the first samples in Fig. 3.13 are excluded or not. As a consequence it is not possible to fit all data samples for low frequencies ($<$ 5 Hz) with a simple power-law decay model.
To summarise, we found an attenuation factor for the far field of 0.77 to 1.59, dependent on the frequency. For the near field, we observe an attenuation factor of 0.71 to 1.31 for the first 600 m, but with no clear frequency dependency. For distances less than 100 m to the WT, we detected a clear decrease of the *b* value with increasing frequency of about 5.96 to 1.49. Again the fit at 4.6 Hz shows a large uncertainty for the 95% confidence bounds (see Tab. 3.4), which should be considered for the interpretation.

3.8 Discussion

The main task of this study is the clear identification of WT-induced signals. Influences due to wind on seismological records affect a broad frequency band without any discrete frequencies, although the impact of wind related signals depends strongly on many site specific factors. Withers et al. (1996) or Lott et al. (2017) illustrated a clear upward trend of the power of ground motion velocity with increasing wind speed. However, clear wind-related discrete frequency peaks in the range of 0.5 Hz to 10 Hz are not visible in their publications due to the absence of any WT nearby to the analyzed area. We observe this upward trend in our seismic data with increasing wind speed resp. rotation speed. But there is also a clear appearance of discrete frequency peaks which can be correlated with rotation speed or blade-passing frequency of a WT (see Fig. 3.3) and its multiples and which were also observed

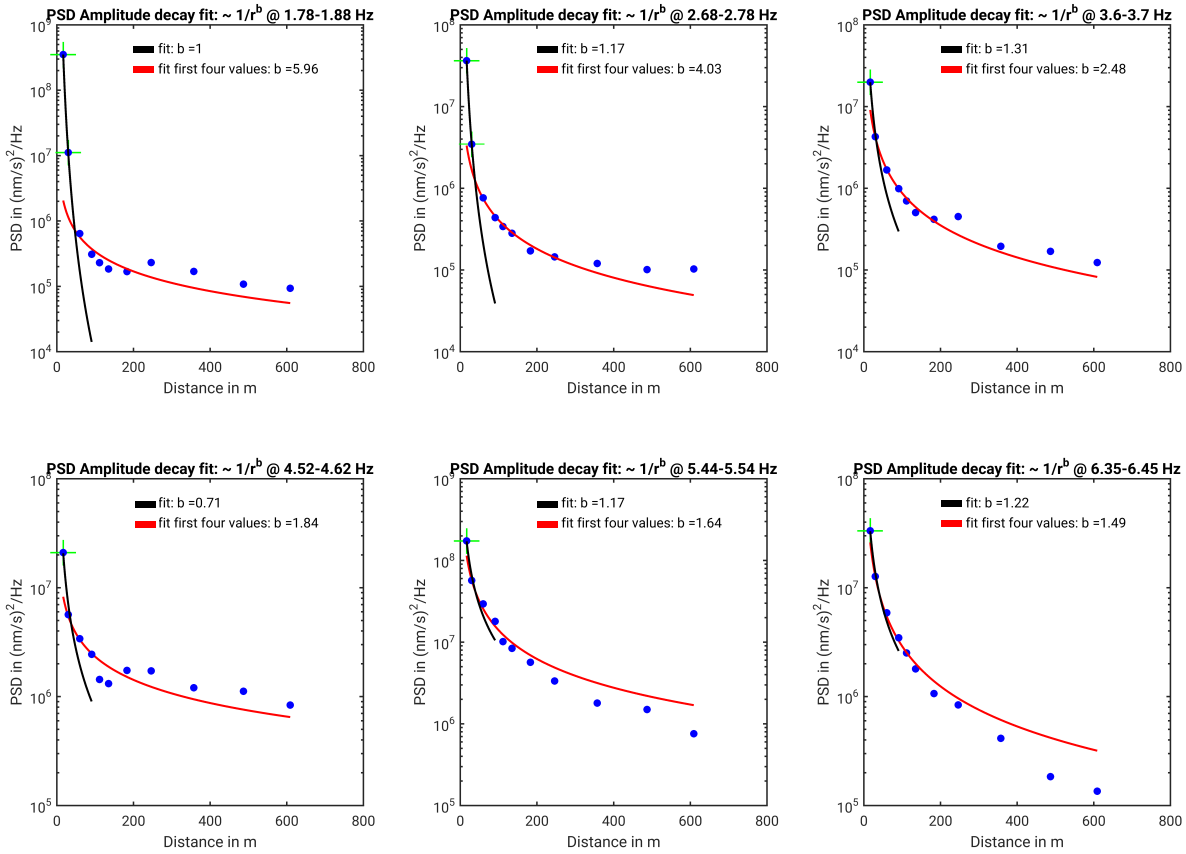

Figure 3.13: Attenuation relation at six different frequencies for the near field. We fit a power-law decay proportional to $1/r^b$ to the seismic data (dots), indicated by a red line. Note that the nearest samples (for 1.8 Hz and 2.7 Hz also the second sample, indicated by crosses) are excluded for the red fit. To investigate the attenuation factor b for the first 100 m, we also fit the same power-law decay to the first four seismic data points with no excludes (black line). The legend indicates the different b values.

at other studies near to WTs, like Stammler and Ceranna (2016). These frequencies can change in their intensity level along their ray path, which is probably due to focusing and defocusing effects of the subsurface as well as interference effects of induced signals (seismic and acoustic) of multiple WTs of different types. In which way the noise level of a seismic station near to several WTs is influenced by these different effects of WT-induced signals must be studied in future investigations. Furthermore, the comparison of the ground motion before and after the installation of WTs shows an increase in the lower frequency part (< 2 Hz). This is interpreted as a clear evidence for a WT origin related with the signals.

In section 3.6, we assume the WT as a radiative point source, to compare recording stations with a different azimuth to the WT. Reports about the Eskdalemuir wind farm in Scotland, like Xi Engineering Cosultants Ltd (2014), suggest a higher noise level in-line with the wind direction from station to WT than at cross-wind direction. During our far field profile measurement (section 3.6), the wind came mostly from the southwest direction. Therefore, both profiles do not lie in the wind direction and we are able to combine the data of both profiles. Otherwise, we would have to differentiate between both profiles, dependent on their in-line or cross-wind direction from station to WT.

Because of the non-circular station distribution around the wind farms at Landau and with that an absence of suitable data, the dependency of the wind direction of WT-induced signals (which was shown at the Eskdalemuir Array) can not be confirmed. This effect must be investigated with circular measurements around one single WT in future studies. It is also questionable if wind direction effects will influence the attenuation analyses in relation to the distance.

Table 3.4: Table with the results of the attenuation measurement for the first 100 m, as well as the 95% confidence bounds for the b value and the root means square error (RMSE) of the fit.

Frequency in Hz	b	95 % confidence bounds	RMSE in $\frac{(\frac{nm}{s})^2}{Hz}$
1.8	5.96	(5.7, 6.22)	3.95e+05
2.7	4.03	(3.01, 5.05)	4.88e+05
3.7	2.48	(1.23, 3.72)	8.4e+05
4.6	1.84	(0.2, 3.49)	1.83e+06
5.5	1.64	(0.68, 2.6)	1.05e+07
6.4	1.49	(0.95, 2.03)	1.3e+06

To estimate the influence of a single WT, Stammler and Ceranna (2016) divided the PSD value by N, which corresponds to the number of contributing WTs. The distinction of influences of one single WT and multiple WTs is a main challenge for seismologists. At our investigated location, we were not able to compare seismic data of a single WT with multiple WTs to confirm the assumption of Stammler and Ceranna (2016). However, we assume that the first 20-30 m of the profile measurement (see section 3.7.2 and Fig. 3.11 resp. Fig. 3.12) is just influenced by only the next WT to the station locations. At this small distance we can neglect interference effects of other WTs. Beyond 30 m distance, the signal of the PSD-values changes below 1.5 Hz (see Fig. 3.12). This variation of PSD-values is small, especially when we focus our research on discrete frequencies above 1.5 Hz. But it could explain effects which we observe after the installation of new WTs. Then the noise level increases significantly below 2 Hz and could not be explained just with multiples of the blade-passing frequency of one WT.
The attenuation factors b for the far field range from 0.77 at 1.8 Hz to 1.59 at 5.5 Hz. Schofield (2001) found a attenuation factor of b =1 for a 4.34 Hz peak. This slightly differs from our results, but by looking at the 95% confidence bounds we can confirm this attenuation for the first 3 km. The b factor depends on the attenuation properties of the local subsurface which needs also to be considered. For higher wind speeds, all PSD values may increase, however the b values should not change. This was not tested yet with profile measurements and should be part of further studies, also at different locations.
This work cannot give a general recommendation for working with seismic data near to WTs. The impact of WT-induced signals on a seismic station depends on the distance, geological conditions, the background noise level of the station and the number of WTs. We showed a reduction of WT-induced signals primarily with depth, although WT-induced signals can be observed even in depths of more than 300 m. To transfer this results to other regions, further investigations at different locations must be done in the future.

3.9 Conclusion

Based on PSD-spectra of long-term measurements at wind farms around the town of Landau, SW Germany, we find clear evidence for WT-induced signals on nearby seismic stations. These signals can be verified to distances up to 5 km from the location of the WT. Discrete frequency peaks, which we can associate as multiples of the blade-passing frequency with interference effects of plant-specific eigenfrequencies, increase strongly with increasing rotation speed. This leads to an increase of the noise level up to 100 times in the immediate vicinity of the turbine. Also borehole stations, with 100 m to 300 m depths, observe clear signals from WTs. Based on a comparison with surface stations, we assume a stronger effect of attenuation with depth than due to attenuation in the horizontal direction. Furthermore, it is possible to identify the installation of a new wind farm in the seismic data and to allocate the WT-induced signals to the characteristics of the turbine (height of the tower). After the WT installation, we obtain an increased noise level of more than 10 times at a distance of about 3 km at frequencies of 0.9 Hz to

1.3 Hz. By plotting PSD-maxima in different frequency bands over distance, we obtain a power-law decay of b = 0.77-0.85. This value increases with higher frequency for the far field (up to 1.59), which can be explained by scattering and anelastic attenuation effects of the signal along the wave path. Near field observations show generally higher b values (0.71-1.31) for the first 600 m, but with no clear frequency dependence. The attenuation results for the first 100 m show a clear influence of near field effects. Here, the b value decrease from 5.96 for low frequencies to 1.49 for 6.4 Hz.

Acknowledgements

The project “TremAc” is funded by the Federal Republic of Germany. Awarding authority: The Federal Ministry for Economic Affairs and Energy based on a resolution of the German Bundestag. Seismic data were provided by “Erdbebendienst Südwest”, “Federal Institute for Geosciences and Natural Resources” and “Karlsruher Broadband Array (KABBA)”. We would like to thank “pfalzwind GmbH (Ludwigshafen/Germany)” for the provision of data and their support of this work. We would like to thank Werner Scherer for help with technical work, as well as installation and service of seismic stations; Mohsen Koshesh for calibrating the instruments; Rainer Plokarz for helping with data handling and Petra Knopf for solving IT-problems. We also thank the two anonymus reviewers and the editor for their helpful und constructive suggestions and comments.

4 Locating wind farms by seismic interferometry and migration

This study identifies the WT (or in this case wind farms) as a seismic noise source by using a seismic interferometry approach. This approach was introduced by Horstmann and Forbriger (2010) and applied on seismic data of the TIMO network around Landau by Tobias Friedrich within the framework of a master thesis. I contributed to this work by supervising the thesis and as a contributing author of the following paper, especially chapter 4.2, 4.3, 4.7 and 4.8.
This chapter has been published in:

Friedrich, T., Zieger, T., Forbriger, T., Ritter, J.R.R. (2018),
Locating wind farms by seismic interferometry and migration,
J. Seismol., 22: 1469 - 1483
DOI: https://doi.org/10.1007/s10950-018-9779-0

4.1 Abstract

We present a case study on the detection and quantification of seismic signals induced by operating wind turbines (WTs). We spatially locate the sources of such signals in data which were recorded at 11 seismic stations in 2011 and 2012 during the TIMO project (Deep Structure of the Central Upper Rhine Graben). During this time period, four wind farms with altogether 12 WTs were in operation near the town of Landau, Southwest Germany.
We locate WTs as sources of continuous seismic signals by application of seismic interferometry and migration of the energy found in cross-correlograms. A clear increase of emitted seismic energy with rotor speed confirms that the observed signal is induced by WTs. We can clearly distinguish wind farms consisting of different types of WTs (different hub height and rotor diameter) corresponding to different stable frequency bands (1.3 Hz – 1.6 Hz, 1.75 Hz – 1.95 Hz and 2.0 Hz – 2.2 Hz) which do not depend on wind speed. The peak frequency apparently is controlled by the elastic eigenmodes of the structure rather than the passing of blades at the tower. From this we conclude that vibrations are coupled into the ground at the foundation and propagate as Rayleigh waves (and not as infrasound). The migration velocity of 320 m/s corresponds to their group velocity.
The applied migration method can contribute to the assessment of local sources of seismic noise. This topic gets growing attention in the seismological community. In particular, the recent boost of newly installed wind farms is a threat to seismological observatories such as the Black Forest Observatory (BFO) and the Gräfenberg array (GRF) or gravitational wave observatories (e.g. LIGO, VIRGO) in terms of a sensitivity degradation of such observatories.

4.2 Introduction

The influences of wind turbines (WTs) on local seismic stations, seismological observatories and gravitational wave observatories is becoming an important topic inside the seismological community, especially after the large increase of new installations of WTs to boost renewable energy all over the world. Several studies (e. g. Schofield, 2001; Styles et al., 2005; Saccorotti et al., 2011; Xi Engineering Cosultants Ltd, 2014; Stammler and Ceranna, 2016; Flores Estrella et al., 2017; Zieger and Ritter, 2018; Neuffer and Kremers, 2018) investigate the seismic

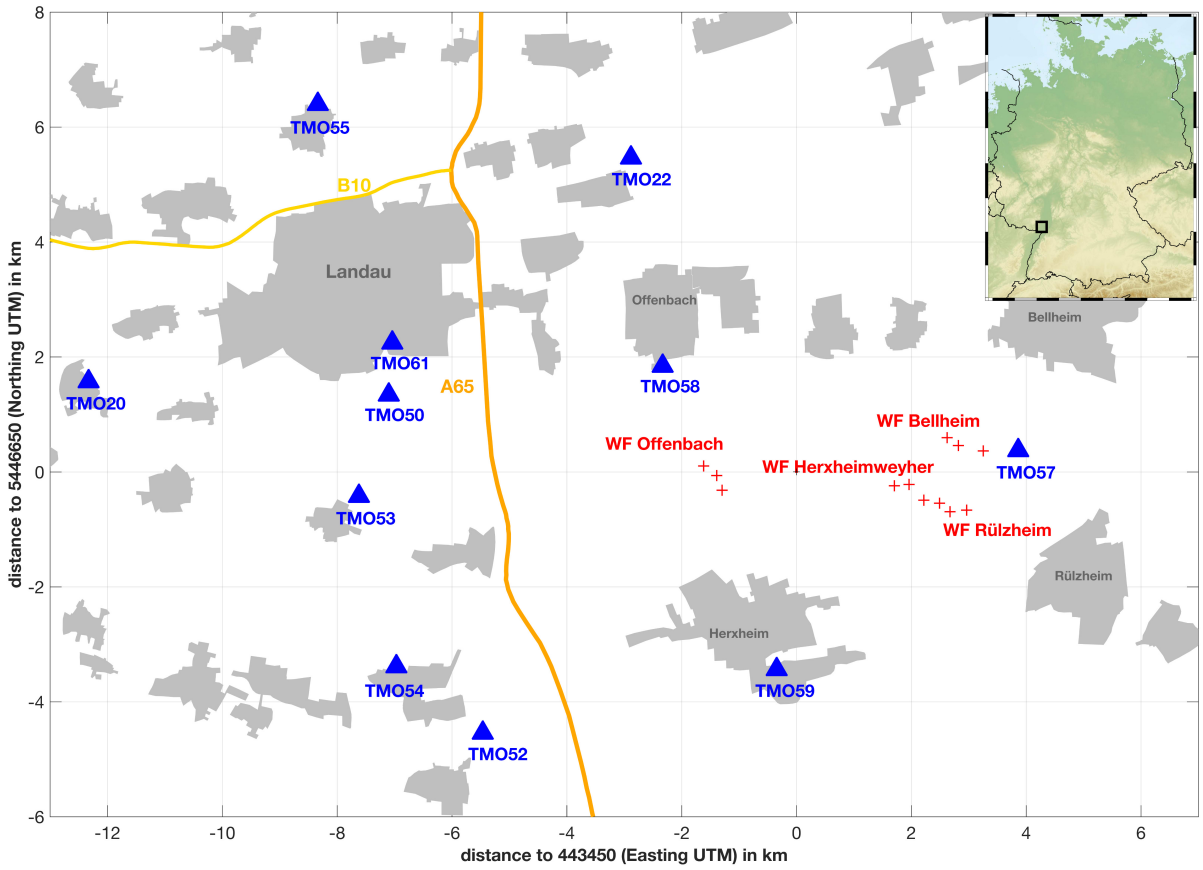

Figure 4.1: Map of the study area with the seismic stations (blue triangles) used in this study, the wind turbines (red plus icons), the villages (grey), the state road B10 (yellow), and the highway A65 (orange).

emissions of WTs. The majority of them focus on the increase of the seismic noise level going along with the installation of new WTs in the vicinity of the seismic stations. However, the data analyses do not clearly identify the WTs as the cause of the increased seismic signal level by locating the sources of the observed seismic waves. In the present study we demonstrate how sources of continuous signals can be located by the migration approach of Horstmann and Forbriger (2010) and be identified as wind farms. After a slight modification this procedure enables us to investigate the characteristic increase of generated seismic energy with increasing wind speed for a single, selected wind farm in the presence of other sources.

An early, comprehensive study on WT-induced signals in seismic recordings was published by Styles et al. (2005). They identify the characteristic frequencies of the WTs such as the blade-passing frequency (three times the rotation frequency) and their multiples at the Eskdalemuir Array in Scotland, Great Britain. They assume seismic waves propagating as vertically polarised P-SV (Rayleigh) waves excited by the WTs and demonstrate an increase of the amplitude with increasing wind speed. Schofield (2001) suggests that the propagation of WT-induced signals is partly through infrasound with an attenuation factor proportional to $1/R$ (where R is the distance between WT and observation point) for seismic measurements at the Stateline Wind Project. Saccorotti et al. (2011) investigate the vibrations produced by a wind farm near the VIRGO Gravitational Wave Observatory in Italy and present a simple model of wave propagation: the combination of direct surface waves with dominating Love waves and body waves reflected at the boundary between marine, fluvial, and lacustrine sediments and the carbonate basement in approximately 800 m depth. Gassenmeier et al. (2015) developed a single-station approach to investigate the direction of the incoming seismic noise and identify emitted Rayleigh waves of a nearby wind farm. Stammler and Ceranna (2016) examine the influence of WTs on seismic recordings at the Gräfenberg Array (GRF). They

Table 4.1: List of the WTs near Landau (Fig. 4.1) which were in operation during 2011 and 2012. Specified are date of commissioning, the WT-type, the nominal electric power P, the rotor diameter d and the hub height h of the turbines. The WTs of GE and Fuhrländer have the same technical specifications. The WTs of the type Vestas V90 have a larger rotor diameter, larger hub height and more power (URL: www.energieatlas.rlp.de/earp/daten/ee-anlagen/, de.wikipedia.org/wiki/Liste_von_Windkraftanlagen_in_Rheinland-Pfalz).

Wind farm	Commissioning	WT type	P in MW	d in m	h in m
Bellheim	27-09-2004	GE Wind Energy 1.5sl	1.5	77	100
Bellheim	27-09-2004	GE Wind Energy 1.5sl	1.5	77	100
Bellheim	27-09-2004	GE Wind Energy 1.5sl	1.5	77	100
Rülzheim	18-05-2005	Fuhrländer FL MD77	1.5	77	100
Rülzheim	18-05-2005	Fuhrländer FL MD77	1.5	77	100
Rülzheim	23-03-2006	Fuhrländer FL MD77	1.5	77	100
Herxheimweyher	28-09-2005	Fuhrländer FL MD77	1.5	77	100
Herxheimweyher	30-09-2005	Fuhrländer FL MD77	1.5	77	100
Herxheimweyher	10-10-2005	Fuhrländer FL MD77	1.5	77	100
Offenbach	22-02-2008	Vestas V90	2.0	90	105
Offenbach	22-02-2008	Vestas V90	2.0	90	105
Offenbach	22-02-2008	Vestas V90	2.0	90	105

demonstrate a decrease of the detection capability of the GRF stations in the frequency band of 1 Hz – 7 Hz due to an increasing number of WTs with a dependence on wind speed of the levels of noise spectra of all stations. They also present signals emitted by WTs close to 1.15 Hz which are detectable at distances larger than 15 km to the nearest seismic station.

In the current study we focus on WT-induced signals identified by Zieger and Ritter (2018) in the area around the town of Landau, Southwest Germany, and on locating their sources by application of seismic interferometry. We use the migration method (see section 4.4) introduced by Horstmann and Forbriger (2010) for locating industrial noise sources in Bucharest, Romania. A very similar approach was applied by Mündel (2009) to locate WTs near Ketzin, Northeast Germany, and by others to locate sources of ocean microseisms (Shapiro et al., 2006; Zeng and Ni, 2010) or source regions of seismic tremors in volcanic areas (e. g. Ballmer et al., 2013; Droznin et al., 2015). An advancement of this method is the so-called *double-correlation method* by Li et al. (2017), who use cross-correlations of cross-correlograms of two station pairs (three stations in total, one of these as a reference station). As a consequence, noise is suppressed in a superior way and the source region is focussed more distinctly. Sgattoni et al. (2017) use this method to locate tremor at the Katla volcano, Iceland.

4.3 Setting

The town of Landau is located in the southwestern part of Germany, about 30 km northwest of the city of Karlsruhe. The area is within the central Upper Rhine Graben with a ca. 300 m thick layer of unconsolidated Cenozoic sediments at the surface. The region is of seismological interest because of the natural seismicity of the Upper Rhine Graben and because of induced seismicity at two geothermal power plants (Vasterling et al., 2017; Ritter et al., 2008). Due to the seismic monitoring long-term broadband recordings of a dense seismic network are available. Data are provided by the “Erdbebendienst Südwest”, the “Federal Institute for Geosciences and Natural Resources (BGR)”, and the “Karlsruher Broadband Array (KABBA)”. Several WTs are located in the vicinity of the seismic network which went into production of electrical power at different times. Table 4.1 gives an overview of the WTs in operation during 2011 and 2012. The exact locations of these WTs are shown in Fig. 4.1. With

overall four wind farms and a dense seismic network, the area around Landau is well suited for the current study. As shown in Table 4.1, the first WTs were installed in September 2004. Seismic data are not available for times before December 2004. Hence, we are unable to analyse seismic signals without influences of WTs.

4.4 Method and Data Processing

In the following section we explain our approach to seismic interferometry and migration of source energy. All steps of data processing are implemented in MATLAB.

The seismic waveform recordings of one day (vertical component) are divided into non-overlapping time windows, whereby the length of these windows depends on the maximum distance between the seismic stations. In the current setting we use time windows with a length of 10 minutes (approximately six times the maximal time lag, after Groos, 2010). In the next step we use a noise classification after Groos and Ritter (2009) to reject time windows containing corrupt data (e.g. due to technical problems). For most days, no time windows are excluded by the noise classification. Where time windows are rejected, their share in the total number of windows of one day is negligible ($< 2.5\,\%$). The cross-correlation of each seismic pair of stations is computed for a maximum time lag of 100 s. A maximum time lag of $t = S/v$ should be considered, if S is the largest inter-station distance in the network and v is a lower bound for the expected propagation velocity (we set this lower bound to 200 m/s based on the local geology). Next, a spectral whitening routine is applied to the cross-correlations for a normalization in the frequency domain. At this step, the Fourier coefficients are normalized to their maximum modulus. This routine is applied after the cross-correlation to reduce computing time. The spectral whitening leads to an enhancement of weak signals and improves the quality of our results. We stack (average) all cross-correlations of one day and apply a band-pass filter in the time domain using a 4-th order Butterworth filter to investigate signals in different specific frequency bands. The filter is applied twice (once forward and once backwards in time) to maintain the signals phase. These final, filtered stacks are the input to the migration analyses.

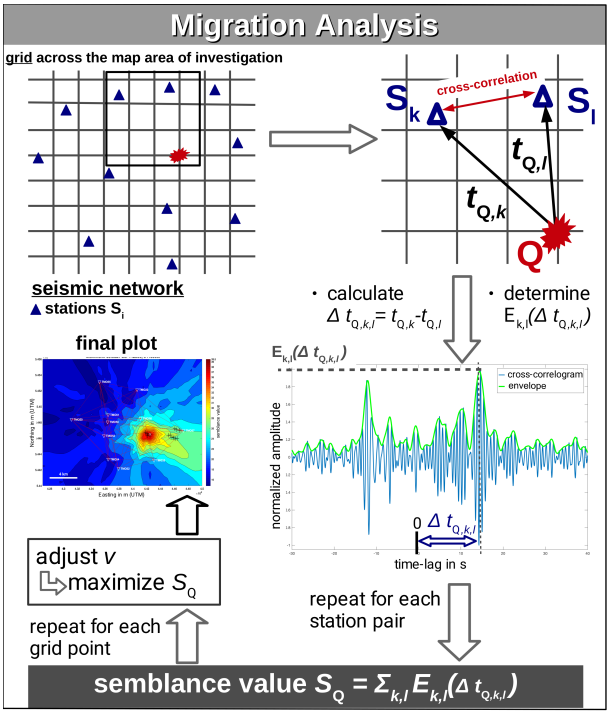

Figure 4.2: Workflow of the migration analysis.

The stacking procedure enhances signals which appear coherent at both stations for a long time and dilutes incoherent components. We expect that the coherency of signals is due to emission by a common source. To locate these sources, we apply a migration technique which was implemented by Horstmann and Forbriger (2010) to map sources of seismic energy in the urban area of Bucharest (Romania). We illustrate the workflow of this method in Fig. 4.2.

Signals, continuously generated by a localized source (Q in Fig. 4.2) and recorded by two stations (S_k, S_l), become apparent as a transient signal in the stacked cross-correlograms at a lag time equal to the difference

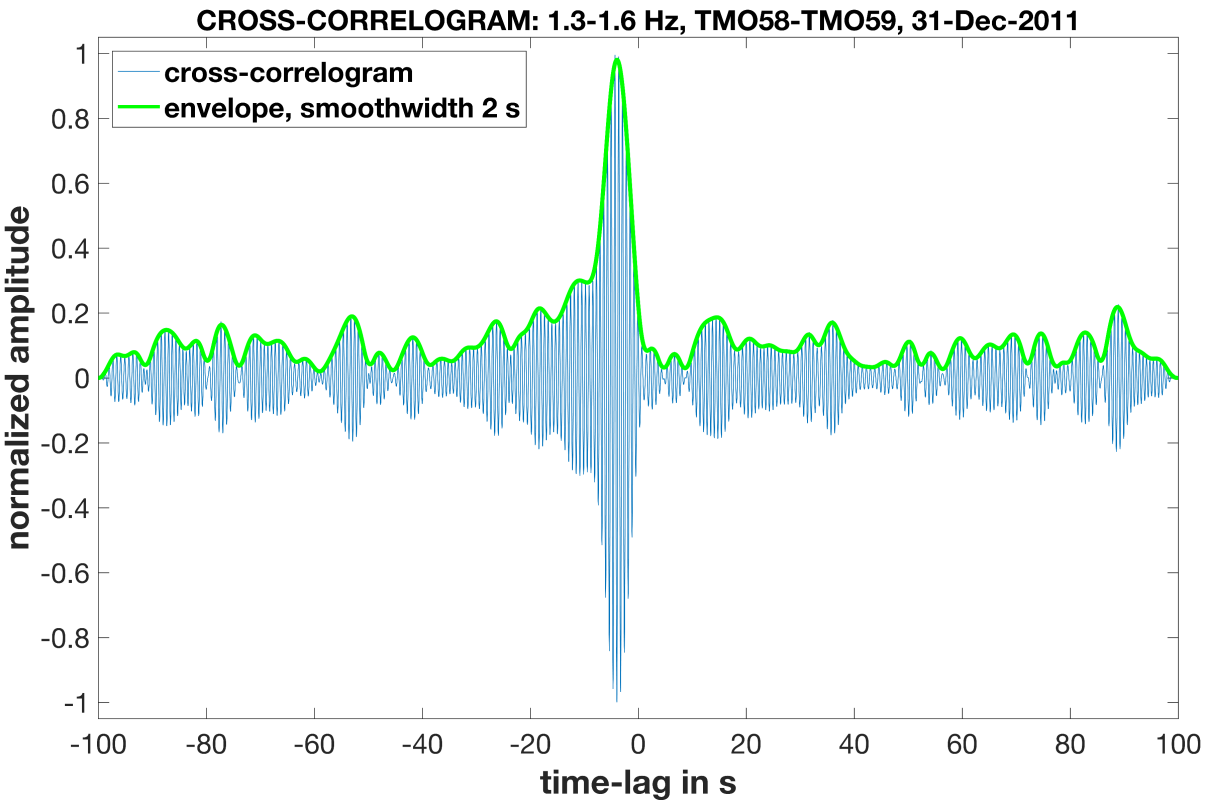

Figure 4.3: Example of a cross-correlogram (normalized to its maximum) and its smoothed envelope. The maximum is located at lag time -5 s.

$\Delta t_{Q,k,l} = t_{Q,k} - t_{Q,l}$ in travel time for the two sites. We analyse data in narrow frequency bands and therefore assume a uniform propagation velocity of the observed signals. Given a hypothetical propagation velocity v (the *migration velocity*), a hypothetical source location $\vec{x}_\mathrm{Q}$, and the locations $\vec{x}_{\mathrm{S}k}$ and $\vec{x}_{\mathrm{S}l}$ of stations S_k and S_l, respectively, the expected lag time is

$$\Delta t_{\mathrm{Q},k,l} = \frac{\left|\vec{x}_{\mathrm{S}k} - \vec{x}_\mathrm{Q}\right| - \left|\vec{x}_{\mathrm{S}l} - \vec{x}_\mathrm{Q}\right|}{v} \tag{4.1}$$

with

$$t_{\mathrm{Q},k} = \frac{\left|\vec{x}_{\mathrm{S}k} - \vec{x}_\mathrm{Q}\right|}{v} \tag{4.2}$$

as the expected travel time from the source Q to station S_k. We take the envelope $E_{k,l}(t)$ of the normalized cross-correlogram for stations S_k and S_l and smooth it by applying a moving average of 2 s length (see Fig. 4.3 as an example). We read the value $E_{k,l}(\Delta t_{\mathrm{Q},k,l})$ of the envelope at the expected lag time $\Delta t_{\mathrm{Q},k,l}$ for the source location under consideration. The sum

$$S_\mathrm{Q} = \sum_{k=1}^{N-1} \sum_{l=k+1}^{N} E_{k,l}(\Delta t_{\mathrm{Q},k,l}) \tag{4.3}$$

for all available pairs of the N stations is called the *semblance value*. It is a relative measure of how much signal energy a hypothetical source at location $\vec{x}_\mathrm{Q}$ might have contributed to the recordings. The maximum semblance value is $S_\mathrm{max} = N(N-1)/2$. If S_Q reaches this maximum value, the respective source location apparently contributes to the dominant signal in all cross-correlograms.

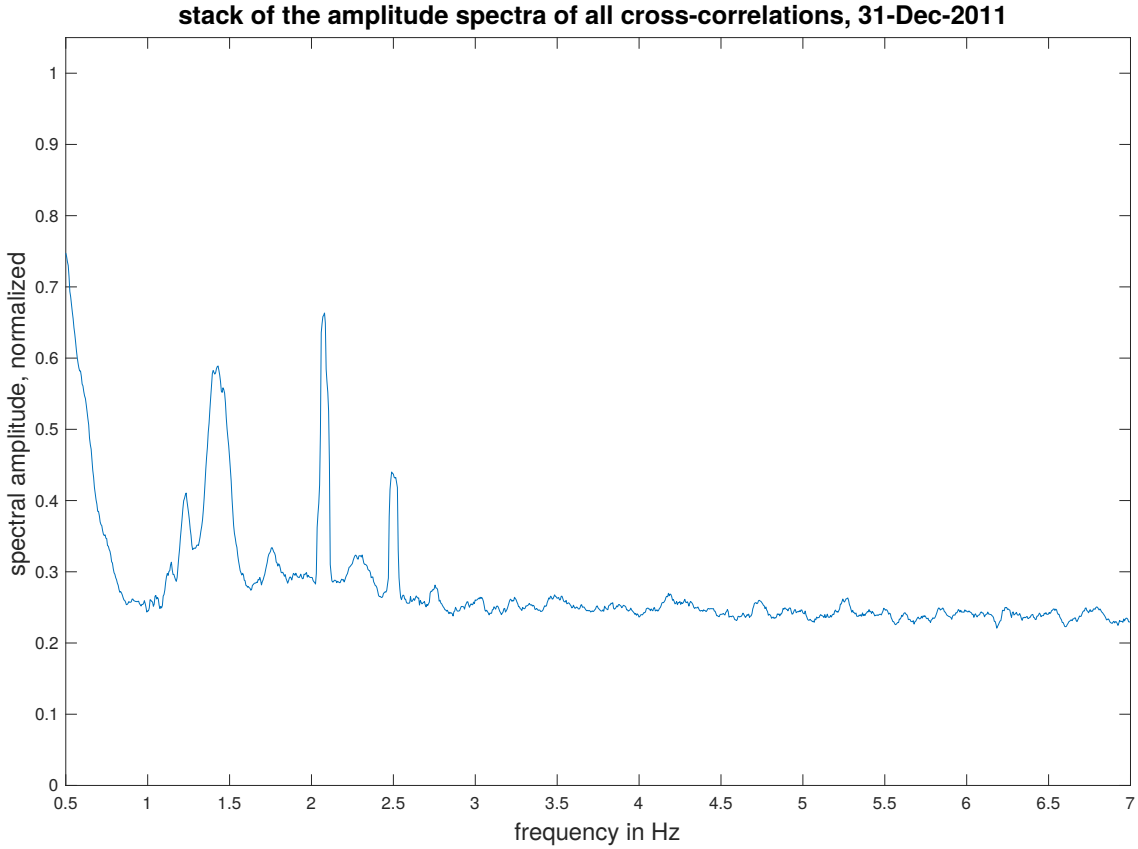

Figure 4.4: Stack of the amplitude spectra of all cross-correlations for the 31st December 2011. Each single spectrum is normalized to one in the analysed frequency range.

For the purpose of mapping we define a grid in UTM coordinates for the area of investigation (Fig. 4.2) with a grid interval of 500 m. The semblance value is then computed at each grid point and interpolated in between. Because the actual propagation velocity is unknown, we repeat the mapping for a range of values for the migration velocity v. We analyse the highest semblance value in the map as a function of v. We take the value of v for the highest value of semblance as an approximation of the actual propagation velocity of the coherent signal. Typically, the highest semblance values in our study appear in strongly localized spots in the area of wind farms or close to them.

4.5 Migration results for different frequency bands

Fig. 4.4 shows the normalized stack of the amplitude spectra of all cross-correlations (each normalized to its maximum in the displayed frequency range) for the 31st December 2011. Frequency bands with coherent signals are apparent through large amplitudes in Fig. 4.4. We focus on the bands 1.3 Hz – 1.6 Hz, 1.75 Hz – 1.95 Hz, and 2.0 Hz – 2.2 Hz. Signals at frequencies smaller than 0.8 Hz are not relevant for our investigation. Stein (2013) showed that seismic noise signals in the range of 0.5 Hz to 0.8 Hz are caused by a seismic source northwest of the area of investigation and that also ocean microseisms contribute to this.

We compute migration analyses with cross-correlation (CC) stacks of one day (*daily stack*), CC-stacks of the daily stacks of one week (*weekly stack*) or one month (*monthly stack*) in December 2011 and January 2012. These stacks are band-pass filtered for the frequency bands 1.3 Hz – 1.6 Hz, 1.75 Hz – 1.95 Hz, and 2.0 Hz – 2.2 Hz. We tested other frequency bands as well but they lack sufficiently coherent signals.

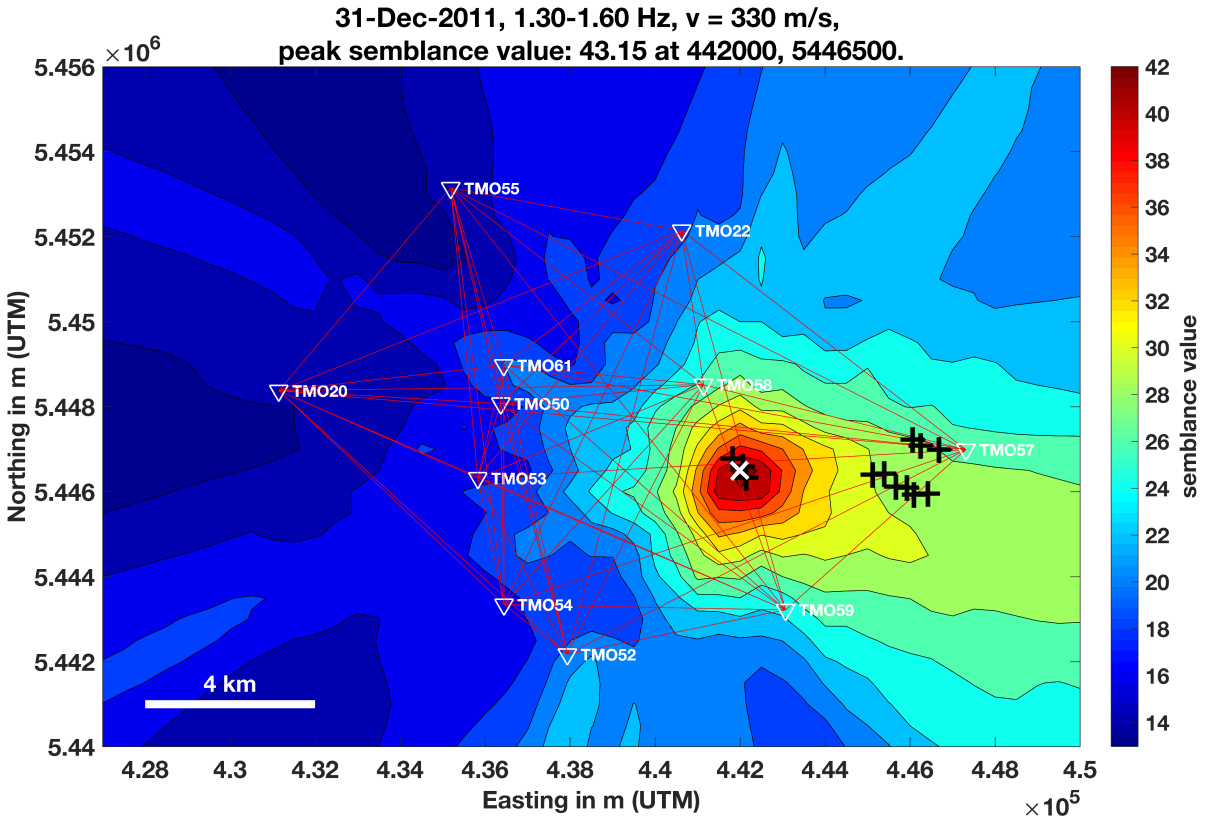

Figure 4.5: Result of the migration analysis for the daily stack of the 31st December 2011 in the frequency band 1.3 Hz–1.6 Hz. The stations are marked as white reversed triangles, the wind turbines with black plus icons and the location of the peak semblance value with a white cross.

4.5.1 Migration analysis for 1.3 Hz to 1.6 Hz

In this frequency band the semblance peaks at similar locations in each of the stacks (daily, weekly and monthly). The peak semblance value varies between 43.14 and 44.93 (= 78.4 and 81.7 % of the maximum semblance value of 55). We obtain these values for a migration velocity of about 330 m/s. Fig. 4.5 shows the result for the 31st December 2011. The mapped semblance value is specified by color. The peak semblance value (dark red) is situated in the middle of the wind farm *Offenbach*. The three eastern wind farms *Bellheim*, *Rülzheim* and *Herxheimweyher* (see Fig. 4.1) are clearly marked off and apparently do not contribute to the signal. The determined location is stable for all stacks (daily, weekly, monthly) and at least for migration velocities in the range from 300 m/s to 350 m/s.

4.5.2 Migration analysis for 1.75 Hz to 1.95 Hz

In contrast to the results in the frequency band 1.3 Hz – 1.6 Hz, the area of the peak semblance values varies stronger with the time period under investigation. Commonly, the peak location is north to northeast of the wind farm *Bellheim* and it is close to station TMO57 (about 600 m distance to wind farm *Bellheim*). For different days and migration velocities, the source location varies by about one (easting) to two (northing) grid intervals of 500 m. We suggest that the close proximity of station TMO57 might result in some bias, though data from this station is required to provide sufficient azimuthal coverage. All remaining stations are located west of the peak location.
Fig. 4.6 presents the results for the weekly stack from 31.12.2011 to 06.01.2012 as an example. The wind farms *Bellheim*, *Rülzheim* and *Herxheimweyher* are in the region of high semblance. They are composed of WTs with similar specifications (Table 4.1). Therefore, we expect them to generate similar seismic signals in the frequency band from 1.75 Hz to 1.95 Hz. In this frequency band, the wind farm *Offenbach* is located in a region of distinctly

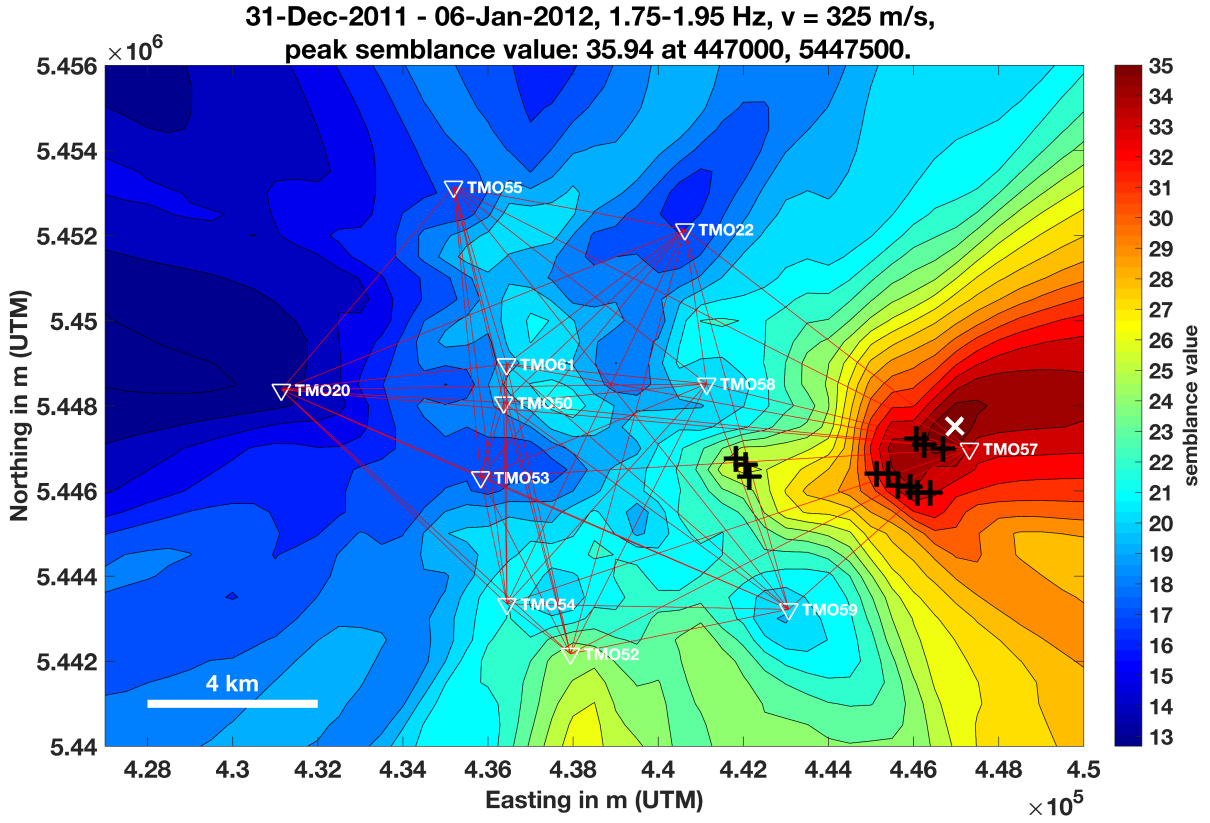

Figure 4.6: Results of the migration analysis in the frequency band 1.75 Hz to 1.95 Hz: weekly stack for 31st December 2011 to 6th January 2012.

lower semblance.

We obtain high peak values of semblance when using migration velocities in the range of 280 m/s to 340 m/s. The lowest peak semblance in this range is 30.66, the highest is 37.95 (55.7 % and 69.0 % of the maximum semblance value of 55, respectively). We assume that the variation in semblance value and location of the peak semblance with time and migration velocity reflects the varying contributions of the individual WTs within the three wind farms. With the available seismic data, however, we are not able to obtain the necessary spatial resolution to track this down to an individual WT. Wavelength of the analysed signals is about 150 m and hence too large to resolve individual WTs with a smaller distance within the wind farm.

4.5.3 Migration analysis for 2.0 Hz to 2.2 Hz

In this frequency band, semblance typically peaks northeast of the wind farm *Bellheim*, as is displayed for the 6th January 2012 in Fig. 4.7. For the other analyses (daily, weekly and monthly stacks), the location of peak semblance does not differ by more than one grid interval (easting and northing). The wind farms *Rülzheim* and *Herxheimweyher* are situated in or at the boundary of the regions with high semblance values. Similar to the frequency band 1.75 Hz to 1.95 Hz, it is likely that each WT of the three eastern wind farms emits signals in the frequency range of 2.0 Hz to 2.2 Hz. We obtain large peak values for the semblance when using values for the migration velocity in the range of 280 m/s to 330 m/s. Depending on the migration velocity, the location of peak semblance varies only by one grid interval in north and east direction as well. There is a large variation within the peak semblance values of about 32.77 to 41.51 (59.6 % to 75.5 % of the maximum semblance value of 55), comparable to the frequency band 1.75 Hz to 1.95 Hz.

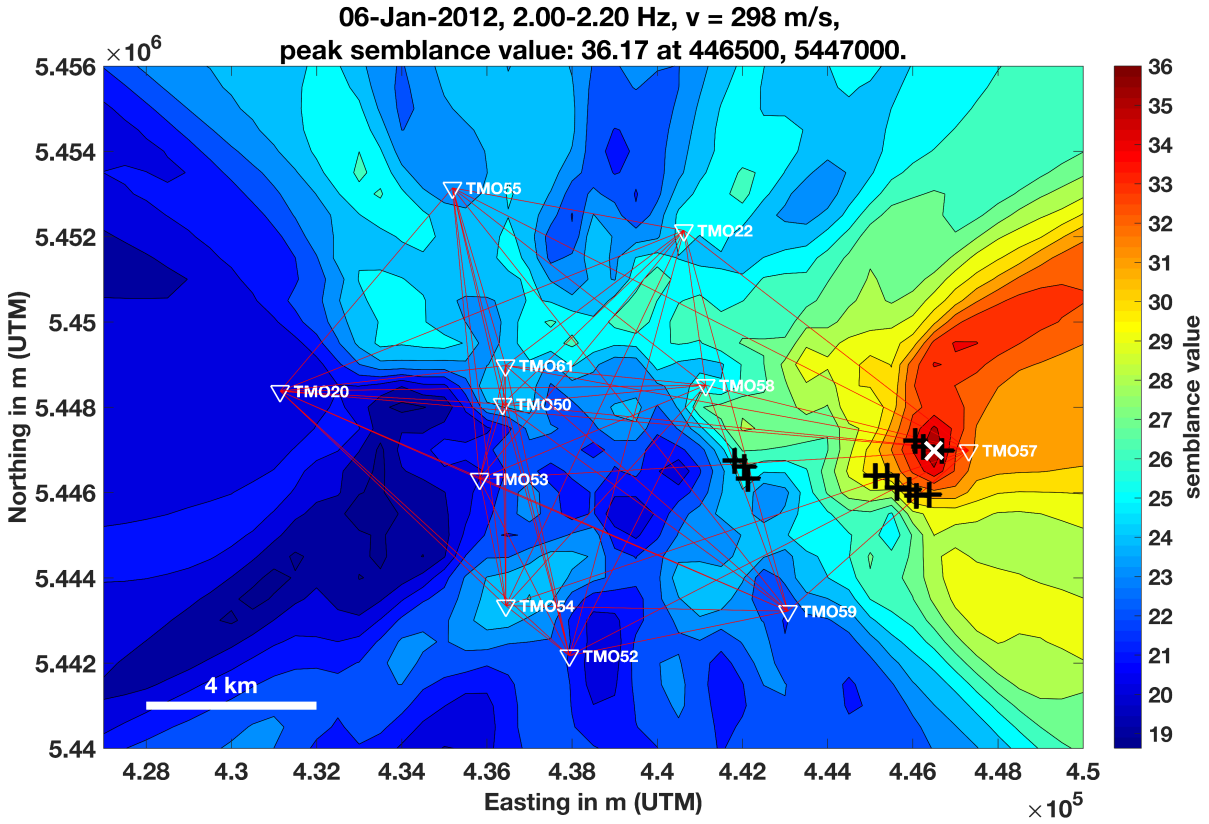

Figure 4.7: Result of the migration analysis in the frequency band 2.0 Hz to 2.2 Hz: daily stack for the 6th January 2012.

4.6 Dependence on wind speed

Semblance typically peaks in the vicinity of a wind farm. We take this as a confirmation that the WTs are the main source of the dominating seismic signals in the respective frequency band. A dependency on wind speed of the signal energy mapped to the peak semblance would make this statement even stronger.

The migration analysis looses this dependency when the envelope of the cross-correlogram is normalized to its maximum prior to migration. We discard this step by a modified version of the migration analysis to study the dependency of seismic energy emitted by the wind farms with data recorded in November and December 2011.

The *pfalzwind GmbH (Ludwigshafen, Germany)* provided turbine specific data such as wind speed and rotor speed of the easternmost turbine of the wind farm *Bellheim*. Available are average values for intervals of 10 minutes measured at the nacelle height of about 100 m. We assume a sufficiently coherent wind field such that these data are valid for the whole area of investigation. We then assign the cross-correlograms of seismic recordings for the 10 minutes long time windows to wind speed classes. Table 4.2 specifies the range of wind speed for each wind class. The cross-correlograms are then averaged to extract coherent signal energy for each wind class. Envelopes (non-normalized) of these averaged cross correlograms are migrated like in the previously described mapping procedure. We call the mapped value *cumulative energy* (in contrast to *semblance*), because it is proportional to the recorded wave energy due to the cross correlation processing. It peaks at locations of strongly contributing sources and can be understood as a measure of coherent signal energy in the network. We like to point out that cumulative energy (c. e.) must not be taken as an absolute measure of seismic energy generated by a WT and we do not attribute physical units to this quantity. The recorded signal energy decays with distance from the source and the processing does not compensate for that. Cumulative energy hence depends on the spatial configuration of the seismic network and the distance between signal source and seismic stations in particular.

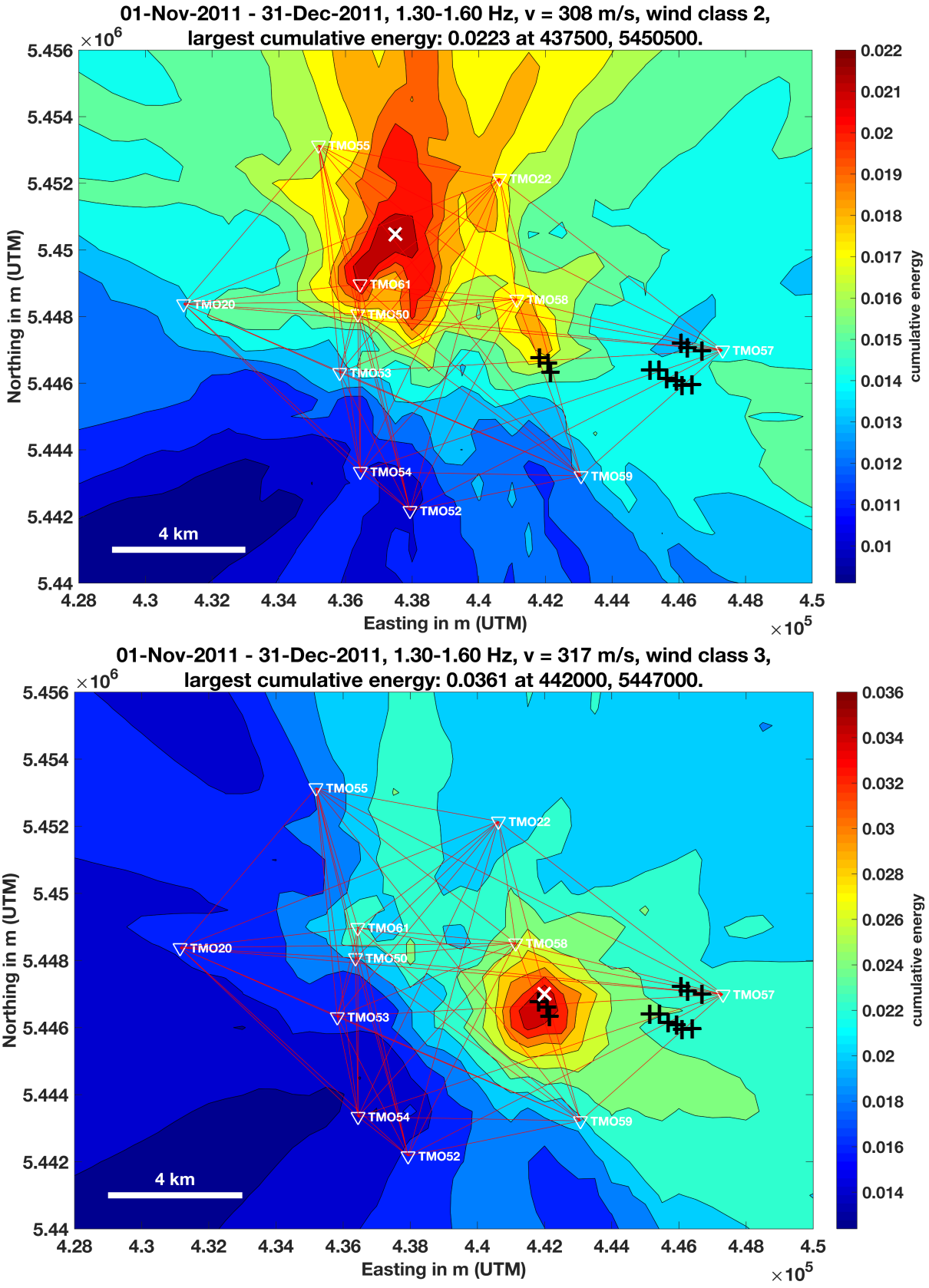

Figure 4.8: Results of the migration analysis for the frequency band 1.3 Hz to 1.6 Hz at wind class 2 (top) and wind class 3 (bottom).

Table 4.2: Definition of the wind speed classes depending on the wind speed v_{wind}. The number of cross-correlations (CCs) per station pair, which are averaged at the particular wind class, is also listed.

Wind class		1	2	3	4	5	6	7	8	9
v_{wind}	from	0	2	4	6	8	10	12	14	16
in m/s	to	2	4	6	8	10	12	14	16	18
Number of CCs		1731	1823	1527	1564	1048	643	270	76	19

Equally strong signal sources can result in different peak values of cumulative energy, depending on source location. Nevertheless, a temporal variation of the cumulative energy (c. e.) mapped to the same location with an unchanged configuration of the network is a valid measure of the variation of source strength at this location. We use this property, when attributing maps of c. e. to classes of wind speed or rotor speed.

For wind class 3 and larger in the frequency bands 1.3 Hz – 1.6 Hz and 1.75 Hz – 1.95 Hz and for wind class 4 and larger in frequency band 2.0 Hz – 2.2 Hz cumulative energy clearly peaks at the known wind farms. The locations of highest c. e. in the particular frequency bands correspond to the locations of peak semblance in section 4.5. For lower wind classes (1 and 2), the peak c. e. is situated in the area of the town of Landau for all three frequency bands. Spatially secondary maxima appear for wind class 2 in the frequency band 1.3 Hz – 1.6 Hz or for wind class 3 in the frequency band 2.0 Hz – 2.2 Hz. At lower wind classes the emitted signals were not dominant in the area of investigation, presumably because the WTs were not producing power.

Fig. 4.8 examplarily shows the results for the frequency range 1.3 Hz to 1.6 Hz for wind class 2 (top) and wind class 3 (bottom). A spatially secondary maximum near the wind farm *Offenbach* can be observed for wind class 2. For wind class 3 c. e. clearly peaks at this wind farm.

The evolution of the largest value of c. e. with increasing wind class is presented in Fig. 4.9 for all three considered frequency bands. In this figure the c. e. is normalized to the particular maximum. The c. e. for lower wind classes is not shown due to the absence of dominating WT-induced signals in the recordings. At 1.3 Hz to 1.6 Hz (blue line in Fig. 4.9) there is a distinct and nearly linearly increasing c. e. for wind classes 3 to 5. For wind classes 5 to 6, we observe a weaker increase until the value is relatively stable for wind classes 6 to 9. The reason for this behaviour presumably is a pitch of the rotor blades at a specific maximum rotor speed which is reached at wind class 6.

Signals from the wind farm *Bellheim* are dominating in the frequency band 1.75 Hz to 1.95 Hz. In that band (green line in Fig. 4.9), the c. e. increases also from wind classes 3 to 6 with different slopes. The value decreases slightly from wind classes 6 to 8 and increases again from wind classes 8 to 9. It has to be mentioned that the number of averaged cross-correlations is clearly smaller for wind classes exceeding 7 and thus a statistical uncertainty must be taken into account.

In the frequency band 2.0 Hz to 2.2 Hz (red line in Fig. 4.9) there is an approximately stable increase of c. e. from wind classes 4 to 7. The c. e. decreases from wind classes 7 to 8 and increases significantly from wind classes 8 to 9. Again, we like to point to the small number of cross-correlograms being available for the analysis of wind classes 7 and larger.

Fig. 4.10 displays the rotor speed as a function of the wind speed. The operating range of the WTs starts at about 11 rpm at wind class 3. Consequently, the seismic emissions of the WTs do not dominate at wind classes 1 or 2. From wind class 6 onwards, the rotor speed is constant because the maximum permitted rotor speed of the turbine is reached. The rotor blades are adjusted (depending on the wind speed) to maintain the maximum permitted rotor speed. Due to the constant rotor speed, we expect no further increase of c. e. at wind classes larger than 6.

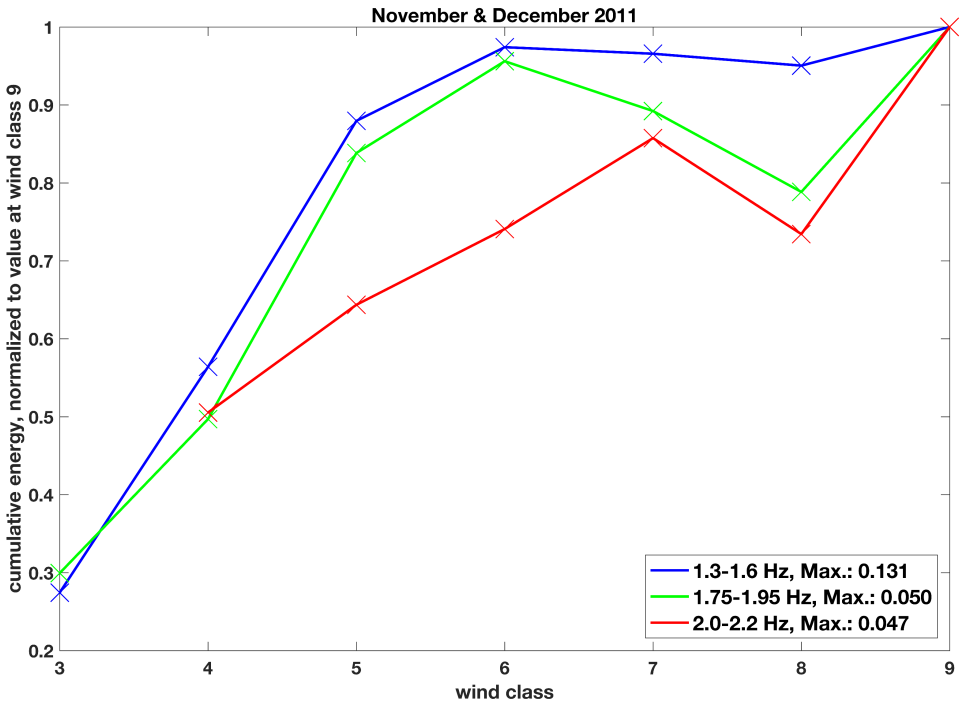

Figure 4.9: Evolution of the peak cumulative energy (c. e.), normalized to the particular maximum value, with increasing wind class for the frequency bands 1.3 Hz – 1.6 Hz (blue), 1.75 Hz – 1.95 Hz (green) and 2.0 Hz – 2.2 Hz (red). The particular maximum value of the c. e. is shown in the legend. Cumulative energy peaks at the location of wind farms when wind speed falls into wind class 3 or larger.

We summarize that WT-induced signals get dominant for wind classes larger than 3 (4 m/s to 6 m/s) or 4 (6 m/s to 8 m/s) and that the c. e. increases clearly with increasing wind class (up to 6) respectively wind speed.

4.7 Mechanism of propagation of energy

Previous studies consider seismic waves as well as infrasound as possible mechanisms of propagation of energy. A major cause for vibrations in WTs are the rotor blades passing at the tower. They excite vibrations in the structure of the WT as well as pulses of air-pressure. The vibrations of the structure couple into the ground and generate seismic waves (predominantly Rayleigh waves) which propagate to the receiver. The pulses of air-pressure, however, can propagate as infrasound and couple into the ground at a distance to the WT, such resulting in seismic ground motion too.

In the migration analysis of data recorded at Landau, semblance peaks in the vicinity of wind farms for values of migration velocity at about 320 m/s. This value is quite close to the speed of sound. Nevertheless, we believe that energy in the area of the current study predominantly propagates as seismic waves (probably Rayleigh waves).

First, a propagation velocity of 320 m/s not necessarily implies infrasound. The MAGS2 research project (Spies et al., 2017) reports values of phase velocity of 330 m/s with only weak dispersion for a frequency range of 1 Hz to 10 Hz for the fundamental mode Rayleigh wave at different array locations near Landau. Similarly low values of shear wave velocity are also consistent with the local geology. The uppermost layers consist of loose, unconsolidated sediments which are mostly water saturated. Hence, group velocity of Rayleigh waves in the whole area appears to be close to the speed of sound and close to the migration velocity used in the current study.

Second, infrasound typically peaks at integer multiples of the blade passing frequency. Pilger and Ceranna (2017, Fig. 4) resolve at least seven harmonics in a spectral analysis of infrasound pressure level, with the largest pressure signal being carried by the second harmonic.

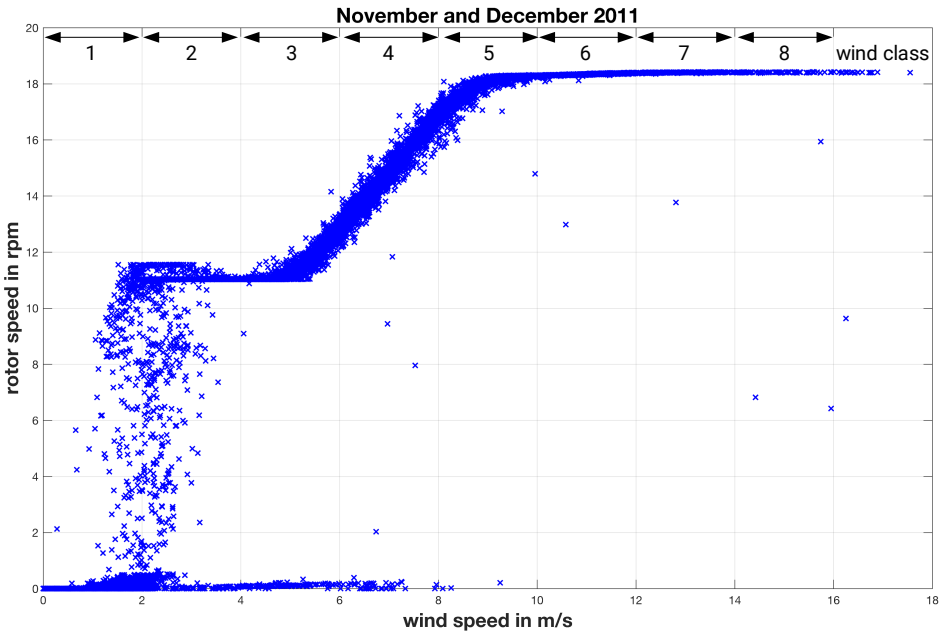

Figure 4.10: Rotor speed as a function of wind speed. Measured at the easternmost turbine of the wind farm Bellheim. The wind classes are also marked.

As a consequence the frequency of peaks in power spectral density depends on rotor speed and wind speed, respectively. Operational limits of rotor speed as displayed in Fig. 4.10 are 11 rpm at the onset of energy production at small values of wind speed and saturates at 18.5 rpm at high wind speed. The range of the first and second harmonic of the blade-passing frequency are 0.55 Hz to 0.93 Hz and 1.1 Hz to 1.85 Hz, respectively. We do not observe a dependency of peak-frequency in these bands on wind speed in data from Landau. In the current study and in the diagrams of power spectral density presented by Zieger and Ritter (2018, Figs. 3, 6, and 7, or rather Fig. 3.3, Fig. 3.6 and 3.7 in this thesis) for the same study area peak-frequency is stable, independent of wind speed. The frequency of peaks more likely is controlled by the elastic eigenfrequencies of the resonant structure of the towers of the WTs, which are practically constant within the resolution obtained in the analysis. This clearly indicates that vibrational energy propagates through the tower into the ground where Rayleigh waves are excited. Thus, we suppose that WT-induced signals in the area of Landau are coupled into the ground at the foundation of the WTs and propagate as Rayleigh waves with a group velocity of about 320 m/s.

4.8 Summary and Conclusion

By migrating the energy of cross-correlograms computed for continuous seismic signals, we locate individual wind farms as distinct sources of this energy. Wind farms (WFs) in the area under investigation are groups of three wind trubines (WTs) each. All WFs together are situated in an area extending 5 km in east-west direction and 2 km in north-south direction (Fig. 4.1). None of the seismic stations is positioned within this area. In a spectral analysis we observe three clear bands of spatially coherent energy at 1.3 Hz – 1.6 Hz, 1.75 Hz – 1.95 Hz, and 2.0 Hz – 2.2 Hz which are independent of wind speed. Seismic energy in the frequency band 1.3 Hz to 1.6 Hz clearly originates from the WF *Offenbach* (the westernmost) with no apparent contribution by the other WFs. Signals at 2.0 Hz to 2.2 Hz appear to be primarily generated by WF *Bellheim* (the easternmost), while WFs *Bellheim*, *Herxheimweyher*, and *Rülzheim* contribute to signals at 1.75 Hz to 1.95 Hz. The latter three WFs are composed of WTs with the same parameters of 1.5 kW nominal power production, 100 m hub height, and 77 m rotor diameter. As demonstrated we can clearly distingiush them (through frequency band and peak location) from WF *Offenbach* which is composed

of larger WTs (2.0 kW, 105 m, and 90 m).

Operating data for a WT in WF *Bellheim* is available in the current study. The range of the first and second harmonic of the blade-passing frequency in the operating range of the WT are 0.55 Hz to 0.93 Hz and 1.1 Hz to 1.85 Hz, respectively. The frequencies depend on rotor speed and wind speed, where both are highly correlated (Fig. 4.10). We do not observe this dependency of signal frequency on wind speed in seismic data. For this reason, we are convinced that the specific observed frequencies are controlled by the elastic resonance of the WTs structure. The vibrations are coupled into the ground at the foundation and probably propagate as Rayleigh waves with a group velocity of about 320 m/s.

Other than previous studies, the method proposed here enables us to study the characteristic relation between wind speed and generated seismic energy for a specific wind farm within a group of several wind farms. Migrating the observed seismic energy we are not limited to evaluate the integral seismic power of all sources. A wind farm, which presents a clear spatial peak of source energy in the migration result, can be studied independently of other WFs being present in the same study area at the same time. This way we demonstrate, that the seismic energy generated by the WTs drops to an insignificant level at values of wind speed smaller than 5 m/s. For smaller values of wind speed, source energy peaks at other locations than WFs, e.g. in an industrial area near the town of Landau. For values of wind speed higher than this threshold, continuous seismc energy in the analysed frequency bands predominantly is generated by WFs with energy level increasing with wind speed up to the upper saturation of rotor speed at about 10 m/s (Figs. 4.9 and 4.10).

Acknowledgements

Seismic data were provided by the “Erdbebendienst Südwest”, the “Federal Institute for Geosciences and Natural Resources (BGR)” and the “Karlsruher Broadband Array (KABBA)”. We thank “pfalzwind GmbH (Ludwigshafen/Germany)” for the provision of data and their support of this work. T.Z. was financed by the project “TremAc”, which is funded by the Federal Republic of Germany. Awarding authority: The Federal Ministry for Economic Affairs and Energy based on a resolution of the German Bundestag. We would also like to thank the two anonymous reviewers and the editor for their helpful and constructive suggestions and comments.

5 Pfinztal - Simultaneous identification of wind turbine vibrations by using seismic data, elastic modeling and laser Doppler vibrometry

This chapter compare seismic recordings of a single wind turbine with numerical simulations of the tower and optical measurements at the tower wall using a laser Doppler vibrometer. We identify the eigenfrequencies of the tower-nacelle-system and the influence of the rotational motion of the blades on seismic recordings. The laser Doppler vibrometry validates our results. This study uses an interdisciplinary approach to understand the WT as a seismic source.
This chapter has been submitted in :

Zieger, T., Nagel, S., Lutzmann, P., Kaufmann, I., Ritter, J., Ummenhofer, T., Knödel, P., Fischer, P.
Simultaneous identification of wind turbine vibrations by using seismic data, elastic modeling and laser Doppler vibrometry,
Wind Energy

5.1 Abstract

This work compares continuous seismic recordings over several months on top of the foundation of a common wind turbine at Pfinztal, Germany, with numerical tower vibration simulations and optical measurements. We are able to distinguish between the excitation of eigenfrequencies of the tower-nacelle-system and the influence of the blade rotation on seismic data by analyzing different wind and turbine conditions. We can allocate most of the major spectral peaks to either different bending modes of the tower, flapwise and edgewise bending modes of the blades or multiples of the blade-passing frequency after comparing seismic recordings with tower simulation models. These simulations of dynamic properties of the tower are based on linear modal analysis performed with finite beam elements. To validate our interpretations of the comparison of seismic recordings and simulations, we use optical measurements of a laser Doppler vibrometer at the tower of the turbine at a height of about 20 m. The calculated power spectrum of the tower vibrations confirms our interpretation of the seismic peaks regarding the tower bending modes. This work gives a new understanding of the source mechanisms of wind turbine-induced ground motions and their influence on seismic data by using an interdisciplinary approach. Furthermore, it demonstrates how numerical simulations of wind turbines can be validated by using seismic recordings and laser Doppler vibrometry.

5.2 Introduction

Due to eminent climate challenges, countries all over the world are trying to reduce their CO_2 emissions, especially in terms of electricity generation. To achieve globally negotiated climate objectives, a huge increase of new regenerative energy sources can be observed, including the installation of wind turbines (WTs). Therefore, the public acceptance of WTs is essential and can be enhanced by a better understanding of the emitted seismic wavefields of WTs and their interaction with the human health or highly sensitive instruments, like seismometers or laboratories for high-precision measurements.

WTs and their seismic emissions were the subject of many publications in the last few years (Styles et al., 2005; Saccorotti et al., 2011; Stammler and Ceranna, 2016; Flores Estrella et al., 2017; Neuffer and Kremers, 2018; Zieger and Ritter, 2018; Friedrich et al., 2018). Thereby the authors found significant indications for WTs as a seismic noise source, regarding their interaction with the subsurface and the propagation behavior of emitted seismic wavefields. Several discrete frequency peaks up to 20 Hz could be observed at seismic stations in short distances (up to several kilometers) to WTs by using spectral analyzing techniques, like PSD spectra (power spectral density) at different wind conditions. The origin of these spectral peaks were assumed to be due to an interaction of vibrations with eigenfrequencies of the tower-nacelle-system and the blade-passing frequency (BPF, defined as the number of blades times the WT-specific rotation frequency).
Styles et al. (2005) show in their comprehensive study the occurrence of characteristic frequencies of wind farms near the Eskdalemuir Array in Scotland, Great Britain. They interpret the mechanism of these frequencies as the BPF and its multiples. Thereby they show a correlation of the seismic amplitude with the wind speed. Furthermore, they assume the propagation of WT-induced seismic waves as vertically polarised P-SV (Rayleigh) waves (P: P-wave or compressional elastic wave, SV: vertically polarized elastic shear wave). A recent study of Stammler and Ceranna (2016) observe an increase of the overall seismic noise level in the range of 1 Hz to 7 Hz at the Gräfenberg-Array in Germany after the installation of several new WTs in the vicinity of seismic recording stations and with that a decrease of the detection capability of the array. They detect the WT-induced signals up to several kilometers and show a clear dependence of the increase of the seismic noise level with increasing wind speed. The main frequency peak is observed close to 1.15 Hz and is detectable at seismic stations with distances of more than 15 kilometers to the next WT. These results are confirmed by a study of Zieger and Ritter (2018) at wind farms around the town of Landau, Germany. They correlate the seismic signals with the rotation rate of a WT nearby a seismic station and observe discrete frequency peaks during time windows with high rotation speeds. These WT-induced frequency peaks could even be identified up to depths of 300 m below surface in seismic borehole data (Zieger and Ritter, 2018). Thereby they observe a higher attenuation of WT-induced signals with depth than an attenuation with distance, which again indicates an emission of seismic surface waves. This study found also frequency dependent attenuation factors of $b = 0.77 - 1.59$ for unconsolidated Cenozoic sediments.
Despite these mentioned studies, a clear comparison of seismic recordings with simulations of dynamic properties of the WT and laser Doppler vibrometry has not yet been shown, especially regarding the identification of eigenfrequencies of the tower-nacelle-system. In section 5.3, we identify the main spectral peaks in the seismic recordings by comparing time windows during a regular operation of the WT with windows in which no rotation occurred. In section 5.4, we interpret the identified spectral peaks by performing numerical tower simulations considering two different local soil conditions. Thereby we can allocate most of the frequency peaks to different tower bending modes or to the BPF and its multiples. These results will be validated by section 5.5, where we use laser Doppler vibrometry to measure the vibrations of the tower shell at a height of 20 m. Other frequency peaks could be allocated to flapwise and edgewise bending modes of the blades. However, a clear validation of this contention by using seismic recordings or laser Doppler vibrometry is beyond the scope of this study. This work is especially important for possible optimization methods regarding the reduction of seismic emissions of WTs, which may also help to increase the public acceptance of wind energy. The identification of the impact of these emissions on seismic recordings is therefore a crucial requirement.

5.3 Seismic signals on top of the WT foundation

Broadband seismometers are highly sensitive instruments for continuously measuring very weak ground vibrations across a broad frequency range, including earthquakes or explosions over large distances around the globe. These measurements are necessary for detecting the precise location of the seismic source and to locate areas in terms of seismic hazards as well as to control nuclear test bans. Another information provided by such highly sensitive

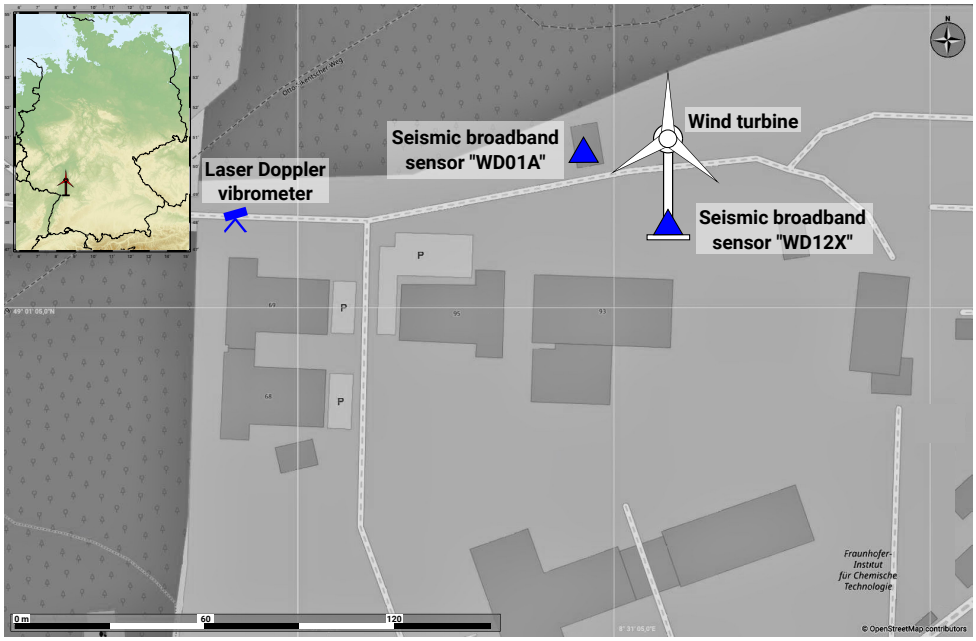

Figure 5.1: Map of the study area. Seismic stations are indicated as blue triangles, the location of the LDV measurement is also marked with the blue vibrometry symbol. The small map show the Pfinztal site within Germany.

Table 5.1: Measured frequency values of power spectral density peaks (A) during high wind speeds and a stable rotation rate of about 14 rpm (Fig. 5.3, red line), which corresponds to a BPF of about 0.7 Hz, and frequency peaks (B) during high wind speeds without blade rotation (Fig. 5.3, blue line).

Peaks:	A1		A2		A3		A4		A5		A6
f in Hz:	0.7		1.4		1.97		2.8		3.5		4.2
Peaks:	B1	B2	B3	B4	B5	B6	B7	B8	B9	B10	B11
f in Hz:	0.34	1.21	1.59	2	2.27	3.97	4.79	5.28	6.56	7.76	8.39

measurements is the inner structure of the Earth, using observations of seismic phases travelling through the Earth's core or along the surface of the Earth. However, there are still several questions that needs to be answered and therefore locations with quiet local site conditions are required, especially regarding anthropogenic noise which includes seismic emissions of WTs. We use seismic broadband sensors to investigate the motion of a single WT and to differentiate between the eigenfrequencies of the tower-nacelle-system and the BPF.

Two Streckeisen STS-2 broadband sensors (0.008 Hz - 50 Hz) with an eigenperiod of 120 s were installed on the foundation (WD12X) inside of a WT and in 40 m distance (WD01A) at the Fraunhofer Institute for Chemical Technology (FHG-ICT) in Pfinztal, Southwest Germany, which is located about 8 km northeast of the city of Karlsruhe (see Fig. 5.1). The WT of the type Qreon Q82 has a hub height of 101 m and a maximum power output of 2 MW. Both sensors were connected to an Earth Data Portable Field Recorder (EDL) with a sampling rate of 200 Hz to record the seismic signals. In order to achieve the true ground motion velocity of the seismic signal, the continuous vertical-component recordings were preprocessed by a deconvolution of the instrument response. After this step, the power spectral density (PSD) of the true ground motion velocity was calculated.

Figure 5.2 (top) shows the spectrogram of the vertical seismic signal in a frequency range of 0.05 Hz to 10 Hz during three days in March 2018 for the seismic station WD12X on top of the foundation inside the WT. The color symbolizes the intensity of the normalized PSD in dB. Figure 5.2 (middle) shows a spectrogram of the same time window for the seismic station WD01A, which is located in a distance of 40 m to the WT. The intensity of the PSD is again normalized to its specific maximum. The seismic data is then correlated with 1-minute Supervisory

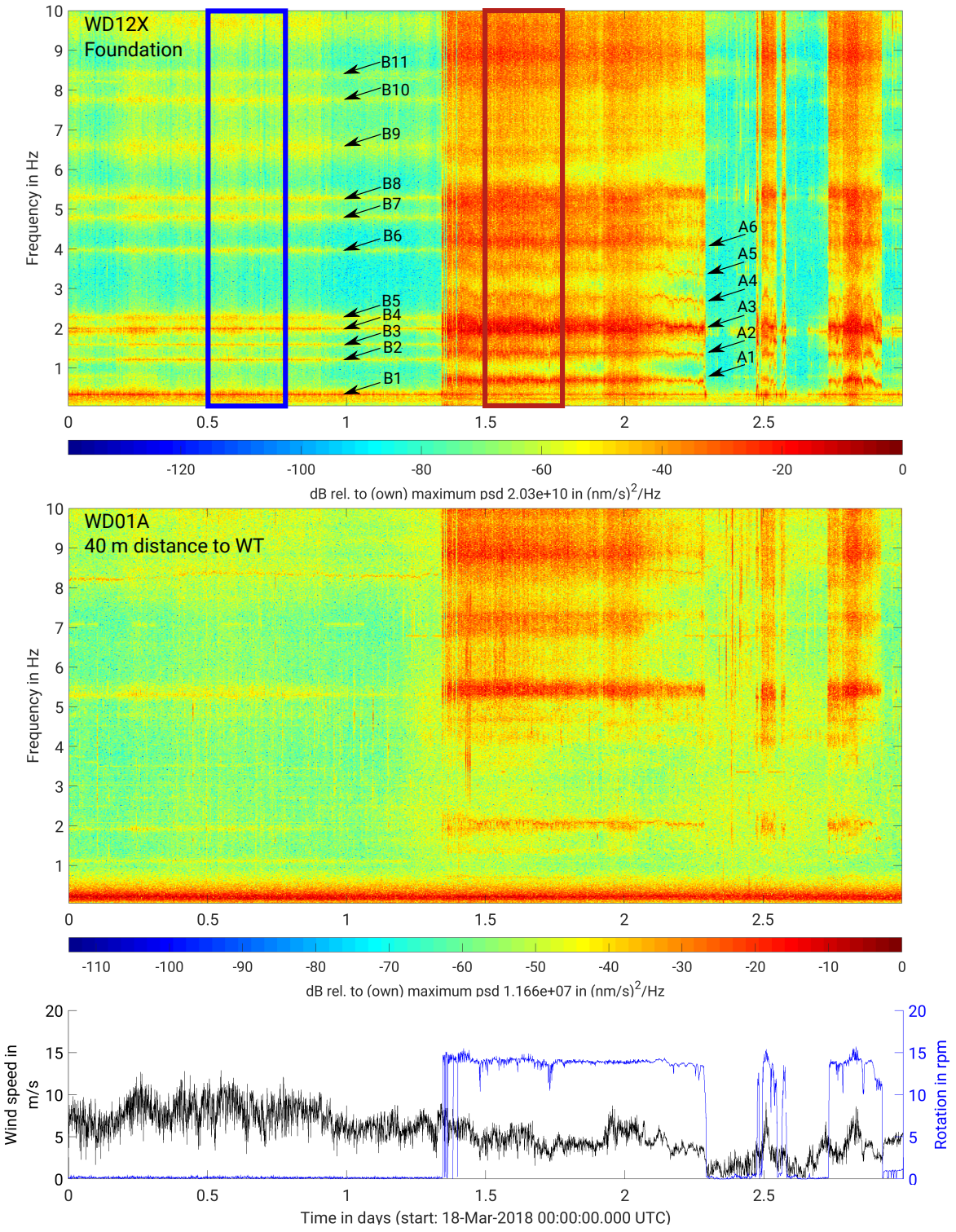

Figure 5.2: Top: Frequency spectrum of the vertical component recordings over three days in March 2018 in the frequency range of 0.05 Hz to 10 Hz on the WT foundation (WD12X). The color corresponds in each case to the normalized PSD value. Two time windows are marked for station WD12X with (red curve) and without (blue curve) WT rotation. The clear frequency peaks related to the BPF (A1 - A6) are annotated for a clearer illustration. Also the peaks corresponding to eigenfrequencies of the tower-nacelle-system (B1 - B11) are marked. Middle: The same spectrum for the seismic station WD01A, located in 40 m distance to the WT. Bottom: The wind speed (black) and the rotation rate of the WT (blue).

Control and Data Acquisition (SCADA) data of the WT, in particular the wind speed and rotation rate. Figure 5.2 (bottom) shows the wind speed (left axis, black), measured at the nacelle in 101 m height, and the rotation rate (right axis, blue).
Two different operating conditions of the WT can be identified during this time window of three days (Fig. 5.2, blue resp. red box):

1. The first time window shows the frequency spectrum during high wind speeds of about 5-10 m/s. Due to technical problems, the WT was out of service according to the zero rotation motion. However, clearly excited vibrations can be observed in the frequency spectrum, represented as discrete lines with high PSD values (B1 - B11, Fig. 5.2). The vibrations are most probably triggered by the wind load on the tower and the standing blades and can be observed at recording station WD12X in particular, while at station WD01A we find just a minor impact of these vibrations compared to the background noise due to attenuation effects during the propagation of the induced signals through the subsurface.

2. The second time window shows the spectrum during high wind speeds with a relatively stable rotation rate of around 14 rpm, which corresponds to a BPF of around 0.7 Hz (three times the rotation rate divided by 60 s). We observe a higher overall level of the PSD in the displayed frequency range and an excitation of various discrete frequencies (A1 - A6), which mostly differ from the spectral peaks according to the first time window. Some of these frequencies follow the variations of the rotation rate (symbolized with arrows in Fig. 5.2, top) and can therefore be associated with the BPF and its multiples. For a clearer separation we enumerate the different multiples from A1 to A6 for station WD12X. Remarkable is the fact that the second harmonic of the BPF, A3, is located around 2 Hz and clearly visible on both sensors. However, also an eigenfrequency of the tower-nacelle-system is located in this frequency range (B4, see Tab. 5.1), which can be clearly observed in the time window before the start-up of the WT. We will discuss a possible interaction between those excitations in section 5.4.

Figure 5.3 shows the calculated PSD spectra of vertical component recordings, measured at WD12X, for the two specific time windows defined in Fig 5.2 (top) by using the arithmetic mean of the squared Fourier transform of several overlapped time segments during an overall time window of six hours containing stable operating conditions of the WT. This method was introduced by Welch (Welch, 1967). Furthermore we are using a multi taper method (Thomson, 1982; Percival and Walden, 1998). As the name of the method already implies, a variable number of multiple orthogonal tapers (Slepian sequences: Slepian, 1978) are multiplied to the seismic data and the corresponding eigenspectrum will be computed. By averaging over all eigenspectra, we obtain the final spectrum of each time segment. Here we use an adaptive approach with a frequency-dependent weighting factor for a weighted average of the different tapered PSD estimates to compensate the variable energy content of the Slepian sequences. This method provides a good protection against spectral leakage for a spectrum with very high dynamic ranges. For a detailed description of the adaptive approach we refer to the book of Percival and Walden (1998).
Due to the absence of a rotational motion of the WT blades during the first time window, the resulted spectrum shows WT-induced seismic signals at high wind speeds without any influence of the BPF (Fig. 5.3, blue line). These conditions are equal to shutdown experiments at WTs at high wind speeds, which are in general very expensive and difficult to implement. For a clearer illustration we enumerate the main peaks in Figure 5.3, which also corresponds to the numbering in Fig. 5.2 (top) for the BPF and its multiples.
The first peak appears at around 0.34 Hz (B1 in Fig. 5.3). This frequency peak can now be identified as the first bending mode of the tower (see section 5.4). Furthermore, several other major frequency peaks (B2 - B11) can be observed in the PSD spectrum, corresponding to the discrete lines in the spectrogram shown in Figure 5.2 (top). The specific peak values are given in Table 5.1, second row.

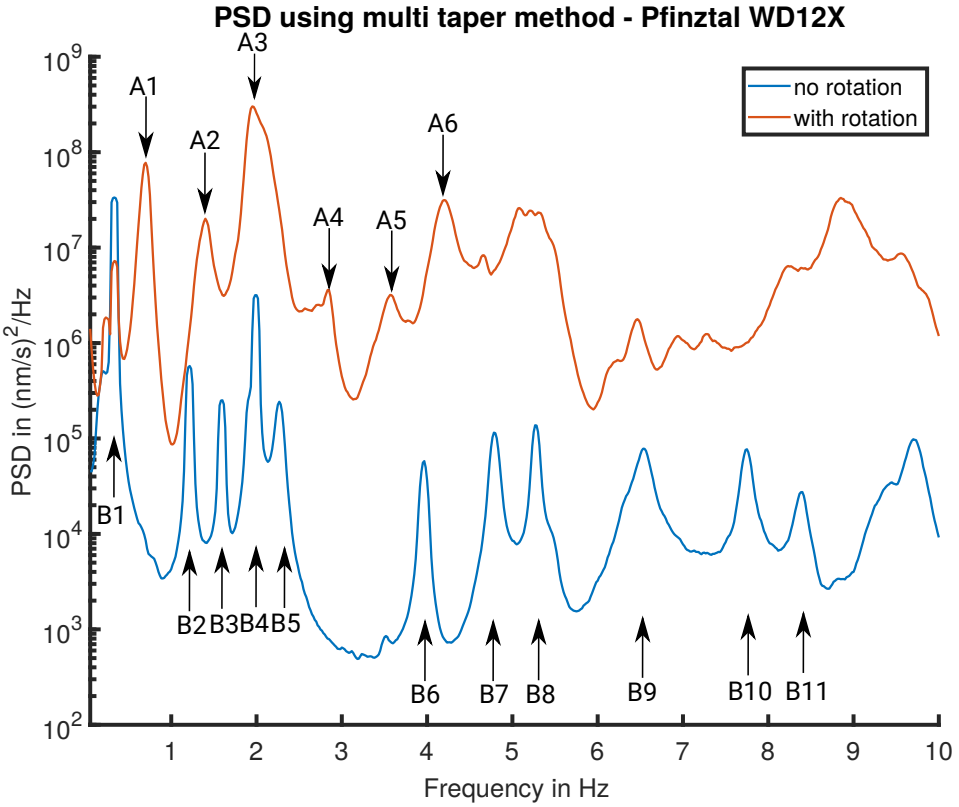

Figure 5.3: PSD spectrum of the station WD12X at the foundation of the WT for two different operating conditions: with (red) and without (blue) a rotational motion of the WT. The colors correspond to the defined time windows for the PSD calculation in Fig. 5.2. Major frequency peaks are annotated.

Contrary to the blue line in Figure 5.3, representing the WT without rotation, the red line shows the PSD spectrum with a rotational motion of the WT blades at high wind speeds. In this operating mode, additional frequency peaks arise which fit very well with the BPF of 0.7 Hz and its multiples (see Tab. 5.1, first row). Obviously, the frequency peaks of the first time window (without rotation) are also present in the second time window, but widely overlain by the influence of rotational vibration. The PSD spectrum of the second time window (Fig. 5.3, red line) is characterized by a much higher overall PSD level and an appearance of additional discrete frequency peaks, compared with the time window described before. The difference between both lines can be explained by the influence of the blade rotation (the wind speed remains more or less stable in both time windows).
Using the spectrogram (Fig. 5.2) we are now able to distinguish between the influence of the blade-passing frequency (A-symbols) and the eigenmodes of the tower-nacelle-system without rotation (B-symbols). To identify the specific eigenmodes of the system, the eigenvalue problem considering mass and stiffness distributions of the tower as well as the top mass was done as described in the following section by finite beam elements.

5.4 Simulation of tower bending modes

The interaction of the top mass (approx. 90 t) consisting of the blades (approx. 20 t), the generator, the hub, the gear, and the nacelle on top of a 101 meter high flexible tower (320 t) dominates the overall dynamic behavior of a WT. To describe the behavior sufficiently, the simple approach of a single degree of freedom system (SDOF) (top mass and tower stiffness) has to be expanded by a distributed tower mass, a height-dependent tower stiffness and, for further calculations, by a flexible foundation. Detailed blade or generator properties as well as information on the control system are not necessary with respect to the lowest natural frequencies. The tower of the analyzed

WT in Pfinztal follows the concept of a steel-shell-tower and consists of six circular segments connected by bolted flanges. To depict the local situation precisely, certain tower diameters d have been measured on site and extended to the full tower height by graphical evaluations (d = 2.5 - 4.3 m). The distribution of the wall thickness t_{wall} is the second dominating parameter to describe the stiffness and mass properties of a circular section and has been detected by ultrasonic testing (t_{wall} = 25 - 40 mm). Based on this information, a beam-element based finite element model was built up and validated by ultimate limit state calculation, which considers the failure of the tower. More decisive for the validation is the accordance with the design goal of a soft-stiff-tower concept. Meaning that the first natural frequency of the WT occurs between the 1P (excitation of one blade) and 3P (excitation of three blades, corresponds to the BPF) for all operating conditions. All remaining higher eigenvalues have to be above the 3P excitations. Campbell diagrams (Campbell, 1924) are commonly used to describe and evaluate this state. Herein 1P represents the rotation speed of the WT and 3P is the BPF. Considering the operating speed range of the analyzed WT (7 to 17.9 rpm, Qreon Technical Data: Downloaded 14.09.2018) this leads to a sharp design goal for the lowest natural frequency of 0.34 Hz.

All calculations of the dynamic properties discussed in this article are based on linear modal analysis performed with finite beam elements in Ansys v.19.1 (ANSYS, 2018). This simplification joins in the scope of this paper: the identification of the measured seismic wave excitation. Therefore, the focus in the modeling process was solely on parameters that effect the motion of the foundation significantly.

More detailed shell-element based models considering the potential of noise emission due to surface vibrations are going to be published soon. Comprehensive studies on the actual vibrations of the foundation under specific operating conditions, based on harmonic (frequency domain) and transient (time domain) simulations, will be presented in this context as well. Anticipating the results, a similar behavior, independently of the tower concept (Steel-Shell-, Hybrid- or Bolted-Steel-Shell-Towers) is identified and the findings of this present paper are going to be underlined. For rotationally symmetrical structures, such as towers, natural frequencies pop up in clusters due to two numerically identical directions. Special attention was paid to an effect caused by the eccentricity of the top mass. The common center of gravity of blades and all parts built-in the nacelle lies about 700 mm outside the centerline of the tower. In structural considerations, this leads to additional actions on the tower structure and in the dynamic behavior to a preferred direction in the tower motions. The calculations show that these only prevail for higher modes significantly and their influence can by neglected in the investigated frequency range for this specific WT. Apart from the tower structure and the top mass, the foundation stiffness, including the local soil conditions, are influencing the dynamic behavior. In these considerations, two limiting states have been investigated:

1. infinite soil stiffness (upper boundary for natural frequencies).

2. softest possible design values for the expected local soil conditions around the foundation (gravel). The foundation is represented by beam elements with a circular cross section.

In case 2 the diameter of the circular flat foundation was set to 15 m and the dynamic soil stiffness to G_{dyn} = 70 MN/m^2 and ν = 0.25. The resulting natural frequencies along with the characteristic mode shapes are presented in Fig. 5.4 for both cases. A summary is given in Table 5.2.

With the results of the simulations of the tower vibrations, we are now able to interpret most of the spectral peaks that can be observed in the seismic PSD spectrum during different operating conditions (Fig. 5.3). The interpretation is shown in Table 5.3. Whereas the assignment of the A-peaks as harmonics of the BPF is trivial, the identification of the different bending modes (B-peaks) requires the additional use of other techniques like finite element models or LDV-measurements (section 5.5).

As can be seen in Tab. 5.2, the simulated value of the second tower bending mode (1.81 Hz) is located between the peaks B3 and B4. A clear allocation to the observed peak is not possible for this specific time window. However,

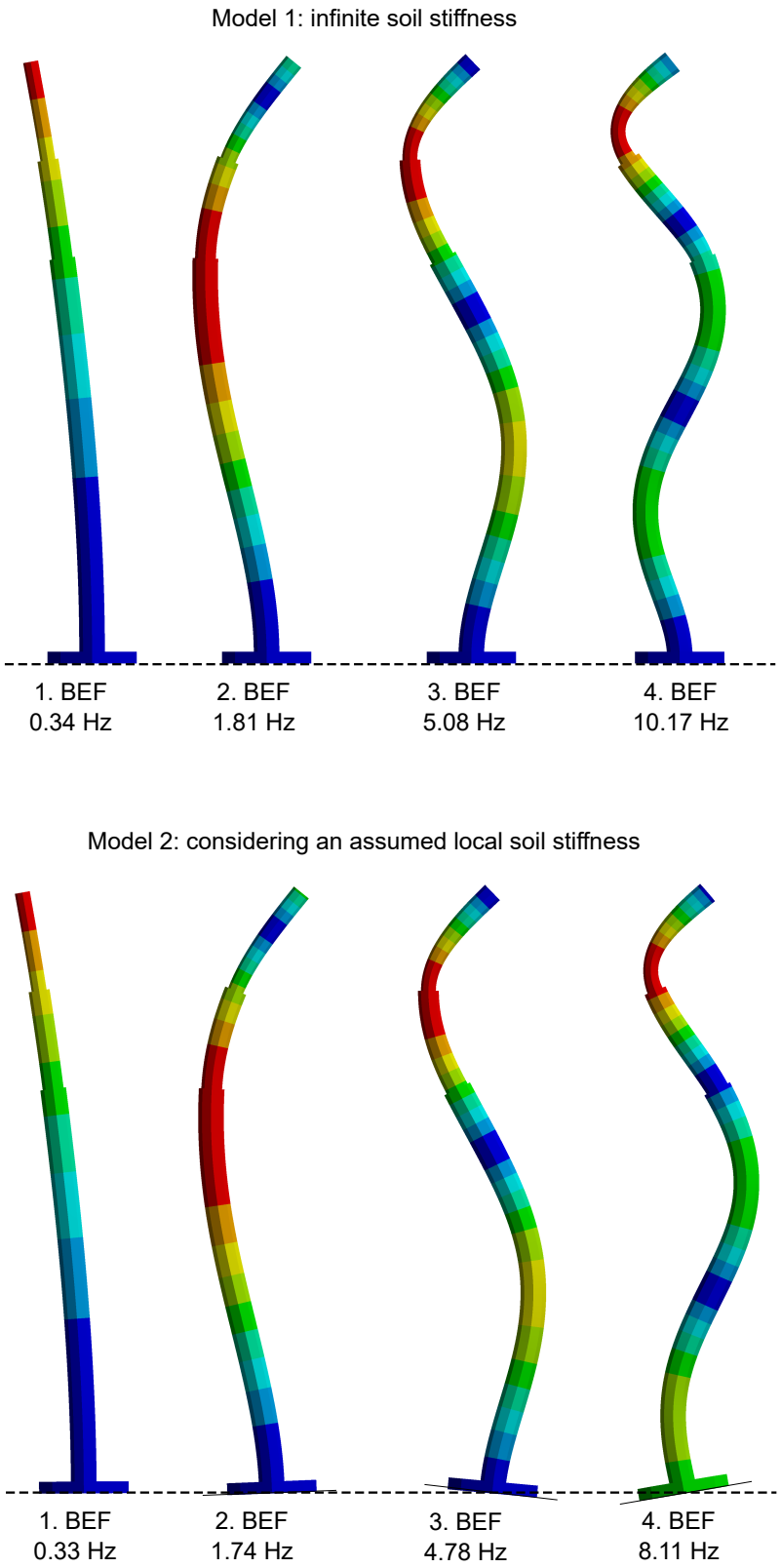

Figure 5.4: Characteristic mode shapes of the tower-nacelle-system, from finite beam element modeling. Top: stiff model 1. Bottom: soft model 2.

Table 5.2: Natural frequencies in Hz of the tower-nacelle-system for model 1 (stiff soil) and model 2 (soft soil).

Model 1	0.34	1.81	5.08	10.17
	1st bending	2nd bending	3rd bending	4th bending
Model 2	0.33	1.74	4.78	8.11
	1st bending	2nd bending	3rd bending	4th bending

Table 5.3: Interpretation of the peaks symbolizes in the PSD spectrum (Fig. 5.3 and Fig. 5.5). The interpretation is based on the tower simulations (Section 5.4) and the results of the LDV measurement (Section 5.5).

Peaks:	A1	A2	A3	A4	A5	A6
Mode:	BPF	1st harm. BPF	2nd harm. BPF	3rd harm. BPF	4th harm. BPF	5th harm. BPF
Peaks:	B1	B3	B4	B5	B7	B8
Mode:	1st tower bending	1st edge-wise bending	2nd tower bending	2nd edge-wise bending	3rd flapwise bending	3rd tower bending

nonstructural components such as ladders cables or an elevator are not considered within the simple beam element based models and could affect the dynamic properties leading to slightly higher eigenfrequencies. Under this assumption, the second bending mode can be likely allocate to B4.

Not all visible peaks can be allocated to different eigenmodes of the tower as demonstrated by the comparison of Tab. 5.2 with the seismic recordings. Needless to say there are several other parts at a WT with a potential excitation of vibrations, such as the blades. Based on a generic WT model of identic rotor diameter and similar characteristic performance values designed at the Wind Energy Institute (WEI) of the Technical University of Munich and Stuttgart Wind Energy (SWE) of the University of Stuttgart (Nagel et al., 2019), we can speculatively allocate some other visible frequency peaks to flapwise or edgewise bending modes of the blades. These eigenfrequencies were excited by a stochastic wind field including turbulences. The results are also shown in Tab. 5.3. A simulation of the bending modes of the blades for this specific WT to proof this assumption is beyond the scope of this study.

The peak A3 (1.97 Hz) does not fit very well with the theoretical second harmonic of the BPF (2.1 Hz). As mentioned before, A3 is located close to an eigenfrequency of the tower-nacelle-system at 2 Hz (B4). Therefore we assume a likely interaction of both mechanisms and with that an increase of the WT-induced signals around 2 Hz. Also several other discrete frequency peaks, like eigenfrequencies of the blades (B3 and B5, Fig. 5.3), are located close to 2 Hz. This dense accumulation of eigenfrequencies could lead to a superposition during time windows with blade rotations as an interaction of the second BPF, which is probably also the explanation for the relatively high PSD value of A3 in comparison with other multiples of the BPF.

5.5 Laser Doppler vibrometry at the tower of the WT

Laser Doppler vibrometry (LDV) allows non-contact measurement of vibrations of a WT from a distant sensor on the ground. The Doppler effect shifts the light frequency of a laser beam that is scattered at a moving surface. Thus, a vibrating surface results in a frequency modulation of the backscattered laser light, carrying the informa-

tion of the movement. Using an interferometric technique, the receiver of the LDV can measure the frequency shift and calculate the movement of the underlying vibration by demodulating the signal. This technique enables vibration measurements from a distance, completely independently of the object itself (for more information see: www.polytec.com/uk/vibrometry/technology). Commercial LDVs are available for various applications, but generally only for small ranges and stationary targets or for spinning objects viewed from a point on their spinning axis. The Fraunhofer Institute IOSB therefore developed its own LDV, with a short-wavelength infrared (SWIR) laser (λ = 1.5 μm), which meets laser safety requirements and being not visible for human eyes. It is appropriate for measurement distances of up to 250 m and more (Lutzmann et al., 2016). To measure the vibrations at a certain surface point of an object, laser beam and receiver field of view have to be directed and adjusted to this point. For this purpose, the optics of the LDV were mounted on a pan-tilt unit (PTU). This also enables a sequential recognition of an array of measurement points resulting in spatially resolved patterns of the vibration modes of an object. Furthermore, the laser spot is able to follow a desired moving measurement point. The LDV and PTU were combined with a tracking system based on a SWIR sensitive camera and a specially developed image recognition software. It enables us to examine vibrations of the rotating rotor blades while the WT is under operation.
For the purpose of this study we performed LDV measurements at the tower of the same WT at the Fraunhofer Institute ICT in Pfinztal that was used for the seismic measurements. Fig. 5.5 shows a combined PSD spectrum of the tower vibration at a height of about 20 m by using LDV (yellow) and seismic E-W-component recordings on the foundation of the WT (blue) resp. in 40 m distance (red). The seismic E-W-component corresponds to the sensitivity direction of the laser (line-of-sight velocities). For the LDV analysis, a 20 s time sequence in June 2018 was taken, scaled at velocity units (mm/s) and averaged over the frequency domain amplitudes. The overall detectable frequency range of LDV measurements could be up to 1 kHz, which is of special interest e. g. for sound emission monitoring. Zooming to the low frequency range up to 10 Hz, the PSD corresponds well with the results of the seismic measurements during this time window. In contrast to the LDV measurements, a 20 min time interval was used for the calculation of the seismic PSD spectra in order to achieve a stable result (Fig. 5.5). It is important to point out that the used seismic time window in Fig. 5.5 (June 2018) differs to the analyses of section 5.3 (March 2018). During these measurements, the rotation rate was about 16 rpm, corresponding to a BPF of about 0.8 Hz which can be well observed in all spectra. Furthermore, already identified eigenfrequencies of the tower-nacelle-system by the finite beam element model (section 5.4) can be recognized in the seismic and LDV measurements and are visualized by vertical lines in Fig. 5.5. The most prominent spectral peak in Fig. 5.5 can be again identified at around 2 Hz and corresponds to peak A3 in section 5.3. A clear allocation of this peak is not possible due to the chosen modeling depth. But for reasons we already mentioned before, we think that this peak corresponds to the second bending mode of the tower, interacting with the BPF and several other eigenfrequencies of the system.

5.6 Conclusion

We present continuous seismic recordings on top of the foundation of a modern WT in comparison with a simulation model of the tower and LDV measurements. By using seismic recordings of more than one year we are able to distinguish between several operating conditions of the WT. As a result, it is possible to identify major spectral peaks, which were also visible at different seismological studies in the past, to the BPF, to specific tower bending modes or to eigenfrequencies of the blades of the WT.
Based on linear modal analysis using finite beam elements, the first bending mode is in the range of 0.34 Hz. The peak around 5.28 Hz could be allocated to the third bending mode, whereas the major peak at around 2 Hz is more difficult to identify. We find a likely interaction of the second bending mode of the tower with the BPF and eigenfrequencies of the blades, which could also be the reason for possible resonance effects and thereby an amplification of induced signals in this frequency range. The BPF strongly depends on the dominating wind speed

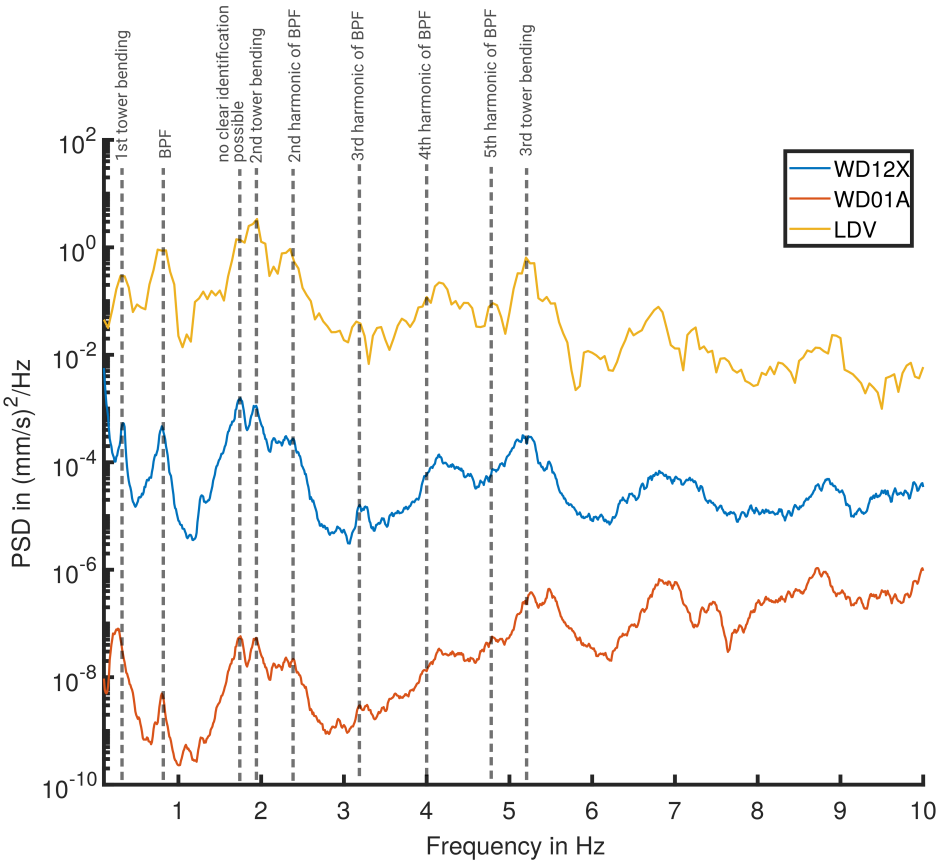

Figure 5.5: PSD spectrum of the tower vibration during operation of the WT (blade rotation) from a single tower point LDV-measurement (yellow) in comparison with the seismic E-W-recordings on top of the foundation (blue) and in 40 m distance (red). Vertical lines symbolizes the resulted bending modes from the numerical simulation of the tower vibrations in section 5.4.

during a specific time window. In this study we use two different time windows with a rotation rate of around 14 rpm and 16 rpm, which corresponds to a BPF of 0.7 Hz and 0.8 Hz, respectively. These frequencies with their corresponding multiples are also clearly visible in the seismic spectra.

To substantiate our results, we compare seismic data with LDV measurements at the tower of the WT during a 20 s time sequences. The calculated power spectrum of vibrations at about 20 m height corresponds well with the seismic measurements which have been performed simultaneously. With respect to the BPF and the specific bending modes of the tower, the results of the LDV confirm our interpretation of the tower vibration simulations.

This work is based on an interdisciplinary approach to understand the behavior of WTs as a seismic noise source. Our results allow new insights in the interpretation of WT-induced signals. With more detailed shell-element based models we will be able to simulate the noise emissions of WTs in a more elaborated way, to identify the remaining peaks observed in the field data and to validate how these induced signals interact with seismic observations.

Acknowledgements

The WT at Pfinztal is part of the RedoxWind project. We gratefully acknowledge the funding by the Ministry of Economics, Labor and Housing of Baden-Württemberg, the Federal Ministry of Education and Research of Germany and the “Fraunhofer-Gesellschaft zur Förderung der angewandten Forschung e.V.” for this project. Laser vibrometry measurements were carried out as part of the project WEADYN, supported by: Federal Ministry for Economic Affairs and Energy on the basis of a decision by the German Bundestag. T.Z. and S.N. were financed by the project “TremAc”, which is funded by the Federal Republic of Germany. Awarding authority: The Federal

Ministry for Economic Affairs and Energy based on a resolution of the German Bundestag. Seismic recording stations were provided by the KArlsruhe BroadBand Array (KABBA) at KIT.

6 SMARTIE1 – A large-scale experiment to investigate and predict the induced seismic signals of a single wind turbine

In this chapter I present results of the large-scale experiment SMARTIE1 (seismic monitoring and research of wind turbine induced emissions). As part of this field experiment we deployed 36 seismic stations for 21 days around a single wind turbine in Pfinztal, SW Germany, in cooperation with Leipzig University. In the following, I determine a frequency-dependent attenuation factor for a layer of loess over limestone (Muschelkalk) as well as the radiation pattern of a single wind turbine at different distances. An additional overview of the SMARTIE1 experiment is given in Appendix C.

This chapter is prepared for submission.

6.1 Introduction

The effect of climate change has a global impact and affects our environment more and more. As one consequence, climate-friendly technologies to produce green electricity are developing rapidly. A way to produce such electricity is the transformation of kinetic energy of the natural wind field into electrical energy by wind turbines (WTs). These WTs are controversial due to emissions in a number of ways, which could e.g. disturb sensitive measurements like seismic recordings. Nevertheless, in order to allow a peaceful co-existence between WTs and sensitive instruments, we need to understand how WTs emit seismic signals for different wind conditions, in particular in terms of the spectral content and radiation pattern, and how these signals propagate through the local subsurface. This is the aim of the large-scale experiment SMARTIE1 (seismic monitoring and research of wind turbine induced emissions) at a single WT in Pfinztal, SW Germany, where we installed in total 36 seismic instruments as ring-like and profile measurements for a period of 21 days during wintertime (December and January).
In the last few years, several studies regarding the impact of WT-induced signals on seismic stations have been published. Styles et al. (2005) investigate the impacts of a wind farm on the Eskdalemuir-Array in Scotland, Great Britain, and identify discrete frequency peaks which they associate with the blade-passing frequency (BPF) and its multiples. For a WT containing three blades, this BPF corresponds to three times the rotation frequency. The increasing overall noise level of the seismic stations can be correlated with the wind speed, which is an indication for the influence of WTs on seismic recordings at the Eskdalemuir-Array. As seismic stations should be deployed at locations with a very low background noise, WTs could influence the sensitivities and tasks of such seismic stations. Saccorotti et al. (2011) detect an amplitude peak in the frequency spectrum at 1.7 Hz at seismic stations in the vicinity of the Virgo Gravitational Wave Observatory (VIRGO) in Italy and allocate the generation of this peak to a wind farm nearby. This peak can be observed up to a distance of 11 km to the WTs. Stammler and Ceranna (2016) analyze the influence of several WTs in the vicinity of the Gräfenberg-Array in Germany. They can correlate an increase of the overall seismic noise level with the start-up of new WTs near seismic stations during high wind speeds. This increased noise level leads to a higher threshold for the detection of seismic signals, which directly impacts the functional capability of the seismic array. Neuffer and Kremers (2018) analyze the impact of WTs on a seismic network in the vicinity of natural gas fields in Northern Germany. They determine the azimuthal direction of incoming Rayleigh waves and observe that waves with back-azimuths pointing to WTs in operation

are dominating the wavefield in a frequency band of 3 Hz to 4 Hz. Zieger and Ritter (2018) calculate attenuation factors for emitted seismic signals of wind farms in the area around the town of Landau, SW Germany, for the near- and far-field of WTs. They find a decay of the WT-induced signals proportional to $1/r^b$ with frequency-dependent b values, ranging from 0.78 to 1.59 for unconsolidated sediments in the Upper Rhine Graben. Additionally, they observe a higher decrease of wind-dependent signals with depth than with distance. Friedrich et al. (2018) use the identified frequency peaks around Landau described before and localize the origin of these peaks at the location of the wind farms by using a wavefield migration approach. They can clearly distinguish between different types of WTs, depending on the analyzed frequency range. Also, Flores Estrella et al. (2017) find an amplitude attenuation model equal to $1/r^b$ with b values ranging from 0.73 to 1.87 in Saxony, Germany. They point out that these decay factors strongly depend on the local geology.

6.2 Setting

The single WT is located at the Fraunhofer Institute for Chemical Technology (ICT) in Pfinztal, Germany, about 8 km northeast of the town of Karlsruhe. In the framework of the SMARTIE1 experiment, we deployed 36 seismic stations in a linear profile- and ring-like design. In detail, we installed 16 3-D PE-6/B geophones (Fig. 6.1, A + B) as two ring layouts with radii of 50 m and 200 m, respectively. 20 MARK L-4C-3D geophones (Fig. 6.1, C + D) were deployed as two linear profile layouts with azimuths of around 0° (north direction) and 270° (west direction) and a total length of nearly 3 km each. All sensors operated in combination with Omnirecs *DATA-CUBE*^{3} data loggers. The 20 MARK sensors and corresponding CUBEs were provided by the Geophysical Instrument Pool Potsdam (GIPP). In order to obtain the real ground motion velocity, we restitute the continuous seismic recordings with their specific instrument response. The sampling frequency of the data logger was set to 100 Hz. In total, we are able to analyze about six days of seismic data for the ring- and 21 days of data for the profile-measurements. The difference in the recording time is due to the use of various power supplies.

The WT of type Qreon Q82 has a hub height of 101 m and a maximum power output of 2 MW. The so-called SCADA data (supervisory control and data acquisition) are available for the whole period of our measurement with a resolution of one minute, which includes the rotation rate of the WT, the wind speed and the wind direction, measured at the top of the nacelle. The measurement campaign was conducted during the Christmas holidays, to benefit from a reduced seismic noise level due to marginal anthropogenic activities at the Fraunhofer Institute and its surroundings.

The main geological properties around the WT correspond to a layer of loess over limestone (Muschelkalk). The profiles end at the western edge of the Upper Rhine Graben, a rift valley filled with unconsolidated sediments. Therefore, we expect an impedance contrast at the rock-sediment-boundary, which could lead to a limited coupling of seismic signals into the rift valley and thus an abrupt decline of the amplitudes along the profile due to transmission and reflection effects at the layer boundary. In addition, an increased attenuation for unconsolidated sediments can be expected for the propagation of seismic signals inside the rift valley compared to limestone.

The rotation rate of the WT during our experiment is shown in Fig. 6.2 for a one-minute resolution. The rotation rate ranges from 0 rpm to a maximum of around 18 rpm.

6.3 Attenuation of seismic emissions at Pfinztal along profiles with different azimuths

The attenuation along the propagation path of WT-induced signals is a fundamental characteristic and necessary for evaluating the impact of these signals on residents or sensitive infrastructure, like seismometers, nearby. As mentioned before, this attenuation depends on the frequency and the local geology. Moreover, we must differen-

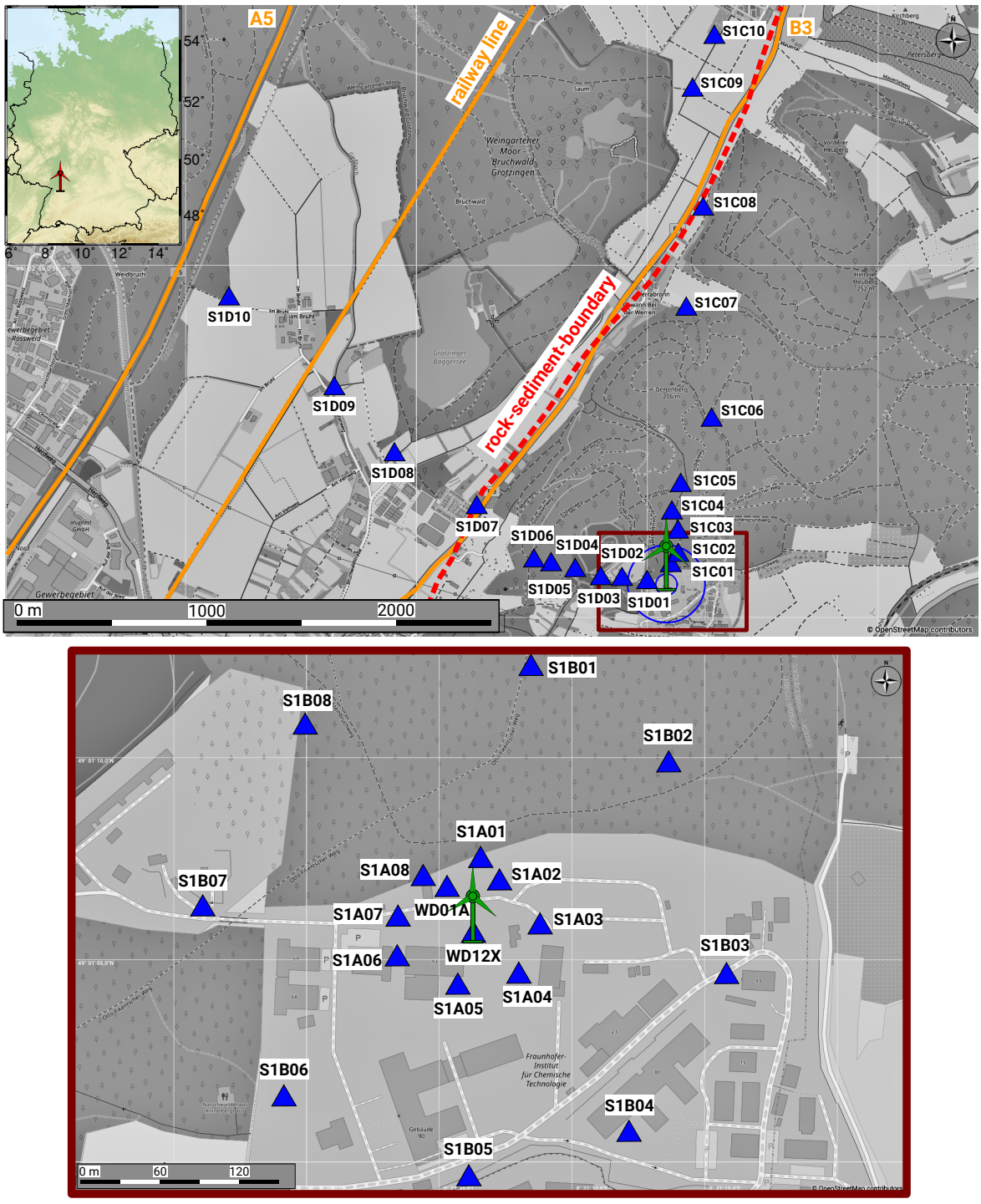

Figure 6.1: Top: Map of the region of interest around the Fraunhofer Institute in Pfinztal, Germany, including the deployed seismic recording stations of the profiles (blue triangles) with their specific designation and the WT (green). Infrastructure like roads or railways are highlighted in orange, as well as the rock-sediment-boundary (red dashed line, after LGRB - Federal State Office for Geology Resources and Mining Baden-Württemberg, Germany). Bottom: Zoomed map section for the exact locations of the seismic recording stations (blue triangles) of the ring-like measurements with radii of 50 m and 200 m, respectively, as well as the both permanent seismic broadband stations WD01A and WD12X.

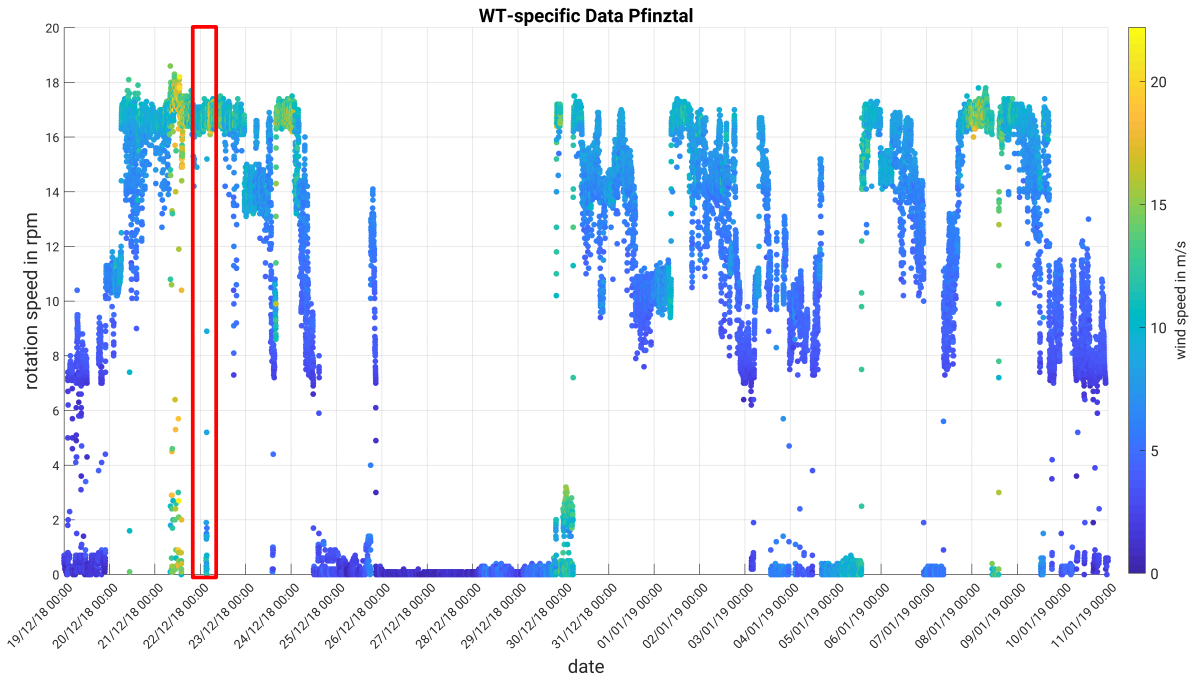

Figure 6.2: The rotation rate (ordinate) of the WT during the measurement period (abscissa) for a one-minute resolution. The corresponding wind speed is color coded (blue for low wind speeds, yellow for high wind speeds). The used time window for the PSD calculation in section 6.3 is marked with a red box.

tiate between near- and far-field effects according to the observed wavelengths and the distance to the recording stations.

As shown in Fig. 6.1, we deployed two linear profiles (C and D) with different azimuths (0° and 270°) and a length of nearly 3 km each. For analyzing the effect of attenuation, we calculate the power spectral density (PSD) in a time window of six hours during the night of 21/12/18 to 22/12/18 (red box in Fig. 6.2). In this time window we observe relatively high and stable wind conditions in combination with a constant rotation rate. We use the method of Welch (Welch, 1967) for the calculation of the PSD spectrum: splitting the overall time window into several small overlapping time segments and then calculating the PSD in each time segment using an adaptive multi-taper method, introduced by Thomson (1982). This method provides a good protection against spectral leakage, especially for signals with a very high dynamic range. For a detailed description of the adaptive multi-taper method we refer to the book of Percival and Walden (1998). By averaging over all time segments, we obtain the final PSD spectrum. This approach reduces the variability of our calculations and provides a statistical significance for the PSD values.

The resulting PSD spectra for the linear profiles are shown in Fig. 6.3 in a frequency range between 0.1 Hz and 10 Hz. We will focus our investigations on this frequency range since this range is also highly interesting for detecting local seismic events (e.g. Hensch et al., 2019). We combined both linear profiles with different azimuths in one plot as there is no azimuth-dependence in the radiation pattern of the WT at these distances. An explanation of this absence will be given in section 6.4, Fig. 6.8. The different colors symbolize the distance from the WT to the seismic station (blue color corresponds to short distances, green color corresponds to large distances). Attentive readers also recognize that Fig. 6.3 only shows the PSD up to the stations S1C07 and S1D06 of the profiles, respectively. More distant seismic stations (S1C08 – C10 and S1D07 – D10) do not show any impact of WT-induced signals and are therefore neglected for the attenuation calculation (see Appendix C for the

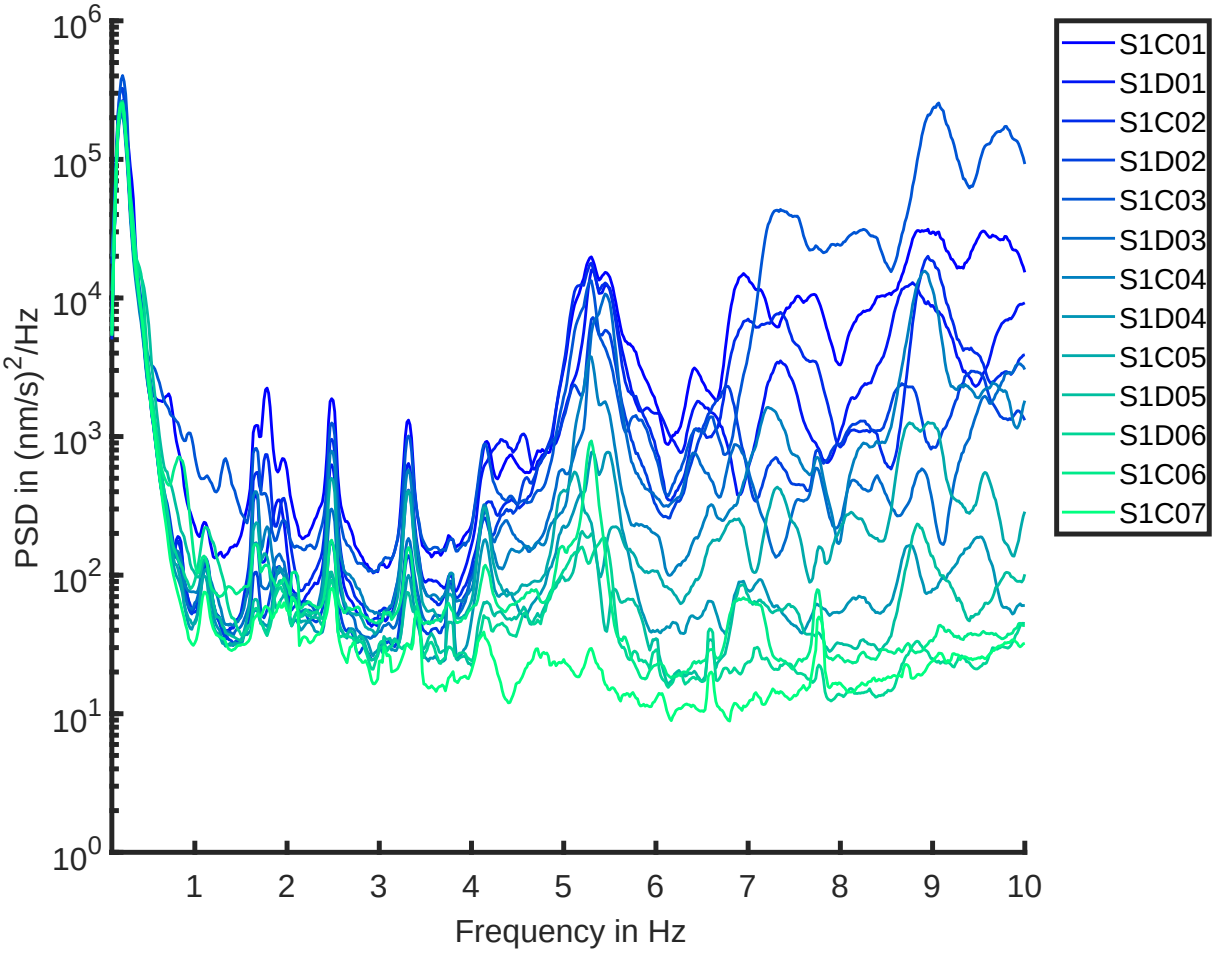

Figure 6.3: The PSD over the frequency range from 0.1 Hz to 10 Hz. The colors symbolize the distance of the corresponding seismic station to the WT: distances $\leq$ 300 m are shown in blue and distances $>$ 300 m are shown in green.

technical report). The absence of WT-induced signals at distant stations ($>$ 1500 m) can be explained by two factors:

- Towards the western direction there are many anthropogenic activities. A highway (A5), a railway line and a state road (B3) are directly located near the distant seismic stations, in addition to several villages in this area. Therefore, the overall noise level at each of the western recording stations is increased by anthropogenic noise which overlays the WT-induced signals.
- As mentioned in section 6.2, the profiles were deployed at the edge of the Upper Rhine Graben. At the boundary faults, where the rift flanks (mainly consisting of limestone) encounter the Cenozoic sediments of the valley, we expect an impedance contrast (energy will be partially reflected at the boundary) and an increased wave damping along the profile due to the sediments inside the rift valley.

For the reasons described above, we are able to analyze the attenuation of 13 seismic stations with a maximum distance of around 1.5 km to the WT. Several discrete frequency peaks can be observed in this frequency range from 0.1 Hz to 10 Hz (Fig. 6.3), decreasing with the distance to the WT (blue to green). The main peaks can be found around 1.13 Hz, 1.67 Hz, 2.5 Hz, 3.32 Hz, 4.17 Hz and 5.3 Hz. These specific frequency peaks can slightly vary at different recording stations. The PSD maximum of these peaks is picked automatically in a narrow frequency band of the PSD spectra and plotted over the distance.
This is shown in Fig. 6.4, where the individual PSD peaks of each station are plotted as blue dots over the distance to the WT. We fit a power-law decay proportional to $1/r^b$ (Stammler and Ceranna, 2016) to the PSD values, shown

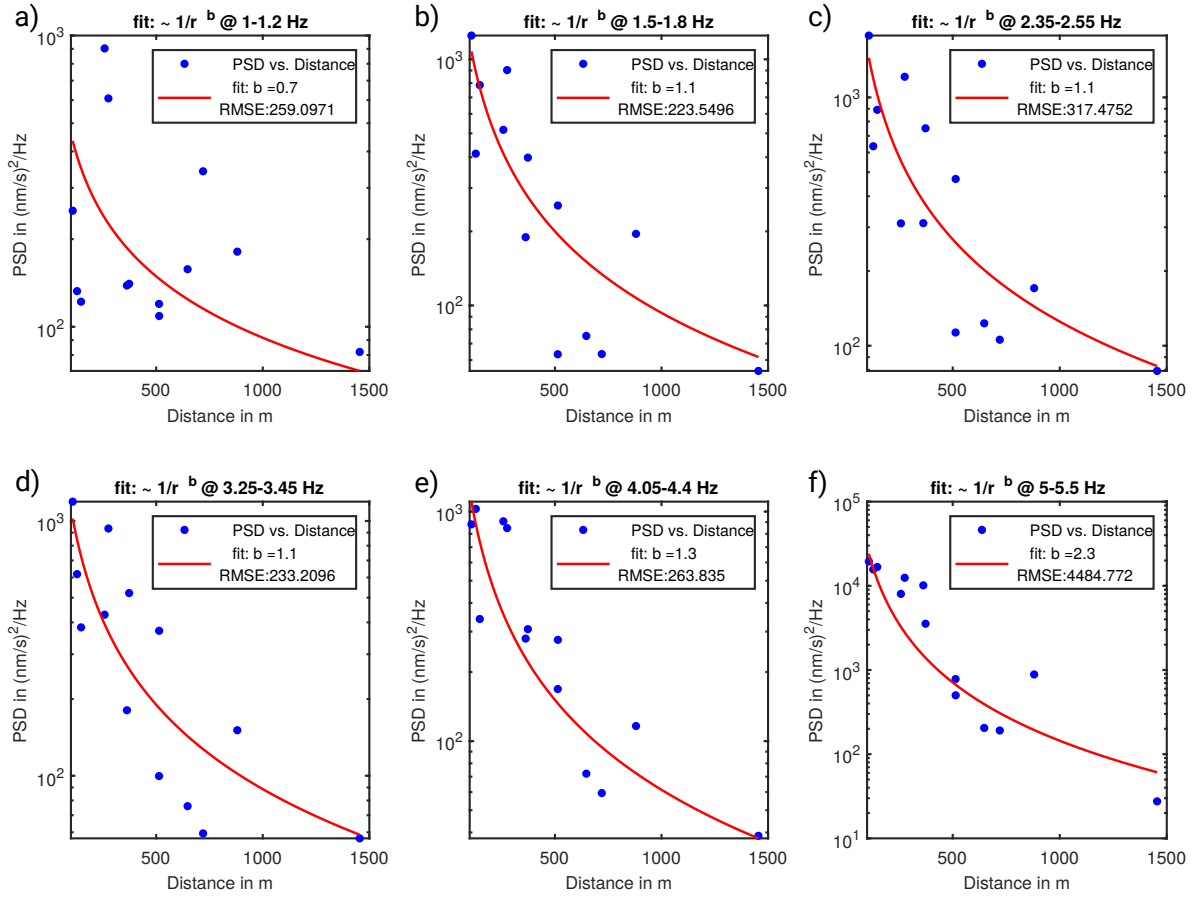

Figure 6.4: Attenuation relation for six different frequency bands (a – f). A power-law decay (red) proportional to $1/r^b$ was fitted to the PSD values (blue dots). The specific b value and the associated RMSE (root mean square error) value are shown in the legend. Error bars for the picked PSD values and the calculated distances to the WT are smaller than the blue dot symbols and are not shown in the figure.

by the red line. The b value, a measure for the strength of attenuation of the PSD, depends on the observed frequency band. The focus of the fit validity was not just by minimizing the associated RMSE (root mean square error) value, but also by appropriately fitting the lower PSD peaks at more distant stations. We could reduce the RMSE value by a more suitable fit for the few higher PSD values from nearer stations, which would result in an underestimation of the lower PSD peaks farther away ($>$ 500 m).

Fig. 6.4a shows the attenuation for the first frequency peak around 1.13 Hz. The PSD values are widely spread and a clear fit for the b value cannot be found because there is no clear decreasing trend of the PSD values with distance. Assuming a surface-wave velocity around v =1500 m/s for limestone, the wavelength would correspond to 1.5 km, equivalent to the maximum distance of the profile. All of the seismic stations would be located still within the near-field. In contrast, the PSD values of the second major frequency peak around 1.67 Hz can be fitted with the used power-law decay where b corresponds to 1.1 (Fig. 6.4b). The same attenuation behavior can be observed for the frequency peaks around 2.5 Hz and 3.32 Hz (Fig. 6.4c,d). A b value of around 1, which can be observed for the lower frequency ranges (1.13 Hz, 1.67 Hz, 2.5 Hz, 3.32 Hz), indicates a seismic amplitude decay proportional to $\frac{1}{\sqrt{r}}$ (the spreading loss of seismic amplitudes is given by our calculated b values divided by two, to eliminate the squaring during the PSD calculation). This amplitude decay would correspond to a cylindrical spreading loss of surface waves. As a consequence, we assume a more major damping effect due to geometrical spreading than an influence of heterogeneities in the subsurface for the amplitude decay of the emitted waves with distance for frequencies up to 3.32 Hz. With increasing frequency, also the b value increases. The PSD values at 4.17 Hz (Fig.

6.4e) decay with b = 1.3. The PSD values for the highest clear frequency peak around 5.3 Hz (Fig. 6.4f) decay proportional to $\frac{1}{r^{2.3}}$. This frequency dependency for b was already observed in e.g. Zieger and Ritter (2018) and is explained by scattering and anelastic attenuation effects through heterogeneities along the propagation path. This suggests that we observe the influence of the subsurface for higher frequencies by an increase of the attenuation (or b value), where we assume a minor impact of near-field effects and a domination of the far-field.

6.4 Radiation pattern of a single WT at different distances

The aim of the ring measurements (A and B, Fig. 6.1) at different distances is the identification of the radiation characteristics of a single WT for different wind conditions, like wind speed and wind direction. A dependency of the ground motion amplitudes with wind direction was first observed by Xi Engineering Cosultants Ltd (2014). They define two directional bins (in-line and cross-line) and compare the ground motion amplitudes, averaged over 10 minutes, for each bin at one seismic station near a wind farm:

- In-line: The in-line data set is defined as a combination of the up-wind and down-wind bin, corresponding to an imaginary line from the nacelle to the seismic station, each with a size of 20°.
- Cross-line: The cross-line data set corresponds to the two bins perpendicular to the respective wind direction, also with a size of 20°.

For certain wind farms (Craig and Dun Law wind farm), they find a higher ground motion amplitude when the seismic station is located in-line to the wind farm than in cross-wind position for a wind speed of 8 m/s. The ground motion amplitude is 1.38 (for Craig wind farm) and 1.15 (for Dun Law wind farm) times higher when measured in in-line direction, relative to cross-line.
The design of the SMARTIE1 experiment allows us to simultaneously analyze seismic recordings of 16 3-D geophones with an eigenfrequency of 4.5 Hz, which are equally distributed around the WT, for more than five days containing different wind conditions. The early morning of the 21 December offers a suitable time window for our purpose, since the wind speed ranges from 8 m/s to 12 m/s and the WT operates with a stable rotation rate of around 17 rpm (see Fig. 6.2), equivalent to nearly the maximum rotation rate of the WT. As a first step, we calculate the PSD spectra for all seismic stations of the ring measurements (A and B) for a time period of six hours with a stable wind speed and wind direction as described in section 6.3. Due to technical problems, we exclude the station B1 for our analyses. To sum up, we use seismic recordings of eight geophones in a distance of 50 m and seven geophones in a distance of 200 m to the WT.
As can be seen in Fig. 6.5, several sharp frequency peaks are visible in the PSD spectra for all stations, which we allocate to the WT. In particular, the decreased PSD value of the more distant stations (B-ring, green color) in comparison with the stations nearer to the WT (A-ring, blue color) is clearly visible. This, again, is an indication for the WT as the seismic source of these peaks. The most prominent peak can be identified in the narrow frequency range of 5 Hz to 6 Hz at all seismic stations. In the next steps we will focus on this peak to describe the radiation characteristics of a single WT.
To illustrate the oscillation near 5.5 Hz, we use a zero-phase second order Butterworth bandpass filter with a lower cutoff frequency of 5 Hz and a higher cutoff frequency of 6 Hz. As an example of the radiation behavior we show a randomly chosen time window with a duration of 20 s for the seismic station S1A01 (Fig. 6.6). During this time window, the wind direction was south-southwest/north-northeast ($\sim$ 220°, measured clockwise from North). The progression of time is color coded for a clearer illustration and the amplitude corresponds to the ground motion velocity in nm/s. The three recordings (vertical Z, N-S and E-W) of the seismic sensor differ significantly over time. Beat-like effects can be observed with increasing and decreasing amplitudes, which may be the result of different interference patterns.

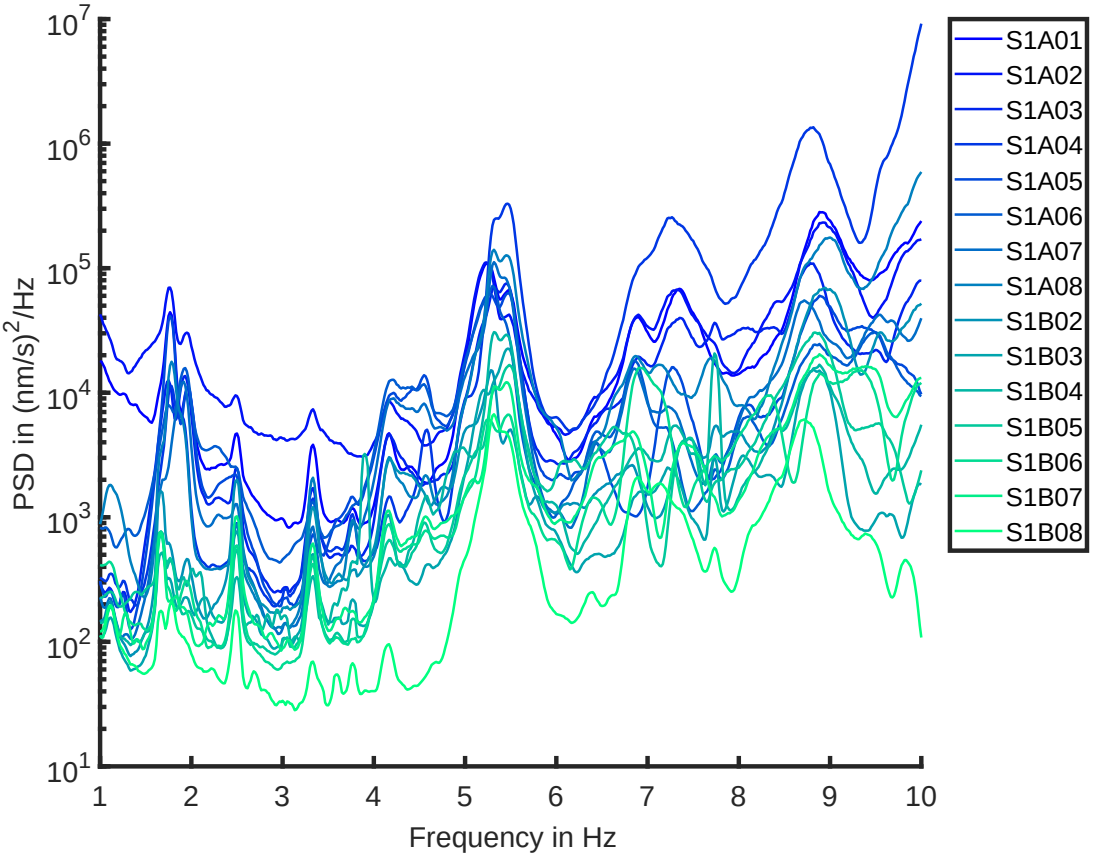

Figure 6.5: PSD spectra for the A- and B-ring measurements (Fig. 6.1) during a time period of six hours with stable wind conditions. A major PSD peak can be recognized between 5 Hz and 6 Hz.

As next step we calculate the particle motion of station A1 for the ground velocity (Fig. 6.7). The colors correspond to the progression of time, similar to Fig. 6.6. The diagram provides several consecutive particle motions in time, which we numbered for a clearer illustration:

1 The chosen time window starts with a north-east/south-west oriented particle motion (dark blue, ca. 3 s long), which corresponds to the wind direction. However, as we mentioned before, the SCADA-data of the WT has a resolution of one minute. The exact wind direction of this time interval (20 s) is therefore only known approximately.

2 The direction of the particle motion changes slightly to north-northeast/south-southwest for ca. 4 s, which again corresponds to an oscillation in-line with the wind direction (light blue).

3 With progression of time, a new effect can be observed in the diagram: the particles start to spin in an elliptical motion again for ca. 4 s (turquoise).

4 The elliptical motion changes to a north-northwest/south-southeast oriented directivity for 3 s (green). This motion is now perpendicular to the assumed wind direction during the period of time.

5 Again, the particles start to spin in an elliptical way but now with a decreased amplitude for 3 s (orange). The major axis of the ellipse has two different orientations (N/S and E/W).

6 The amplitude of the elliptical motion starts to increase and forms an almost perfectly shaped circle for 3 s (yellow).

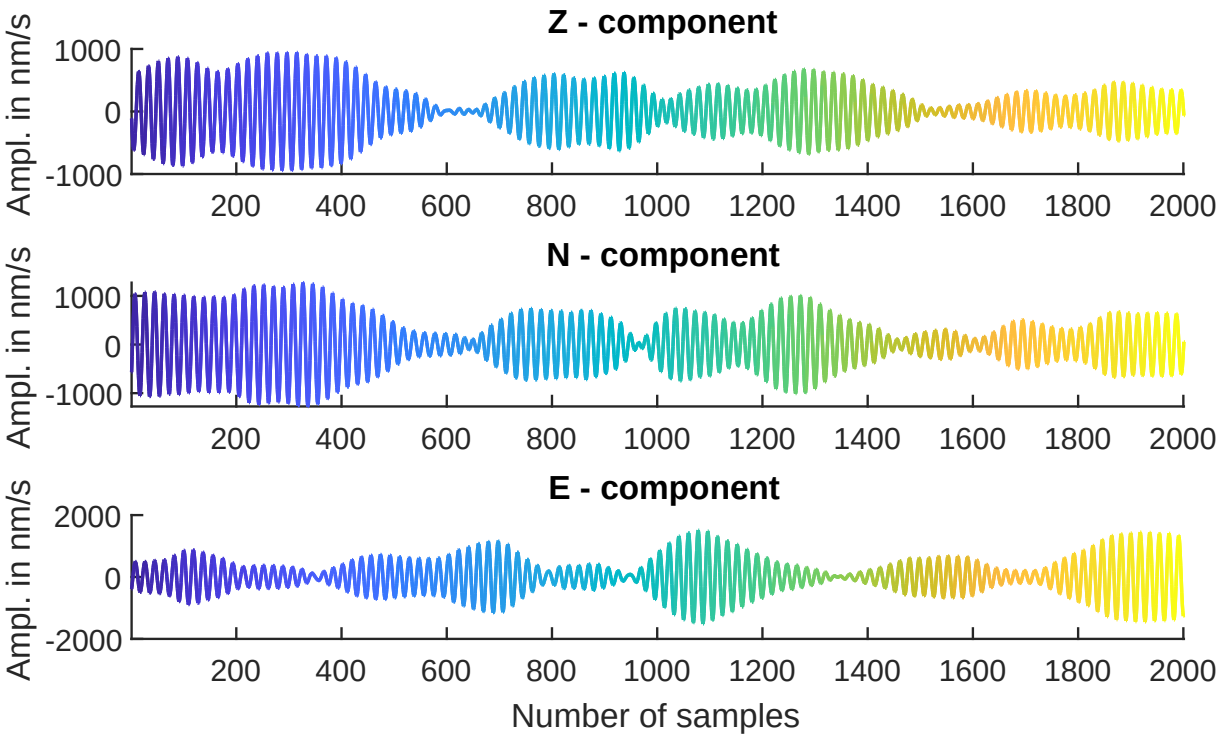

Figure 6.6: Time signal for the vertical component (Z) and the two horizontal components (N-S and E-W) of seismic station S1A01 during 2000 samples, which corresponds to a time period of 20 s ($\Delta t = 0.01$ s).

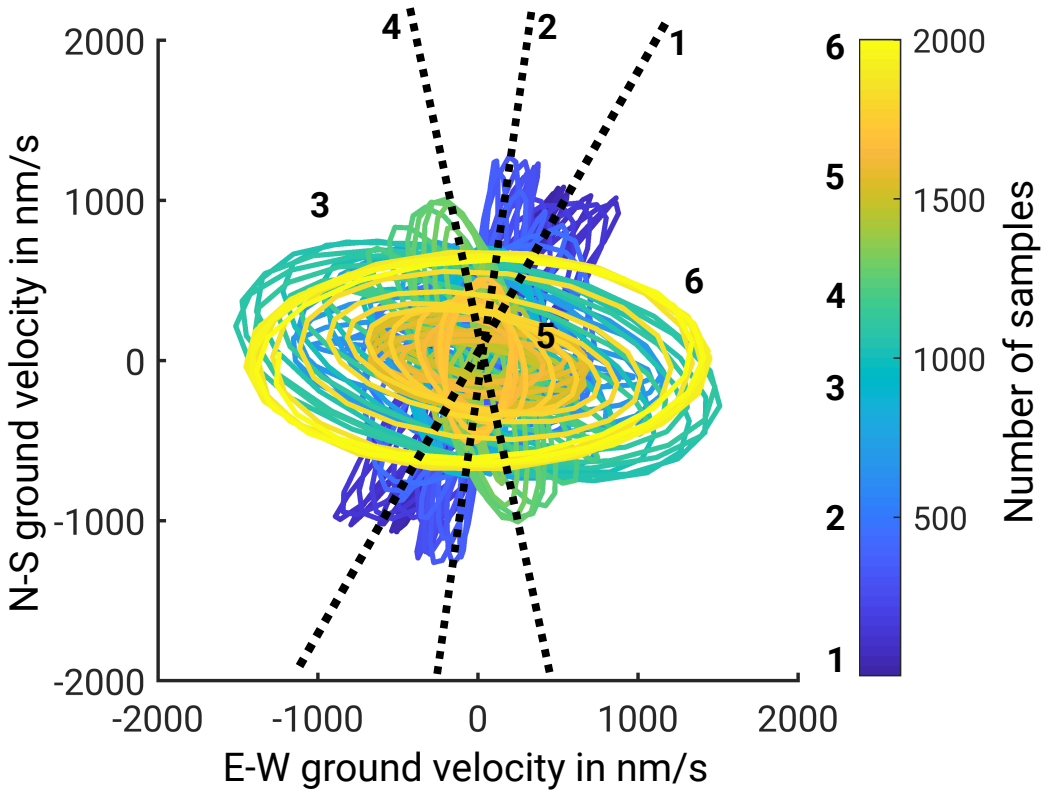

Figure 6.7: The polarization diagram of the seismic station S1A01 for the time period shown in Fig. 6.6. The colors correspond to the progression of time in samples ($\Delta t = 0.01$ s).

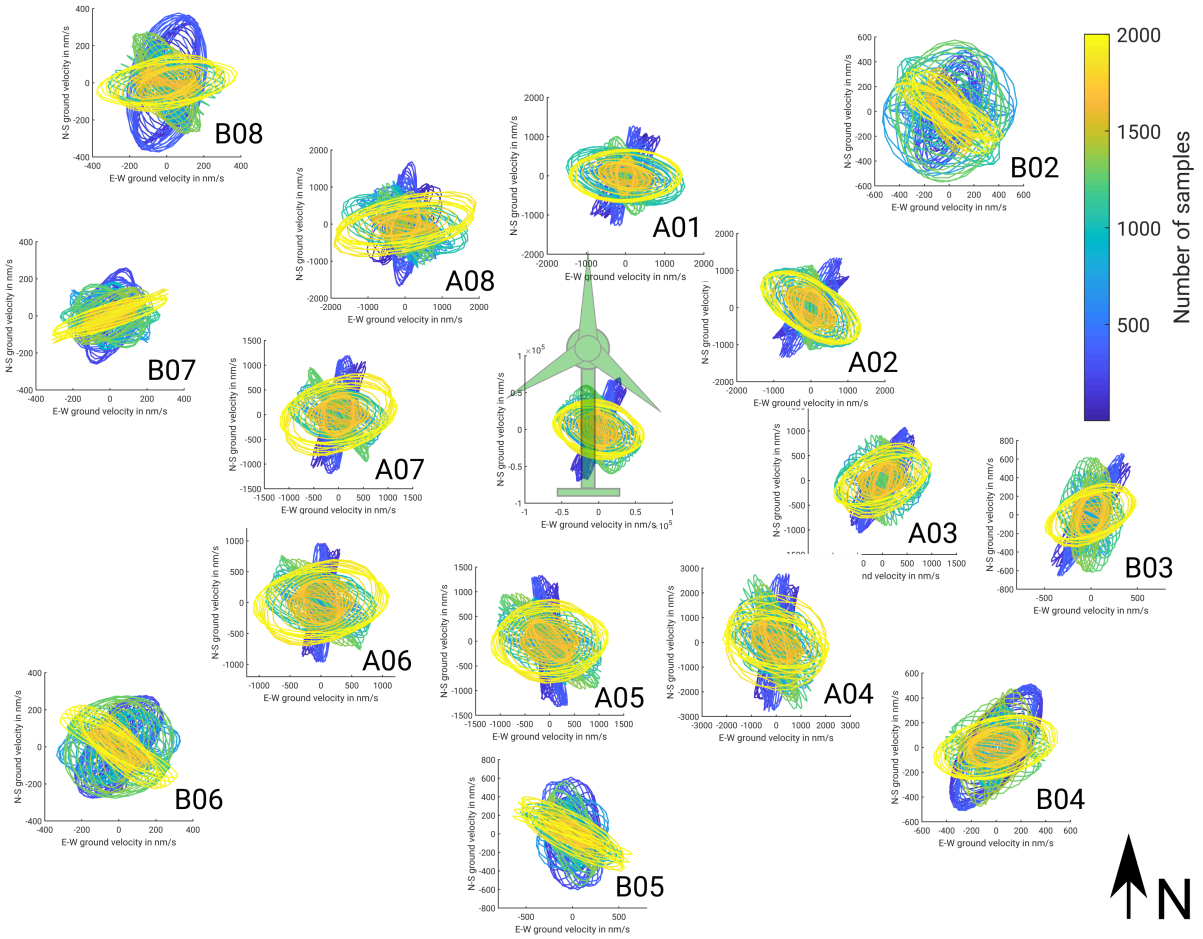

Figure 6.8: The polarization diagrams at all seismic stations within the A- and B-ring measurements.

In order to illustrate the particle motion for different azimuths, we calculate the diagrams for all seismic stations and bin them to their position relative to the WT (Fig. 6.8). In general, all of these diagrams show a similar behavior as described before. However, small variations in the orientation of the directivity can be observed, especially for stations of the inner circle A. These discrepancies can be explained by either a deviation in the northward orientation of the seismic stations or heterogeneities along the propagation path from the WT to the station, which could influence the orientation of the incoming seismic wave.

Except for station S1B03 the particle motion of the outer circle B shows no clear directivities with a preferred orientation. This again can be explained with heterogeneities and seismic site effects in the subsurface along the propagation path, which could lead to a broadening of the directivity effect. Since the amplitude of the WT-induced signals decreases with distance to the WT, the particle motion of the outer circle B could be also more affected by other possible seismic noise sources in this frequency range compared to stations of the inner circle A.

In contrast to the observations of Xi Engineering Cosultants Ltd (2014), especially for distances $x > 200$ m, we observe an equally distributed radiation of induced seismic signals in all directions. This conclusion also confirms the absence of a clear distinction in the radiation pattern of the WT for the linear profiles in section 6.3. However, we cannot rule out a directivity in the radiation pattern for larger distances at other locations, for instance due to channeling effects in the subsurface. For small distances ($x \approx 50$ m), the radiation shows a directivity in different orientations as well as an elliptical motion of the particles.

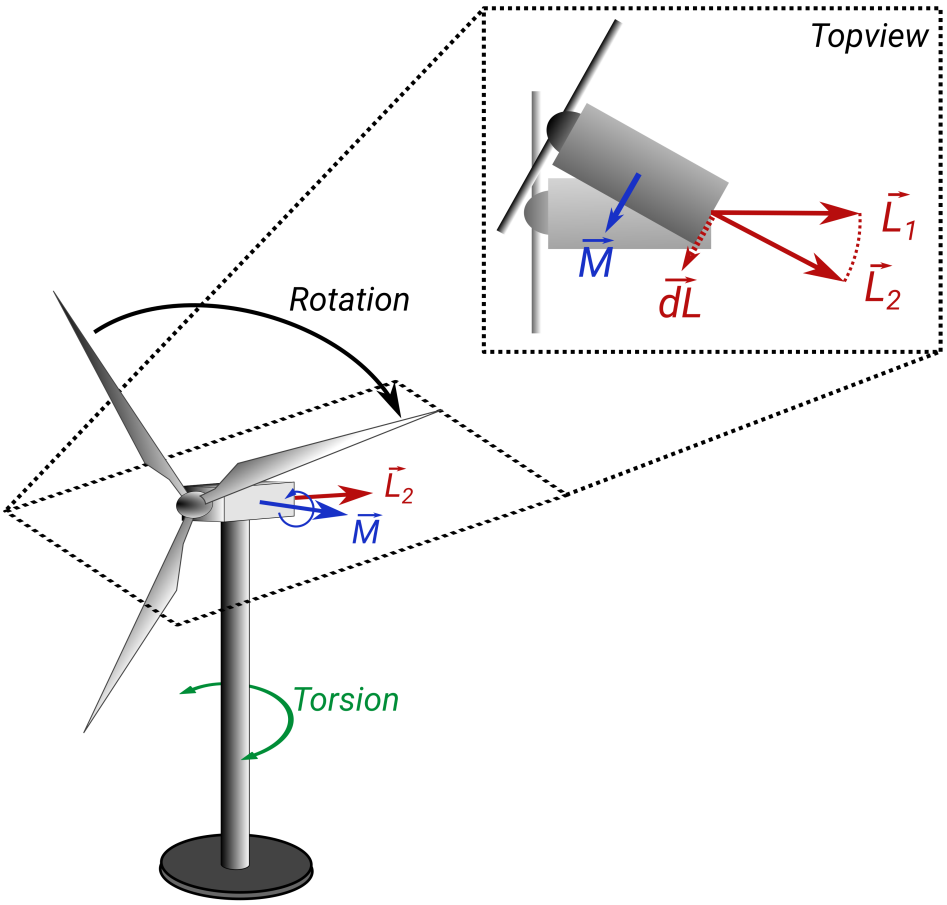

Figure 6.9: Sketch of the WT for a torsional mode (green) of the tower, which induces a torque M (blue). The change of the angular momentum is illustrated in red. The interaction between these effects could lead to an elliptical motion of the nacelle.

The reason for the elliptical motion can be explained by an excitation of gyroscopic forces due to a change of the angular momentum of the rotor. As indicated in Tab. 5.3 in chapter 5, the third bending mode of the tower can be located in the observed frequency range of 5 Hz to 6 Hz. However, also torsional modes of the tower could occur in this specific range, which lead to a rotation of the tower around the vertical axis. The rotation by the torsional modes results in a horizontal change of the angular momentum, induced by the rotational motion of the blades. This change is illustrated in Fig. 6.9 ($\vec{L_1}$ to $\vec{L_2}$). Since the relation between the angular momentum and the torque is

$$\frac{\vec{dL}}{dt} = \dot{\vec{L}} = \vec{M}, \tag{6.1}$$

the forced change of the angular momentum to $\vec{L_2}$ will induce a so-called *pitching moment* $\vec{M}$. The interaction between the torsion mode and the induced pitching moment leads to a nearly circular movement of the nacelle. This movement will be induced through the tower and the foundation into the subsurface and propagates to the seismic station. This description is just a first attempt of explanation of the observed elliptical motion and must be subject of future studies.

7 Comparison of induced seismic signals from a single wind turbine (WT) and a wind farm with nine WTs

The following chapter determines the differences between WT-induced seismic signals of a single WT and a wind farm containing nine WTs of the same type. First, I allocate related frequency peaks to different parts of a single multimegawatt WT by comparing seismic records for different operational conditions with numerical simulations. These results have been published (Nagel et al., 2019) and will be briefly summarized in section 7.2. The related frequency peaks will be evaluated in terms of their decay with distance in section 7.3. As next step, the seismic emissions of a wind farm will be analyzed and compared to results of measurements at the single WT. To determine possible interference effects between the induced seismic signals of several WTs, we implemented a start-up experiment where we start the wind farm turbine by turbine.
Due to a non-disclosure agreement between all involved partners of the research project "TremAc" we will not mention the exact types and locations of the WTs in the following chapter.

7.1 Setting

7.1.1 Measurement campaign at a single WT

The single WT with a hub height of nearly 140 m and a maximum power output of 2 MW is located within an area where the underground is composed of a layer of loess over limestone (Muschelkalk). Two small villages are located south and east of the WT with a distance of about 2 km each. For detecting the WT-induced seismic signals we used seven seismic broadband stations of the type *Trillium Compact Posthole* with an eigenperiod of 20 s and three *Trillium Compact* with an eigenperiod of 120 s. The seismic stations were deployed along a profile with a total length of 1.8 km (see Fig. 7.1 for exact positions) towards the eastern village. The measurement period of nearly three weeks (17 days) during summertime 2018 contains just a limited set of suitable time windows with high and stable wind conditions. In order to obtain the real ground motion velocity, we restitute the continuous seismic recordings with their specific instrument response. The sampling frequency of the data loggers was set to 100 Hz.

7.1.2 Measurement campaign at a wind farm

The wind farm consists of nine multimegawatt WTs whose type is equivalent to the type of the single WT described before. The nearest WT is located in a distance of around 1.5 km to a village east of the wind farm. Most of the WTs are located on a layer of phragmites peat (Riedtorf) and sapric peat (Bruchtorf). Along the wave propagation path to the village, the geology changes to mainly fine- and middle-grained sands. The village itself is located on a layer of sediments. Thus, the geological properties differ significantly to the setting of the single WT described before. We deployed in total 15 seismic broadband stations of various types (*Trillium Compact Posthole 20s*, *Trillium Compact 120s* and *LE-3Dlite MkIII 1s*). The exact locations of the stations (blue triangles) and WTs (green symbols), as well as the changing geological properties along the propagation path, are shown in Fig. 7.2. We were collecting more than two months of continuous seismic recordings during wintertime (2018 – 2019).

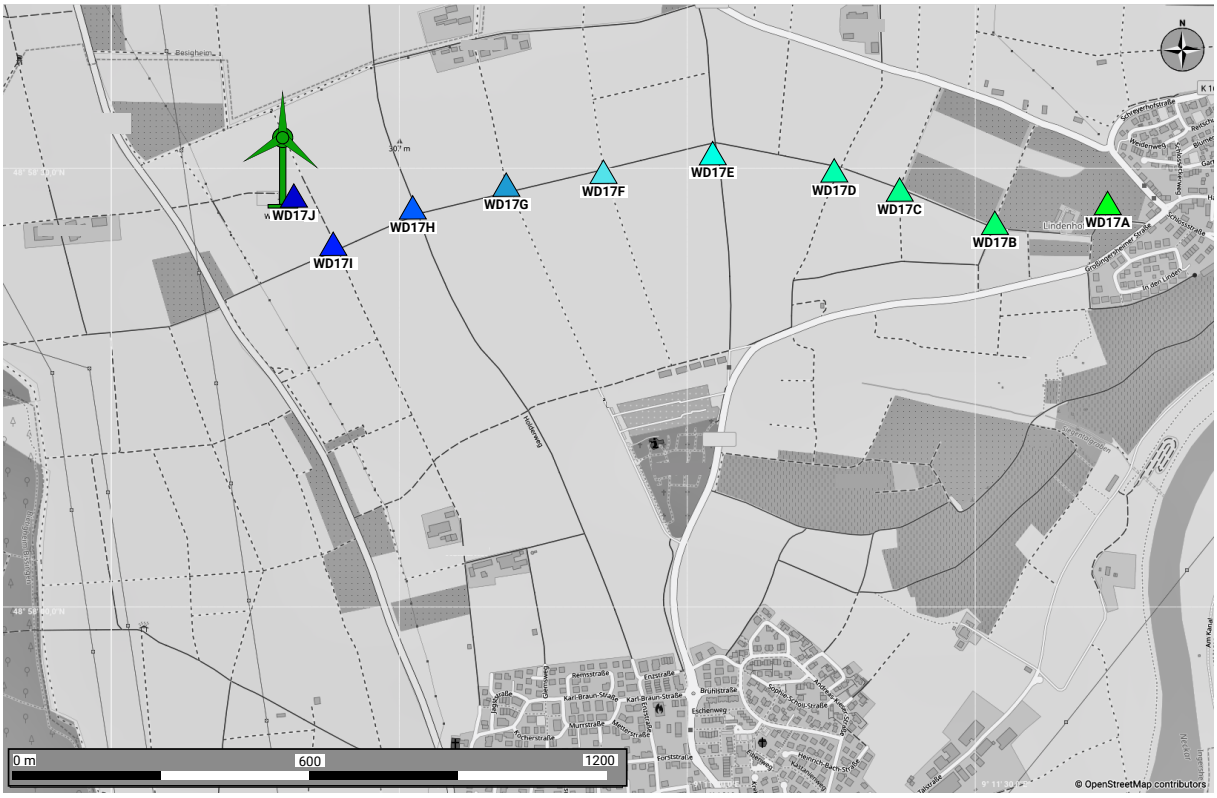

Figure 7.1: Map of the region of interest around a single WT (green). Locations of the seismic stations during the profile measurement are marked as triangles. The color of the triangles corresponds to the calculated PSD spectra (Fig. 7.6).

Unfortunately, some seismic stations (WD18M, WD18N and WD18O) had operating failures due to an incorrect operation of the power supply. This led to a limited data volume for these stations, whereas all other seismic stations provided nearly the full amount of data. Nevertheless, the relatively long measurement period provides a good data set of seismic recordings in combination with stable and high wind conditions.

7.2 Main results of the publication “Soil Vibrations Induced by Wind Turbines”

The publication *Erschütterungsemissionen von Windenergieanlagen* (Soil Vibrations Induced by Wind Turbines, Nagel et al., 2019) deals with the validation of numerical simulations by seismic measurements on the foundation of a single WT and the identification of the main emitted PSD peaks related to different parts of the WT. Here the authors determine a strong influence of the tower structure on ground motion amplitudes in the direct vicinity of the WT.

The study only uses ground motion velocities of the seismic station WD17J (Fig. 7.1, dark blue triangle), located on top of the WT-foundation, to minimize the influence of the subsurface during the seismic wave propagation to the recording station. Fig. 7.3 shows the spectrogram of the vertical ground velocity during a time period of three hours by using overlapping time windows with a duration of 20 s after the method of Welch (Welch, 1967). The frequency ranges from 0.1 Hz to 30 Hz. The colors correspond to the power spectral density (PSD) for each time window, normalized to its maximum. Clear discrete horizontal lines with high PSD values (red color) can be recognized in the spectrogram below 20 Hz. Some of these frequencies vary clearly with time (e.g. 0.8 Hz, 1.6 Hz, 2.4 Hz, etc.). The slight shift of frequency over time can be observed especially around 20 Hz. Similar frequency components were already recognized before at other seismic stations in the vicinity of WTs, where the variation in frequency corresponded to the variation of the rotation rate of the nearby WT. Therefore, we allocate these

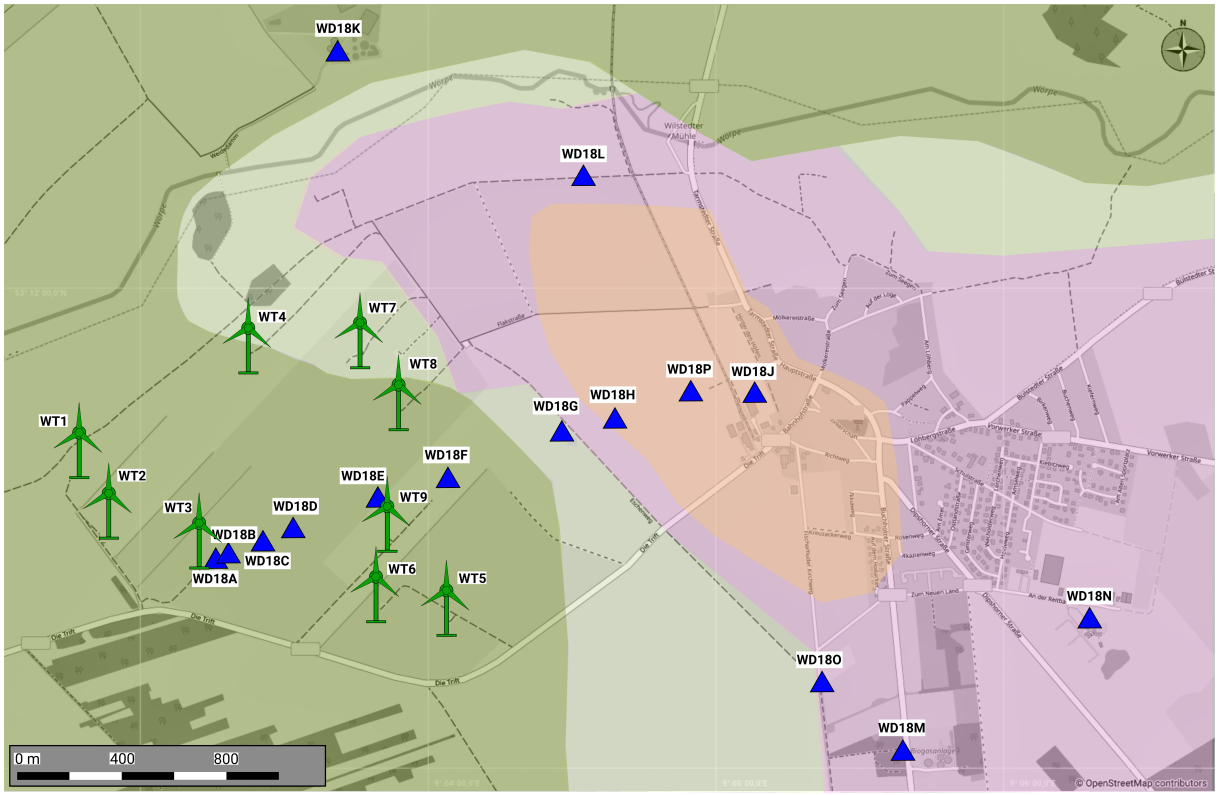

Figure 7.2: The study area around a wind farm consisting of nine equal WTs (green). Locations of the seismic stations during the measurement are marked as blue triangles. The geological properties are color coded after a geological map provided by the “State Office for Mining, Energy and Geology of Lower Saxony (LBEG)”: dark green corresponds to phragmites and sapric peat , light green and purple are fine- and middle-grained sands from different geological periods (stratigraphy) and orange is equivalent to silts.

varying frequencies to the BPF and its multiples. This assumption is also confirmed by analyzing the SCADA data (supervisory control and data acquisition) of the WT, like wind speed or rotation rate, measured on top of the nacelle (see Appendix A). Here the BPF and its multiples are directly marked in the seismic spectrogram as thin black dotted lines. As can be seen in Fig. A.1, the excited frequencies fits very well with the BPF and its multiples. The 20 Hz signal can be explained by effects of the generator technology, where rotating poles inside the generator emit a signal equal to the number of pole pairs multiplied by the rotation rate. Whether this signal is induced by electromagnetic waves or propagates as elastic seismic signal is part of ongoing studies. During the measurement campaign we implemented several shutdowns of the WT with a respective time period of 20 min. The shutdown period can be clearly recognized at t = 100 min in Fig. 7.3. Although a rotational motion is missing during these 20 min, several excited frequencies can be observed during this specific time window, probably triggered by the wind load on the tower and the blades. We allocate these frequencies to eigenfrequencies of different WT parts. With the beginning of the rotation at t = 123 min, we can observe again variable frequencies in the spectrogram, similar to the time window before the shutdown. These two time windows with a respective length of 10 min (Fig. 7.3, marked red and blue) are the basis of further PSD calculations. Thereby we investigate the influence of a rotational motion of the WT on seismic recordings. Wind measurements conducted simultaneously by the University of Stuttgart (Stuttgart Wind Energy) in 150 m distance to the WT and at a height of 10 m in combination with an extrapolation to the height of the nacelle results in a mean wind velocity of 8 m/s to 9 m/s and an associated rotation rate of around 16 rpm for the night of 30 August 2018, which is confirmed by the SCADA data of the WT (see Appendix A). This rotation rate corresponds to a BPF of around 0.8 Hz.

To investigate the eigenmodes with numerical simulations, it is sufficient to use a reduced model by assuming the WT as a tower structure (hub height $h \approx 140$ m) with head mass. Therefore, KIT-VAKA developed a finite-

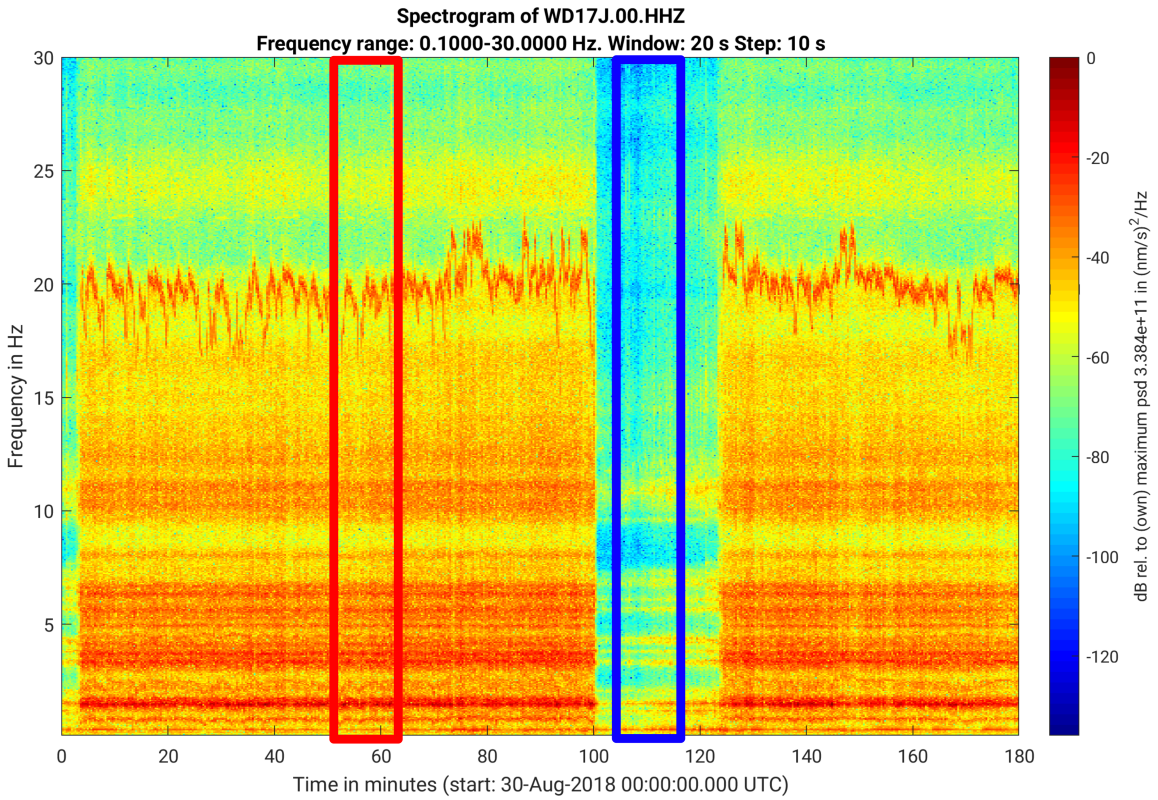

Figure 7.3: Frequency spectrogram of the vertical ground motion velocity, measured on the foundation of the WT during a time interval of 3 hours.

Table 7.1: Comparison of the natural frequencies in Hz assuming a rigid foundation clamping. Beam and shell model was developed by KIT-VAKA, the multi-body simulation by UST-IFB.

eigenmode of the tower	beam model in-/crosswind direction	shell model	multi-body simulation
1. tower bending	0.35/0.35	0.35	0.36
2. tower bending	1.45/1.46	1.46	1.52
3. tower bending	3.30/3.30	3.33	3.33
4. tower bending	6.17/6.19	6.22	6.69

element model, based on beam elements, as well as a shell element-based surface model in the scope of this study. The aim of the shell model is a closer examination of the variation of tower stiffness and mass distribution over height and the identification of shell modes, which are important for possible sound emissions. The comparison of eigenfrequencies, calculated by using both modelling approaches, is shown in Table 7.1. The difference of both concepts is less than 2 %.

The distinction between in- and crosswind direction for the beam model is due to the eccentricity of the head mass with respect to the center of gravity of the tower cross section. However, the influence of this eccentricity only plays a minor role for low eigenfrequencies, as can be seen in Table 7.1. Both modeling approaches (beam and shell model) result in only minor differences, that is why in the following we will focus on the less computing-intensive beam model. The calculations were made by using the software Ansys v19.2 (ANSYS, 2019).

Fig. 7.4 shows the PSD spectrum of the two marked time windows of Fig. 7.3 (red and blue) in a frequency range between 0.1 Hz to 5 Hz. Results of the numerical simulations using the beam model are marked as vertical lines.

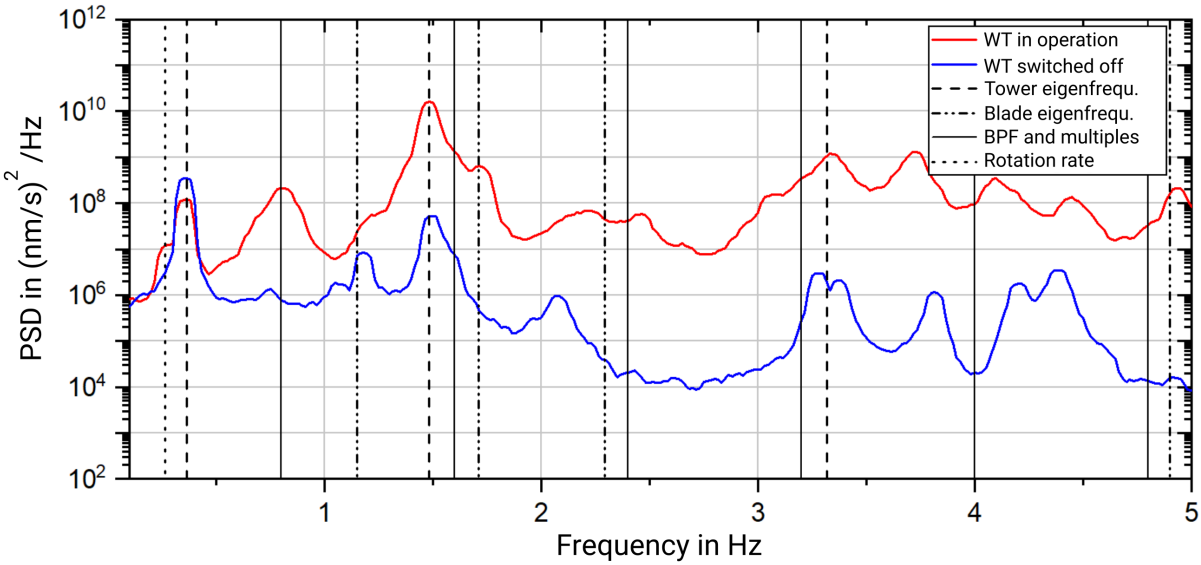

Figure 7.4: Comparison of the PSD during WT operation (red) and when the system is switched off (blue). The colors correspond to the marked time windows in Fig. 7.3.

During operating conditions (red), the frequency peaks correspond to the BPF of 0.8 Hz and its multiples, indicated by the wind measurements mentioned before. Eigenfrequencies of the tower-nacelle-system can be determined in the PSD spectrum during the time window when the WT was switched-off (blue). The peak at 0.36 Hz can be allocated to the first bending mode of the tower and is present for both operating conditions (red and blue). The second bending mode at 1.5 Hz is also visible in both PSD spectra, even as the major PSD peak during operating conditions (red). As mentioned before, the first harmonic of the BPF (6-P excitation) can be assumed around 1.6 Hz and with that it is located near the second bending mode of the tower. As a consequence, the increased PSD peak at 1.6 Hz is probably the result of an interference between the first harmonic of the BPF with the second tower bending mode and bending modes of the blades, which also occur near 1.5 – 1.6 Hz. The third bending mode of the tower (3.33 Hz) can be validated by seismic measurements as well (blue curve).

To simulate the entire dynamic loads on the tower in the time domain, a multi-body simulation of the analyzed WT with estimated parameters was developed by the University of Stuttgart, Institute of Aircraft Design, using the software SIMPACK (http://www.simpack.com). This simulation combines several stiff or flexible bodies with kinematic conditions to an overall WT model. Thereby structural dynamic relevant properties, like stiffness or mass distribution of WT components (hub, rotor, gearbox, tower and foundation), as well as aerodynamic interactions with turbulent conditions and the control system can be considered. By using numerical integration methods, the solution of the equation of motion can be solved in the time domain. A simulated time series at the tower base is used to validate the developed model with seismic recordings. Results of several tower bending modes are shown in Table 7.1. Small differences can be observed for the eigenfrequencies compared to the reduced beam and shell models. These differences can be explained by an interaction of blade and tower oscillations or a moment of inertia, which is not considered for the reduced models with a point-like head mass.

To validate the multi-body simulation by seismic recordings, we compare the PSD spectra of both methods (simulation and real seismic data) for similar wind velocities (Fig. 7.5). To achieve a clear illustration we normalized the spectra to each maximum. The results of the multi-body simulation are in good agreement with the observed seismic recordings. Effects described before, such as the BPF and its multiples or the interaction between the rotational motion and eigenfrequencies, are also visible in the numerical model. However, several frequency peaks in the simulation as well as in seismic recordings cannot be explained yet and must be part of further investigations.

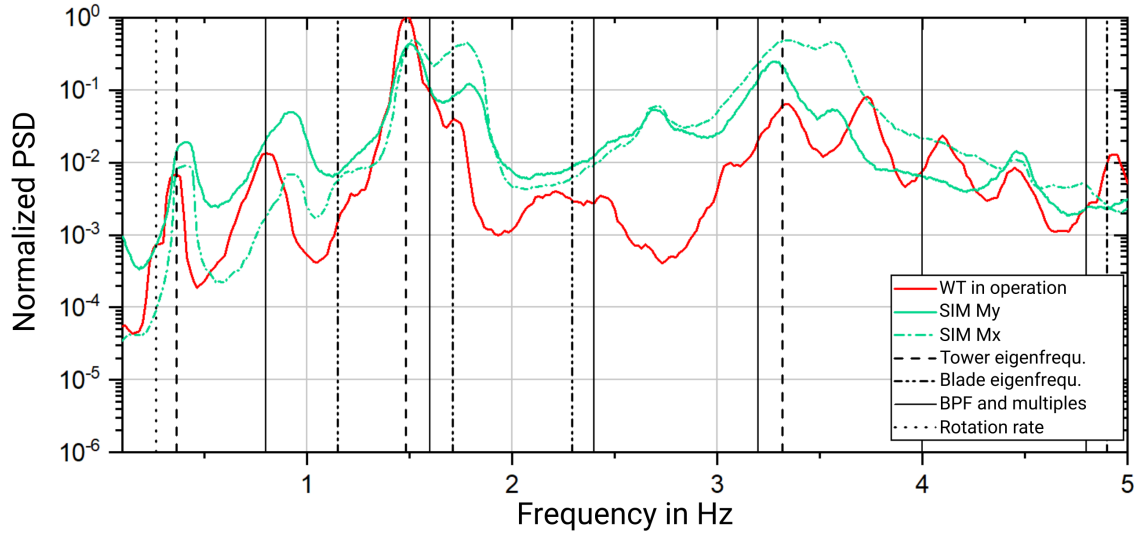

Figure 7.5: Comparison of the normalized power density spectra of the rotating WT (red) with the multi-body simulation (UST-IFB, green). SIM My constitutes simulated oscillations in wind direction, SIM Mx perpendicular to wind direction.

To conclude, the validation of numerical simulations with seismic recordings at the foundation of WTs is generally possible and improves the understanding of the oscillating characteristics of WTs.

7.3 Attenuation of induced seismic signals from a single WT and from a wind farm with respect to their geological subsurface

To analyze the wave attenuation characteristics for the region of interest regarding the induced seismic signals of a single WT, we deployed ten seismic broadband stations as a profile with a total length of 1.8 km as described in section 7.1.1. The goal of this measurement is on the one hand to determine the behavior of the WT-induced signals with distance and, on the other hand, to detect the strength of the peak ground velocity of these induced signals during several different wind conditions at residencies next to the WT. The measurement period of three weeks in August does not provide many time windows containing high wind speeds, which is demonstrated by wind measurements of the University of Stuttgart (Stuttgart Wind Energy). However, during a time interval in the night of 30 August 2018 there were high wind speeds in combination with a stable and high rotation rate of the WT (as shown in Appendix A, Fig. A.1). We select the time window used in section 7.2 with a length of 10 min to calculate the PSD spectrum for each seismic station, using the approach described in section 2.2.1. The spectra, shown in Fig. 7.6, has clear discrete PSD peaks, especially below 10 Hz, where the PSD values decrease with increasing distance (from blue to green). We already allocated these PSD peaks to the BPF of the WT and its multiples, which correspond well to the assumed rotation rate during the observed time interval ($\sim$ 0.8 Hz, small discrepancies of the PSD values to the BPF and its multiples can be explained by averaging over the time window, containing small variations of the rotation rate). The main frequency peaks are located at 1.5 Hz, 3.3 Hz, 4.1 Hz, 4.9 Hz, 6.7 Hz and 7.4 Hz. By picking the local maxima of each spectrum for different narrow frequency bands and plotting them over the relative distance to the WT, we can determine a power-law decay of the PSD values proportional to $\frac{1}{r^b}$, with a frequency-dependent b value indicating the strength of attenuation for the respective frequency band (Fig. 7.7). We exclude the first two points for the fitting in order to neglect probable near-field effects.

Fig. 7.7a shows the attenuation proportional to $\frac{1}{r^{0.95}}$ for the frequency range between 1.44 Hz and 1.56 Hz. An

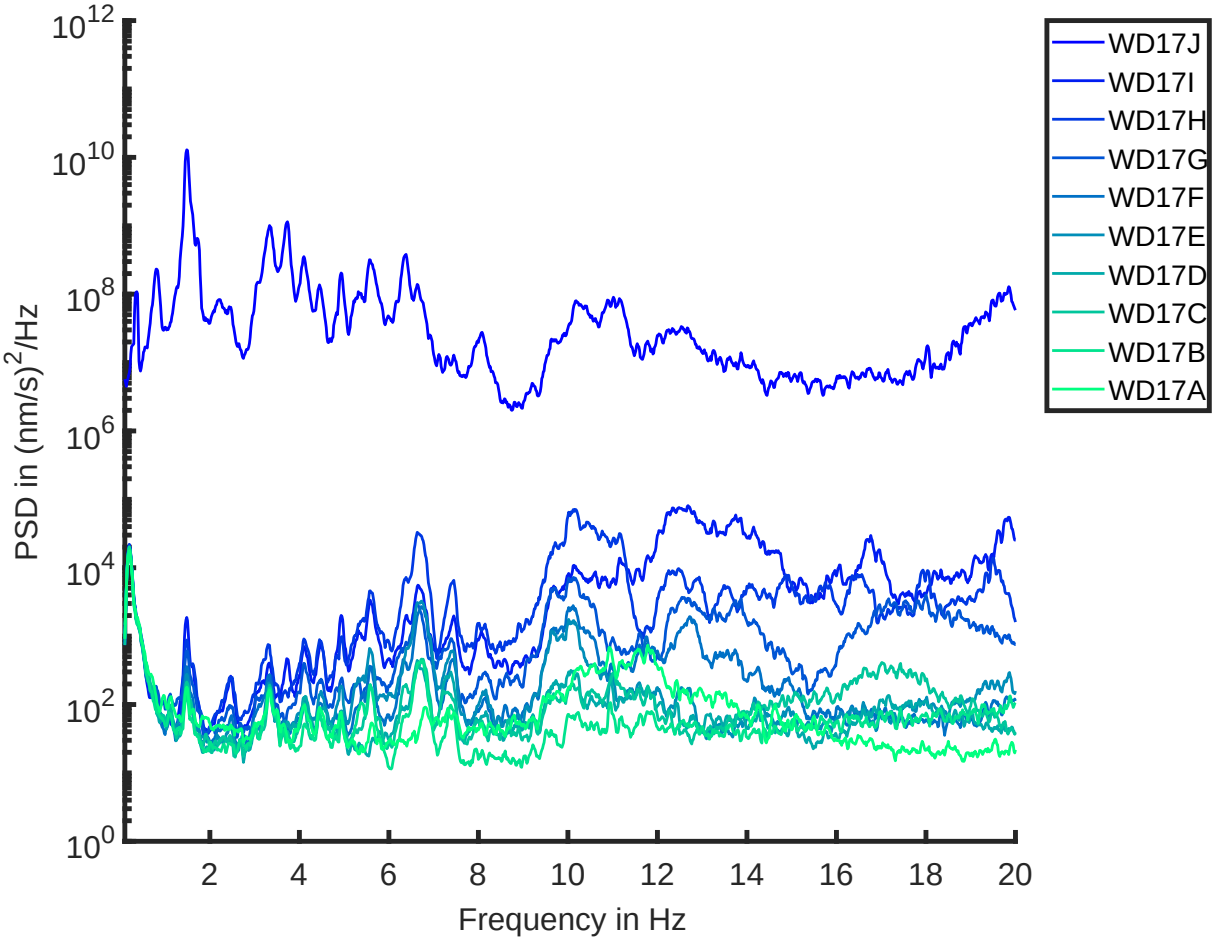

Figure 7.6: The PSD over the frequency range from 0.1 Hz to 20 Hz. The colors symbolize the distance (see also Fig. 7.7) of the corresponding seismic station to the WT: smaller distances are shown in blue, larger distances are shown in green.

almost similar attenuation behavior can be observed for the frequency band between 3.25 Hz and 3.45 Hz ($b = 1.01$, Fig. 7.7b). As already pointed out in chapter 6, section 6.3, a decay of the PSD values with $b \approx 1$ is equivalent to a seismic amplitude decay with $\frac{1}{\sqrt{r}}$, which corresponds to a cylindrical spreading loss of surface waves. Thus, we assume a major damping effect due to geometrical spreading rather than an influence of intrinsic attenuation and heterogeneities (scattering) in the subsurface for the amplitude decay of the emitted waves below 3.45 Hz. Moreover, the geological properties at both locations are nearly identical (layer of loess over limestone) and are therefore comparable.

Above a frequency of 4 Hz the influence of heterogeneities and anelasticity on the attenuation of WT-induced seismic signals increases, leading to a higher b value with increasing frequency. The PSD values decay for the frequency range between 4.05 Hz and 4.2 Hz proportional to $\frac{1}{r^{1.64}}$ and for the frequency range between 4.85 Hz and 5.1 Hz proportional to $\frac{1}{r^{2.15}}$. We observe the highest decay in the frequency range between 6.6 Hz to 6.9 Hz and 7.2 Hz to 7.6 Hz, with $\frac{1}{r^{3.76}}$ and $\frac{1}{r^{3.23}}$, respectively. A b value equivalent to 3, for example, would correspond to a reduction of the PSD values by a factor of 1000 in a distance of 1000 m to the WT, compared to the PSD values in 100 m distance. As mentioned before, the damping behavior is comparable to the results of chapter 6, where there are similar geological properties.

In contrast to the attenuation characteristics of a single WT on a layer of loess over limestone, we now determine the attenuation of WT-induced seismic signals of a wind farm, located on a soft surface (peat and sediments), as described in section 7.1.2. For the calculation of the attenuation behavior we use four seismic stations, located along a linear profile from the edge of the wind farm to the village ($\Delta x = 1.5$ km). The calculated PSD spectra

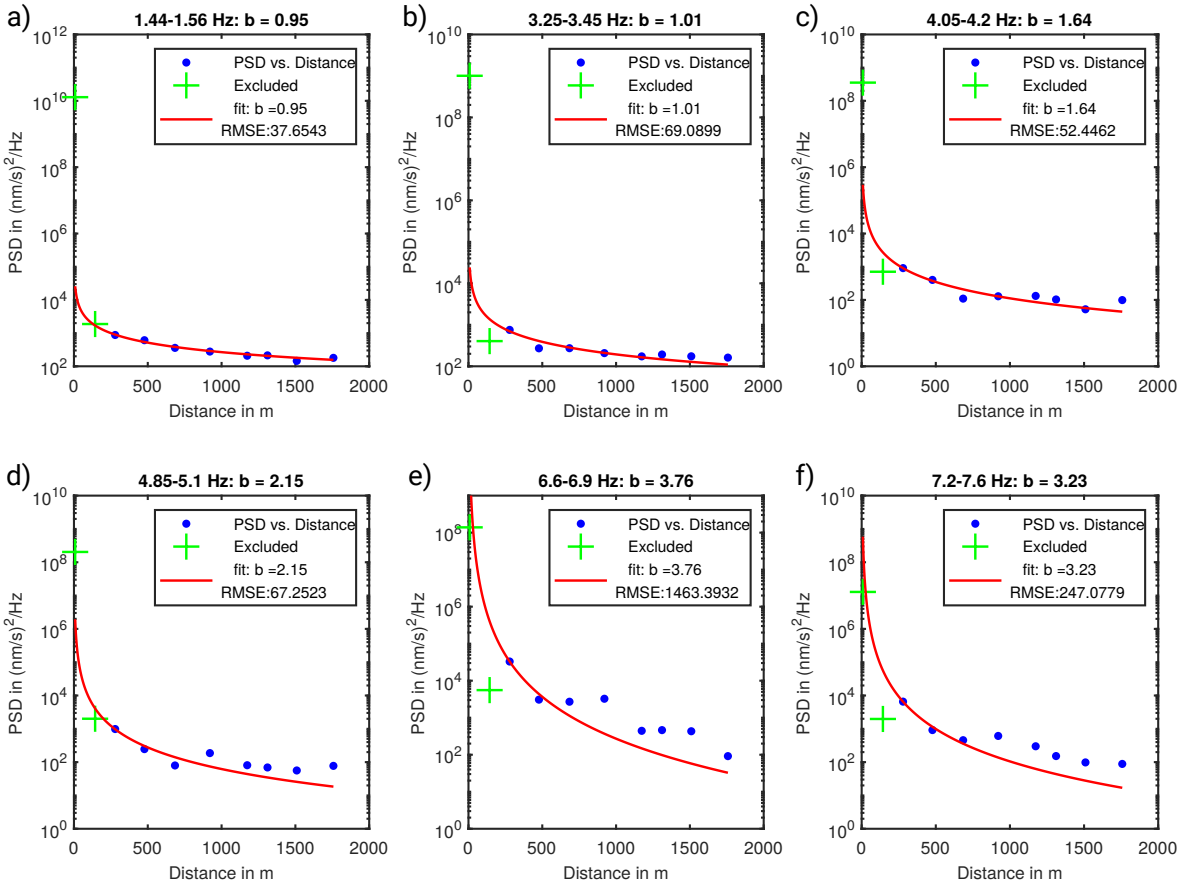

Figure 7.7: Attenuation relation for six different frequency bands. A power-law decay (red) proportional to $1/r^b$ was fitted to the seismic data (blue dots). The specific b value and the associated RMSE (root mean square error) value are shown in the legend. Error bars for the picked PSD values and the calculated distances to the WT are smaller than the blue dot symbols and are therefore not visible in the figure.

for a time interval of one hour are displayed in Fig. 7.8. In contrast to the PSD spectra for a single WT (Fig. 7.6), the spectra for the wind farm show hardly any clear discrete frequency peaks with decreasing PSD values for increasing distances. Two reasons can be considered:

- The geological properties differ significantly between the two locations. The dominant geology and the wind farm consists of much softer material (peat, sand, sediments) compared to the site of the single WT.
- The rotation rate of each WT inside the wind farm can slightly vary, dependent on the specific location. The so-called *wake effect*, where the wind speed is reduced behind a WT, leads to a change of the wind speed inside the wind farm. The reduced wind speed affects the WTs (or rather their rotation rate) located downstream. The slightly different rotation rates of the WTs will lead to a broadening of the PSD peaks over the frequency, measured outside of the wind farm.

As a consequence, we are able to determine the attenuation factor b just for two different frequency bands, which we can allocate to the wind farm. Both fits are shown in Fig. 7.9. We observe a decay of the PSD values proportional to $\frac{1}{r^{1.61}}$ for the frequency range between 0.8 Hz and 1 Hz (Fig. 7.9a). An almost identical b value can be observed for the frequency range between 1.5 Hz and 1.7 Hz (b = 1.78, Fig. 7.9b). Due to the geological properties, the influence of intrinsic attenuation due to anelastic material or scattering attenuation in the subsurface can be increased even for lower frequencies (< 2 Hz). Since the seismic wave length λ within this frequency range is much larger than potential heterogeneities inside the peaty subsurface, the influence of intrinsic attenuation should

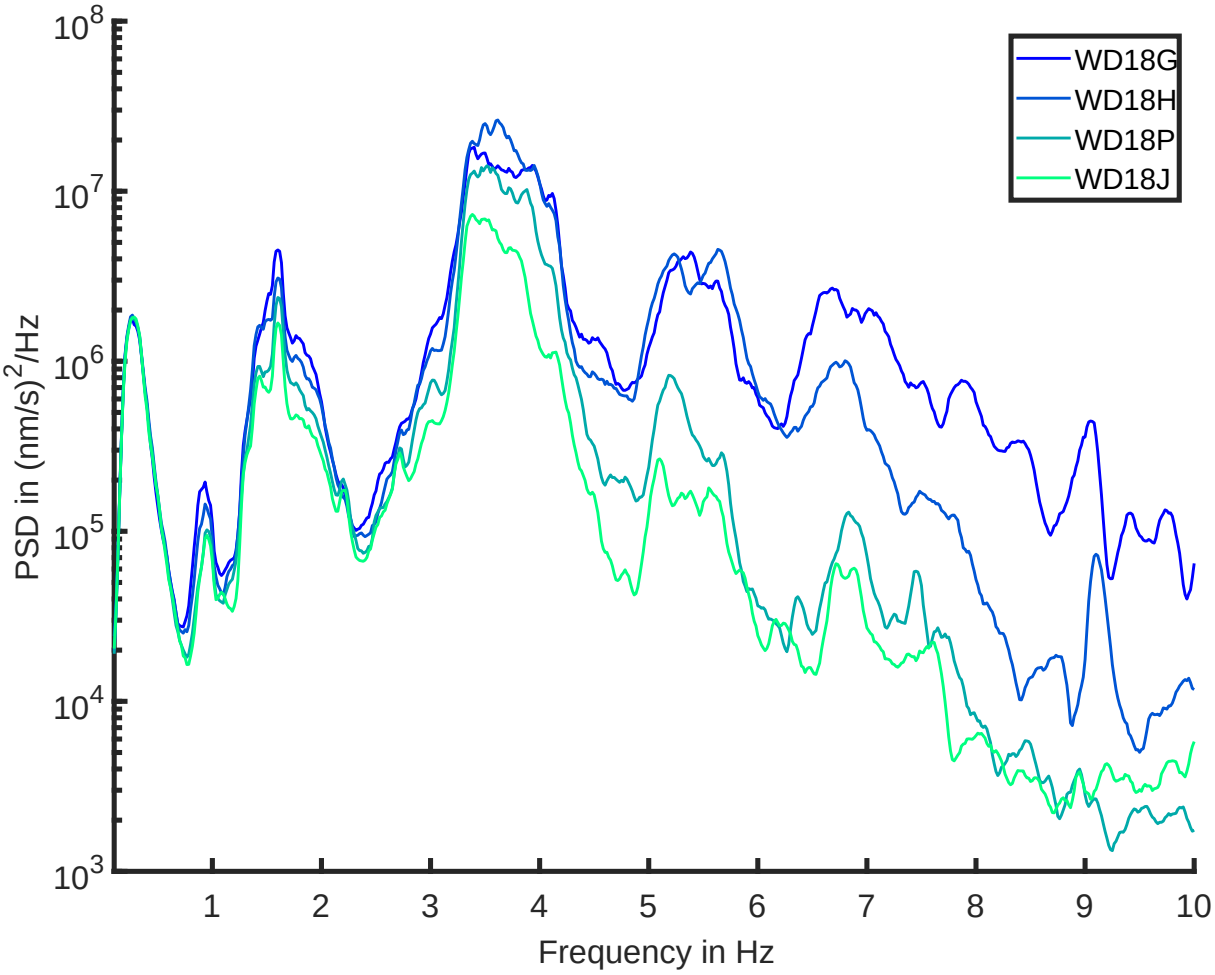

Figure 7.8: The PSD over the frequency range from 0.1 Hz to 10 Hz. The colors symbolize the distance (see also Fig. 7.9) of the corresponding seismic station to the specific WT along the profile in Fig. 7.2.

dominate the wave damping along the profile. Higher frequencies ($>$ 3 Hz) show a higher overall seismic noise level, but clear discrete PSD peaks for an attenuation calculation are not visible in the PSD spectra.

7.4 Start-up experiment of a wind farm

A step by step start-up of a wind farm with a time interval of 20 min for the different WTs was conducted during the measurement campaign described in section 7.1.2. The numbering of the WTs in Fig. 7.2 corresponds to the step-wise order of activation. Fig. 7.10 shows the spectrogram of the vertical ground velocity of the seismic station WD18J near the village during the start-up experiment. Black vertical lines represent the respective time after the commissioning of a new WT, whereby the first line indicates the time of complete deactivation of the whole wind farm. This deactivation is also clearly visible in the spectrogram as an immediate decrease of the PSD values, especially in the lower frequency range from 0.1 Hz to 10 Hz. Moreover, several discrete spectral lines disappear in the absence of a rotational motion of WTs inside the wind farm. This phenomenon was already observed for a single WT of the same type, as described in section 7.2. The wind speed was relatively stable during the period of interest. With increasing number of operating WTs, also the intensity of the PSD of the vertical ground velocity increases at the seismic station WD18J, in addition with the appearance of new spectral lines in the frequency range up to 10 Hz. The appearance and the exact frequency values of the mentioned spectral lines can be illustrated by calculating the PSD spectra for each time interval after the start-up of a new WT, shown

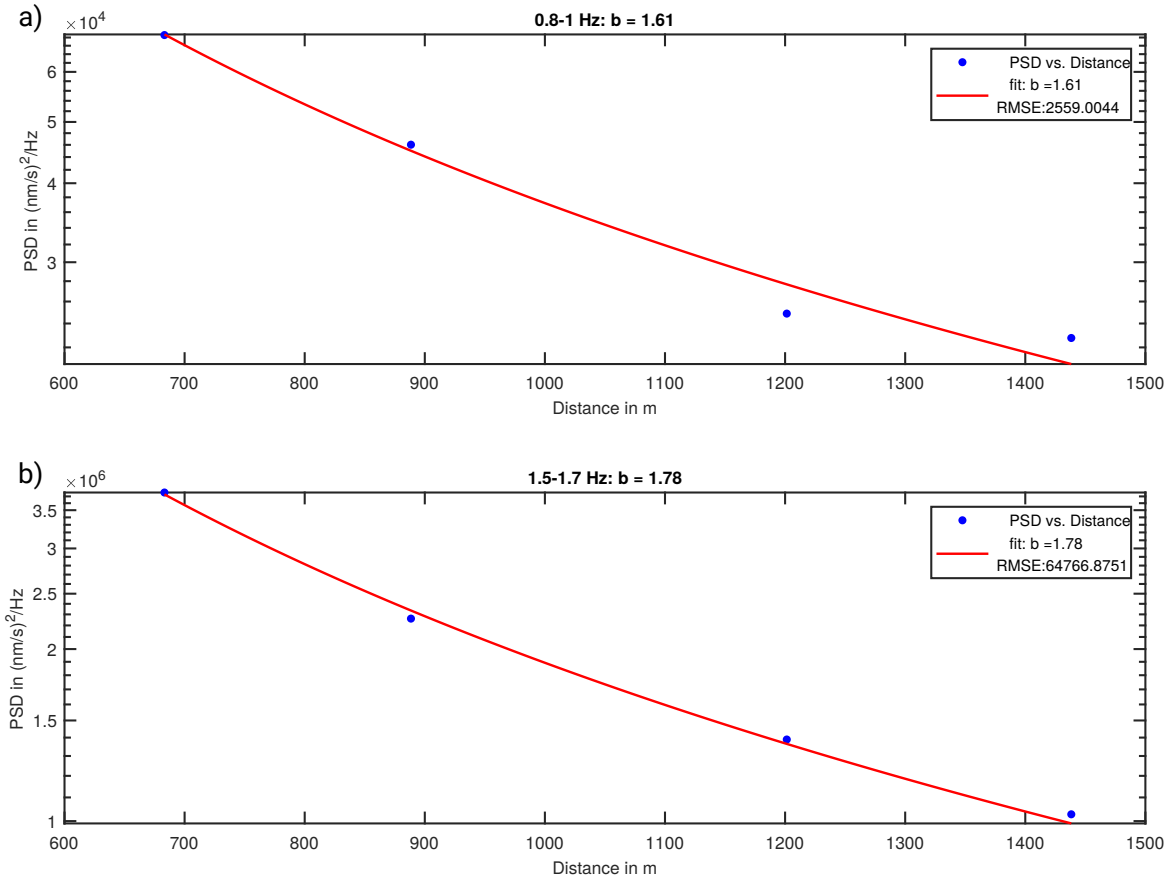

Figure 7.9: Attenuation relation for two different frequency bands. A power-law decay (red) proportional to $1/r^b$ was fitted to the PSD values (blue dots). The specific b value and the associated RMSE (root mean square error) value are shown in the legend. Error bars for the picked PSD values and the calculated distances to the WT are smaller than the blue dot symbols and are therefore not visible in the figure.

in Fig. 7.11. The colors represent the number of operating WTs (from blue to green). In contrast to previous PSD spectra in this work, where we have shown a semi-logarithmic plot, we now choose linear axes for a clearer visualization of the increase of the PSD values. It is important to mention that these spectra are not independent of the distance to the seismic station. A launch of a WT near a recording station WD18J has obviously a larger impact on the calculated PSD spectrum than more distant WTs. With a minimum wavelength of around 100 m (based on a surface wave velocity of ca. 500 m/s) for the frequency range below 5 Hz, the wind farm cannot be assumed as a point source, as the distance from the seismic station WD18J to the center of the wind farm is 2 km. This should be kept in mind for predictions of the seismic noise level of wind farms at other locations. As the aim of this measurement was the identification of the impact of WT-induced signals at the nearby village, we will not eliminate the distance dependency for further calculations. However, a clear increase of the noise level for several narrow frequency ranges (1.35-1.65 Hz, 3.15-3.45 Hz, 3.65-3.95 Hz and 3.95-4.25 Hz) can be observed in the PSD spectra with the start-up of new WTs. The PSD values for the frequency around 3.3 Hz, for example, increases by a factor of 100 from zero operating WTs to nine operating WTs.

To validate the increase of the PSD values at the recording station WD18J for different frequency ranges, we fit a power-law proportional to n^b (red line, Fig. 7.12) to the picked maxima in the PSD spectra (blue dots, Fig. 7.12) for varying number of operating WTs. Schofield (2001) suggests that the seismic signals from multiple WTs sum in quadrature. He finds a final model for the seismic amplitude at the Laser Interferometer Gravitational-Wave

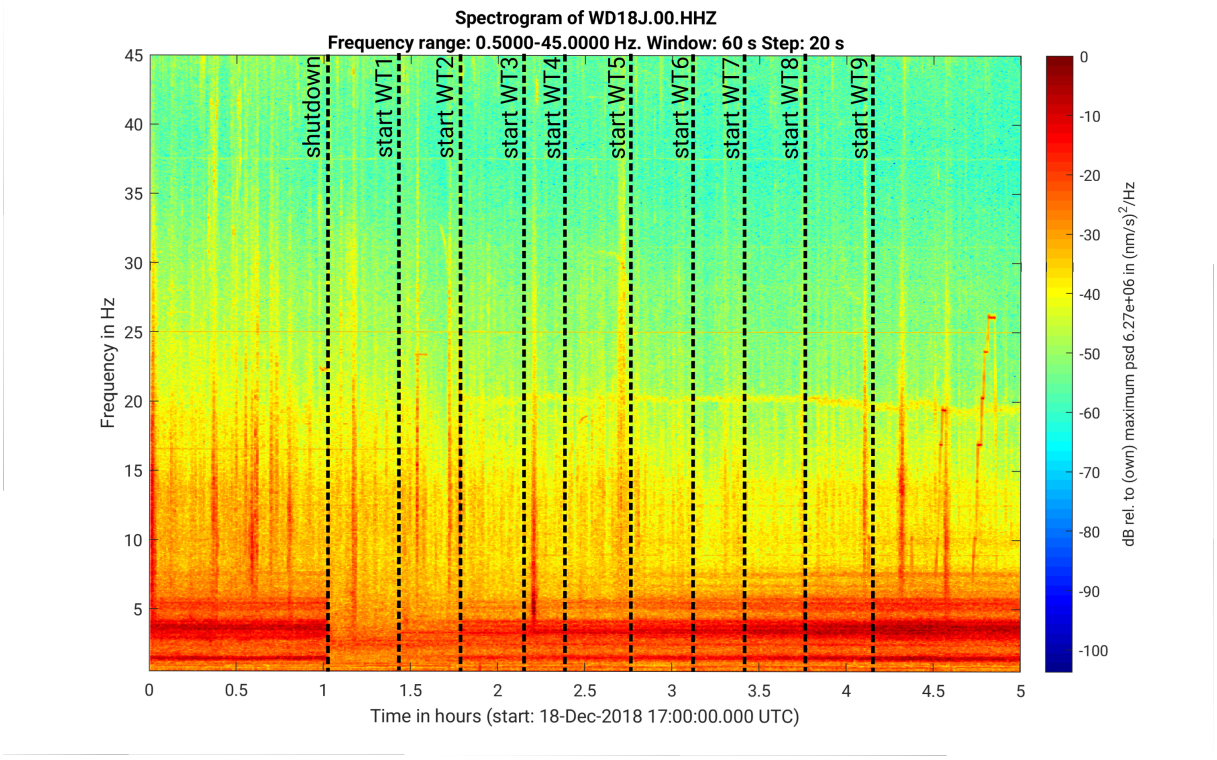

Figure 7.10: Spectrogram of the seismic station "WD18J" during the gradual start-up of the wind farm (see Fig. 7.2). The recording station is located close to the village. The vertical lines correspond to the switch-on times of each WT, whereby the first line represents the switch off time of the whole wind farm.

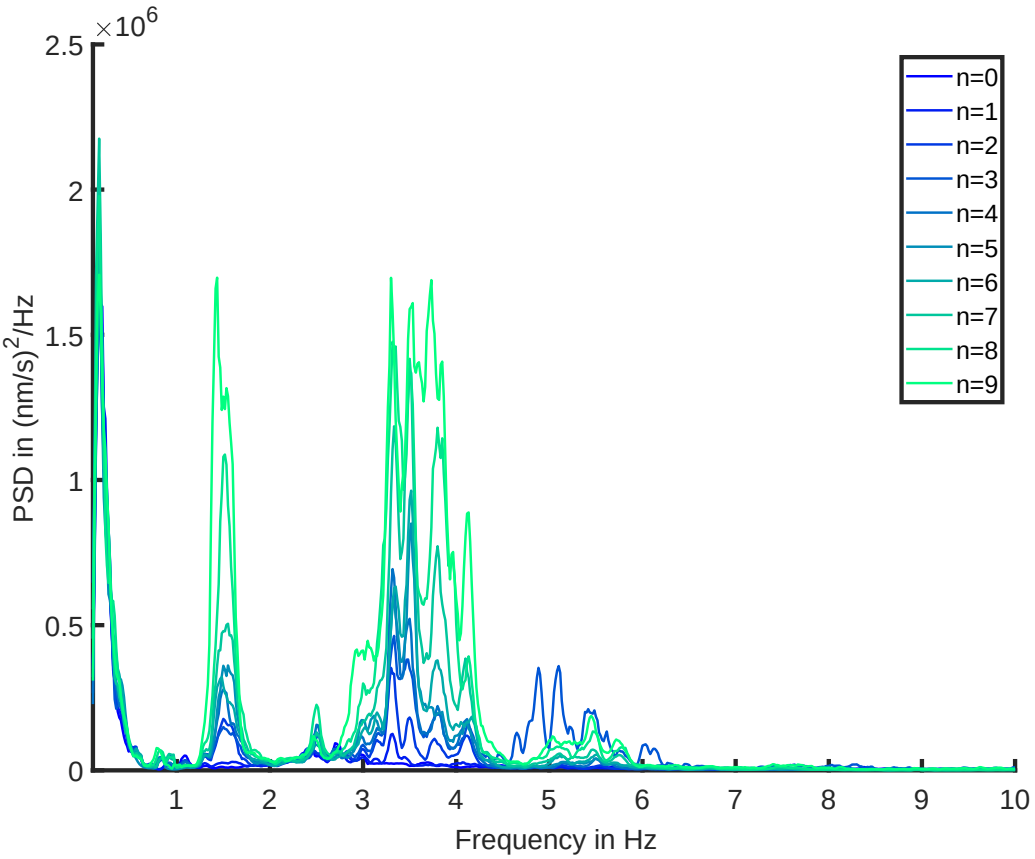

Figure 7.11: The PSD spectra of each time interval after the start-up of a new WT. The colors correspond to the number of running WTs (from blue to green). A clear increase of the PSD can be observed with increasing number of running WTs.

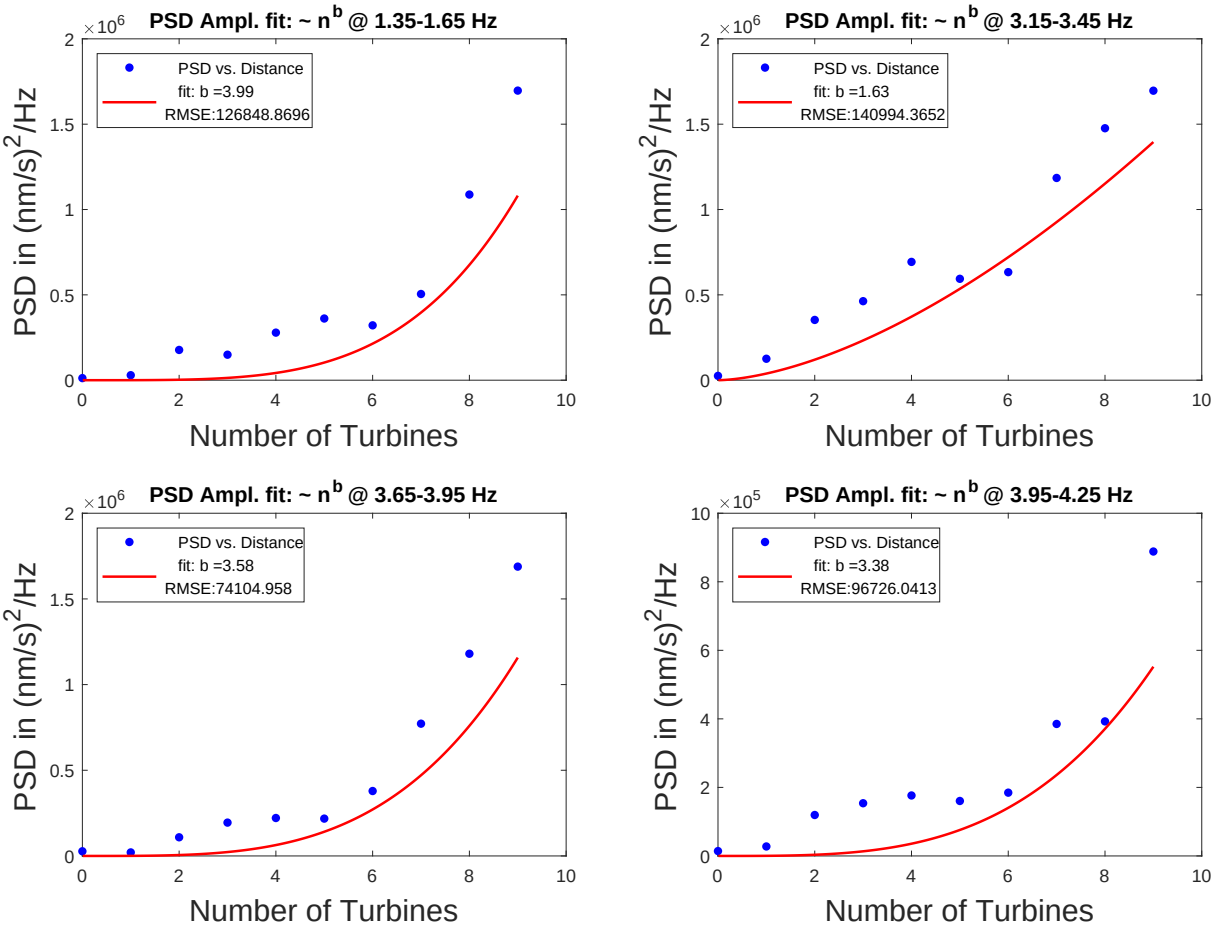

Figure 7.12: Increase of the PSD values at the seismic station WD18J for four different frequency bands during the start-up experiment at a wind farm. We fit a power-law proportional to n^b (red) to the picked PSD maxima in Fig. 7.11 (blue dots).

Observatory (LIGO) for a predominant frequency peak at 4.3 Hz after the start-up of a theoretical wind farm, dependent on the number of WTs on the proposed site (Maiden, USA):

$$A_{LIGO} = A_{1SL} \left(\frac{v}{15}\right)^{1.5} \sqrt{N_M} \sqrt{\frac{P_M}{P_{SL}}} \frac{r_1}{R_{ML}}, \tag{7.1}$$

where A_{LIGO} is the predicted seismic amplitude at LIGO by the Maiden wind farm, A_{1SL} is the amplitude of one single WT at the Statline wind farm measured at 18 km distance (already exisiting), v is the wind speed in m/s, N_M corresponds to the proposed number of WTs at Maiden, P_M is the power rating of the WTs at Maiden, P_{SL} is the power rating of the WTs at Stateline, r_1 is the distance to the WT producing the A_{1SL} signal and R_{ML} is the distance from Maiden to LIGO.

The model (7.1) takes into consideration the differences in power rating of various WT types, which leads to a high degree of uncertainty for the estimation of the seismic amplitude besides uncertainties due to geographic differences between both sites. However, the estimated increase of the seismic amplitude at LIGO is proportional to the square root of the number of WTs ($\sqrt{N_M}$) proposed for the Maiden wind farm. This is equivalent to an increase proportional to n for the PSD values (due to the squaring of the seismic amplitudes during the PSD calculation). In this case, we can detect a much higher increase of the noise level (PSD) with the number of WTs. As mentioned before, the way of increase highly depends on the distance from the starting WT to the measuring point, which is why a simple power-law fit proportional to n^b mostly fails for the seismic station WD18J. Also a simple distance reduction is not possible since the unknown interference effect between the WTs can not be eliminated from the

seismic recordings. This interference effect can be evaluated by shutting down the WTs in the same order in which they were started, starting with WT1. This step by step shutdown of the wind farm, however, was not done in this case and should be subject of future studies. The WTs in the model by Schofield (2001) were assumed to be a point-like source at a constant distance of 20 km. This assumption clearly differs in our experiment, where an assumption of a point-like source is not valid as the distance from the center to the seismic station is about 2 km. There are examples of other seismic stations (e.g. WD18D, see Appendix B) in the center of the wind farm where the influence of the distance is reduced. Here the increase of the PSD values with an increase of operating WTs shows a more linear trend, which better fits to the model by Schofield (2001). Nevertheless, possible interference effects due to concordant rotation rates of the WTs or eigenfrequencies can lead to a higher increase of the PSD values with the number of WTs than estimated by the model of Schofield (2001).

8 Attenuation models of WT-induced seismic signals for different geological settings

This chapter provides a summary of all results found in the scope of this study with regard to the attenuation of WT-induced signals. To illustrate these results, I compare all geological sites, independent of the type or the number of WTs, with regard to their specific amplitude damping of emitted seismic waves for different narrow frequency bands. The goal of this comparison is to determine possible differences in the propagation behavior of WT-induced signals dependent on the geological properties and, thus, create a basis for future prediction models.

8.1 Geological sites

The dampening effect of seismic signals emitted by WTs, which have been described in the last chapters, shows a clear dependency on the local geology. As the goal is to predict the increase of the seismic noise level of sensitive measurements, like seismometers, with the construction of new WTs in the future, a knowledge of the mentioned damping behavior for specific local geological conditions is essential. In the following I would like to give a short overview of the main geological properties in combination with the associated *b* values, analyzed in the framework of this study.

8.1.1 Unconsolidated sediments

The main near-surface geological setting around the town of Landau is a thick layer of poorly unconsolidated sediments (Cenozoic sediments) in the Upper Rhine Graben, Germany. We used ten seismic broadband stations, deployed as a profile with a total length of more than 3 km, and calculated the PSD spectra during three hours for each station. We determined the following *b* values with regard to the observed frequency peak allocated to WTs in the vicinity of the stations (details about the exact calculation or uncertainties can be found in chapter 3):

1.8 Hz: $b = 0.78$

3.7 Hz: $b = 0.77$

4.6 Hz: $b = 0.85$

5.5 Hz: $b = 1.59$

8.1.2 Loess over limestone

Profile measurements were conducted at two different locations, both consisting of a layer of loess over limestone. The profiles had a total length of 1.5 km (chapter 6) and 1.8 km (chapter 7), respectively. The allocated frequency peaks of the induced signals slightly differ in value due to various WT-types at both locations with different rotation rates. In order to combine the results of the profile measurements, we averaged the *b* values for both locations in narrow frequency bands. The following averaged *b* values were determined for limestone as the main local geology (details about the exact calculation or uncertainties can be found in chapter 6 and 7):

1 – 2 Hz: $b = 0.92$

2 – 4 Hz: $b = 1.1$

4 – 6 Hz: $b = 1.85$

$>$ 6 Hz: $b = 3.5$

8.1.3 Peat and sand

To determine the attenuation behavior for peaty and sandy subsurface conditions, we deployed 15 seismic broadband stations near a wind farm on a layer of phragmites peat (Riedtorf) and sapric peat (Bruchtorf), as well as fine- and middle-grained sands. We used four stations for the determination of the b values for different frequency bands, with a maximum distance of 1.5 km to the edge of the wind farm. Due to slight variations of the rotation rate of the WTs and with that an absence of clear frequency peaks in the PSD spectra, a calculation of the b value for many different frequency ranges failed. However, we determined the following b values for two frequency peaks allocated to the wind farm with regard to the local geology (details about the exact calculation or uncertainties can be found in chapter 7):

0.9 Hz: $b = 1.61$

1.5 Hz: $b = 1.78$

8.1.4 Granite

One goal of this study is to find any influence of WT-induced signals on seismic data recorded by the *STS-1* broadband seismometer of the Black Forest Observatory (BFO), SW Germany. The BFO is jointly operated by the Karlsruhe Institute of Technology (KIT) with the University of Stuttgart and provides one of the best data sets of seismic recordings worldwide. Due to the unique location inside an old mine and far off any anthropogenic impacts, the seismic stations of the BFO show a very low seismic noise level and are therefore particularly vulnerable to nearby seismic noise sources like WTs. To identify any influence of already existing WTs in about 9 km distance, we deployed ten seismic broadband stations along a profile from the WTs towards the BFO. Unfortunately, half of the seismic stations failed due to extremely cold temperatures below -20°C during the measurement period. We were able to use seismic recordings of four stations in combination with the recordings measured by the sensors at the BFO (see Fig. 8.1, colored triangles).

Two types of WTs are located near the town of Bad Rippoldsau-Schapbach, in ca. 9 km distance to the BFO: one *Enercon E-92* with a hub height of 139 m and a maximum power output of 2.35 MW and three

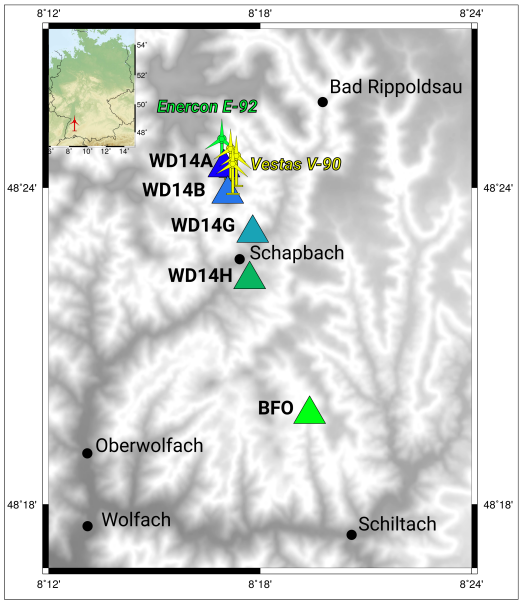

Figure 8.1: Map of the region of interest near to the BFO. Locations of the seismic stations during the profile measurement are marked as triangles. The color of the triangles corresponds to the calculated PSD spectra (Fig. 8.2). Yellow symbols indicate the location of the three *Vestas V-90* WTs, the green symbol shows the location of the *Enercon E-92* WT.

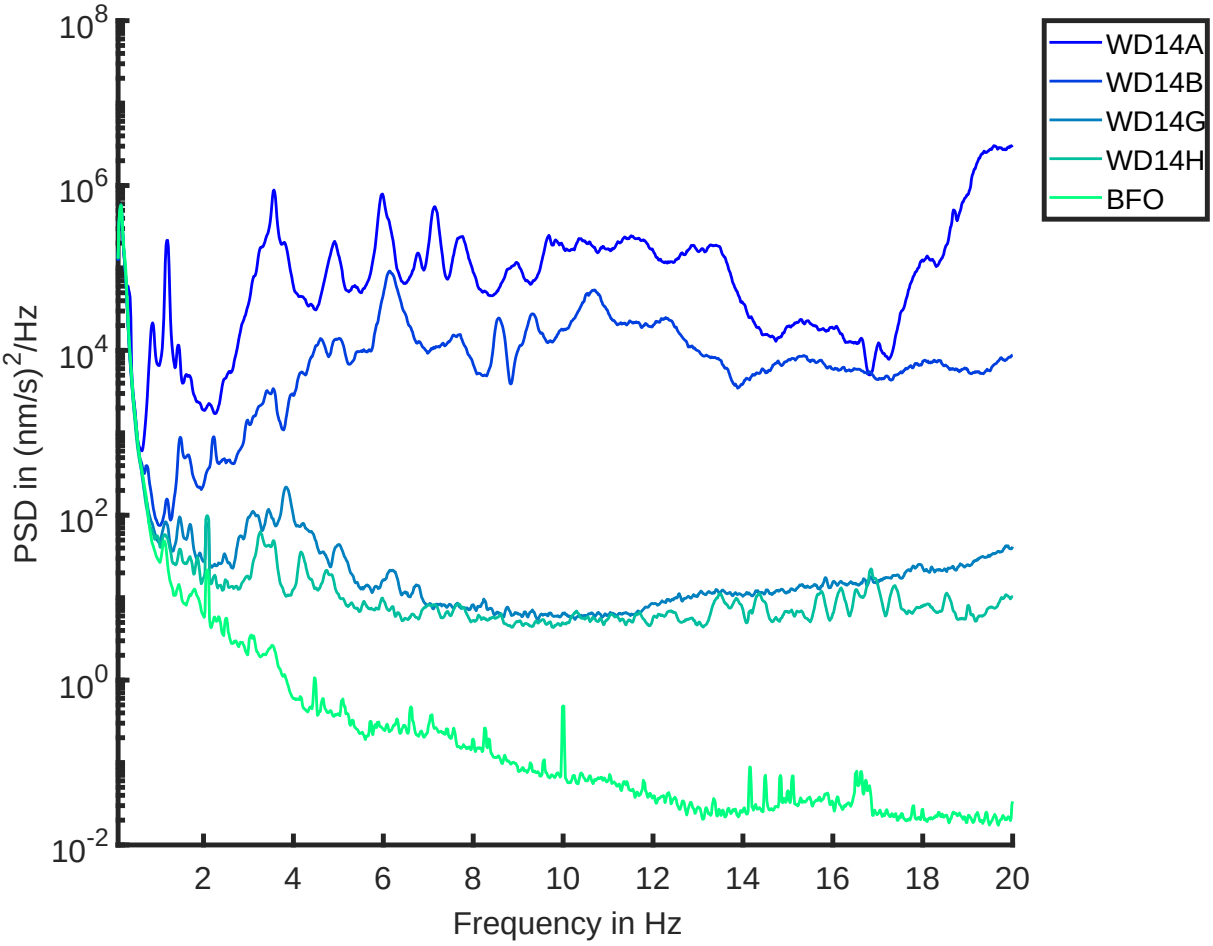

Figure 8.2: The PSD over the frequency range from 0.1 Hz to 20 Hz. The colors symbolize the distance of the corresponding seismic station to the WT: blue (smaller distances) to green (larger distances).

Vestas V-90 with a hub height of 105 m and a maximum power output of 2 MW. The seismic station WD14A is located in the vicinity of the Enercon WT ($\Delta x \approx 100$ m, see Fig. 8.1 as dark blue triangle). The profile continues in the direction of the three Vestas WTs (WD18B) and ends at the BFO. We calculated the PSD spectrum for each station in a time interval of two hours during night (Fig. 8.2) using the approach described in chapter 2, section 2.2.1. Discrete frequency peaks below 10 Hz, which were already observed in the scope of this thesis at other locations and allocated to nearby WTs, can be detected for the station WD18A and WD18B. However, the excited frequencies in the spectra differ due to the various types of WTs near the corresponding seismic station. Nevertheless, some of these frequencies (1.2 Hz, 1.5 Hz and 3.5 Hz) can be detected up to distances of 9 km (station BFO). Especially the frequency peak around 1.2 Hz is clearly visible in the PSD spectrum of station BFO and can now be allocated to the *Enercon E-92* WT, since this frequency peak shows a clear maximum in the PSD spectrum for station WD14A.

To analyze the behavior of these mentioned frequency peaks along the profile in terms of their attenuation along the propagation path, we picked the PSD maxima and plotted them over the distance (Fig. 8.3, blue dots) relative to the *Enercon E-92* WT. We again fitted a power-law decay proportional to $\frac{1}{r^b}$ to the PSD maxima (Fig. 8.3, red line) to determine the attenuation factor b:

1.2 Hz: $b = 0.57$

1.5 Hz: $b = 2.07$

3.5 Hz: $b = 3.12$

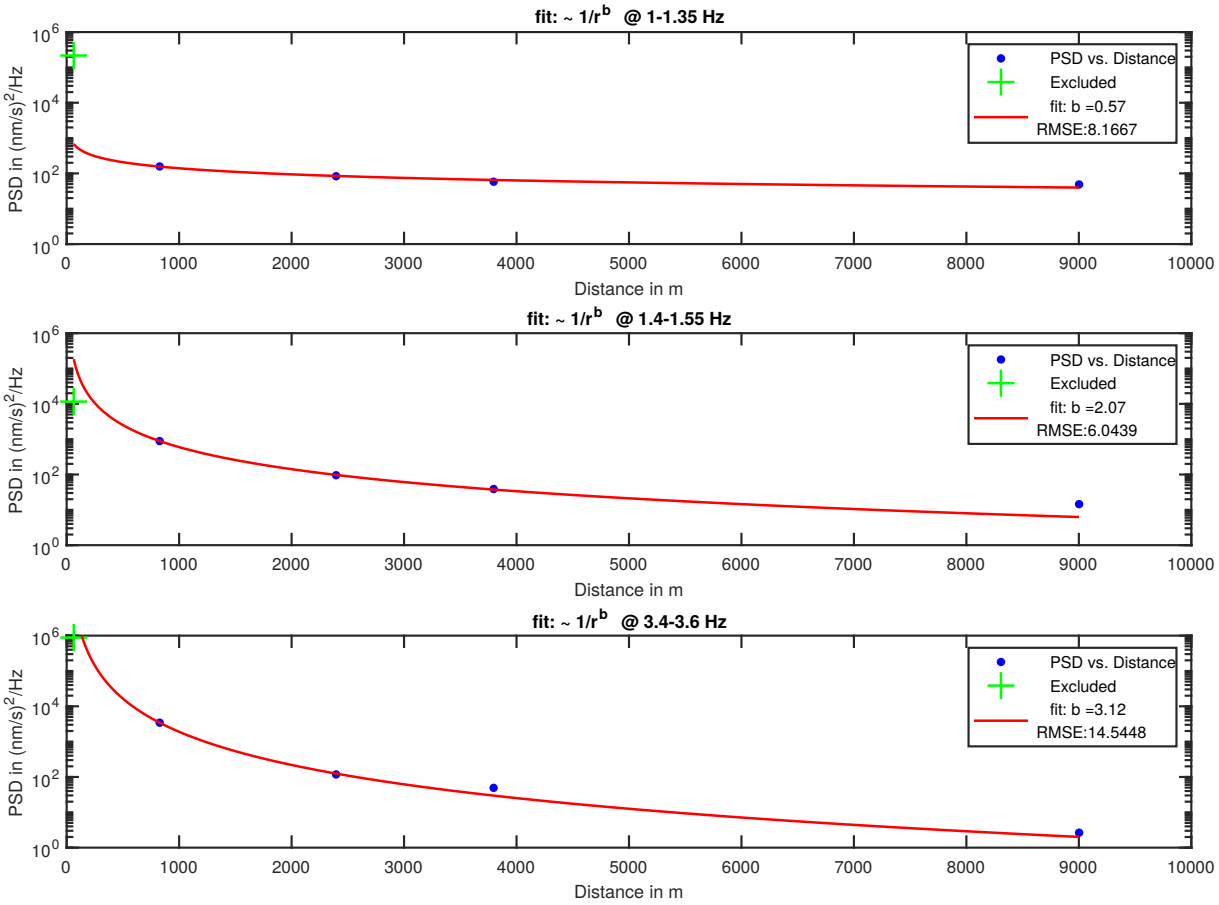

Figure 8.3: Attenuation relation for three different frequency bands. A power-law decay (red) proportional to $1/r^b$ was fitted to the PSD values (blue dots). The specific b value and the associated RMSE (root mean square error) value are shown in the legend. Error bars for the picked PSD values and the calculated distances to the WT are smaller than the blue dot symbols and are therefore not shown in the figure.

As mentioned before, the PSD peak at 1.2 Hz is clearly visible at all seismic stations and decreases in value with increasing distance, which points to the *Enercon E-92* WT as the seismic source of this peak. The peaks around 1.5 Hz and 3.5 Hz are difficult to identify at more distant stations and mentioned primarily for the sake of completeness. The subsurface consists of a mixture of sandstone, gneiss and granite, which is typical for the Black Forest region. As these properties are much harder compared to other examples presented in this study, we would expect a lower attenuation of induced seismic signals for this case since the energy loss is much smaller along the propagation path. This assumption is confirmed by the b value for the frequency peak at 1.2 Hz ($b = 0.57$). It is the first time that evidence for an influence of seismic recordings by nearby WTs was found at the BFO. These results are important for future negotiations about a protection radius around the BFO.

8.1.5 Energieberg

A more or less unique location for WTs is the so-called *Energieberg* (mountain for energy production) in the center of the city of Karlsruhe. The hill with a height of around 60 m is an old human waste disposal site with three WTs and a photovoltaic system on top. We conducted several seismic measurements with varying numbers of WTs to determine the influence of the subsurface on WT-induced seismic signals for this special case.

To analyze the damping behavior of this site, we deployed seven seismic stations along a profile from WT1 towards the west with a total length of nearly 900 m (see Fig. 8.4, WD20, blue triangles). WT1 has a hub height of 85 m and a maximum power output of 1.5 MW. An eighth seismic station was deployed in the vicinity of the eastern WT3 to detect any interference effects between both operating WTs (Fig. 8.4, WD20J). WT3 is an 80 m-high WT

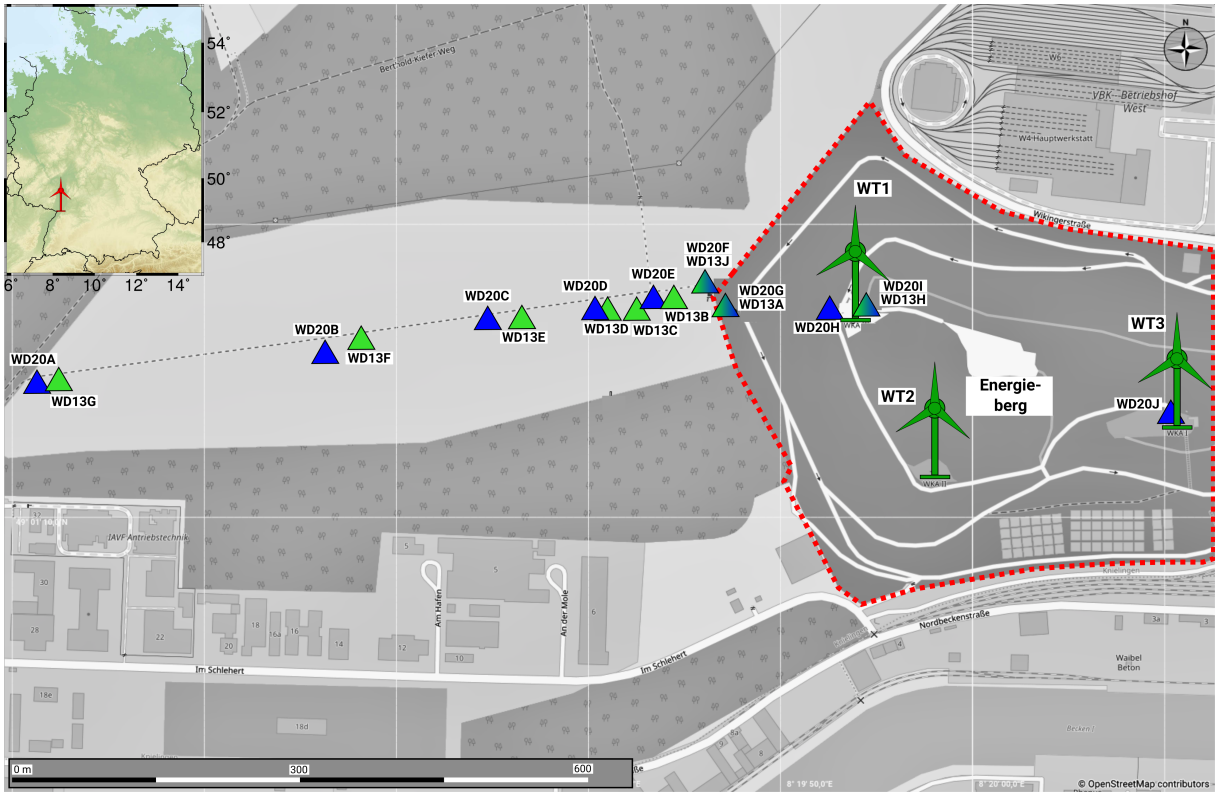

Figure 8.4: Map of the region of interest at the Energieberg in the center of Karlsruhe. Locations of the seismic stations during the profile measurement are marked as triangles. Green triangles correspond to the WD20 measurement campaign in 2019. Blue triangles correspond to the WD13 measurement campaign in 2018. The locations of the WTs are marked with green symbols. The area of the disposal site is highlighted with a red dashed line.

with a maximum power output of 2 MW. WT2 with a hub height of 74 m and a maximum power output of 0.75 MW was not in operation during the WD20 measurement campaign. Since WT3 has no impact on our attenuation calculation due to the absence of related signals at more distant stations, we neglect WD20J in the following. The PSD spectra for the remaining seismic stations were calculated for a time interval of four hours using the approach described in chapter 2, section 2.2.1. The wind speeds during this time interval range from 10 – 16 m/s, measured at 200 m height above ground level by the Institute of Meteorology and Climate Research, KIT. Clear discrete frequency peaks can be detected in the spectra and allocated to the WT for the first two stations (WD20I and WD20H), especially below 6 Hz, whereby the PSD values for station WD12H have become smaller compared to PSD values of station WD20I. The major PSD peak is located around 2.5 Hz. The station WD20G shows an increased overall seismic noise level but clear frequency peaks cannot be observed, except the peak around 2.5 Hz. This peak is visible at all seismic stations as the only clear peak with decreasing PSD value. Rather surprisingly, other induced seismic signals of the WTs are not visible farther away than 130 m. This is contrary to the previous results of this study, where several frequency peaks could be observed at distances of more than 9 km. This observation can be explained as a result of the complex properties of the subsurface. The *Energieberg* consists of highly unconsolidated material with a strong damping of seismic signals along the propagation path. Furthermore, an impedance contrast can be assumed at the bottom of the disposal site between the highly unconsolidated waste material and the natural sediments of the Upper Rhine Graben, similar to the situation described in chapter 6, section 6.3. This could lead to an abrupt decline of the seismic amplitudes along the profile due to transmission and reflection effects at the boundary. As a consequence, it is only feasible to calculate the attenuation factor b for the frequency peak around 2.5 Hz by picking the PSD maximum for each station and fitting a power-law decay

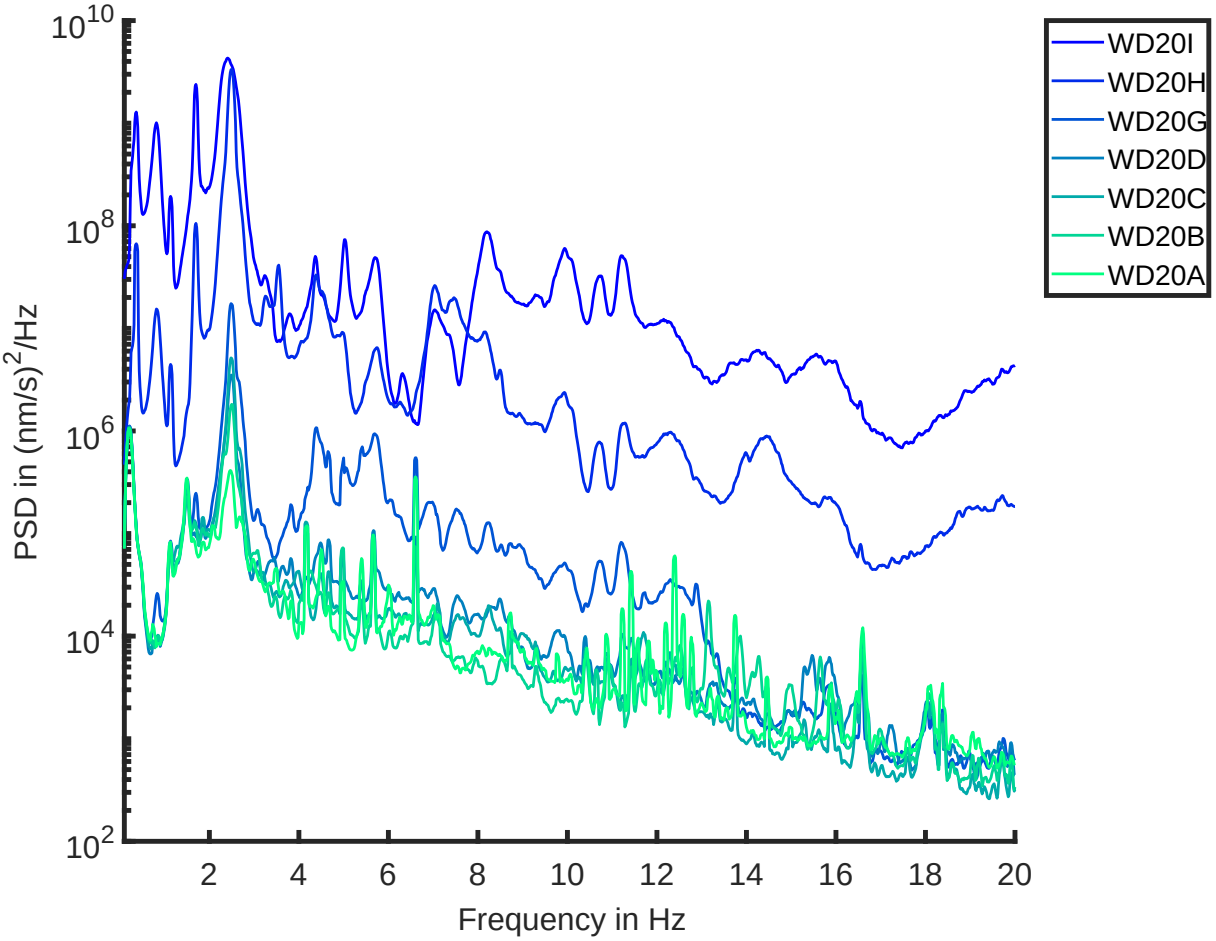

Figure 8.5: The PSD over the frequency range from 0.1 Hz to 20 Hz. The colors symbolize the distance of the corresponding seismic station to the WT: smaller distances (blue) to larger distances (green).

proportional to $\frac{1}{r^b}$ to the data. The first two data points for the fit were excluded to eliminate any near-field effects. The following b value was determined for the *Energieberg*:

2.5 Hz: $b = 1.61$

This example shows the large influence of the local subsurface on WT-induced seismic signals. Thus, it is necessary to develop prediction models for the propagation of induced seismic signals which strongly depend on the specific geological properties.

The setting on top of the Energieberg changed several times in the last few years in terms of the number and types of WTs on top of the mountain. To determine any interference effects due to various WT types, we conducted several seismic measurements with a similar setup. An example of such a measurement is shown in Fig. 8.4 (WD13, green triangles). Here WT3 has the status **before** the repowering process in 2019 and possesses a much smaller hub height (74 m) and power output (0.75 MW) compared to the new one. The PSD spectrum of this measurement campaign is shown in Appendix D. However, clear differences between both measurements cannot be observed in the PSD spectra.

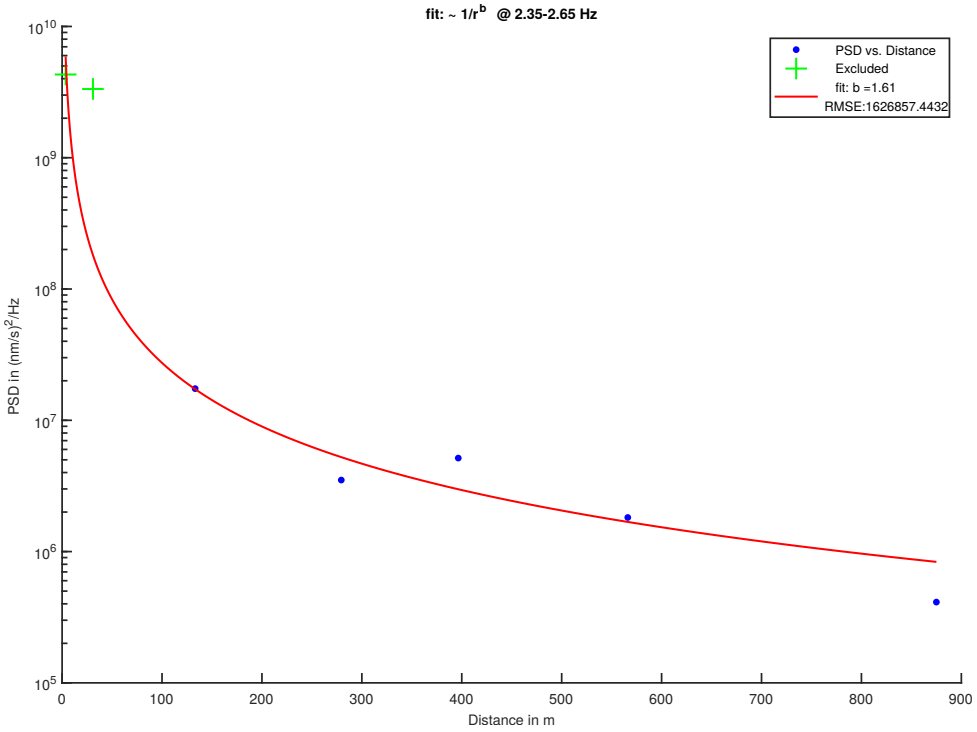

Figure 8.6: Attenuation relation for the frequency peak at 2.5 Hz. A power-law decay (red) proportional to $1/r^b$ was fitted to the seismic data (blue dots). The specific b value and the associated RMSE (root mean square error) value is shown in the legend. Error bars for the picked PSD values and the calculated distances to the WT are smaller than the blue dot symbols and are therefore not visible in the figure.

8.2 Propagation models of WT-induced seismic signals with regard to geological conditions

In this section I combine the specific attenuation factors for four narrow frequency bands (1-2 Hz, 2-4 Hz, 4-6 Hz and $>$ 6 Hz) to illustrate the impact of the subsurface on WT-induced signals. Fig. 8.7 shows the attenuation as a function of the frequency range and the geological properties. In case of more than one detected b value per frequency band and geological site the value corresponds to the mean. The lowest seismic wave damping occurs for hard rock like granite in the frequency range between 1 – 2 Hz (Fig. 8.7, black). Here the induced seismic waves travel faster through the medium than through softer material like sediments and, thus, the seismic amplitude decay remains low. For softer material such as unconsolidated sediments or limestone (Fig. 8.7 blue and green, respectively), b approaches the value of 1. As already pointed out in several chapters, a b value similar to 1 for the PSD decay can be associated with a major influence of geometrical spreading on the seismic amplitude decay ($1/\sqrt{b}$) of induced seismic surface waves. Also for sandy and peaty conditions (Fig. 8.7, blue) the b value corresponds to 1.15. With increasing frequency the observations of seismic signals which can be allocated to nearby WTs reduce at distant stations ($\Delta x > 1$ km). For the frequency range between 2 and 4 Hz the b value remains nearly unchanged for unconsolidated sediments ($b = 0.78$) and limestone ($b = 1.1$), compared to the frequency range described before. Only the attenuation for the *Energieberg* shows an increased b value of 1.61. The specific and unique setting for this case was already described in section 8.1.5. Two observations were made for the frequency range between 4 and 6 Hz for unconsolidated sediments ($b = 1.22$) and limestone ($b = 1.85$). Here the b value has risen significantly compared to lower frequency ranges. This could be explained by an increased impact of heterogeneities in the subsurface with increasing frequency, as the ratio of the size of heterogeneities to the seismic wavelength changes. These heterogeneities could lead to additional seismic scattering due to lateral variations along the propagation path and with that to a higher attenuation of the seismic waves. The influence of heterogeneities should increase with increasing frequency. Also, anelastic attenuation (conversion of seismic energy to heat) has an increasing

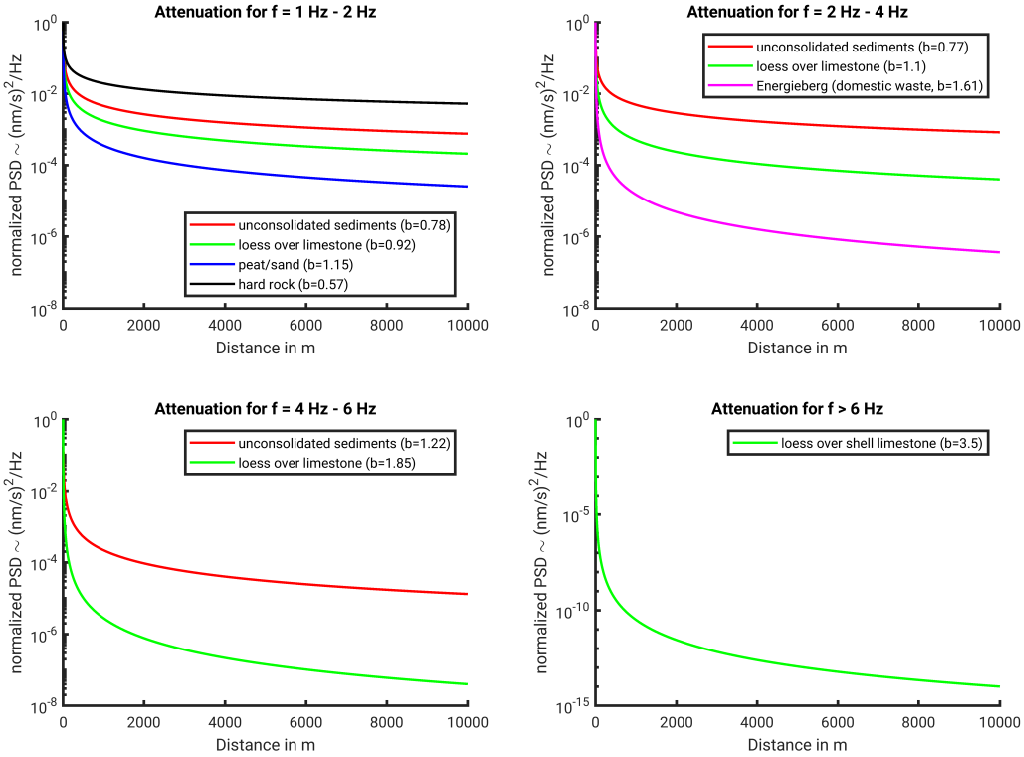

Figure 8.7: Averaged attenuation values b for four narrow frequency bands (1-2 Hz, 2-4 Hz, 4-6 Hz and $>$ 6 Hz). The color indicates the specific subsurface condition: red are unconsolidated sediments, green corresponds to a layer of loess over limestone, blue is equivalent to sandy and peaty conditions and black is the attenuation for hard geological conditions like granite.

influence on the amplitude decay for increasing frequencies.

Clear observations of WT-induced seismic signals for frequencies higher than 6 Hz are missing in our measurements, except for the measurement described in chapter 7, section 7.3 for a layer of loess over limestone (b = 3.5). Such high attenuation factors can be expected due to the reasons mentioned above, like scattering or anelastic attenuation.

These detected attenuation models can be used for further predictions of WT-induced signals to estimate the seismic amplitudes at different distances. However, as the source of these signals differs significantly due to various numbers or WT-types, a so-called *emission coefficient* with regard to those variables must be determined to predict the expected ground motions sufficiently for different wind speeds. This coefficient describes the strength of the WT-induced signals in the direct vicinity of the single or multiple WT's and represents a measure of the seismic source.

9 Discussion

In this chapter I discuss the results presented in the previous chapters within the framework of the research project *TremAc* and give recommendations with regard to monitoring concepts and setups for seismic measurements in the vicinity of WTs. Moreover, I evaluate the possible impact of WT-induced seismic signals on free-field locations near residents as a basis of further discussions about a protection radius with respect to seismic emissions of WTs.

9.1 Recommendations for seismic monitoring concepts near WTs

More than twenty seismic measurement campaigns were conducted in the scope of this study near WTs in order to identify relevant emitted seismic signals and their spectral content. Experiences of these measurements have led to a continuous learning process regarding the installation and operation of seismic broadband stations under WT-specific conditions. The most important aspects will be presented in the following in order to share experiences and to avoid mistakes in future studies:

Deployment of seismic broadband stations: To detect smallest ground motion amplitudes of WT-induced seismic signals, it is recommended to deploy the seismic stations very carefully in order to achieve a suitable data set, especially during time windows with high wind speeds. Within this study, the seismic sensors were buried about 50 cm below the surface using a mechanical hand drill, to minimize the direct impact of wind on the sensor and to improve the signal-to-noise ratio (SNR) of seismic recordings. This direct impact of wind was already analyzed by Lott et al. (2017) and cannot be neglected for our tasks, since the seismic measurements were conducted especially during windy time periods (usually during wintertime) when the corresponding WT (or wind farm) was in full operation. Two types of sensors were preferably used in the framework of this study: (i) *Trillium Compact Posthole* with a nominal eigenperiod of 20 s and (ii) *Trillium Compact* with a nominal eigenperiod of 120 s. I used *DATA-CUBE*^{3} as data logger with a sampling rate of 100 Hz in combination with a break-out-box (BOB) which divides the output voltage of the seismic sensors by a factor of ten. This BOB is necessary to connect the actively powered sensors to the CUBE and to adapt the correct signal voltage level. Neglecting the BOB would lead to a clipping of the seismic amplitudes. The specific instrumentation information is shown in Tab. 9.1. The power supply was a 12 V battery block with 12 Ah, sufficient for a measurement period of ten days. The measuring equipment was also buried in a plastic barrel above the seismic station in order to protect it from dirt and theft. A removable lid allows easy station servicing including battery replacement. The use of a GPS antenna was assured through a small hole inside the barrel. The deployment process of the seismic station is illustrated in Fig. 9.1.

Measurement period: I recommend a minimum time period of two weeks to observe several different weather conditions, especially wind speeds and directions. This recommendation clearly depends on the prevailing local conditions during the measurement. A longer time period is often difficult to achieve, since most measuring points are located on cultivated fields. Nevertheless, an extension of the measuring time period up to eight weeks should be considered.

Integrating WT operators: To distinguish between seismic signals induced by WTs and other seismic noise sources with similar frequency content in the vicinity of the seismic station, it is recommended to conduct so-called *shutdown* experiments where the WT stops to rotate for a specific time period. I recommend a

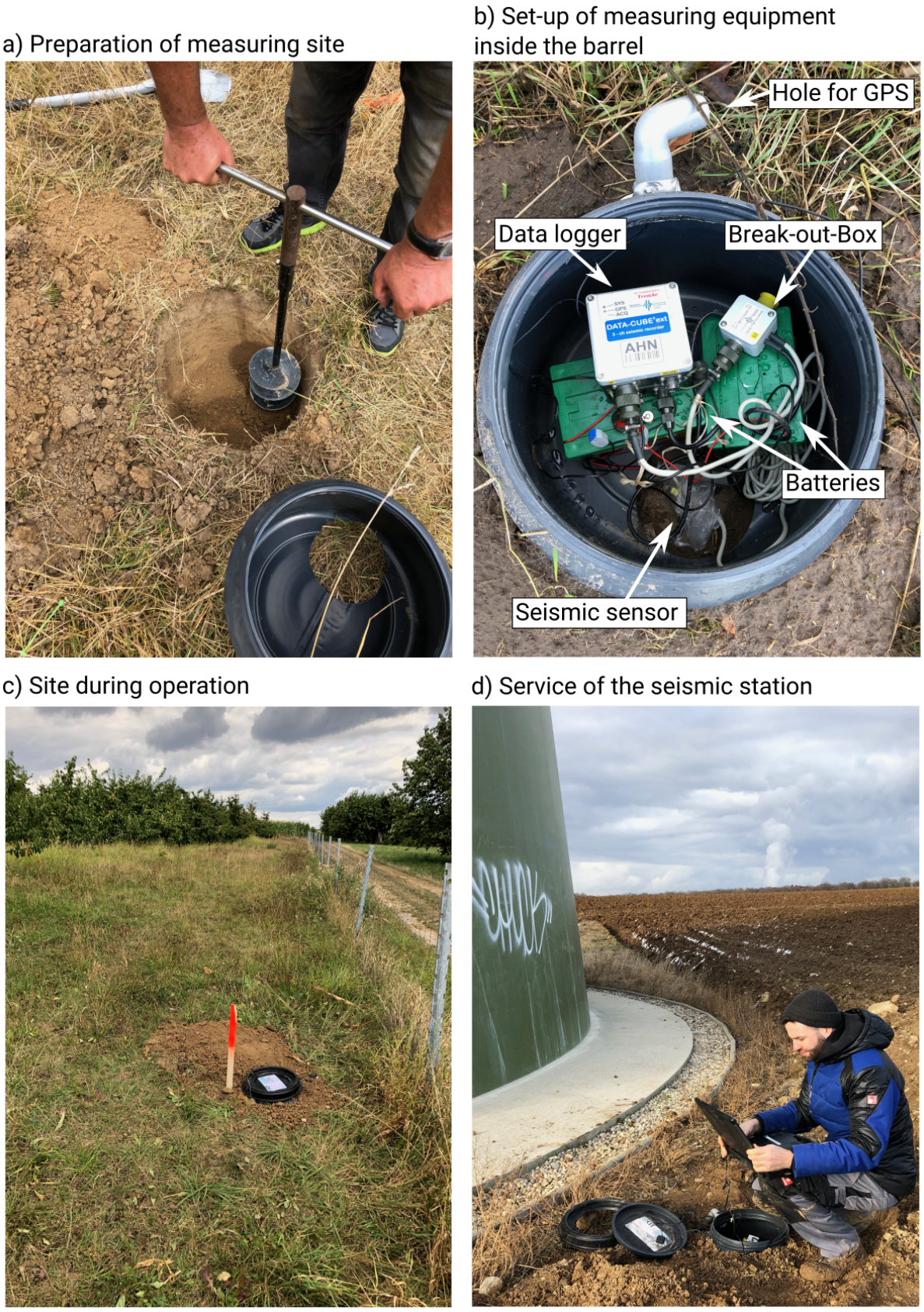

Figure 9.1: Deployment of seismic stations in the vicinity of WTs. The respective headline describes each deployment step.

Table 9.1: Properties of the used sensors (Trillium Compact Posthole and Trillium Compact) and data loggers (DATA-CUBE^3 incl. BOB).

Sensor	A/D conversion in counts/V	Sensitivity in V/(m/s) incl. BOB	Norm. factor	Poles	Zeros
Trillium Compact Posthole 20 s	4.0984E+06	75.31	4.344908E+17	-2.214E-01, 2.221E-01i -2.214E-01, -2.221E-01i -3.430E+02, 0.000E+00i -3.700E+02, 4.670E+02i -3.700E+02, -4.670E+02i -8.360E+02, 1.522E+03i -8.360E+02, -1.522E+03i -4.900E+03, 4.700E+03i -4.900E+03, -4.700E+03i -6.900E+03, 0.000E+00i -1.500E+04, 0.000E+00i	0 0 -3.920E+02, 0.000E+00i -1.960E+03, 0.000E+00i -1.490E+03, 1.740E+03i -1.490E+03, -1.740E+03i
Trillium Compact 120 s	4.0984E+06	75.43	4.344908E+17	-3.691E-02, 3.702E-02i -3.691E-02, -3.702E-02i -3.430E+02, 0.000E+00i -3.700E+02, 4.670E+02i -3.700E+02, -4.670E+02i -8.360E+02, 1.522E+03i -8.360E+02, -1.522E+03i -4.900E+03, 4.700E+03i -4.900E+03, -4.700E+03i -6.900E+03, 0.000E+00i -1.500E+04, 0.000E+00i	0 0 -3.920E+02, 0.000E+00i -1.960E+03, 0.000E+00i -1.490E+03, 1.740E+03i -1.490E+03, -1.740E+03i

shutdown of the WT for a duration of twenty minutes in a two hour interval. According to the available financial resources (such shutdown experiments are usually expensive) the shutdowns can be limited to nighttime when anthropogenic noise is usually low. Moreover, SCADA data provided by the operator should be available in one-minute resolution, at least, to classify seismic recordings in terms of wind speed, rotation rate or wind direction. The integration of potential WT-operators and landowners in the vicinity of the WT must be an essential part of the measurement preparation. Financial compensations should be considered during the application phase.

9.2 Averaging effect during PSD calculation

Fig. 3.3 in chapter 3 shows the PSD spectra of two seismic stations in the vicinity of a wind farm near the town of Landau, SW Germany. The color of each spectrum corresponds to defined rotation rate bins related to a specific WT inside the wind farm. Clear discrete frequency peaks can be observed in the PSD spectra, especially for high rotation rates (Fig. 3.3, green). By comparing WT-induced seismic signals with numerical simulations or optical measurements (e.g. chapter 5) we allocated those peaks to the BPF and its multiples interacting with eigenfrequencies of the tower-nacelle-system. As these peaks can be correlated with the rotation rate, one expect a slight shift of the PSD peaks to higher frequencies with increasing rotation rate. This expected shift, however, cannot be observed in the present case.

To understand why this shift of the PSD peaks is missing, we first need to understand the way of calculating of the PSD values. As reference for the rotation rate we use SCADA data of one WT within the wind farm with a ten-minute resolution, which is in fact the first time-related averaging process. Moreover, we average six rotation

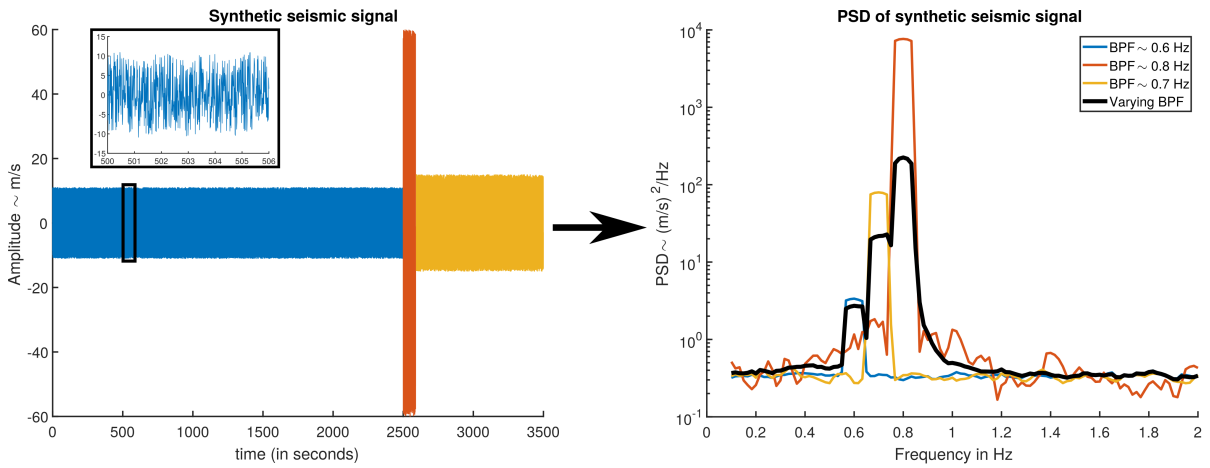

Figure 9.2: Left: Synthetic seismic signal illustrating three different rotation rates (blue $\sim$ 0.6 Hz, red $\sim$ 0.8 Hz, yellow $\sim$ 0.7 Hz). Right: Corresponding PSD spectrum for each specific rotation rate (blue, red and yellow) and the PSD spectrum for the overall signal with varying BPF (black).

rate values to obtain the overall rotation rate for a one-hour time window. As a consequence, a PSD spectrum for this time window (with possible variable rotation rates) is assigned to one averaged rotation rate value. This PSD spectrum also has been calculated by averaging multiple time segments using the method of Welch (1967). Finally, I average the PSD spectra using the mean (or the 75th percentile) of each rotation rate bin. Thus, Fig. 3.3 shows in fact the result of four different averaging processes.

I created a synthetic seismic signal assuming actual conditions to analyze the effects of averaging processes on seismic data (Fig. 9.2, left). This signal represents three different rotation rate conditions with various frequencies (according to the BPF) and amplitudes. Here I assume an increased amplitude of induced seismic signals with increasing frequency, based on real observations at different locations. As a next step I calculate the PSD spectrum of our synthetic seismic signal for each rotation condition and also for the overall signal (Fig. 9.2, right). The colors of the spectra correspond to the colors of the signal. Each individual spectrum shows a clear frequency peak for the main frequency of the corresponding signal (0.6 Hz, 0.8 Hz and 0.7 Hz). The PSD spectrum of the overall signal, however, shows all three peaks shown for each individual time window. Although the red signal with a main frequency of 0.8 Hz has the shortest duration, it dominates the overall PSD spectrum due to the highest signal amplitude compared to both remaining signals. Fig. 9.2 demonstrates that the PSD spectrum is mainly influenced by the amplitude of the seismic signal. This phenomenon can be directly transferred to the missing shift effect of the PSD values described in chapter 3. The different averaging processes are leading to a constructive summation of the frequency peak with the highest amplitude during the considered time window. As the highest amplitude mostly corresponds to the nominal BPF, where the WT operates at full capacity (0.9 Hz), this frequency dominates the averaged PSD spectrum over a long time period (here corresponding to one month). The difference in PSD values for each rotation rate bin is related to the occurrence of time segments with the nominal BPF. For example, the bin with the highest rotation (17 – 19 rpm, Fig. 3.3 green curve) consists of many time windows with the nominal rotation rate leading to the highest PSD value for the BPF and its multiples. As a consequence, I recommend the use of SCADA data at a one-minute resolution for the correlation with seismic recordings. Although this will not totally avoid the influence of averaging effects of WT-specific data on the PSD calculation, it will improve the accuracy of classification to different operating conditions.

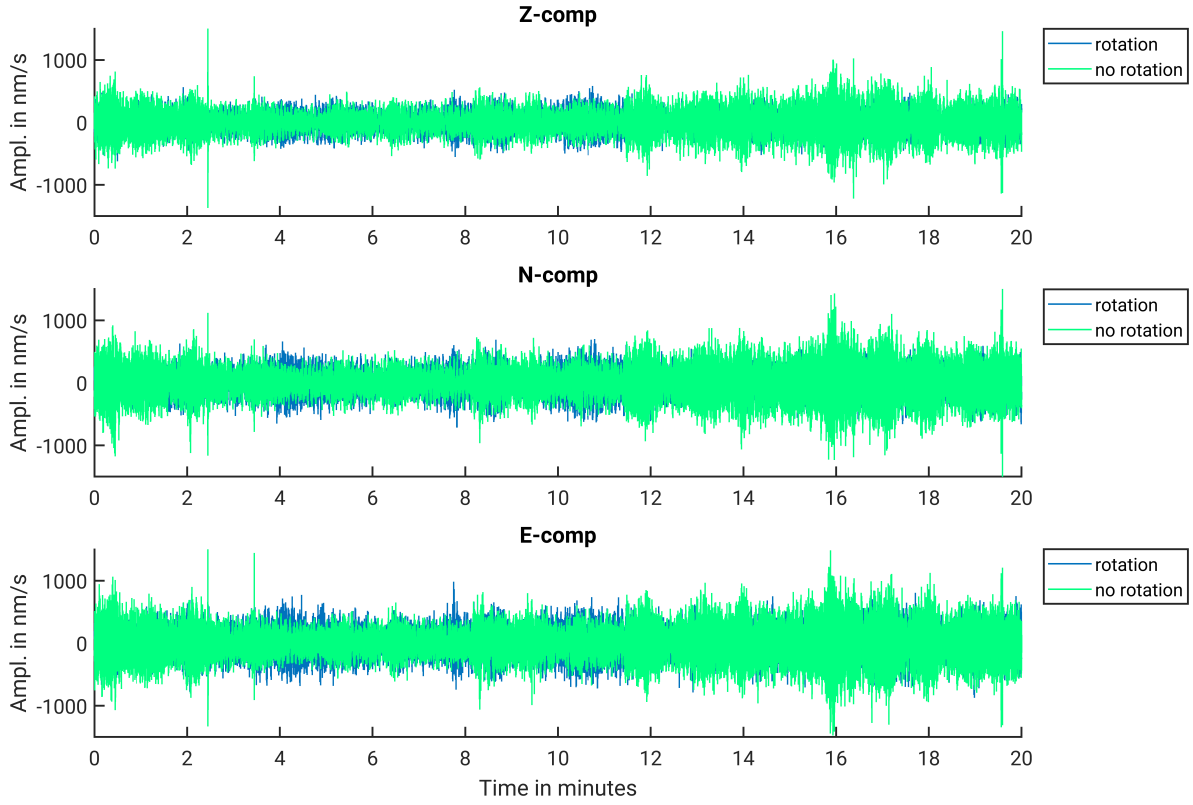

Figure 9.3: Ground velocity of the seismic station "WD17B" during a 20 min-long time window with (blue) and without (green) a rotational motion of a single WT in 1.5 km distance.

9.3 Impact of the emitted seismic signals on residents

As mentioned in the beginning of this thesis, one goal of the research project *TremAc* is the detection of the impact of emitted seismic signals by WTs on residents living nearby. A part of this task is the identification of related frequencies by comparing seismic recordings with numerical simulations (e.g. chapter 5) or the attenuation with distance (chapter 8). A basis of the evaluation for the impact of vibrations on humans is the DIN standard 4150/2+3. This standard assesses different frequency-dependent vibrations on humans as well as buildings and provides thresholds with regard to noticeability and building damages. In general, the noticeability limit of a stationary person is set to a value of around 0.1 mm/s for the ground velocity. This value slightly differs depending on the sensitivity of the person but can be an initial indication for the impact of WT-induced signals on human beings.

To determine the rotational effect of a single WT on the ground motion in the free-field, I select a 20 min time interval with (Fig. 9.3, blue) and without (Fig. 9.3, green) a rotational motion of the WT during high wind speeds (approx. 8 – 9 m/s). Fig. 9.3 shows the ground velocity of station "WD17B" at a single WT in SW Germany (see chapter 7, section 7.1.1, for exact location) for all three seismic components (Z, N and E). Both time windows show hardly any differences with regard to the seismic amplitude of the ground velocity. Moreover, the amplitudes range between 500 to 1000 nm/s on average for both operational conditions. These values are equivalent to 0.0005 mm/s and 0.001 mm/s and therefore more than a factor of 100 below the noticeability limit (0.1 mm/s) for a distance of about 1.5 km to the WT. I would like to point out that this observation is only valid for the ground velocity in the free-field. Any interaction with, for example, buildings is part of ongoing studies by the Institute of Soil Mechanics and Rock Mechanics at the KIT. Amplitudes of the ground velocity in the immediate vicinity of the WT (ca. 3 m distance) are shown in Nagel et al. (2019). Here, the amplitudes exceed the noticeability limit during

time windows in which the WT is in full operation (v_Z = 0.3 mm/s). However, I would like to remind that the limit is frequency-dependent and only valid for a stationary person in a quiet environment (which is obviously not the case in the immediate vicinity of the WT during high wind speeds). To conclude, the seismic recordings in the free-field do not exceed the recommended limits of the DIN standard 4150/2+3 by WT-induced seismic signals, even in the immediate vicinity of the WT.

To illustrate the impact of a rotational motion, Fig. 9.4 shows the PSD spectra corresponding to the time windows shown in Fig. 9.3 for each component, again with (Fig. 9.4, blue) and without (Fig. 9.4, green) an influence of the rotational motion. Especially the frequency range between 4 Hz and 8 Hz shows an increase of the PSD values, partially by a factor of 100, in combination with an arise of several discrete PSD peaks. These peaks were already allocated to the BPF and its multiples of the WT (see chapter 7, section 7.3). This increase is highly relevant concerning sensitive instruments like seismometers within observatories in the vicinity of WTs at high wind speeds, as was already pointed in the introduction of this thesis.

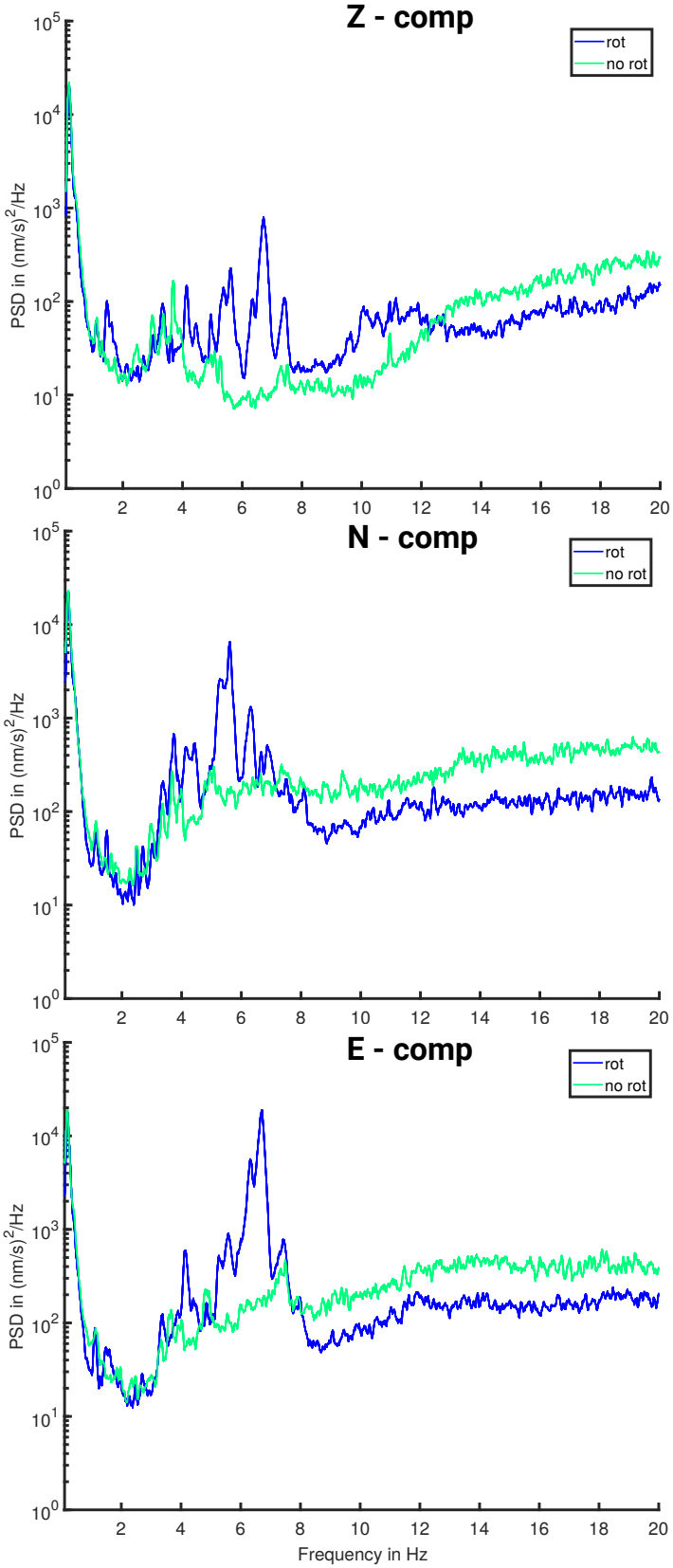

Figure 9.4: The PSD over the frequency range from 0.1 Hz to 20 Hz for the seismic station “WD17B” according to ground velocity shown in Fig. 9.3. The seismic noise level clearly depends on the used time window, especially for frequencies higher than 8 Hz.

10 Conclusions and outlook

In this thesis I present results of more than twenty seismic measurement campaigns conducted in the vicinity of single wind turbines (WTs) and wind farms. Thereby I identified several power spectral density (PSD) peaks at different discrete frequencies which can clearly be classified as WT-induced seismic signals. The investigation of source mechanisms and the impact on seismic recordings of nearby seismic stations as well as on residents represent a major part of this study. The influence of the local geological settings was analyzed by determining the attenuation factor for each specific site with respect to the frequency. The defined attenuation models (chapter 8) form the essential basis for future prediction models, especially in terms of an increase of the seismic amplitude (or PSD value) at different distances for various frequency bands. Numerical simulations of generic WT models similar to the properties of WTs measured within the scope of this thesis (e.g. chapter 5) allowed the allocation of observed peaks in the seismic PSD spectra to either the blade-passing frequency (BPF, three times the rotation rate) and its multiples or to eigenfrequencies of the tower-nacelle-system. Moreover, an interaction of both mechanisms could be observed and evaluated for the first time using the interdisciplinary approach within the research project *TremAc*. The large-scale experiment SMARTIE1 with more than 36 seismic stations offered the opportunity to simultaneously analyze the radiation pattern of a single WT at different distances and to observe the behavior of the induced seismic signals along linear profiles with different azimuths up to 1.5 km distance. An equally distributed radiation of induced seismic signals in all directions could be determined for the WT located at the Fraunhofer Institute for Chemical Technology (ICT) in Pfinztal, SW Germany. The effect of several operating WTs within a wind farm was analyzed in chapter 7 using a gradual start-up experiment and was compared to results of measurements conducted at a single WT of the same type. The relative distance to the seismic station in the immediate vicinity of the wind farm has a stronger influence on the seismic recordings than the number of operating WTs. Seismic measurements near the town of Landau, SW Germany, have shown a stronger effect of attenuation with depth than in the horizontal direction using seismic borehole recordings. Furthermore, a localization of individual wind farms as distinct seismic sources has been possible by migrating the signal energy of cross-correlograms computed for continuous seismic signals in the same area (chapter 4). In the following I answer the key questions formulated in chapter 1 to summarize the main results within the framework of this thesis.

1. Is it possible to identify WT-induced seismic signals based on their spectral content and allocate them to the BPF or different parts of the WT using seismic recordings in combination with numerical simulations?

This study demonstrates that seismic recordings are heavily influenced by WTs in the frequency range from 0.1 Hz to 20 Hz up to 9 km distance away relative from the location of these WTs. This influence appears to be less prominent with distance, depending on the local geological conditions. Moreover, seismic recordings in the immediate vicinity of the WT (e.g. on top of the tower foundation) represent an appropriate validation for numerical simulations (multi-body simulations or beam-element based finite-element models). By analyzing seismic recordings in combination with high-resolution SCADA data, this thesis shows that the major PSD peaks at nearby seismic stations correspond to the BPF of the WT and its multiples. The excited oscillations are coupled through the WT's tower and the foundation to the subsurface and propagate to the seismic stations. In addition, this work also demonstrates that the most prominent peak in the PSD spectrum around 1.6 Hz (section 7.2) constitutes a result of an interaction of the first harmonic of the BPF (also known as the 6-P excitation) with the second bending mode of the tower in combination with eigenfrequencies of the WT's blades. This specific peak is visible at distances up to several kilometers away and was already observed by previous studies (e.g. Stammler and Ceranna,

2016). By identifying the source mechanisms of WT-induced seismic signals, future studies may be able to develop strategies and methods to optimize WTs with respect to reducing vibration emissions, for instance by decoupling the foundation from the subsurface. This could lead to a harmonic co-existence of WTs and sensitive technical instruments like seismometers. Furthermore, I compared seismic recordings with optical measurements (here laser Doppler vibrometry) at the tower wall of a WT (section 5.5). This comparison shows a very good agreement with the findings mentioned before and would be a useful complement for future studies. New developments in this research field (like tracking systems) may lead to a better understanding of tower and blade vibrations and their coupling into the subsurface.

2. What is the influence of the local subsurface on the attenuation behavior of the induced seismic signals with respect to distance?

A major part of this thesis focused on determining the influence of the geological conditions at each measuring site, especially in terms of the attenuation behavior of the WT-induced signals. To summarize, this work provides attenuation models for five different geological settings by fitting a power-law decay proportional to $1/r^b$, with r as the distance between the WT and the recording station. I demonstrated for the first time that geometrical spreading has the main influence on the attenuation of WT-induced seismic surface waves in the lower frequency range up to 4 Hz. Here, the seismic amplitudes decay mostly with $1/\sqrt{r}$ (equivalent to a PSD decay with 1/r), independent of the geological setting. However, the b value rises significantly for higher frequencies. This could be explained by an increased impact of intrinsic and scattering attenuation in the subsurface with increasing frequency, as the ratio of the size of the heterogeneities to the seismic wavelength changes. These heterogeneities lead to seismic scattering due to lateral medium variations along the propagation path and with that to a higher attenuation of the seismic waves. Also intrinsic attenuation (conversion of seismic energy to heat) due to anelastic effects needs to be considered, especially for softer material like peat or sediments. A unique location of highly unconsolidated material is represented by the *Energieberg* (mountain for energy production) in the center of the city of Karlsruhe. Induced seismic signals of WTs on top of the hill are not visible farther away than 130 m (except a PSD peak at 2.5 Hz) due to a strong damping of seismic signals along the propagation path (section 8.1.5). An example of solid rock (more precisely granite) is shown for the Black Forest Observatory (BFO), SW Germany (section 8.1.4). I identified an influence of seismic recordings at the BFO in the frequency range from 1 Hz to 2 Hz of already existing WTs in about 9 km distance. Especially the PSD peak around 1.2 Hz is clearly visible in the PSD spectrum of station BFO at high wind speeds and can now be allocated to the *Enercon E-92* WT.
The influence of heterogeneities and anelasticity, and with that the influence of the geological setting at each site, should increase with increasing frequency. For frequencies higher than 6 Hz, the attenuation factor b increases up to 3.5 for the PSD decay. Clear observations of WT-induced seismic signals with higher frequencies are very sparse for distances of more than 1 km. However, it cannot be ruled out that permanent seismic stations at very quiet locations, provided there is a low background seismic noise level, could be influenced even in higher frequency bands. As mentioned before, the resulted attenuation models may form the basis of future prediction models and are essential to estimate the increase of the seismic noise level in a certain frequency band for nearby observatories or sensitive structures.

3. Is there a significant impact of emitted vibrations on residents living in the immediate vicinity of WTs?

The impact of seismic and acoustic emissions originating from WTs on the human health is part of ongoing discussions within the society, which are partly based on non-scientific facts and emotional reasoning. This thesis has the aim to provide reliable arguments for the evaluation of any possible impact with regard to WT-induced seismic signals. The basis of the evaluation is the DIN standard 4150/2+3. This standard assesses different frequency-dependent vibrations on humans as well as buildings and provides thresholds with regard to noticeability and building damages. In general, the noticeability limit of a stationary person is set to a value of around 0.1 mm/s for

the ground velocity. An example of the ground velocity for free-field conditions in 1.5 km distance is shown in chapter 9, section 9.3. The maximum amplitude of the ground velocity ranges from 500 to 1000 nm/s on average and shows hardly any difference between an operating or stationary WT for all three seismic components (Z, N and E). These values are equivalent to 0.0005 mm/s and 0.001 mm/s and are therefore more than a factor of 100 below the above-mentioned noticeability limit. A frequency dependency is not included and also not necessary because a weighting of the noticeability limit for different frequencies leads to an even higher threshold. The limit of 0.1 mm/s is exceeded in the immediate vicinity of the WT (3 m distance). Here, the amplitudes of the ground velocity could reach maximum values of about 0.3 mm/s (Nagel et al., 2019). This specific case, however, constitutes an extreme example and is irrelevant for studies aiming to analyze the impact of WT-induced seismic signals on the human health. Any interaction of the identified seismic signals with buildings is part of ongoing studies by the Institute of Soil Mechanics and Rock Mechanics at the KIT.

10.1 Outlook

The subject of seismic and acoustic signals induced by WTs is becoming more and more relevant for the proper evaluation of new WT sites, especially with regard to existing seismic stations, as the trend in power production is towards eco-friendly technologies such as WTs. As this study pointed out, WTs represent a complex seismic source and their interaction with seismic recordings is not fully understood. This thesis now shows that a validation of numerical simulations with actual measurements is feasible and highly recommended. Future studies must focus on further developments of the simulations, also in order to create prediction models with regard to local conditions such as the geological setting or the number and types of WTs. To improve the simulations it is necessary to involve manufacturers to integrate exact dimensions into already existing generic models and to obtain permission to publish the results. Moreover, numerical modelling of seismic noise radiated by WTs using the Boundary Element Method, as presented in Gortsas et al. (2017), must be further improved and validated by various seismic measurements.

The knowledge of the “undisturbed” seismic noise level at a specific site, i.e. before the start-up of new WTs, is of fundamental importance to clearly evaluate the influence on seismic recordings. Therefore, an involvement of seismic station operators at an early stage, for instance already during the planning stage of new WTs, should be obligatory. By analyzing the current seismic noise level in conjunction with prediction models, the operators are then able to calculate and evaluate the estimated impact on future seismic recordings (or other sensitive measurements).

This study demonstrates the complex radiation pattern of a single WT (chapter 6) using simultaneously recorded particle motions. The calculated particle diagrams of a randomly chosen 20 s-long time window show multiple foundation movements of the WT, including tilt and rotation. Explanations of these effects must be the subject of future studies. This can be done, for instance, by using rotational seismometers on the foundation and in the immediate vicinity of the WT. Rotational seismology is an emerging research field within the seismic community (e.g. Schmelzbach et al., 2018). New rotational sensors are able to record translational motion as well as rotation. As the particle ground motion has six degrees of freedom, the sensors are able to characterize the complete seismic wavefield at a single point. Using this new technology, future studies will provide a much more detailed understanding of the radiation pattern of WTs.

Additional projects related to this study are currently in progress. The project *Definition von Schutzradien um seismologische Messeinrichtungen bei der Errichtung von Windkraftanlagen*, funded by the Saxonian Office for Environment, Agriculture and Geology, determines a protection radius around seismic stations during the start-up of new WTs. The ongoing project *Minderung der Störwirkung von Windenergieanlagen auf seismologische Stationen* (MISS, URL: https://www.uni-muenster.de/Physik.GP/en/MISS/project.html, last accessed: 06.06.2019) wants to investigate methods to reduce the impact of WT-induced seismic signals on seismic stations using, for

instance, vibration absorbers inside the WT or metamaterials. Also, measurement campaigns at offshore WTs are in the planning stage to investigate any influence on marine life such as dolphins or whales. Bringing together all those studies concerning the triggering of seismic signals by WTs will help to get a better understanding of WT vibrations and their interaction with the environment. This will finally lead to a harmonic co-existence of WTs, sensitive instruments and residents, which is necessary for a successful energy turnaround towards eco-friendly power production.

Acknowledgments

I would like to express my appreciation and gratitude to colleagues, friends and my family without whom this work would not have been possible.

First of all, I would like to thank **apl. Prof. Dr. Joachim Ritter** for supervising this thesis and the opportunity to work in his research group. He has always had a sympathetic ear for topics of any kind as well as valuable suggestions regarding publications or this thesis. Despite supporting rivaling football teams, the interaction with each other has always been very respectful and friendly. I also thank him for the opportunity to participate countless national and international conferences.

Next, I would like to thank **Prof. Dr. Andreas Rietbrock** for being the second supervisor of this thesis and for providing new lines of thinking.

It was a pleasure to work within the research project *TremAc*. I am thankful to all participants for fruitful discussions during several workshops and meetings. In particular, I would like to thank **Sven Nagel**, **Birger Luhmann** and **Dr. Gerhard Huber** for hours of intense discussions.

Many thanks to **Prof. Dr. Peter Styles**, **Sam Toon**, **Prof. Dr. Chris Fogwill** and the working group at Keele University for hosting me in the framework of the Networking Grant trip, kindly provided by the **Karlsruhe House of Young Scientists (KHYS)**. The intensive discussions gave me new fundamental insights into my research topic and I really appreciate the time and energy you have shown for hosting me.

No scientific work would be possible without a well-performing institute. For this reason I am immensely grateful to all members of the Geophysical Institute (GPI) at the KIT for providing the environment to make this thesis possible. I thank **Petra Knopf**, **Claudia Payne**, **Kerstin Dick**, **Rainer Plokarz** and **Thomas Nadolny** for solving technical and formal issues during my time at GPI. A special thanks goes to **Werner Scherer** who became a good friend during the time we spent on several measurement campaigns. Your humorous and direct approach was always a pleasure, especially when solving many annoying technical problems. I wish you all the best for the future! I am thankful to **Tobias Friedrich** and **Dr. Thomas Forbriger** who gave me the permission to print our joint results in the scope of this thesis. I really enjoyed our collaborative research! Also many thanks to **Dr. Thomas Hertweck** for proofreading this thesis and providing constructive feedback.

My colleagues **Sarah**, **Michi** and **Mohsen** deserve special thanks for many conversations about geophysical and non-geophysical topics. It has been a lot of fun spending time with you and I hope we will keep in touch with each other!

Last but not least I would like to thank my family (**Susanne**, **Uwe** and **Thomas**) as well as my beautiful wife **Sandra** who have always believed in me and gave me steady support. I really look forward to becoming a trio!

Funding

TremAc was funded by the **Federal Ministry for Economic Affairs and Energy** on the basis of a decision of the German Bundestag (project number 0325839).

The author was supported by the *Networking Grant* of the **Karlsruhe House of Young Scientists (KHYS)** which allowed him to visit Keele University in June 2018.

A Comparison between a seismic spectrogram and SCADA data of the WT

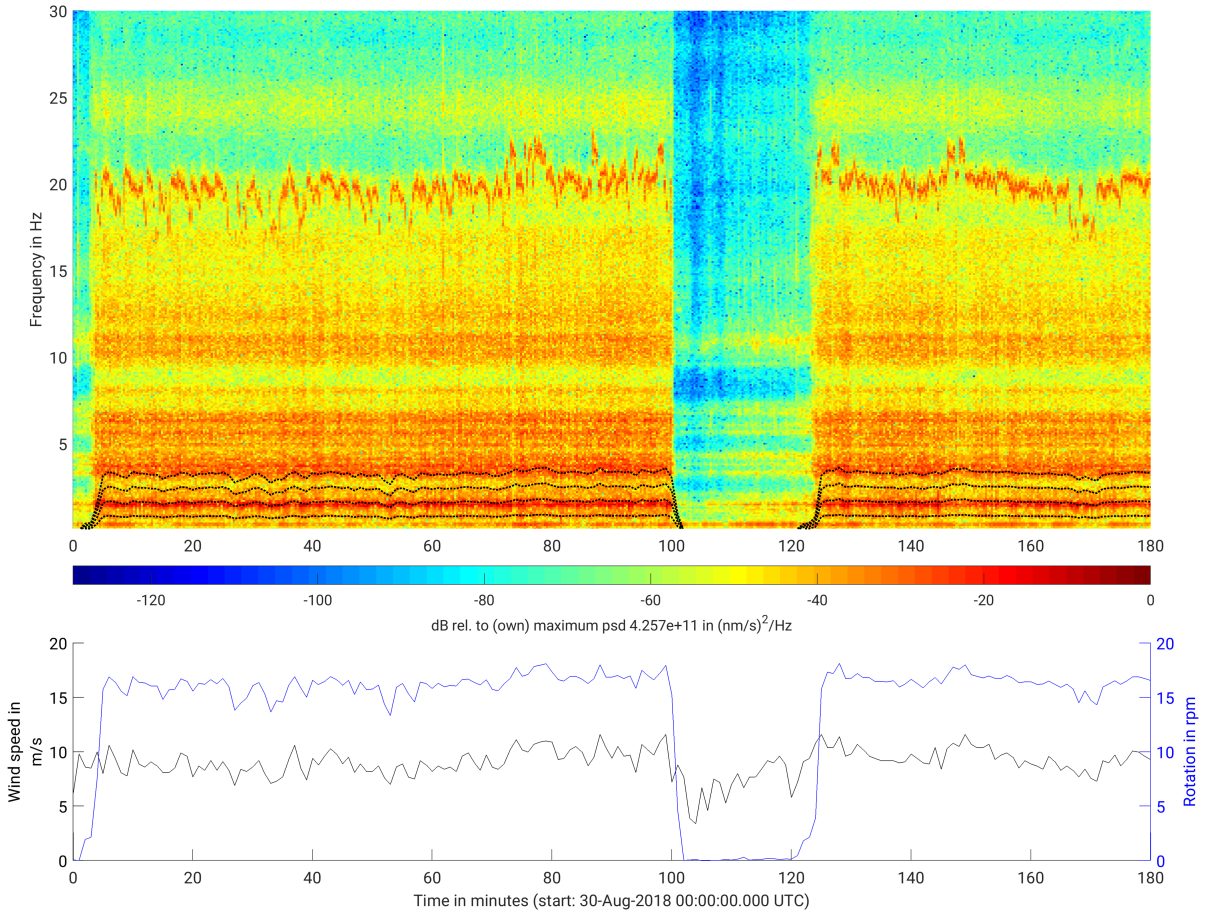

Figure A.1: Top: Frequency spectrogram of the vertical ground motion velocity, measured on the foundation of the WT during a time interval of 3 hours. The BPF and its multiples are marked as black dotted lines. Bottom: The corresponding wind speed (black) and the rotation rate (blue) measured on top of the nacelle.

B Gradual start-up of a wind farm

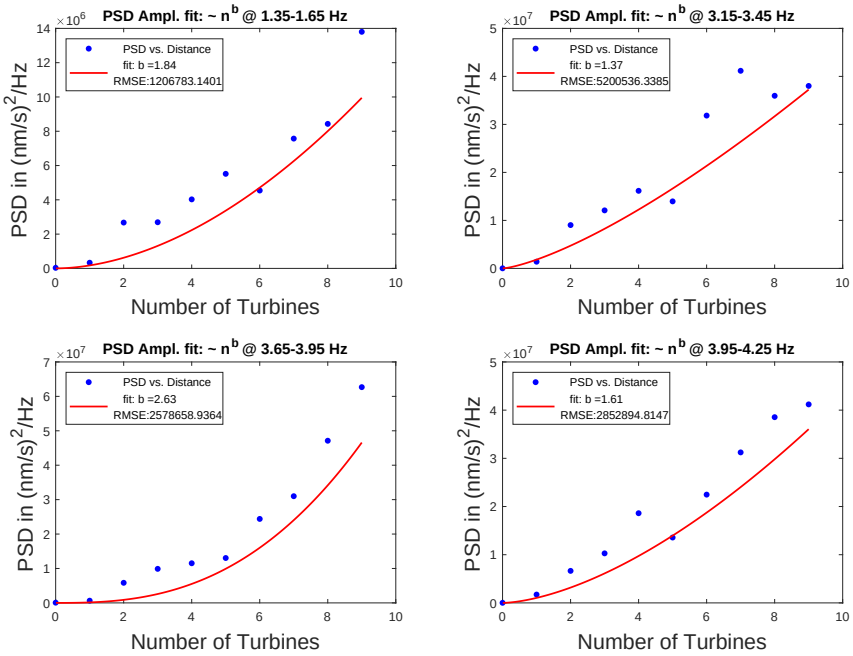

Figure B.1: Increase of the PSD values at the seismic station WD18D (see Fig. 7.2) for four different frequency bands during the start-up experiment at a wind farm. We fit a power-law proportional to n^b (red) to the picked PSD maxima (blue dots).

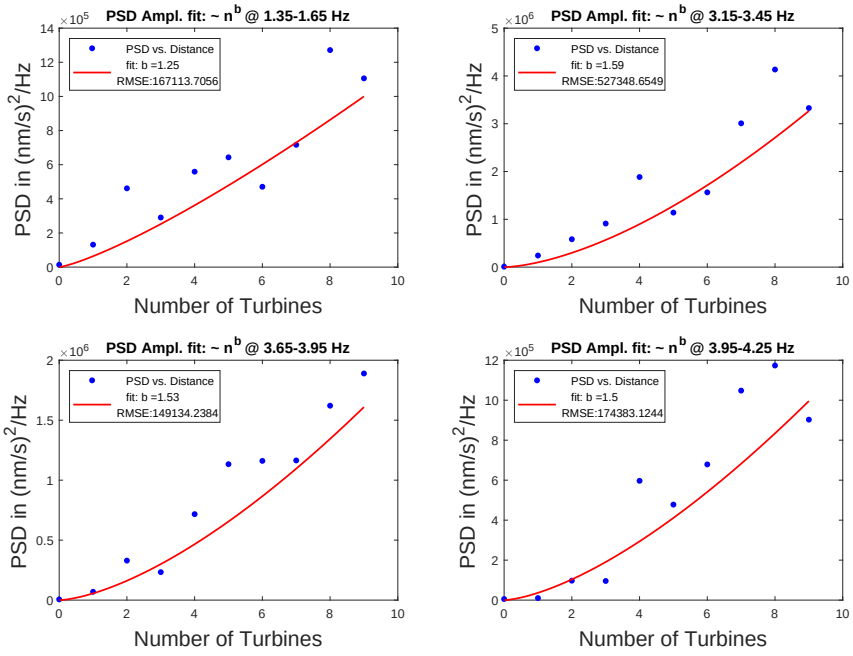

Figure B.2: Increase of the PSD values at the seismic station WD18K (see Fig. 7.2) for four different frequency bands during the start-up experiment at a wind farm. We fit a power-law proportional to n^b (red) to the picked PSD maxima (blue dots).

C Seismic Recordings for SMARTIE1: Seismic Monitoring And Research of Wind Turbine Induced Emissions 1, DEC. 2018 – JAN. 2019, Pfinztal, SW Germany

This chapter focuses on the SMARTIE1 experiment, in particular on the used sensors and data loggers as well as the data quality. It provides additional information to chapter 6 with regard to data accuracy and availability. This chapter has been published in:

Zieger, T., Lerbs, N., Ritter, J.R.R., Korn, M. (2019),
Seismic Recordings for SMARTIE1: Seismic Monitoring And Research of Wind Turbine Induced Emissions 1, DEC. 2018 – JAN. 2019, Pfinztal, SW Germany,
Scientific Technical Report STR – Data 17/02, GIPP Experiment and Data Archive, Potsdam: GFZ German Research Centre for Geosciences

C.1 Abstract

SMARTIE1 is a joint seismological experiment of the Karlsruhe Institute of Technology (KIT) and the Leipzig University. We installed in total 36 seismic stations as ring-like and profile-like measurements near to a single wind turbine (WT) at the Fraunhofer Institute for Chemical Technology (ICT) in Pfinztal, SW Germany, for 21 days. The main goals of this project are a better understanding of a single WT as a seismic source and the development of propagation models for the WT-induced seismic signals, depending on the geological properties.

C.2 Introduction

The impact of wind turbines (WTs) and their seismic emissions on seismic stations are the subject of several studies in the last few years. A significant increase of the overall seismic noise level with increasing wind speed have been found for seismic stations in the vicinity of WTs. Moreover, discrete frequency peaks can be allocated to the tower oscillation and the blade passing frequency of the WT (BPF, three times the rotation rate) as well as its multiples. These frequency peaks appear during time windows with high wind speeds.
The main goals of the joint large-scale experiment (SMARTIE1) are the determination of the radiation pattern of the WT at different distances and the development of propagation models through the subsurface, to estimate protection radii for seismic stations in the future. Since a single WT will not cause possible interference effects compared to multiple WTs in wind farms, the area around the Fraunhofer Institute for Chemical Technology (ICT) is highly suitable for our purposes. The WT of the type Qreon Q82 has a hub height of 101 m and a maximum power output of 2 megawatt (MW). SCADA (Supervisory Control And Data Acquisition) data are provided by the ICT for the measurement period, including wind speed and rotation rate.
In December 2018, in total 36 seismic stations have been deployed with ring-like and profile-like layouts. Twenty seismic stations (CUBE3 data loggers with Mark 1s sensors) were provided by the GIPP (Geophysical Instrument

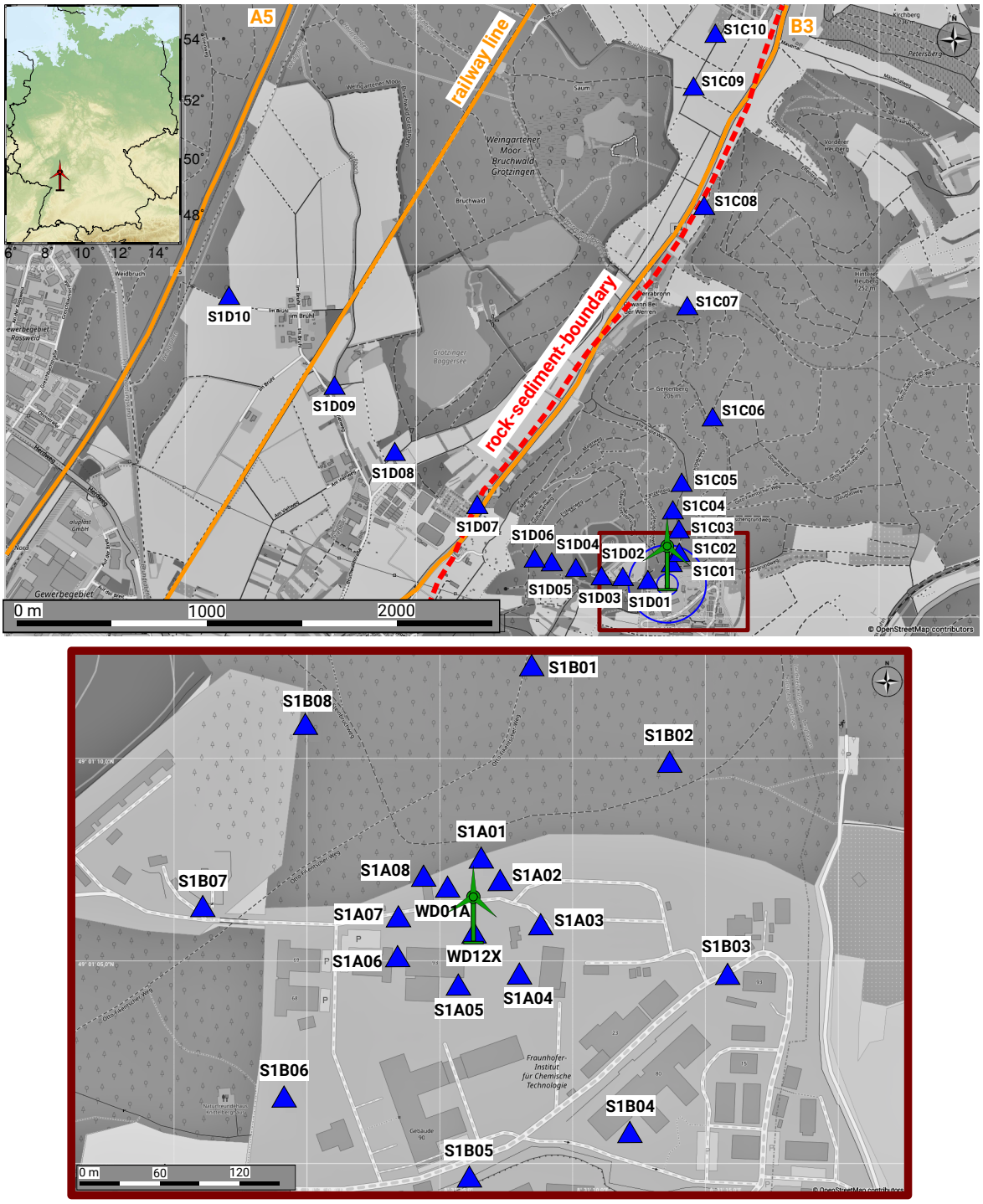

Figure C.1: Map of the study area around a single WT (green symbol) at the Fraunhofer Institute of Chemical Technology. Seismic stations are marked as blue triangles. Top: Seismic stations provided by the GIPP as two profile layouts with an azimuth of 0° and 270°, respectively, to the WT. Bottom: Seismic stations provided by the Leipzig University as two ring-like layouts with a radius of 50 m and 200 m, respectively, as well as two seismic broadband stations provided by the KArlsruhe BroadBand Array (KABBA). Both stations were deployed in 2016 (WD01A) and 2017 (WD12X).

Figure C.2: Exemplary instrument installations at recording station S1D3. The sensors were protected with plastic bags (black) against moisture and buried to a depth of about 30 cm. Left: Buried sensor inside the plastic bag. The CUBE3 data logger is located at the surface to ensure a stable GPS connection. Right: The seismic sensor during the installation.

Pool Potsdam) and sixteen seismic stations (geophones and CUBE3 data loggers) were provided by the Leipzig University. The seismic stations operated for twenty-one and seven days, respectively, due to the usage of various power supplies. In addition, two permanent broadband stations were provided by the KArlsruhe BroadBand Array (KABBA).

C.3 Data Acquisition

C.3.1 Experiment Design and Schedule

Within the framework of SMARTIE1, we deployed and operated in total 36 seismic stations for a time duration of 21 days at a single WT, as well as two permanent seismic broadband stations (Fig. C.1). The measurement was conducted during the Christmas holidays to achieve a reduced seismic noise level due to marginal anthropogenic activities in the region of interest.

20 temporary seismic stations (S1C01–C10 and S1D01–D10) were deployed as two profiles with an azimuth of 0° (north direction) and 270° (west direction) to the WT, respectively, with a total length of 3 km each. 16 temporary seismic stations (S1A01–A08 and S1B01–B08) were deployed as two ring-like layouts with a radius of 50 m and 200 m, respectively. As power supply we used eight 1.5 V block batteries for the profile-like measurements and two 1.5 V block batteries for the ring-like measurements. The sensors were buried during the installation to a depth of about 30 cm to minimize the direct impact of wind on the sensors. The installation took place on 19–20 December 2018. The stations were removed on 10 January 2019.

The stations WD01A and WD12X are two permanent seismic broadband stations deployed in 2016 (WD01A) and 2017 (WD12X). The station WD12X is located on the foundation inside the WT.

C.3.2 Network Geometry and Location

Table C.1 lists the station names with corresponding locations, elevations, sensor type and data logger type including serial numbers (IDs) as well as runtime periods of the individual data loggers.

Table C.1: Instrumentation information including serial numbers of the used sensors and data loggers for each recording station.

Station	Location	Alt/m	Sensor, ID	Logger, ID	Runtime
S1A01	49.01871N, 08.51848E	249	PE-6/B	CUBE3-B2L	2018/12/19-2018/12/25
S1A02	49.01859N, 08.51866E	249	PE-6/B	CUBE3-AUF	2018/12/19-2018/12/25
S1A03	49.01827N, 08.51911E	241	PE-6/B	CUBE3-B2K	2018/12/19-2018/12/25
S1A04	49.01793N, 08.51888E	243	PE-6/B	CUBE3-B2W	2018/12/19-2018/12/25
S1A05	49.01787N, 08.51826E	249	PE-6/B	CUBE3-AUD	2018/12/19-2018/12/25
S1A06	49.01805N, 08.51761E	259	PE-6/B	CUBE3-B2T	2018/12/19-2018/12/25
S1A07	49.01833N, 08.51763E	248	PE-6/B	CUBE3-B2N	2018/12/19-2018/12/25
S1A08	49.01862N, 08.51790E	247	PE-6/B	CUBE3-B2X	2018/12/19-2018/12/25
S1B01	49.02010N, 08.51902E	208	PE-6/B	CUBE3-B2S	2018/12/19-2018/12/25
S1B02	49.01940N, 08.52046E	240	PE-6/B	CUBE3-B2P	2018/12/19-2018/12/25
S1B03	49.01795N, 08.52109E	235	PE-6/B	CUBE3-AUE	2018/12/19-2018/12/25
S1B04	49.01683N, 08.52003E	244	PE-6/B	CUBE3-B2M	2018/12/19-2018/12/25
S1B05	49.01654N, 08.51836E	241	PE-6/B	CUBE3-B2V	2018/12/19-2018/12/25
S1B06	49.01708N, 08.51641E	237	PE-6/B	CUBE3-AUC	2018/12/19-2018/12/25
S1B07	49.01842N, 08.51559E	240	PE-6/B	CUBE3-B2U	2018/12/19-2018/12/25
S1B08	49.01965N, 08.51666E	247	PE-6/B	CUBE3-B2R	2018/12/19-2018/12/25

S1C01	49.01921N, 08.51844E	242	MARK-3047	CUBE3-817	2018/12/19-2019/01/10
S1C02	49.01954N, 08.51876E	240	MARK-3046	CUBE3-823	2018/12/19-2019/01/10
S1C03	49.02068N, 08.51903E	230	MARK-4200	CUBE3-815	2018/12/19-2019/01/10
S1C04	49.02159N, 08.51854E	216	MARK-3051	CUBE3-813	2018/12/19-2019/01/10
S1C05	49.02282N, 08.51928E	202	MARK-3055	CUBE3-873	2018/12/19-2019/01/10
S1C06	49.02588N, 08.52153E	220	MARK-3043	CUBE3-821	2018/12/19-2019/01/10
S1C07	49.03130N, 08.51944E	175	MARK-2861	CUBE3-812	2018/12/20-2019/01/10
S1C08	49.03599N, 08.52075E	144	MARK-3050	CUBE3-818	2018/12/20-2019/01/10
S1C09	49.04163N, 08.51993E	112	MARK-3049	CUBE3-826	2018/12/20-2019/01/10
S1C10	49.04402N, 08.52151E	113	MARK-2933	CUBE3-819	2018/12/20-2019/01/10
S1D01	49.01836N, 08.51664E	239	MARK-3044	CUBE3-889	2018/12/19-2019/01/10
S1D02	49.01838N, 08.51487E	233	MARK-4193	CUBE3-824	2018/12/19-2019/01/10
S1D03	49.01842N, 08.51344E	224	MARK-3039	CUBE3-607	2018/12/19-2019/01/10
S1D04	49.01883N, 08.51143E	219	MARK-3053	CUBE3-827	2018/12/19-2019/01/10
S1D05	49.01906N, 08.50963E	218	MARK-3040	CUBE3-848	2018/12/19-2019/01/10
S1D06	49.01933N, 08.50869E	215	MARK-4180	CUBE3-876	2018/12/19-2019/01/10
S1D07	49.02189N, 08.50441E	125	MARK-3054	CUBE3-608	2018/12/19-2019/01/10
S1D08	49.02436N, 08.49835E	117	MARK-4181	CUBE3-830	2018/12/19-2019/01/10

S1D09	49.02754N, 08.49405E	114	MARK-3048	CUBE3-816	2018/12/19-2019/01/10
S1D10	49.03166N, 08.48649E	112	MARK-4201	CUBE3-822	2018/12/19-2019/01/10
WD01A	49.0185N, 08.5178E	246	STS-2	EDL PR6-24	2016/04/21
WD12X	49.0182N, 08.5183E	246	STS-2	EDL PR6-24	2017/06/14

C.3.3 Instrumentation

Sensors and data loggers of the profile measurements (C and D) were kindly provided by GIPP, in combination with external battery boxes. Sensors and data loggers of the ring-like measurements (A and B) were kindly provided by the Leipzig University. The seismic stations recorded data with three components (vertical, N-S, E-W) and a sampling rate of 100 Hz. Station WD01A and WD12X were kindly provided by the KArlsruhe BroadBand Array (KABBA) and recorded with a sampling rate of 200 Hz.

Sensors :

20 MARK L-4C-3D (nominal eigenfrequency: 1 Hz)
16 3-D Geophone PE-6/B (nominal eigenfrequency: 4.5 Hz)
2 Streckeisen STS-2 Broadband Sensor (nominal eigenfrequency: 0.008 Hz) For additional information see: http://www.gfz-potsdam.de/en/section/geophysical-deep-sounding/infrastructure/geophysical-instrument-pool-potsdam-gipp/instruments/seismic-pool/

Loggers :

36 seismic stations were equipped with DATA-CUBE3 (see https://www.gfz-potsdam.de/en/section/geophysical-deep-sounding/infrastructure/geophysical-instrument-pool-potsdam-gipp/pool-components/seismic-pool/recorder-dss-cube3/). The CUBE3 recorded continuously with 100 samples per second. The gain was set to 16.
Both STS-2 Broadband sensors were equipped with an EDL EarthData PR6-24, recorded continuously with 200 samples per second.

To achieve the true ground velocity, the instrument response needs to be deconvolved from the raw data via the logger and sensor characteristics listed in Table C.2.

C.4 Data Quality and Accuracy

Except of the seismic station S1B01, which suffered from numerous technical problems like an in-correct GPS position and inaccurate seismic amplitudes, all seismic stations contribute to the full data set during the measurement campaign in combination with continuous GPS recordings.
Fig. C.3 shows a record section for an earthquake near to Kamchatka (Russia) with a magnitude Mw = 7.2 for the vertical component. The seismic data is bandpass filtered between 0.5 – 2 Hz and the amplitude is normed per trace. The distance of each station is relative to the location of the WT at the Fraunhofer Institute for Chemical Technology (49.0182°N, 8.5183°E). All seismic stations recorded a clear onset of the earthquake P-phase. The signal to noise ratio (SNR) decreases with increasing distance. This can be explained by the locations of the sensors. The stations near to WT were installed on the shoulder of the Upper Rhine Graben. The more distant stations were located inside the Upper Rhine Graben, a rift valley filled with unconsolidated sediments. The overall seismic

Table C.2: Properties of the used sensors and data loggers.

Sensor	A/D conversion in counts/V	Sensitivity in V/(m/s)	Norm. factor	Poles	Zeros
MARK L-4C-3D	6.5574E+07	170	1	-4.443, 4.443i -4.443, -4.443i	0 0
3-D Geophone PE-6/B	6.5574E+07	28.8	1	-15.88, 23.43i -15.88, -23.43i	0 0
STS-2 Broadband Sensor	1.0E+06	1500	1	-3.700E-02, 3.700E-02i -3.700E-02, -3.700E-02i -1.564E+01, 0.000E+00i -9.734E+01, -4.007E+02i -9.734E+01, 4.007E+02i -2.552E+02, 0.000E+00i -3.748E+02, 0.000E+00i -5.203E+02, 0.000E+00i -1.053E+04, 1.005E+04i -1.053E+04, -1.005E+04i -1.330E+04, 0.000E+00i	0 0 -1.515E+01, 0.000E+00i -1.766E+02, 0.000E+00i -4.631E+02, 4.305E+02i -4.631E+02, -4.305E+02i

noise level of these stations is increased due to stronger anthropogenic activities inside the rift valley, e.g. due to nearby the highway (A5) or the main road (B3). Fig. C.4 shows the PSD spectra of all 36 seismic stations for two days with respect to the New Low Noise Level (NLNM) and the New High Noise Level (NHNM) after Peterson (1993).

C.5 Data Availability and Access

Data is archived at GFZ-GIPP datacenter and the Karlsruhe Institute of Technology (KIT), Geophysical Institute, where it will be provided freely available for further use after December 2019. The corresponding network code provided by FDSN is **X8**. When using the data, please give reference to this Scientific Technical Report STR - Data and to the respective data publication.

Acknowledgements

The WT at Pfinztal is part of the “RedoxWind” project. We gratefully acknowledge the funding by the Ministry of Economics, Labor and Housing of Baden-Württemberg, the Federal Ministry of Education and Research of Germany and the “Fraunhofer-Gesellschaft zur Förderung der angewandten Forschung e.V.” for this project. T.Z. is financed by the project “TremAc”, which is funded by the Federal Republic of Germany. Awarding authority: The Federal Ministry for Economic Affairs and Energy based on a resolution of the German Bundestag. Seismological instruments were kindly provided by the Geophysical Instrument Pool Potsdam (GIPP) at GFZ. We also thank the Saxonian Office for Environment, Agriculture and Geology, which finances the project “Definition von Schutzradien um seismologische Messeinrichtungen bei der Errichtung von Windkraftanlagen”, that is part of the project SMARTIE1. We thank Mohsen Koushesh, Veronika Koch and Philip Sarnecki for technical support during the field work.

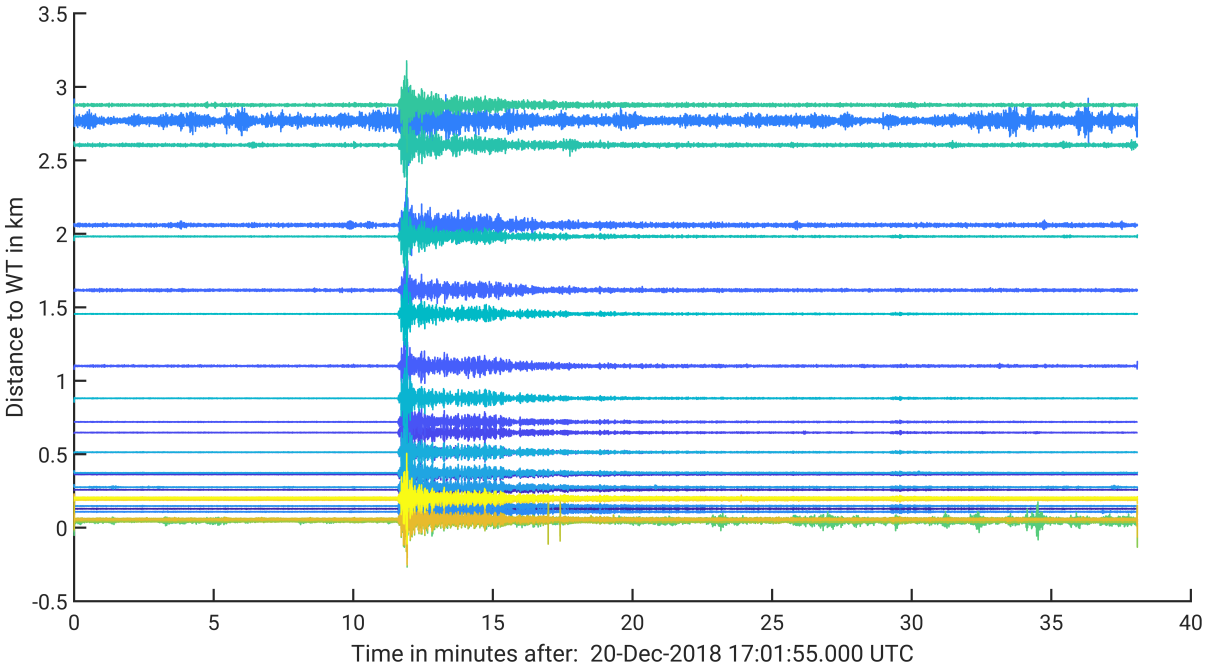

Figure C.3: Record section for an earthquake with a magnitude Mw = 7.2 near to Kamchatka. The distance of each seismic station is relative to the WT. The seismic data is bandpass filtered between 0.5 - 2 Hz. The color corresponds to the legend of Fig. C.4.

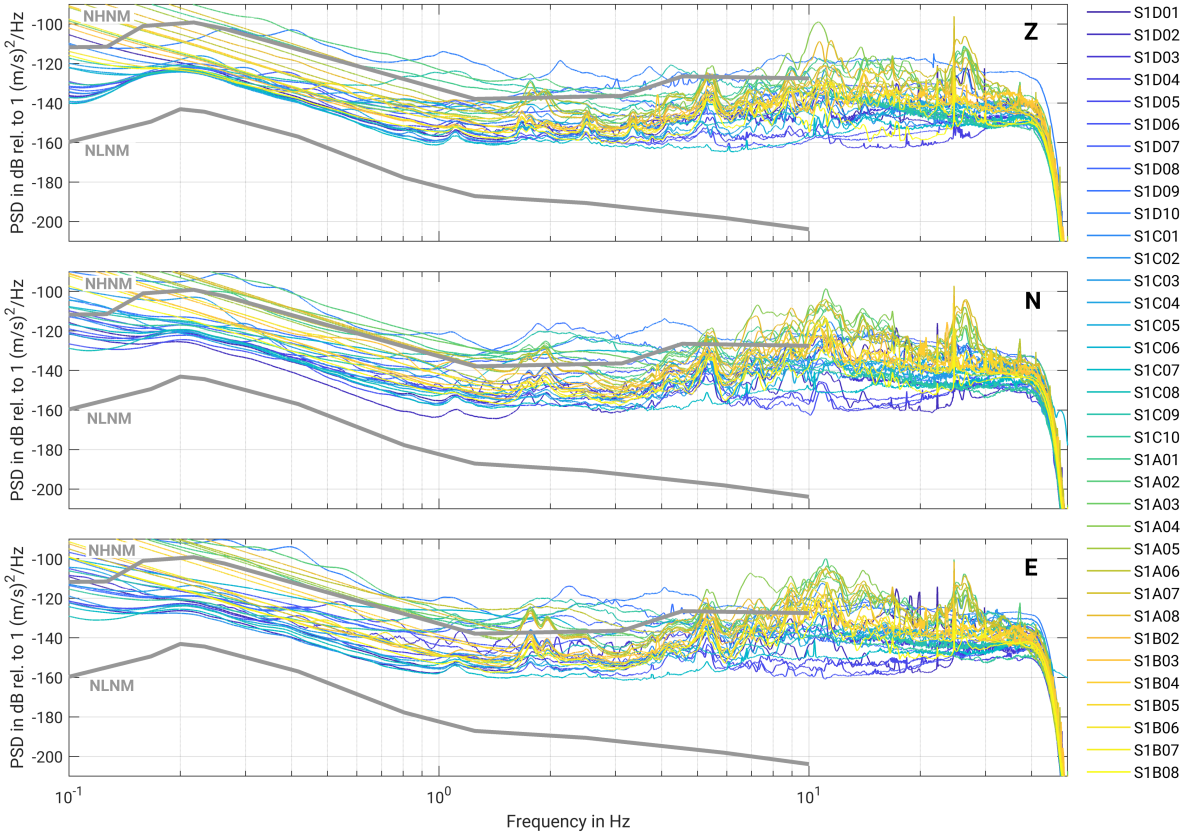

Figure C.4: PSD spectra for all used recordings calculated for a two-day period. The NLNM and NHNM after Peterson (1993) are indicated as gray lines.

D Energieberg WD13

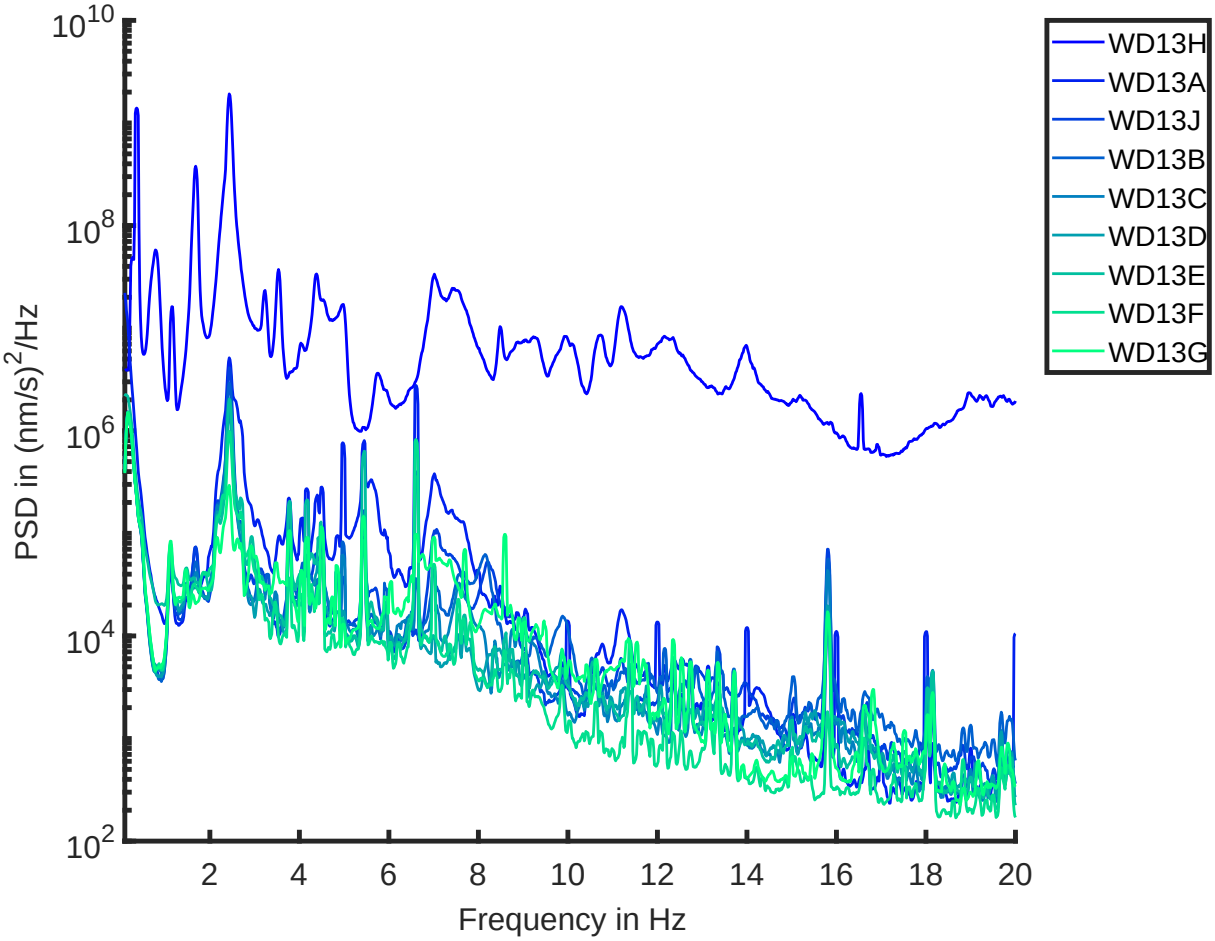

Figure D.1: The PSD over the frequency range from 0.1 Hz to 20 Hz for the seismic measurement campaign WD13. The colors symbolize the distance of the corresponding seismic station to the WT: blue (smaller distances) to green (larger distances). The wind speeds during the used four hours long time interval range from 10 – 13 m/s, measured at 200 m height by the Institute of Meteorology and Climate Research, KIT.

List of Figures

List of Tables

Bibliography

Aki, K. and Richards, P. (1980). *Quantitative seismology, Vol. 1*. W. H. Freeman and Company, New York.

ANSYS (2018). Inc. Ansys Documentation, Workbench Version 19.1. Manual. Canonsburg.

ANSYS (2019). Inc. Ansys Documentation, Workbench Version 19.2. Manual. Canonsburg.

Baisch, S., Fritschen, R., Groos, J., Kraft, T., Plenefisch, T., Plenkers, K., Ritter, J., and Wassermann, J. (2012). Empfehlungen zur Überwachung induzierter Seismizität - Positionspapier des FKPE e.V. *Mitteil. Deut. Geophys. Gesell.*, 3/2012:17–31.

Baisch, S. and Vörös, R. (2010). Reservoir induced seismicity: where, when, why and how strong? *Proceedings of World Geothermal Congress 2010, Bali, Indonesia, 25 - 29 April*.

Ballmer, S., Wolfe, C. J., Okubo, P. G., Haney, M. M., and Thurber, C. H. (2013). Ambient seismic noise interferometry in Hawai'i reveals long-range observability of volcanic tremor. *Geophys. J. Int.*, 194:512–523.

Betz, A. (1920). Das Maximum der theoretisch möglichen Ausnützung des Windes durch Windmotoren. *Zeitschrift für das gesamte Turbinenwesen*, 26.

Bormann, P. and Wielandt, E. (2002). Seismic signals and noise. *New Manual of Seismological Observatory Practice (NMSOP)*, 1.

Burton, T., Jenkins, N., Sharpe, D., and Bossanyi, E. (2011). *Wind Energy Handbook*. John Wiley & Sons, Ltd.

Campbell, W. (1924). Protection of Steam Turbine Disk Wheels from Axial Vibration. *Transactions of the ASME*, pages 31–160.

Cramér, H. (1942). On Harmonic Analysis in Certain Functional Spaces. *Kotz S., Johnson N.L. (eds) Breakthroughs in Statistics. Springer Series in Statistics (Perspectives in Statistics).*

Droznin, D. V., Shapiro, N. M., Droznina, S. Y., Senyukov, S. L., Chebrov, V. N., and Gordeev, E. I. (2015). Detecting and locating volcanic tremors on the Klyuchevskoy group of volcanoes (Kamchatka) based on correlations of continuous seismic records. *Geophys. J. Int.*, 203:1001–1010.

Flores Estrella, H., Korn, M., and Alberts, K. (2017). Analysis of the Influence of Wind Turbine Noise on Seismic Recordings at Two Wind Parks in Germany. *Journal of Geoscience and Environment Protection*, 5:76–91, doi: 10.4236/gep.2017.55006.

Friedrich, T., Zieger, T., Forbriger, T., and Ritter, J. R. R. (2018). Locating wind farms by seismic interferometry and migration. *J. Seismol.*, 22(6):1469–1483, doi: 10.1007/s10950–018–9779–0.

Gassenmeier, M., Sens Schönfelder, C., Delatre, M., and Korn, M. (2015). Monitoring of environmental influences on seismic velocity at the geological storage site for CO2 in Ketzin (Germany) with ambient seismic noise. *Geophys. J. Int.*, 200:524–533, doi: 10.1093/gji/ggu413.

Gortsas, T. V., Triantafyllidis, T., Chrisopoulos, S., and Polyzos, D. (2017). Numerical modelling of micro-seismic and infrasound noise radiated by a wind turbine. *Soil Dynamics and Earthquake Engineering*, 99:108–123, doi: 10.1016/j.soildyn.2017.05.001.

Groos, J. (2010). Broadband seismic noise: classification and greens function estimation. *Dissertation at the Karlsruhe Institute of Technology, KITopen ID: 1000021099*.

Groos, J. and Ritter, J. R. R. (2010). Seismic noise: a challenge and opportunity for seismological monitoring in densely populated areas. *Cahiers du Centre Européen de Géodynamique et de Séismologie*, 30:87–97.

Groos, J. C. and Ritter, J. R. R. (2009). Time domain classification and quantification of seismic noise in an urban environment. *Geophys. J. Int.*, 179:1213–1231.

Hau, E. (2008). *Windkraftanlagen - Grundlagen, Technik, Einsatz, Wirtschaftlichkeit*. Springer-Verlag Berlin Heidelberg.

Hensch, M., Dahm, T., Ritter, J., Heimann, S., Schmidt, B., Stange, S., and Lehmann, K. (2019). Deep low-frequency earthquakes reveal ongoing magmatic recharge beneath Laacher See Volcano (Eifel, Germany). *Geophys. J. Int.*, 216:2025–2036, doi: 10.1093/gji/ggy532.

Horstmann, T. and Forbriger, T. (2010). Verbesserung einer Kreuzkorrelationsanalyse mit ungünstiger Quellverteilung durch Slant Stack und Migrationsanalyse. *DGG Mittlg.*, 2/2010:19–28, doi: 10.5445/IR/1000021244.

Klein, L., Gude, J., Wenz, F., Lutz, T., and Krämer, E. (2018). Advanced computational fluid dynamics (CFD)–multi-body simulation (MBS) coupling to assess low-frequency emissions from wind turbines. *Wind Energ. Sci.*, 3:713–728, doi: 10.5194/wes–3–713–2018.

Li, K. L., Sgattoni, G., Sadeghisorkhani, H., Roberts, R., and Gudmundsson, O. (2017). A double-correlation tremor-location method. *Geophys. J. Int.*, 208:1231–1236.

Lokmer, I. and Bean, C. (2010). Properties of the near-field term and its effect on polarisation analysis and source locations of long period (LP) and very-long-period (VLP) seismic events at volcanoes. *J. of Volcanology and Geothermal Research*, 192:35–47, doi: 10.1016/j.jvolgeores.2010.02.008.

Lott, F., Ritter, J. R. R., Al-Qaryouti, M., and Corsmeier, U. (2017). On the analysis of wind-induced noise in seismological recordings. *Pure and Applied Geophysics*, 174(3):1453–1470, doi: 10.1007/s00024–017–1477–2.

Lutzmann, P., Göhler, B., Hill, C. A., and van Putten, F. (2016). Laser vibration sensing at Fraunhofer IOSB: review and applications. *Opt. Eng.*, 56(3):031215, doi: 10.1117/1.OE.56.3.031215.

Marcillo, O. E. and Carmichael, J. (2017). The detection of wind-turbine noise in seismic records. *Seismological Research Letters*, 211:1319–1327, doi: 10.1093/gji/ggx370.

Mündel, R. (2009). Überwachung zeitlicher Änderungen in der Ausbreitung elastischer Wellen als Folge von CO2-Einlagerungen im Untergrund. *Diploma Thesis, Institute for Geophysics und Geology, Leipzig University*.

Nagel, S., Zieger, T., Luhmann, B., Knödel, P., Ummenhofer, T., and Ritter, J. (2019). Erschütterungsemissionen von Windenergieanlagen. *Stahlbau*, 88(6):559–573, doi: 10.1002/stab.201900039.

Neuffer, T. and Kremers, S. (2018). How wind turbines affect the performance of seismic monitoring stations and networks. *Geophys. J. Int.*, 89(5):1826–1837, doi: 10.1785/0220170271.

Percival, D. B. and Walden, A. T. (1998). *Spectral analysis for physical applications: Multitaper and conventional univariate techniques*. Cambridge University Press, Cambridge.

Peterson, J. (1993). Observations and modelling of background seismic noise. *Open-file report 93-322. Albuquerque, New Mexico: U.S. Geological Survey*.

Pilger, C. and Ceranna, L. (2017). The influence of periodic wind turbine noise on infrasound array measurements. *Journal of Sound and Vibration*, 388:188–200, doi: 10.1016/j.jsv.2016.10.027.

Ritter, J. R. R., Wagner, M., Wawerzinek, B., and Wenzel, F. (2008). Aims and First Results of the TIMO Project - Tiefenstruktur des mittleren Oberrheingrabens. *Geotectonic Research*, 95:151–154.

Saccorotti, G., Piccinini, D., Cauchie, L., and Fiori, I. (2011). Seismic noise by wind farms: a case study from the virgo gravitational wave observatory, Italy. *Bull. Seismol. Soc. Am.*, 101(2):558–578, doi: 10.1785/0120100203.

Sato, H., Fehler, M. C., and Maeda, T. (2012). Seismic Wave Propagation and Scattering in the Heterogeneous Earth. *2nd edn. Springer, Berlin*.

Schmelzbach, C., Donner, S., Igel, H., Sollberger, D., Taufiqurrahman, T., Bernauer, F., Häusler, M., Van Renterghem, C., Wassermann, J., and Robertsson, J. (2018). Advances in 6C seismology: Applications of combined translational and rotational motion measurements in global and exploration seismology. *Geophysics*, 83(3):WC53–WC69, doi: 10.1190/GEO2017–0492.1.

Schofield, R. (2001). Seismic measurements at the Stateline wind project. *Rept. No. LIGO T020104-00-Z, Laser Interferometer Gravitational-Wave Observatory, available at https://dcc.ligo.org/public/0027/T020104/000/T020104-00.pdf, last accessed: 13.05.2019*.

Sgattoni, G., Gudmundsson, O., Einarsson, P., Federico Lucchi, F., Li, K. L., Sadeghisorkhani, H., Roberts, R., and Tryggvason, A. (2017). The 2011 unrest at Katla volcano: characterization and interpretation of the tremor sources. *J. Volcanol. Geotherm. Res.*, 33:63–78.

Shapiro, N. M., Ritzwoller, M. H., and G. D. Bensen, G. D. (2006). Source location of the 26 sec microseism from cross-correlations of ambient seismic noise. *Geophys. Res. Lett.*, 33:L18310.

Shearer, P. (2009). *Introduction to Seismology, Second Edition*. Cambridge University Press, Cambridge.

Slepian, D. (1978). Prolate spheroidal wave functions, Fourier analysis, and uncertainty - V: The discrete case. *Bell System Technical Journal*, 53:1371–1430, doi: 10.1002/j.1538–7305.1978.tb02104.x.

Spies, T., Schlittenhardt, J., and Schmidt, B. (2017). Abschlussbericht für das Verbundprojekt MAGS2: Mikroseismische Aktivität geothermischer Systeme 2 (MAGS2) - vom Einzelsystem zur großräumigen Nutzung: Einzelprojekt EP4: Ermittlung der seismischen Gefährdung bei tiefer geothermischer Energiegewinnung unter Berücksichtigung der regionalen und lokalen geologisch-tektonischen Strukturen.

Stammler, K. and Ceranna, L. (2016). Influence of wind turbines on seismic records of the Gräfenberg Array. *Seismological Research Letters*, 87(5):1075–1081, doi: 10.1785/0220160049.

Stein, F. (2013). Determination of seismic waveforms using passive seismic interferometry around Landau, SW Germany. *Diploma Thesis at the Karlsruhe Institute of Technology, KITopen ID: 1000037676, available at https://publikationen.bibliothek.kit.edu/1000037676, last accessed: 13.05.2019*.

Styles, P., England, R., Stimpson, I. G., Toon, S. M., Bowers, D., and Hayes, M. (2005). Microseismic and infrasound monitoring of low frequency noise and vibrations from windfarms: recommendations on the siting of windfarms in the vicinity of Eskdalemuir, Scotland. *Keele University, UK, available at https://www.keele.ac.uk/geophysics/appliedseismology/wind/FinalReport.pdf, last accessed: 13.05.2019*.

Sudhaus, H. and Ritter, J. (2009). Broadband frequency-dependent amplification of seismic waves across Bucharest, Romania. *KITopen-ID: 1000013519, available at https://publikationen.bibliothek.kit.edu/1000013519, last accessed: 13.05.2019*.

Thomson, D. J. (1982). Spectrum estimation and harmonic analysis. *Proceedings of the IEEE*, 70:1055–1096, doi: 10.1109/PROC.1982.12433.

Tong, W. (2010). *Wind Power Generation and Wind Turbine Design*. WIT Press, Southampton, Boston.

Vasterling, M., Wegler, U., Becker, J., Bruestle, A., and Bischoff, M. (2017). Real-time envelope cross-correlation detector: application to induced seismicity in the Insheim and Landau deep geothermal reservoirs. *J. Seismol.*, 21:193–208, doi: 10.1007/s10950–016–9597–1.

Welch, P. (1967). The Use of Fast Fourier Transform for the Estimation of Power Spectra: A Method Based on Time Averaging Over Short, Modified Periodograms. *IEEE Trans Audio Electroacoust.*, 15(2):70–73.

Westwood, R. F. and Styles, P. (2017). Assessing the seismic wavefield of a wind turbine using polarization analysis. *Wind Energy*, 20:1841–1850, doi: 10.1002/we.2124.

Widmer-Schnidrig, R., Forbriger, T., and Zürn, W. (2004). Windkraftanlagen als seismische Störquellen. *64. Jahrestagung der Deutschen Geophysikalischen Gesellschaft, Berlin*, page 541.

Withers, M., Aster, R., Young, C., and Chael, E. (1996). High-frequency analysis of seismic backround noise as a function of wind speed and shallow depth. *Bull. Seismol. Soc. Am.*, 86(5):1507–1515.

Xi Engineering Cosultants Ltd (2014). Seismic vibration produced by wind turbines in the Eskdalemuir region.

Zeng, X. and Ni, S. (2010). A persistent localized microseismic source near the Kyushu Island, Japan. *Geophys. Res. Lett.*, 37:L24307.

Zieger, T., Nagel, S., Lutzmann, P., Kaufmann, I., Ritter, J., Ummenhofer, T., Knödel, P., and Fischer, P. (2019). Simultaneous identification of wind turbine vibrations by using seismic data, elastic modeling and laser Doppler vibrometry. *Wind Energy*.

Zieger, T. and Ritter, J. (2018). Influence of wind turbines on seismic stations in the upper rhine graben, SW Germany. *J. Seismol.*, 22:105–122, doi: 10.1007/s10950–017–9694–9.

Ziegler, A. (2017). *Grundlagen der Baugrunddynamik. In: Bauwerksdynamik und Erschütterungsmessungen*. Springer Vieweg, Wiesbaden.